LIDAR AND RADAR STUDIES OF TURBULENCE, INSTABILITIES, AND WAVES IN THE

ARCTIC MIDDLE ATMOSPHERE

By

Jintai Li, M.S.

A Dissertation Submitted in Partial Fulfillment of the Requirements

for the Degree of

Doctor of Philosophy

In

Atmospheric Sciences

University of Alaska Fairbanks

August 2019

APPROVED:
Richard L. Collins, Committee Chair
David E. Newman, Committee Member
William R. Simpson, Committee Member
Denise L. Thorsen, Committee Member
Bifford P. Williams, Committee Member
G. Javier Fochesatto, Chair
Department of Atmospheric Sciences
Leah W. Berman, Dean
College of Natural Sciences and Mathematics
Michael A. Castellini, *Dean of the Graduate School*

Abstract

This dissertation presents new studies of gravity waves and turbulence in the Arctic middle atmosphere. The studies employ lidars and radar to characterize wave activity, instability and turbulence.

In the lidar-based studies, we analyze turbulence and wave activity in the MLT based on lidar measurements of atmospheric temperature, density and sodium density, temperature and wind. This combination of measurements provides simultaneous characterization of both the atmospheric stability as well as material transport that allow us to estimate the eddy diffusion coefficient associated with turbulence. We extend the scope of previous studies by developing retrievals of potential temperature and sodium mixing ratio from the Rayleigh density temperature lidar and sodium resonance density lidar measurements. We find that the estimated values of turbulent eddy diffusion coefficients, K, of 400-2800 m^2/s, are larger than typically reported (1-1000 m^2/s) while the values of the energy dissipation rates, ε, of 5-20 mW/kg, are more typical (0.1-1000 mW/kg). We find that upwardly propagating gravity waves accompany the instabilities. In the presence of instabilities, we find that the gravity waves are dissipating as they propagate upward. We estimate the energy available for turbulence generation from the wave activities and estimate the possible turbulent energy dissipation rate, ε_{GW}. We find that the values of ε_{GW} are comparable to the values of ε. We find that the estimate of the depth of the layer of turbulence are critical to the estimate of the values of both ε and ε_{GW}. We find that our method tends to overestimate the depth, and thus overestimate the value of ε, and underestimate the value of ε_{GW}.

In the radar-based study, we conduct a retrieval of turbulent parameters in the mesosphere based on a hypothesis test. We distinguish between the presence and absence of turbulence based on fitting Voigt-based and Lorentzian-based line shapes to the radar spectra. We also allow for the presence and absence of meteoric smoke particles (MSPs) in the radar spectra. We find examples of Poker Flat Incoherent Scatter Radar (PFISR) spectra showing both the presence and absence of turbulence and the presence and absence of MSPs in the upper mesosphere. Based on the analysis, we find that relatively few of the radar measurements yield significant measurements of turbulence. The significant estimates of turbulence have a strength that is over a factor of two larger than the average of the estimates from all of the radar measurements. The probability of true positives increases with the quality factor of the spectrum. The method yields significant measurements of turbulence with probabilities of true positives of greater than 30% and false positives less than 0.01%.

Table of Contents

This page intentionally left blank

List of Figures

xiii

xiv

List of Tables

Finally and most importantly, I want to express my gratitude to my parents, Xinjiang Li and Yongmei Li, for bringing me to this world, raising me, teaching me, supporting me and loving me. My thanks to my little sister, Jinfang Li. I want to thank my wife, Ping Yang, for encouraging, supporting and loving me, and my son, Sam Yang Li, for being born. My great thanks to my grandparents, my uncles, and aunts, for their love ever since I was born. I want to thank my friends for their friendship and love. I want to thank everyone I love, and everyone who loves me. Their love has been my great motivation ever since.

Chapter 1. Introduction

1.1. The middle atmosphere

The middle atmosphere is the region between the tropopause (~10-16 km) and the homopause (~110 km) that encompasses the stratosphere, mesosphere and lower thermosphere (Andrews et al., 1987). Interest in the middle atmosphere is primarily driven by interest in the ozone layer, as this region contains approximately 90% of the Earth's ozone and the state of the middle atmosphere is crucial to the state of the ozone layer (National Research Council, 1994). The depletion of ozone by chlorofluorocarbons (CFCs) and the appearance of the Antarctic ozone hole prompted the Montreal protocol and thus avoided a world with a globally depleted ozone layer with year-round polar ozone holes in the 21st century (Newman et al., 2009). The Montreal Protocol has resulted in a global effort to monitor the ozone layer and ozone-depleting chemicals and understand both their natural and anthropogenic variations. The recent detection of an increase in CFCs highlights these efforts to both monitor changes in these chemicals and identify sources and sinks (Montzka et al., 2018). Studies of the recovery of the Antarctic ozone hole highlight the interactions between both chemistry and dynamics that determine the structure of the ozone layer (Solomon et al., 2016). The need to understand the meteorology of the ozone layer has resulted in a broad effort to understand the circulation of the middle atmosphere and coupling between the middle atmosphere, lower atmosphere and upper atmosphere.

1.2. Waves and Turbulence in the Middle Atmosphere

Waves and turbulence are crucial to understanding the circulation of the middle atmosphere and how it is coupled to the troposphere below and the thermosphere above. Large-scale planetary waves and smaller-scale gravity waves propagate upward into the middle atmosphere, grow with altitude, become unstable, break, and generate forces that drive the meridional circulations in the stratosphere and mesosphere (see review by Alexander and Holton, 2000). Turbulence in the middle atmosphere is generated by wave-driven instabilities (see review by Fritts & Alexander, 2003). Turbulence couples the mesosphere-lower-thermosphere (MLT) region with the stratosphere and upper thermosphere through mixing and transport of heat, momentum and constituents. (Becker, 2012; Colegrove et al., 1965; Colegrove et al., 1966; Guo et al., 2017; Lindzen, 1971; Lübken, 1997; Meraner et al., 2016). For example, model studies of the thermosphere structure show that imposing a seasonal variation of the eddy diffusion coefficient (due to small-scale gravity waves and turbulence) in the upper mesosphere (~ 97 km) yields better consistency with satellite observations of thermospheric density and composition (Qian et al., 2009). The change in eddy diffusion changes the rate at which atomic oxygen (O) is removed from the thermosphere and changes the composition of the thermosphere, and yields significant changes in density at satellite altitudes (~400 km).

Sudden Stratospheric Warmings (SSWs) events highlight the challenges in describing the role of waves and turbulence in the circulation. During SSWs there is a reversal of the wintertime circulation of the stratosphere and mesosphere and disruption the stratospheric polar vortex (see review by Chandran et al., 2014). Breaking planetary waves trigger SSWs. However, during SSWs there is a complex set of non-linear interactions between waves and the mean flow.

Initially planetary waves break and alter the mean flow, then these changes in the mean flow alter the propagation of gravity waves. This changes the population of gravity waves that propagate into the mesosphere and the resultant forcing of the mean flow and generation of turbulence. These alternation in the mean flow can further alter the propagation of waves in the atmosphere. During SSWs there is significant downward transport from the thermosphere to the stratosphere where transport of nitrogen oxides (i.e., NOx = NO + NO_2) is enhanced (with NOx concentrations up to 50 times higher than usual) relative to winters with no SSWs (Randall et al., 2006; Randall et al., 2009). Researchers have attempted to understand this transport as part of determining how meteorological processes control the impacts of energetic particle precipitation events in the atmosphere (López-Puertas et al., 2005; Mironova et al., 2015; Randall et al., 2006). However, model studies have shown that the wave-driven middle atmosphere circulation alone cannot explain the transport of tracer species from the thermosphere to the stratosphere and that turbulent transport is required to explain the observed transport of NOx (Smith et al., 2011). Model studies have shown that changes of a factor of two in the eddy diffusion coefficients yield significant changes in the transport of minor species (Garcia et al., 2014; Meraner & Schmidt, 2016). The heating rates due to turbulent heating are estimated to be similar to the solar and chemical heating rates (Figure 1.1) and this is a significant source of uncertainty in current models (Lübken, 1997; Mlynczak, 2000; Becker, 2004).

A major challenge in measuring and characterizing mesosphere turbulence is that the measured turbulent parameters vary significantly with different observing methods and environmental conditions (Bishop et al., 2004; Collins et al., 2011; Lehmacher et al., 2006; Lehmacher & Lübken, 1995; Lehmacher et al., 2011; Lübken, 1997). Large variations exist in the measured values of turbulence under different environmental conditions. The value of the turbulent eddy

diffusion coefficient varies between 1-1000 m^2/s, while the value of the energy dissipation rate varies between 0.1-1000 mW/kg. Hence measurements of turbulent parameters under well-defined meteorological conditions are essential. In the Mesosphere-Lower Thermosphere Turbulence Experiment (MTeX) researchers combined rocket-borne measurements of turbulence with ground-based measurements of waves to better understand the relationship between turbulence and the meteorology (Triplett et al., 2018). Comparison of the MTeX measurements with three studies based on rocket-borne ion-gauges in the Arctic (i.e., Lübken, 1997 (L97); Lehmacher et al., 2011 (Letal11), and Szewczyk et al., 2013 (Setal13)) suggests systematic behavior (Figure 1.2). The MTeX and Letal11 profiles were measured on single nights at Chatanika, Alaska (65°N, 147°W) on 25-26 January 2015 and 17-18 February 2009 respectively. The Setal13 profile was measured at Andennes, Norway (69°N, 16°E) on 18-19 December 2010. The L97-W profile represents the average of 12 wintertime measurements over two winters at Andennes, Norway. The L97-S profile represents the average of seven summertime measurements over three summers at Andennes. The MTeX average values are lower than the L97-W values. The turbulent energy dissipation rates in winter (L97-W) are 10 times less than in summer (L97-S) and have been interpreted to indicate low levels of turbulent dissipation and heating in the wintertime Arctic middle atmosphere. The transition from lower wintertime to higher summertime turbulence values has been observed and attributed to seasonal transitions in the breaking of gravity waves associated with seasonal changes in the wind regimes (Müllemann et al., 2002). The low values of turbulent activity reported by both MTeX and Letal11 are similar with the low values of wintertime turbulence reported by L97 and are associated with low levels of gravity-wave activity. The meteorological conditions at Chatanika in both January 2015 and February 2009 are similar with weak winds following an SSW. Thus MTeX and Letal11 report a

consistent scenario of low turbulent activity associated with reduced gravity-wave activity during a period when the circulation of the stratosphere and mesosphere is disturbed and the winds are weak. In contrast to MTeX and Letal11, the values of turbulence reported by Setal13 are significantly higher. Setal13 reports significant wave activity in the upper mesosphere but does not report the stratospheric wave activity. However, the meteorological conditions at Andennes in December 2010 show strong winds associated with an undisturbed middle atmosphere and an unusually strong polar vortex. Thus the higher turbulent activity reported by Setal13 was recorded during a period when the circulation of the stratosphere and mesosphere is undisturbed, winds are strong, and the gravity-wave activity is expected to be higher. The MTeX, Letal11 and Setal13 measurements reveal the occurrence of low (high) levels of turbulence and wave activity in a disturbed (undisturbed) winter middle atmosphere where weak (strong) winds block (allow) the upward propagation of gravity waves. Triplett and coworkers suggested that, given higher planetary wave activity in the northern hemisphere than the southern hemisphere resulting in much greater disturbance of the circulation of the Arctic middle atmosphere than the Antarctic middle atmosphere, there could be systematically lower levels of turbulence in the Arctic wintertime MLT than in the Antarctic wintertime MLT (Triplett et al., 2018).
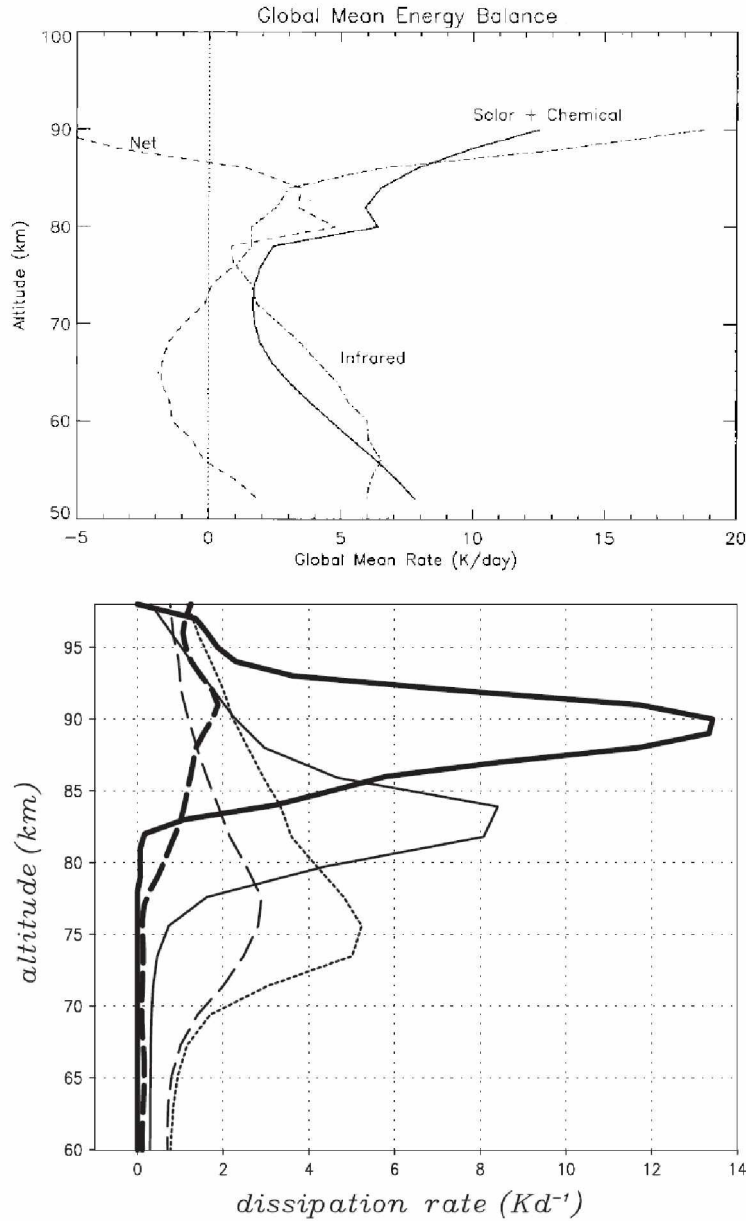
Figure 1.1. Heating rates in the middle atmosphere plot as function of altitude. Top: measured global mean solar and chemical heating rates from Mlynczak (2000); bottom: turbulent heating rates from Becker, (2004). In the top panel, the solid line shows the solar and chemical effect, the dotted dash line shows the infrared cooling effect, and the dashed line shows the net effect. In the bottom panel, the thick lines show the measured turbulent heating during the northern summer (solid) and northern winter (dashed) taken from Lübken (1997). The thin lines show results from simulations of northern summer (solid), northern winter (dashed), and southern winter (dotted).

6
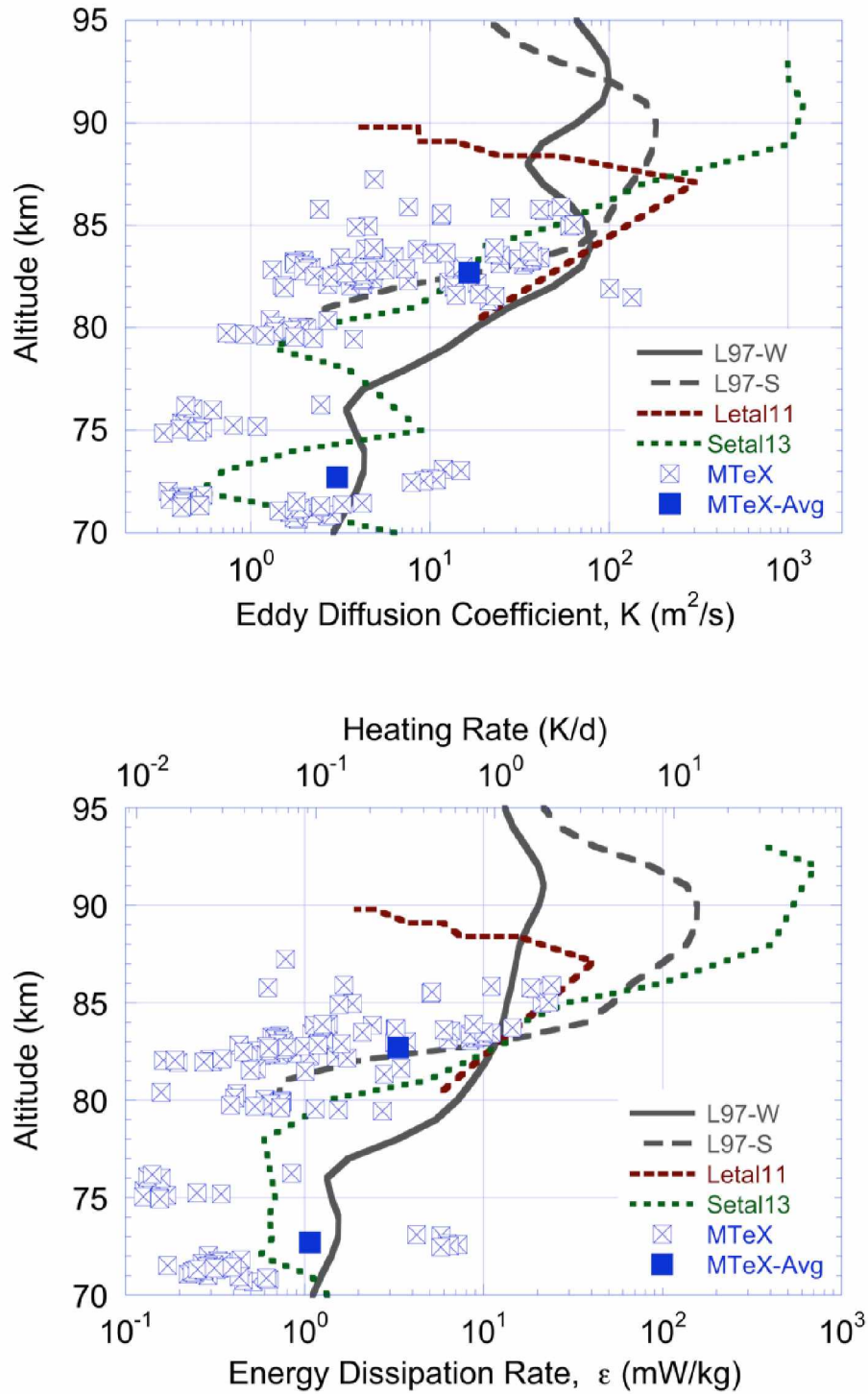
Figure 1.2. Rocket-borne measurements of turbulent energy dissipation rate, heating rate and eddy diffusion coefficients plot against altitude in the Arctic. Top: eddy diffusion coefficients; bottom: energy dissipation rate and heating rate. See text for details.

7

While these results suggest systematic behavior between the turbulent activity and meteorological conditions, rocket-borne measurements are quite rare and there is clearly a need for more measurements. Significant effort has gone into measuring turbulence in the MLT with ground-based radar and lidars (e.g., Guo et al., 2017; Nicolls et al., 2010). Lidars have been used to measure turbulent eddy diffusion coefficients by measuring the diffusion of metal atoms (e.g., sodium) under well-defined environmental conditions (Collins et al., 2011). Radars have been used to measure turbulent energy dissipation rate by measuring the spectral broadening due to turbulent fluctuations (Hocking, 1985; Nicolls et al., 2010).

1.3. Scope of this study

In this dissertation I present studies of waves and turbulence in the middle atmosphere. I present two distinct approaches to characterize turbulence. Using lidar observations I identify regions of convective instability as case studies, and I estimate diffusive turbulent transport associated with these instabilities. I present two new lidar systems that were deployed in support of these studies. Using radar observations, I develop a statistical hypothesis testing approach to detect and characterize turbulence in the MLT without consideration of the meteorological conditions.

In Chapter 2, I estimate turbulent diffusion coefficients and energy dissipation rates in the presence of wave instability and overturning. I base the study on resonance and Rayleigh lidar observations, where the resonance lidar provided measurements of sodium density and the Rayleigh lidar provides measurements of atmospheric density and temperature. The combination of sodium lidar (~75-105 km) and Rayleigh lidar measurements (~40-80 km) allows me to investigate waves propagating from the upper stratosphere to the upper mesosphere. I identify events where there is a well-defined layer of instability and a signature of overturning in the

sodium layer. This combination of measurements allows me to investigate instability (based on temperature) and material transport (based on sodium) associated with wave breaking and turbulence. I extend the scope of earlier studies developing a mass continuity framework and retrieval methods for potential temperature and sodium mixing ratio. I compare the energy dissipation rates to the energy available from dissipating gravity waves. I consider three case studies that include observations from the Mesosphere Lower Thermosphere Experiment (MTeX). During MTeX I operated the resonance lidar that yielded measurements of the sodium layer. I developed the potential temperature and sodium mixing ratio analysis for the initial MTeX study where the turbulence was measured by rocket-borne ionization gauges (Triplett et al., 2018). In this study I use the lidar data to yield an independent estimate of the turbulence activity.

In Chapter 3, I describe the new sodium resonance wind-temperature (SRWTL) lidar that was developed at the Lidar Research Laboratory at Poker Flat Research Range in 2017 (LRL-PFRR). The SRWTL was developed and deployed at PFRR in 2017-2018 as part of a collaborative effort with GATS incorporated, led by Dr. Bifford Williams. I participated in the development and deployment of the SRWTL in 2017-2018 with Dr. Williams, and led the SRWTL observations during the Super Soaker rocket mission in 2018, and subsequent observations in 2018-2019. I present an analysis of the performance of the PFRR SRWTL and compare the performance with other SRWTLs.

In Chapter 4, I present an analysis of wave instability and turbulence using the SRWTL. The study extends the scope of the analysis in Chapter 2 as the SRWTL yields high resolution temperature measurements that allow me to investigate the potential temperatures in the upper

mesosphere and the combination of wind and temperature measurements allow me to better determine the gravity wave characteristics. I apply the turbulent transport analysis of Chapter 2 to again estimate turbulent eddy coefficients and energy dissipation rates. I presented initial analysis and interpretation of these results at the 2018 fall meeting of the American Geophysical Union (Li et al., 2018b).

In Chapter 5, I present a study of turbulence based on measurements made with the Poker Flat Incoherent Scatter Radar (PFISR). This work was carried out in a collaborative effort with SRI International, led by Dr. Roger Varney. PFISR is managed and operated by SRI International. I investigated the ability of the radar to detect and estimate turbulence based on a hypothesis testing approach. I use the results to interpret the turbulence measurements and assess the ability of the radar to measure turbulence. I presented initial analysis and interpretation of these results at the 2018 Coupling Energetics and Dynamics of Atmospheric Regions workshop (Li et al., 2018a).

In Chapter 6, I summarize my key findings, present my conclusions, and make recommendations for further work. In Appendix A, I present the linear theory of atmospheric gravity waves and I combine the theory with lidar measurements to characterize gravity waves. In Appendix B, I present the design and performance of a steerable lidar system that I developed at LRL-PFRR in support of the Super Soaker rocket investigation. The characterization of the lidar receiver was carried out with assistance from Ms. Mikayla Grunin, a University of Alaska Fairbanks physics undergraduate research assistant, during the summer of 2017. The survey of the telescope was carried out with assistance from Dr. Gang Chen, a professor from the College of Engineering and Mining of University of Alaska Fairbanks, and a graduate student working with him,

Mohammad Hoveidafar. I present the details of the steerable lidar system and the Super Soaker

lidar measurements showing the detection of an artificial mesospheric cloud.

This page intentionally left blank

Chapter 2. Lidar study of gravity waves and turbulence

2.1. Introduction

Gravity waves (GWs) are buoyancy waves that have been recognized as integral to the general circulation of the atmosphere since the 1960s (Garcia & Solomon, 1985; Hines, 1960; Holton, 1982, 1983; Houghton, 1978; Lindzen, 1981). These waves are generated by a variety of meteorological processes in the lower atmosphere and propagate upwards. As the atmosphere is stratified with a density that decreases exponentially with altitude, GWs grow exponentially with altitude as they maintain their energy. Eventually these waves grow so large that the nonlinear interactions become important leading to rapid and irreversible deformation of the material surfaces of the waves. This process of deformation is termed wave breaking by analogy of the breaking of ocean waves on a beach and results in the dissipation of the wave (e.g., Andrews et al., 1987; Holton & Alexander, 2000). GW breaking explains how energy is transferred between the lower and upper atmosphere and controls the general circulation of the mesosphere-lower thermosphere (MLT) (See reviews by Fritts & Alexander, 2003; Holton & Alexander, 2000). These breaking GWs drive a mean meridional circulation that result in significant adiabatic cooling and heating in the MLT that results in a cold summer mesopause and a warm winter mesopause. GW breaking also generates turbulence and small-scale mixing in the MLT (e.g., Becker, 2012; Fritts & Alexander, 2003; Fritts et al., 2018a; Fritts et al., 2018b; Fritts et al., 2017; Hines, 1988; Sutherland, 2010).

Turbulent mixing is the dominant mixing process in the MLT (Wayne, 1991). Turbulence contributes to vertical transport and can affect the composition, chemistry and dynamics of the atmosphere. For instance, early model results in the 1960s showed that turbulent diffusion

transports atomic oxygen vertically (Colegrove et al., 1965; Colegrove et al., 1966). The significance of turbulence to the composition and circulation of the mesosphere has been further confirmed by other studies (Garcia & Solomon, 1985; Hodges, 1969; Lindzen, 1971). Vertical transport is also important to the coupling between the mesosphere and lower thermosphere. Recent studies have shown that large scale transport alone cannot explain the transport of NOx from the thermosphere to mesosphere and that mesospheric turbulence is an important component of transport (Meraner & Schmidt, 2016; Smith et al., 2011) . However, sensitivity studies with these models have shown that changes of a factor of two in the eddy diffusion coefficients yield significant changes in the transport of minor species (Garcia et al., 2014; Meraner & Schmidt, 2016). Turbulence also contributes to the energy budget of the middle atmosphere. Observational and modeling studies have shown that turbulent heating is on average as strong as radiative and chemical heating (Becker, 2004, 2012; Guo et al., 2017; Lübken, 1997; Mlynczak, 2000). However, turbulence caused by GWs is one of the least quantified aspects of how gravity waves influence the middle atmosphere.

A major challenge in measuring and characterizing mesosphere turbulence is that the measured turbulent parameters vary significantly with different observing methods and environmental conditions (Bishop et al., 2004; Collins et al., 2011; Lehmacher et al., 2006; Lehmacher & Lübken, 1995; Lehmacher et al., 2011; Lübken, 1997). The energy dissipation rate can vary from 1 mW/kg to 1000 mW/kg across the mesosphere-lower-thermosphere (MLT, 60-90 km) region, which correspond to a heating rate of 0.086 K/day to 86 K/day. Hence, measurements of turbulent parameters under well-defined meteorological conditions are essential for studying and understanding the properties of turbulence, and hence GW-induced vertical transport processes. Measurements of density fluctuations and measurements of expansion of chemical released trials

have reported that higher values of turbulent energy dissipation and eddy diffusion occur in altitude regions of convective and/or dynamic instability (e.g., Bishop et al., 2004; Lehmacher et al., 2006; Lehmacher & Lübken, 1995; Lehmacher et al., 2011; Strelnikov et al., 2017; Szewczyk et al., 2013) . Regions of convective instability, where the temperature gradients are negative and adiabatic or super-adiabatic (i.e., adiabatic or super-adiabatic lapse rates), are often found on the topside of Mesospheric Inversion Layers (MILs). MILs are vertically narrow (~10 km) temperature enhancements with an amplitude of 30-50 K that are superimposed on the temperature profile in the mesosphere (Meriwether & Gerrard, 2004). MILs have been routinely measured by different techniques (Cutler et al., 2001; Gan et al., 2012; Hauchecorne et al., 1987; Irving et al., 2014; Schmidlin, 1976; Williams et al., 2002; Yuan et al., 2014; Yue et al., 2019). Possible formation mechanisms include dynamic heating induced by breaking GWs, tidal-gravity wave interaction and breaking planetary waves (Ramesh & Sridharan, 2012; Ramesh et al., 2013; Szewczyk, 2015; Walterscheid, 2001). The presence of a persistent adiabatic negative temperature gradient rate on the topside of the MILs is consistent with a well-mixed turbulent layer (Whiteway et al., 1995). Turbulence has been observed coincident with these adiabatic gradients (Collins et al., 2011; Lehmacher et al., 2006; Lehmacher & Lübken, 1995; Lehmacher et al., 2011; Szewczyk et al., 2013; Thomas et al., 1996; Triplett et al., 2018).

In this chapter we present case studies from three nights of observations at Poker Flat Research Range (PFRR), Chatanika, Alaska (65°N, 147°W). The nights are the 17-18 February 2009, 23-24 February 2009, and 25-26 January 2015. The February 2009 measurements were made in association with the Turbopause experiment and January 2015 measurements were made in association with the Mesosphere-Lower Thermosphere Turbulence Experiment (MTeX) (Lehmacher et al., 2011; Triplett et al., 2018). We analyze turbulence and wave activity in the

MLT based on lidar measurements of temperature, density and sodium in the presence of MILs. This combination of measurements provides simultaneous characterization of both the atmospheric stability as well as material transport that allow us to estimate the eddy diffusion coefficient associated with turbulence. In this study we extend the earlier analysis of Collins and co-workers in two distinct ways (Collins et al., 2011). First, we calculate the potential temperature and sodium mixing ratio from the lidar data to better characterize the instability, mixing, and eddy diffusion. Second, we characterize the wave activity and estimate the energy available from the waves to generate the turbulence. The chapter is arranged as follows. In section 2, we describe the Rayleigh and resonance lidar techniques and methods used in this study. In section 3 we illustrate our methods in detail using the lidar observations from the first case study. In section 4 and 5 we present the observations and analysis of the second and third case studies. In section 6 we discuss our results in terms of recent studies of turbulence and waves and present our summary and conclusions.

2.2. Experiment and methods

2.2.1. Rayleigh lidar

The Rayleigh Density Temperature Lidar (RDTL) was installed at PFRR in 1997 and ongoing observations of the Arctic middle atmosphere have been acquired ever since (Collins et al., 2011; Cutler et al., 2001; Thurairajah et al., 2010a; Triplett et al., 2018). The transmitter of the RDTL is a flashlamp-pumped Nd:YAG (Neodymium-doped Yttrium Aluminum Garnet) pulsed laser (Powerlite 8020, Continuum). The laser emits light with a wavelength of 532 nm at 20 pulses-per-second (pps). The output power of the laser is typically 8 W, with pulse duration of 5-7 ns, and line width of 1.0 cm^{-1}(28 pm). During the Turbopause experiment, the receiver of the RDTL

was based on a 0.6 m Newtonian telescope with a single receiver channel. The lidar measurements yielded density and temperature profiles in the stratosphere and mesosphere (~40-80 km) using established techniques under the assumption of hydrostatic equilibrium and an initial temperature at the upper attitude (Collins et al., 2011; Thurairajah et al., 2010b). During 2014 in preparation for the MTeX experiment, the RDTL was extended to incorporate a 1.04 m Cassegrain telescope with a two-channel receiver (Triplett, 2016). The two-channel receiver system had a high-altitude channel that received 94% of the total lidar signal and a low-altitude channel that received 6% of the total lidar signal. The high-altitude channel signals were a factor of three greater than the single-channel system obtained during the Turbopause experiment (Collins et al., 2011). The increased signal in the high-altitude channel reduces the uncertainty in the lidar signals and extends the measurements of density and temperature to higher altitudes than in earlier studies. The decreased signal in the low-altitude channel reduces the effects of pulse-pile up and extends the measurements of density and temperature to lower altitudes than in previous studies. The signals from the two channels are combined to yield a single signal profile that again yielded measurements of density and temperature in the stratosphere and mesosphere (~30-90 km). The initial temperature is the major source of uncertainty in the lidar measurement. For these Rayleigh measurements we used MLT temperature measurements made with ionization-gauges carried by the Turbopause and MTeX rockets (Collins et al., 2011; Triplett et al., 2018).

The resolution of the lidar measurements was 50 s and 75 m (Turbopause) and 50 s and 48 m (MTeX). We then integrate the Rayleigh lidar data in time and smooth it in altitude to improve the statistical confidence in the density and temperature measurements. We calculate temperature profiles over 2 h intervals at 15 minute steps and use these profiles to characterize

the temperature structure the stratosphere and mesosphere, the MILs, and calculate potential temperature profiles. The potential temperature profiles are calculated from the temperature profiles by integration upward from some lower altitude z_0,

$$\theta(z,t) = T(z,t)exp\left(\int_{z_0}^{z} \frac{g(r)dr}{c_p T(r,t)}\right), \qquad (2.1)$$

where $T(z, t)$ is the temperature at altitude z and time t, $g(r)$ is the acceleration due to gravity, and c_p is the specific heat of dry air under constant pressure. The method normalizes the potential temperature to the altitude z_0 (i.e., $\theta(z_0, t) = T(z_0, t)$). We calculate density profiles over 1 h intervals at 15 minutes steps and normalize these to radiosonde measurements of the density over the 30-32 km altitude range. The radiosonde measurements are made at the Fairbanks International Airport about 50 km from PFRR. We then combine the normalized density profiles with sodium density profiles to calculate the sodium mixing ratio in the MLT. Finally, we calculate density profiles over 30 minutes intervals at 5 minutes steps to characterize the gravity-wave activity in the stratosphere and mesosphere.

2.2.2. Resonance lidar

Sodium Resonance Density Lidar (SRDL) observations began at PFRR in 1995 and ongoing observations of the Arctic mesospheric sodium layer have been acquired ever since (Collins et al., 1996; Collins et al., 2011). During the Turbopause experiment the SRDL transmitter was a tunable dye laser (Scanmate2, Lambda Physik) that was pumped by an XeCl excimer laser (LPX200i, Lambda Physik) (Hou, 2002). The dye laser operated at 589 nm with a linewidth of 0.14 cm^{-1} (5 pm) and a typical average power of 0.1 W at 10 pps. During MTeX the SRDL transmitter was a tunable dye laser (ND62, Continuum) that was pumped by a Nd:YAG laser

(NY81C-10, Continuum) (Martus, 2013). The dye laser operated at 589 nm with a linewidth of 11 pm and a typical average power of 0.3 W at 10 pps. During both Turbopause and MTeX the SRDL receiver was based on a 1.04 m Cassegrain telescope with a single receiver channel. The lidar measurements yielded sodium profiles (~70-120 km) using established techniques where the lidar signal is normalized to a radiosonde measurement of the atmospheric density (e.g., Collins et al., 1996; Collins & Smith, 2004). The radiosonde measurements are made at the Fairbanks International Airport about 50 km from PFRR.

The resolution of the SRDL measurements was 50 s and 75 m (Turbopause) and 100 s and 75 m (MTeX). We then integrate the resonance lidar data in time and smooth it in altitude to improve the statistical confidence in the sodium density measurements. In this study we calculate sodium profiles over 1 h intervals at 15 minute steps. We then take the ratio of these sodium density profiles to the normalized atmospheric density profiles to calculate the sodium mixing ratio profiles.

2.3. Case study on 17-18 February 2009

2.3.1. Observations

On the night of 17-18 February 2009, a MIL forms at 00:30 LST at 77.6 km and descends to 72.2 km over the remainder of the observations until 06:00 LST (Figure 2.1, top panel). The MIL reaches its maximum amplitude of 28.6±6.9 K at an altitude of 74.2 km at 02:00LST. At this time the topside lapse rate of the MIL reaches its maximum value of -9.2 ±0.3 K and the width of the MIL is 3.1 km. Over the observation the amplitude of the MIL is between 12.5 and 28.6 K with an average value of 20.7 K. The peak altitude of the MIL varies between 77.6 km and 71.0

km with an average value of 73.5 km. The width of the MIL varies between 1.5 and 5.3 km with an average value of 3.4 km. The topside gradient of the MIL varies between -10.1 K/km and -2.7 K/km with an average value of -7.8 K/km. In comparison, the stratopause remains relatively undisturbed with a temperature that varies between 234.7 K and 237.4 K, with an average value of 235.9 K, and an altitude between 48.1 km and 50.7 km, with an average value of 49.6 km.

The sodium layer has an average peak altitude of 86.6 km that varies between 84.6 km and 89.1 km (Figure 2.1, middle panel). The average peak sodium number density is 4.1×10^3 atom/cm^{-3} and varies between 3.2×10^3 atom/cm^{-3} and 4.9×10^3 atom/cm^{-3}. The sodium layer has a scale height of 6.7 km on the topside and a scale height of 4.0 km on the bottomside that is reflected in the narrower spacing of the sodium density contours on the bottomside. This asymmetry is typical of the sodium layer. Wave activity is evident with overturning in the sodium density (~ 80 km at 22:00 LST, ~85 km at 01:00 LST) that is consistent with the passage of large amplitude and/or breaking gravity waves (Collins & Smith, 2004; Hecht et al., 2000; Xu et al., 2006). We highlight the spreading of the sodium density contours in the bottomside of the sodium layer from 00:30 LST to 03:00 LST. The spreading coincides with the appearance of the MIL. The time when the 100 atom/cm^{-3} sodium contour descends below 75 km corresponds to the time and altitude when the MIL has the steepest topside temperature gradient.

This event is characterized by vertical spreading in both the sodium mixing ratio and potential temperature (Figure 2.1, bottom panel). The distance between the two mixing ratio contours, 1.0×10^{-12} and 1.0×10^{-14}, has a mean value of 3.0 km before 0:30 LST, and then increases to a maximum of 6.3 km at 2:00 LST, before returning to 3.0 km. The spreading is also seen in the distance between the 400 K and 440 K potential temperature contours. The distance between the

contours has a mean value of 1.7 km before 0:30 LST and increases to a maximum of 6.4 km at 2:00 LST. The fact that the spreading appears consistently in both the sodium mixing ratio and the potential temperature indicates that material motion has occurred during this event and is associated with a reduction in convective instability. We now analyze this in terms of turbulent transport and determine the eddy diffusion coefficient and energy dissipation rate associated with the turbulence.
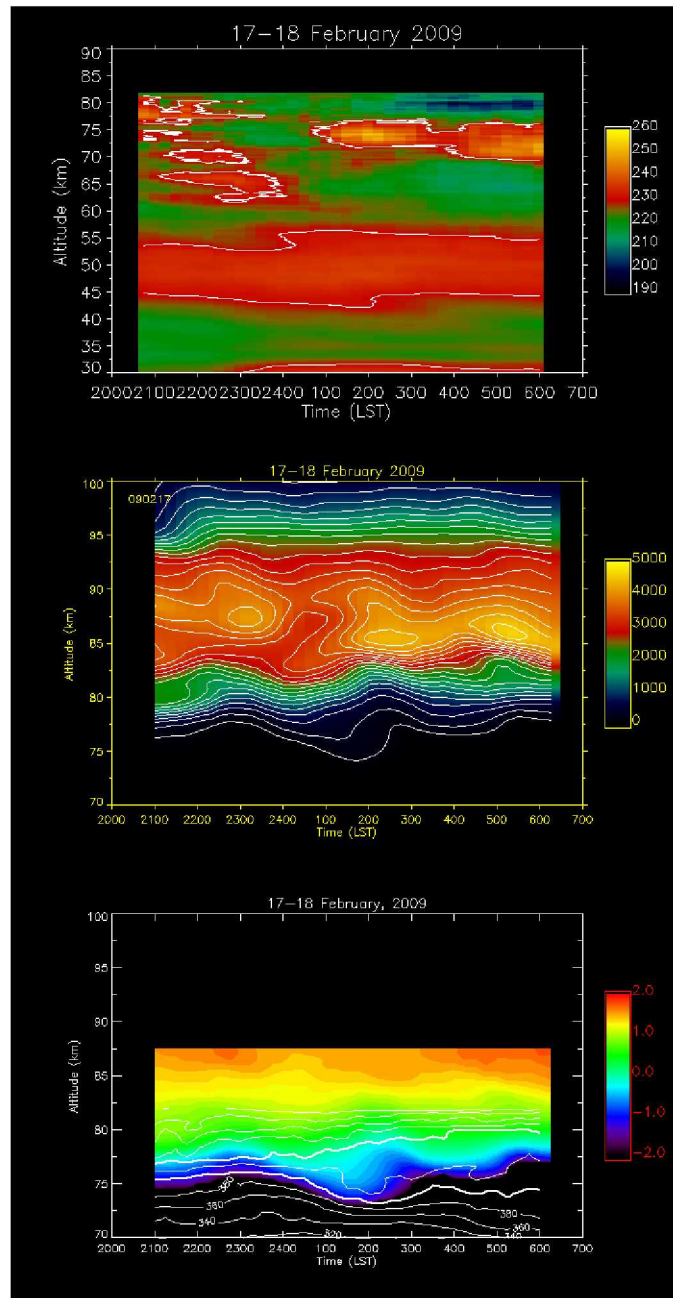
Figure 2.1. Temperature (top), sodium density (middle), potential temperature (bottom, contour) and sodium mixing ratio measured by the RDTL and SRDL on the night of 17-18 February 2009. See text for details.

2.3.2. Estimation of turbulent diffusion coefficient and energy dissipation rates

Our model of the turbulent transport is based on the continuity equation of the number density of sodium atoms. The continuity equation may be expressed as

$$\frac{\partial n_s}{\partial t} = \left[\frac{\partial n_s}{\partial t}\right]_{adv} + \left[\frac{\partial n_s}{\partial t}\right]_{turb} + \left[\frac{\partial n_s}{\partial t}\right]_{chem} \tag{2.2}$$

where n_s is the sodium number density and the three terms on the right represent advection (adv), turbulence (turb), and chemistry (chem) (Jacob, 1999). These terms can be expressed as

$$\left[\frac{\partial n_s}{\partial t}\right]_{adv} = -\nabla \cdot (\vec{u} n_s), \tag{2.3}$$

$$\left[\frac{\partial n_s}{\partial t}\right]_{turb} = \nabla \cdot (\overleftrightarrow{K} n_a \nabla \cdot f), \tag{2.4}$$

$$\left[\frac{\partial n_s}{\partial t}\right]_{chem} = P - L, \tag{2.5}$$

where n_a is the number density of the atmosphere, f is the mixing ratio of sodium atoms, $\overleftrightarrow{K}$ is matrix form of the eddy diffusion coefficients, P is the chemical production, and L is the chemical loss. We consider the one-dimensional situation based on transport in the vertical direction (z) alone. We assume that the advection is negligible and that the steady state density of the atmosphere, sodium atoms, and sodium mixing ratio vary exponentially with height,

$$\bar{n}_s = n_{s0} exp((z - z_0)/H_s), \tag{2.6}$$

$$\bar{n}_a = n_{a0} exp(-(z - z_0)/H_a), \tag{2.7}$$

$$\bar{f} = \bar{n}_s/\bar{n}_a = exp(-(z - z_0)/H_f), \tag{2.8}$$

23

where n_{s0} and n_{a0} are the number density of sodium and the atmosphere at z_0, respectively, H_s H_a, and H_f are the scale height of sodium density, atmosphere, and sodium mixing ratio respectively. The scale heights are related as $H_f = H_s H_a / (H_s + H_a)$.

We assume that, first, the advection term is negligible, and that sodium density is at steady state, $\bar{n}_s$, thus

$$\left[\frac{\partial \bar{n}_s}{\partial t}\right]_{chem} = 0. \tag{2.9}$$

Now consider the case where turbulence is initiated at a certain time, t_0, and a constant eddy diffusion coefficient, K, is induced. The perturbation induced by the turbulence is given by, n_s', and equation 2.2 can be re-written as

$$\frac{\partial(\bar{n}_s + n_s')}{\partial t} = \left[\frac{\partial(\bar{n}_s + n_s')}{\partial t}\right]_{turb} + \left[\frac{\partial(\bar{n}_s + n_s')}{\partial t}\right]_{chem}. \tag{2.10}$$

With equations 2.6-2.10, we can derive an expression for the time derivative of the perturbation in the sodium density,

$$\frac{\partial n_s'}{\partial t} = \left[\frac{\partial n_s'}{\partial t}\right]_{turb} + \left[\frac{\partial n_s'}{\partial t}\right]_{chem}. \tag{2.11}$$

The turbulence term can be expressed in terms of the vertical gradient in the turbulent flux, ϕ,

$$\left[\frac{\partial n_s}{\partial t}\right]_{turb} = -\frac{\partial \phi}{\partial z} = \frac{\partial}{\partial z}(K n_s / H_f). \tag{2.12}$$

The chemistry term can be expressed as

$$\left[\frac{\partial n_s'}{\partial t}\right]_{chem} = -n_s'/\tau, \tag{2.13}$$

where τ is the chemical time constant. Notice that n_s' can be positive, or negative, based on whether sodium is transported from a region of higher to lower, or lower to higher, mixing ratio. This is reflected in the sign of equation 2.12. On the top and bottom side of the sodium layer the turbulent term is positive, while on the central region of the layer it is negative. The minus sign in equation 2.13 indicates that the effect of chemistry is to counteract the perturbation induced by the turbulence. Initially the amplitude of the perturbation, n_s', is small, thus the turbulent term is larger than the chemical term. Thus n_s' increases with time, which causes the absolute value of the chemical term to increase. The effect of turbulence is to diffuse the sodium atoms, thus reducing the gradient of the sodium mixing ratio and increasing the value of H_f, and so from equation 2.12 the absolute value of the turbulent term decreases with time. Eventually, at some time (t_m), the turbulent and the chemical terms in equation 2.11 balance, and the amplitude of n_s' reaches a local maximum. This balance allows us to estimate the eddy diffusion coefficient as follows. First, $\partial n_s'/\partial t$ becomes zero in equation 2.11, and we have

$$-\frac{\partial \phi}{\partial z} = \frac{\partial}{\partial z}(K n_s/H_f) = n_s'/\tau. \tag{2.14}$$

We assume that the turbulent transport occurs over a narrow layer of depth L, where the turbulent flux is confined within the layer and decreases to zero at the bottom of the layer. We integrate equation 2.14 over L and assume that at t_m n_s' reaches it's maximum and is the dominant component of the number density, $|n_s'| \cong n_s$. Under the assumption that the turbulent term is neglectable after t_m, the observed loss time of sodium mixing ratio during the disappearance of n_s' is the chemical time constant. Thus the expression for the eddy diffusion coefficient becomes,

$$K = \frac{L \times H_f}{\tau}. \tag{2.15}$$

The turbulent energy dissipation rate can then be estimated from the eddy diffusion coefficient,

$$\varepsilon = \frac{1}{0.81} N^2 \times K, \tag{2.16}$$

where N is the Buoyancy frequency (Weinstock, 1981). N is calculated as

$$N^2 = \frac{g}{\theta} \frac{d\theta}{dz} = \frac{g}{T}(\Gamma - \gamma), \tag{2.17}$$

where θ is the potential temperature, g is the gravitational constant, T is the temperature, Γ is the dry adiabatic lapse rate (9.5 K/km), γ is the lapse rate (e.g., Dutton, 1986). The square of the buoyancy frequency, N^2, is a measure of the convective stability (Holton & Hakim, 2013). A negative value of N^2 (i.e., $\frac{d\theta}{dz} < 0$) indicates convective instability.

We now use equations 2.15 and 2.16 to characterize the turbulence in terms of eddy diffusion coefficient and energy dissipation rate. First, we determine the time of maximum (t_m), from the variation of the sodium mixing ratio with time in the body of the spreading event. We calculate the sodium mixing ratio averaged between 75.1 km and 76.1 km, and the scale height of the mixing ratio over the 74.1 km to 77.1 km range. The average sodium mixing ratio reaches a local maximum of 0.46 PPT at 01:30 LST that is larger than the local maximum of 0.05 PPT at 04:00 LST (Figure 2.2). Thus we choose 01:30 LST as t_m. The scale height of sodium mixing ratio has typical value of 0.7 km before the spreading event begins (24:00 LST), and then increases to 2.7 km at 01:30 LST, and reaches a local maximum of 3.6 km at 02:00 LST (Figure 2.2). The sodium density profile and the sodium mixing ratio profile both show the decreased vertical

26

gradient and increased scale height at t_m (Figure 2.3). The behavior of the sodium mixing ratio is consistent with our model of turbulent diffusion as discussed above.

In Figure 2.4, we plot the temperature and potential temperature profiles at t_m. The MIL is clearly evident in the temperature profile. The MIL has an amplitude of 25.6±6.7 K at an altitude of 74.4 km. The topside lapse rate of the MIL has a value of -8.7 ±0.3 K and the width of the MIL is 4.3 km. A layer of nearly constant potential temperature coincides with the topside of the MIL. The value of the squared buoyancy frequency calculated over the 3 km range between 74.1 km and 77.1 km is 4.2×10^{-5} s^{-2}. This indicates a layer of reduced stability (equation 2.17) and mixing that corresponds to the spreading in both the number density and mixing ratio profiles. To further analyze this layer, we plot the vertical gradient of the potential temperature in Figure 2.5. We plot three profiles. We calculate the vertical gradient by conducting linear fit to 0.5 km, 1.0 km and 2.0 km intervals of the potential temperature profile respectively. We find that the profile from 0.5 km fit is too noisy, while the profile from 2km fit does not indicate any instable layer. We determine to use the 1 km profile to and find that the layer extends from 75.3 to 75.9 km, with a thickness, L, of 0.6 km. We calculate the chemical time constant from the decrease in the sodium mixing ratio between 01:30 LST and 04:00 LST (Figure 2.2). We summarize the pertinent values derived from the temperature and sodium mixing ratio measurements in Table 2.1. Using equations 2.15 and 2.16, we estimate an eddy diffusion coefficient of 4.1×10^2 $m^2 s^{-1}$ and an energy dissipation rate of 21.1 mW/kg (Table 2.2).
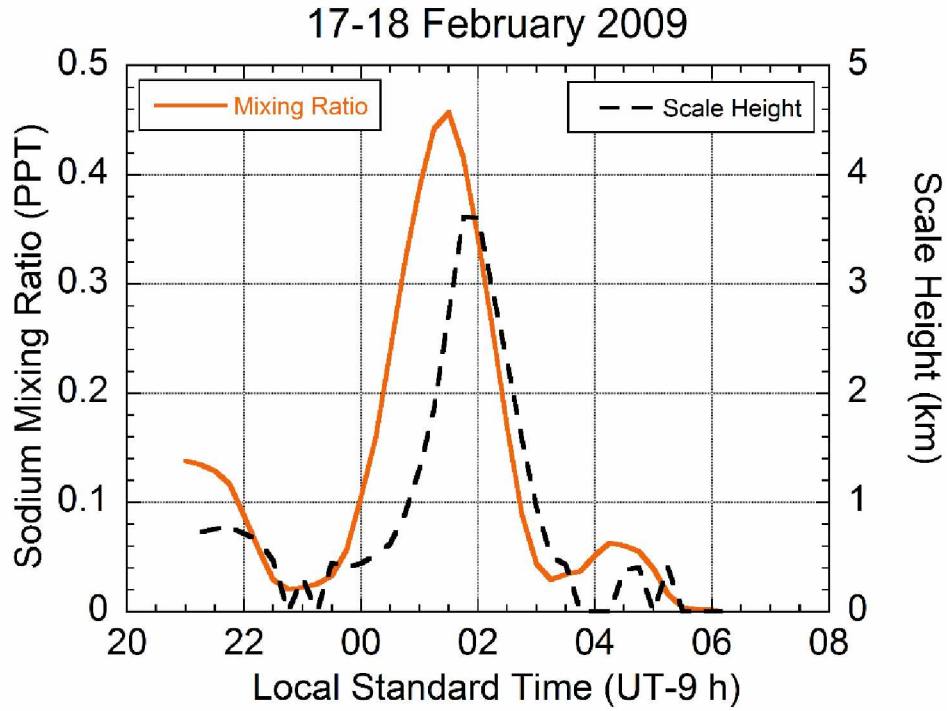
Figure 2.2. Average sodium mixing ratio measured by the RDTL and SRDL between 75.1 km and 76.1 km (solid, yellow) and the scale height of sodium mixing ratio between 74.1 and 77.1 km on the night of 17-18 February 2009.
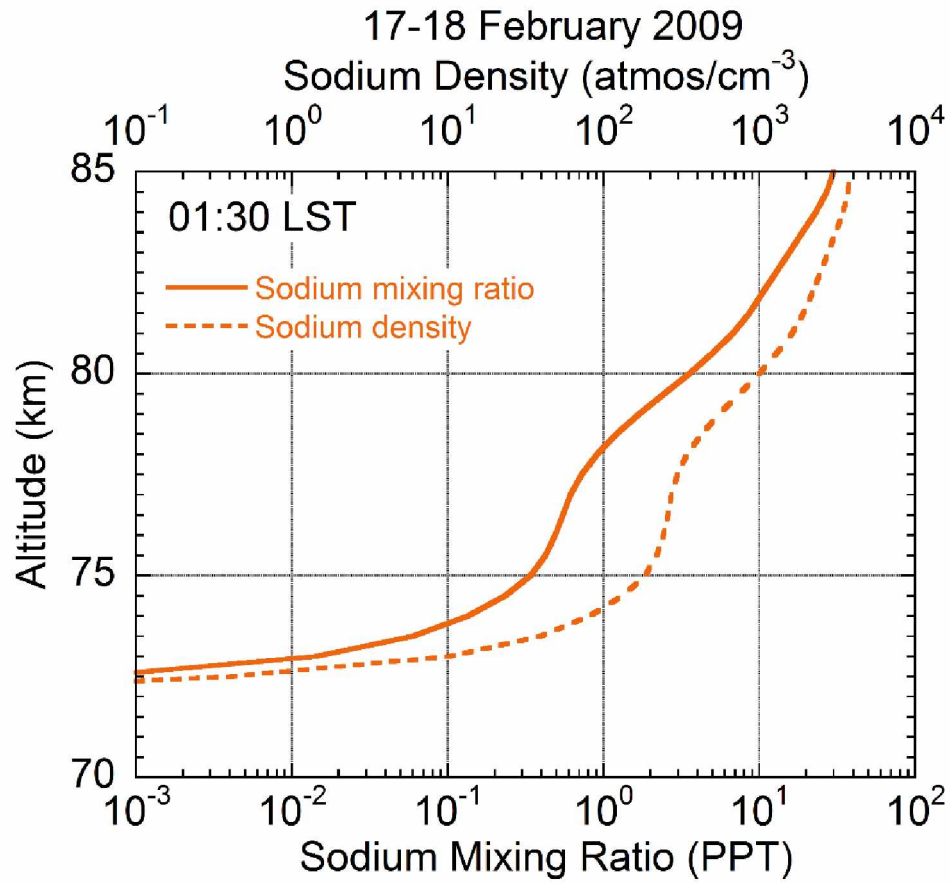
Figure 2.3. Profiles of sodium mixing ratio (solid) and sodium density (dashed) measured by the RDTL and SRDL between 01:00 LST and 02:00 LST on the night of 17-18 February 2009.
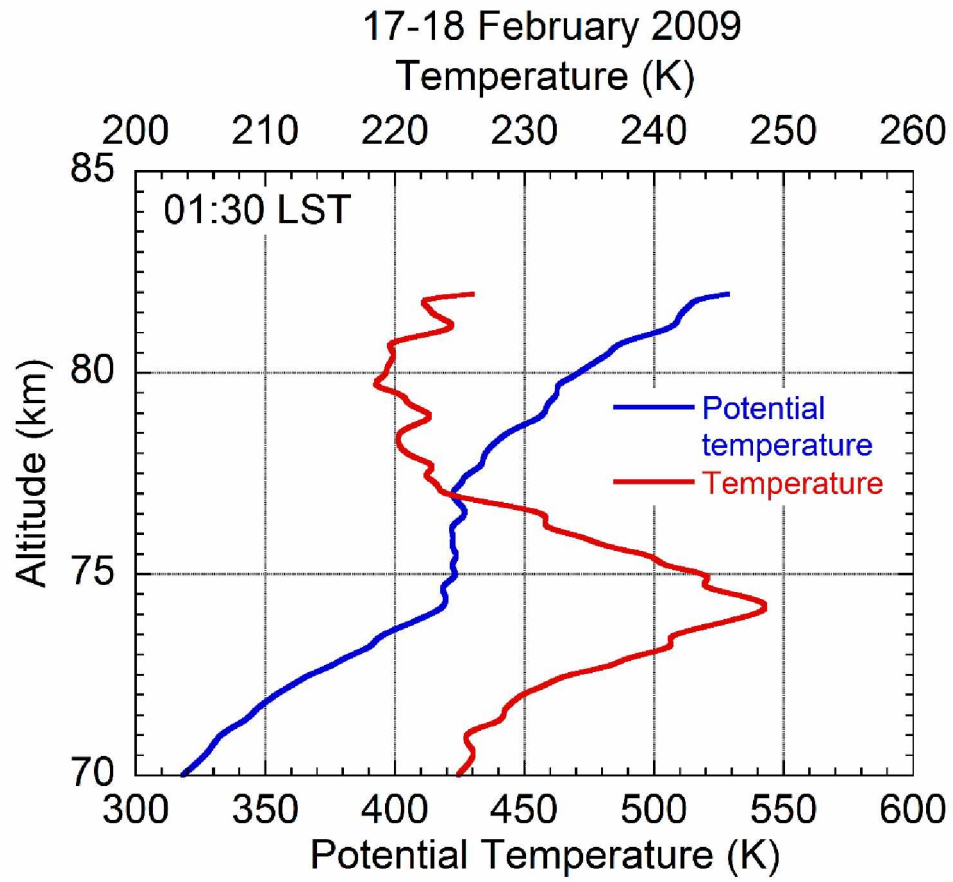
Figure 2.4. Profiles of temperature (red) and potential temperature (blue) measured by the RDTL between 01:00 LST and 02:00 LST on the night of 17-18 February 2009. See text for details.
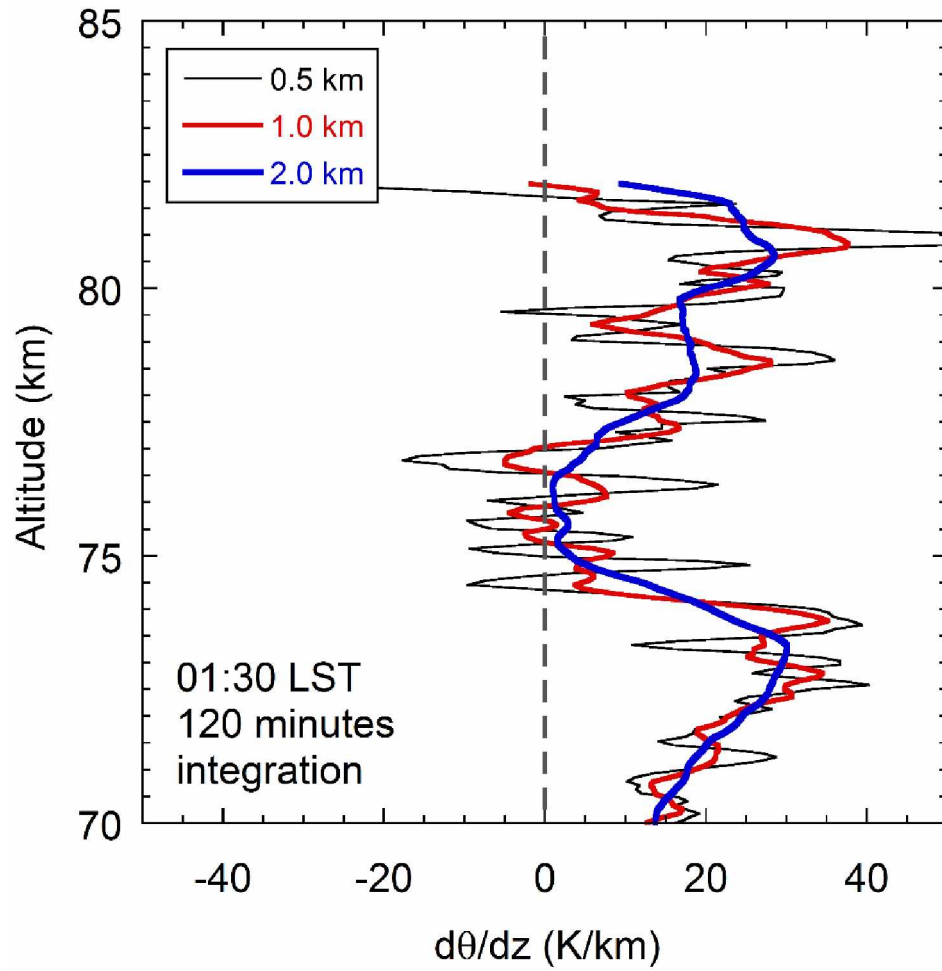
Figure 2.5. Vertical gradient of potential temperature measured by the RDTL between 01:00 LST and 02:00 LST on the night of 17-18 February 2009. See text for details.

Table 2.1: Measured characteristics of the diffusion events

Date	Time	Altitude	Value
17-18 Feb 2009			
Scale height of sodium mixing ratio, H_f	01:30	74.1-77.1 km	2.7 km
Sodium chemical time constant, τ	01:30-03:30	75.1-76.1 km	67 min
Lapse rate, γ	01:30	74.1-77.1 km	-8.5 K/km
Layer thickness, L	01:30	75.3-75.9 km	0.6 km
23-24 Feb 2009			
Scale height of sodium mixing ratio, H_f	01:00	74.6-77.6 km	6.1 km
Sodium chemical time constant, τ	01:00-04:00	75.6-76.6 km	67 min
Lapse rate, γ	01:00	74.6-77.6 km	-9.5 K/km
Layer thickness, L	01:00	75.7-76.5 km	0.8 km
25-26 Jan 2015			
Scale height of sodium mixing ratio, H_f	00:00	84.4-87.4 km	14.5 km
Sodium chemical time constant, τ	00:00-04:00	84.4-86.4 km	130 min
Lapse rate, γ	00:00	84.4-87.4 km	-12.9 K/km
Layer thickness, L	00:00	85.1-86.6 km	1.5 km

Table 2.2: Derived parameters from the diffusion events

Date	Time	Altitude	Value
17-18 Feb 2009			
Buoyancy frequency squared, N^2	01:30	74.1-77.1 km	4.2×10^{-5} s^{-2}
Buoyancy period, T_B	01:30	74.1-77.1 km	16 min
Eddy diffusion coefficient, K	01:30	75.3-75.9 km	4.1×10^2 m^{2}s^{-1}
Energy dissipation rate, ε	01:30	75.3-75.9 km	21.1 mW/kg
23-24 Feb 2009			
Buoyancy frequency squared, N^2	01:00	74.6-77.6 km	3.3×10^{-6} s^{-2}
Buoyancy period, T_B	01:00	74.6-77.6 km	58 min
Eddy diffusion coefficient, K	01:00	75.7-76.5 km	1.1×10^3 m^{2}s^{-1}
Energy dissipation rate, ε	01:00	75.7-76.5 km	4.6 mW/kg
25-26 Jan 2015			
Buoyancy frequency squared, N^2	00:00	85.4-88.4 km	2.8×10^{-6} s^{-2}
Buoyancy period, T_B	00:00	85.4-88.4 km	63 min
Eddy diffusion coefficient, K	00:00	85.1-86.6 km	2.8×10^3 m^{2}s^{-1}
Energy dissipation rate, ε	00:00	85.1-86.6 km	9.7 mW/kg

2.3.3. Gravity waves as source of turbulence

To understand the levels of turbulence, we now investigate GWs as sources of energy for the turbulence on the night of 17-18 February 2009. We consider both the ensemble of GWs and monochromatic GWs. We determine the gravity-wave activity in the stratosphere and mesosphere from the RDTL temperature and density profiles. We first calculate the density fluctuations. We then high-pass filter the fluctuations in time to remove components with periods longer than 4 hr and so represent gravity waves with periods between 1 and 4 hr (with a geometric mean period of 2 hr). We low-pass filter the fluctuations in altitude at 2 km and so represent gravity waves with vertical wavelengths between 2 km and a maximum determined by the altitude range of 15 km. We then characterize the ensemble of gravity waves by their RMS density fluctuations, RMS vertical displacement fluctuations, and specific potential energy of the GWs (e.g., Thurairajah et al., 2010a; Thurairajah et al., 2010b; Triplett et al., 2018).

We examine how the specific potential energy of the waves varies in altitude to estimate the energy available to generate turbulence. Waves propagating freely with altitude conserve their energy, and their specific potential energy of the waves varies with altitude as

$$E_{free}(z) = E_0 \times e^{(z-z_0)/H_a}, \tag{2.18}$$

where E_0 is the specific energy at altitude z_0 and H_a is the density scale height of the atmosphere. For gravity waves that are losing energy or dissipating with altitude the specific potential energy of the waves varies with altitude as

$$E_{diss}(z) = E_0 \times e^{(z-z_0)/H_{diss}}, \tag{2.19}$$

where E_0 is the specific energy at altitude z_0 and H_{diss} is the scale height of the GW specific potential energy. Thus dissipating waves will lose an amount of energy, ΔE, given by

$$\Delta E = E_{free} - E_{diss}. \qquad (2.20)$$

that is available for the production of turbulence. If this energy is deposited over some altitude range, L_d, through which the waves travel at group velocity c_{gz}, then the energy is deposited in a time interval, τ_d, given by

$$\tau_d = L_d/c_{gz}, \qquad (2.21)$$

and the GW energy dissipation rate is given by

$$\varepsilon_{GW} = \Delta E/\tau_d. \qquad (2.22)$$

We assume that L_d is equal to L, the depth of the instable layer derived from the vertical gradient of the potential temperature.

To apply this method to the lidar observations, we first determine the wave activity. The relative density fluctuations over the 37.5 km - 52.5 km and 62.5 km -77.5 km altitude ranges show downward phase progressions typical of upward propagating gravity waves (Figure 2.6). In the lower range, we find a specific potential energy of 1.5 J/kg. In the upper range, we find a specific potential energy of 0.35 J/kg. The specific potential energy decreased by a factor of 4.3, which corresponds to a scale height of -17 km. The scale height of the atmospheric density is 7 km indicating that the specific energy of freely propagating GWs would increase by a factor of 33. These GWs are losing energy as they propagate upward. We summarize the characteristics of the GW ensemble in Table 2.3 and derived parameters in Table 2.4. We estimate an energy

34

dissipation rate of 0.7 mW/kg. This value is considerably lower than the value of 21.1 mW/kg that we estimated from our analysis of the spreading event in section 2.3.2.
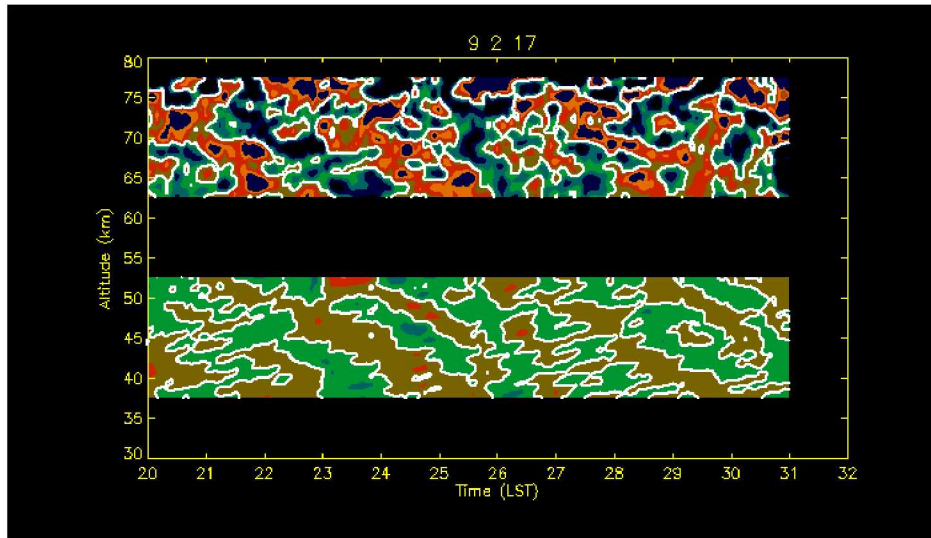
Figure 2.6. Gravity waves as seen in the Rayleigh lidar density perturbations on the night of 17-18 February 2009. The perturbations are derived from 30 minutes data. See text for details.

We detected monochromatic waves in the density profiles by determining the best temporal harmonic fits to the density fluctuations at each altitude and then determining the vertical phase progressions to the harmonic fits. We fitted harmonics to the 2-hr density profiles to find waves with periods greater than 4 hr and conducted fits to the 30-min data to find waves with periods between 1 and 4 hr. We determined the vertical wavelength from the observed frequency and vertical phase progression and then used the gravity wave polarization and dispersion relationships to estimate the horizontal wavelength, horizontal phase speed, group velocity, RMS horizontal velocity, vertical displacement, and specific potential energy (Fritts & Alexander, 2003; Hines, 1960).

We find a 2.5-h monochromatic in the density profiles. We investigated this wave in two ranges, the stratosphere (37.5-52.5 km) and the mesosphere (62.5-77.5 km). This wave exhibits a downward phase progression consistent with a vertical wavelength of 7 km in the stratosphere (41-52 km) and 10 km in the mesosphere (63-74 km). The amplitude of the wave is 0.3% in the stratosphere and 1.2% in the mesosphere. The signal to noise ratio (SNR) of the wave is 0.4 in the stratosphere and 0.4 in the mesosphere. The specific potential energy of the wave is 1.3 J/kg in the stratosphere and 17.2 J/kg in the mesosphere. We also investigate this wave during the first half of the night until the spreading event (00:00 LST) in the mesosphere and find that the amplitude of the wave is 1.6%, and the SNR is 0.7 in the range of 63-71 km. The specific potential energy of the wave is 27.9 J/kg. The turbulence energy dissipation rate is estimated by assuming that the specific potential energy of the wave is dissipated over the thickness of the layer, L, at the speed of the vertical group velocity of the wave. We estimate an energy dissipation rate of 46.5 mW/kg associated with this monochromatic wave. This value is larger than the value of 22.1 mW/kg that we estimated from the diffusion of sodium in section 2.3.2.

Table 2.3: Ensemble gravity-wave activity measured by Rayleigh Lidar

17-18 Feb 2009

Altitude Range	37.5-52.5 km	62.5-77.5 km
RMS relative density	0.36%	0.18%
RMS vertical displacement	83 m	15 m
Specific potential energy	1.4 J/kg	0.35 J/kg
SNR	2.3	0.006

23-24 Feb 2009

Altitude Range	37.5-52.5 km	62.5-77.5 km
RMS relative density	0.32%	0.57%
RMS vertical displacement	76 m	147 m
Specific potential energy	1.1 J/kg	3.7 J/kg
SNR	1.5	0.05

25-26 Jan 2015

Altitude Range	37.5-52.5 km	62.5-77.5 km
RMS relative density	0.37%	0.75%
RMS vertical displacement	94 m	180
Specific potential energy	1.7 J/kg	6.4 J/kg
SNR	3.1	4.1

Table 2.4: Parameters used to estimate turbulent energy dissipation rate from gravity-wave activities.

	H_{air} (km)	H_{damp} (km)	c_{gz} (m/s)	L_d (km)	t_d (hr)	ε_{GW} (mW/kg)
17-18 Feb 2009						
	7	-18	0.74	0.6	0.35	0.7
23-24 Feb 2009						
	7	21	0.74	0.8	0.64	3.6
25-26 Jan 2015						
	7	19	0.74	1.5	0.65	23.7

Altitude (km)	Period (hr)	λ_z (km)	λ_H (km)	$\Delta\rho/\rho$ (%)	PE (J/kg)	ξ (m)	c_{gH} (m/s)	c_{gz} (m/)s	SNR	ε (mW/kg)
17-18 Feb 2009										
41-52	2.5	7.1	211	0.33	1.28	78.5	22.5	-0.8	0.43	
63-74	2.5	9.9	296	1.24	17.2	284.0	31.7	-1.0	0.39	
63-71*	2.5	11.0	330	1.59	27.9	361.0	35.3	-1.2	0.66	46.5
23-24 Feb 2009										
42-48	2.3	7.6	207	0.20	0.44	45.8	24.2	-0.9	0.28	
66-77	2.3	5.2	140	1.45	25.0	352.0	16.3	-0.6	0.17	
66-71*	2.3	6.4	171	1.71	34.3	410.0	20.0	-0.7	0.84	45.8
25-26 Jan 2015										
44-50	2.5	11.2	327	0.30	1.04	71.3	35.0	-1.2	0.17	
65-77*	2.5	6.3	185	0.98	1.14	237	19.8	-0.7	0.54	0.86

Table 2.5: Characteristics of monochromatic gravity waves.

λ_z ,vertical wavelength; λ_H, horizontal wavelength;ξ, RMS vertical displacement; c_{gH}, horizontal group velocity; c_{gz}, vertical group velocity

2.4. Case study on 23-24 February 2009

2.4.1. Observations

On the night of 23-24 February 2009, a MIL forms at 20:45 LST at 75.4 km and descends to 74.1 km over the remainder of the observations until 05:30 LST (Figure 2.7, top panel). The MIL reaches its maximum amplitude of 35.0±10.7 K at an altitude of 75.4 km at the very beginning of the observation. At this time the topside lapse rate of the MIL is -12.2 ± 0.4 K and the width of the MIL is 3.1 km. The MIL then weakens until 23:15 LST and starts to increase again. The MIL reaches another maximum amplitude of 28.4 ± 7.2 K at an altitude of 74.3 km. At this time the topside lapse rate of the MIL is -16.8 ± 0.6 K and the width of the MIL is 5.0 km. Over the observation the amplitude of the MIL is between 7.4 and 35.0 K with an average value of 18.8 K. The peak altitude of the MIL varies between 72.7 km and 77.2 km with an average value of 74.1 km. The width of the MIL varies between 1.7 km and 7.9 km with an average value of 4.2 km. The topside gradient of the MIL varies between -16.8 K/km and -6.1 K/km with an average value of -9.8 K/km. In comparison the stratopause remains relatively undisturbed with a temperature that varies between 230.4 K and 237.1 K, with an average value of 234.1 K, and an altitude between 49.0 km and 52.8 km, with an average value of 50.1 km.

The sodium layer has an average peak altitude of 88.5 km that varies between 83.1 km and 91.0 km (Figure 2.7, middle panel). The average peak sodium number density is 4.5×10^3 atom/cm^{-3} and varies between 3.5×10^3 atom/cm^{-3} and 5.6×10^3 atom/cm^{-3}. The sodium layer has a scale height of 5.4 km on the topside and a scale height of 5.2 km on the bottomside that is reflected in

Figure 2.7. Temperature (top), sodium density (middle), potential temperature (bottom, contour) and sodium mixing ratio measured by the RDTL and SRDL on the night of 23-24 February 2009. See text for details.

the narrower spacing of the sodium density contours on the bottomside. Wave activity is evident with overturning in the sodium density (~ 76 km at 01:00 LST) that is consistent with the passage of large amplitude and or/breaking gravity waves as well. We highlight the spreading of the sodium density contours in the bottomside of the sodium layer from 00:00 LST to 02:00 LST. The height of the spreading coincides with the MIL and the time when the 200 atom/cm^{-3} sodium contour descends below 75 km corresponds to the time and altitude when the MIL begins to strengthen and the time when the 300 atom/cm^{-3} contour descends below 77 km corresponds to the time and altitude when the MIL reaches the second maximum altitude.

This event is observed between 23:00 LST and 2:00 LST and over ~73-78 km. The event is characterized by vertical spreading in both the sodium mixing ratio and potential temperature as well (Figure 2.7. bottom panel). The distance between the two mixing ratio contours, 5.0×10^{-12} and 5.0×10^{-13}, shows the same behavior, having a mean value of 2.2 km before 23:00 LST, and then increasing to a maximum of 6.0 km at 01:00 LST, before returning to 2.0 km. The spreading is clearly seen in the distance between the 400 K and 440 K potential temperature contours. The distance between the contours increases from a mean value of 2.6 km before 23:00 LST to a maximum of 7.4 km at 01:00 LST. Once again, the fact that the spreading appears consistently in both the sodium mixing ratio and the potential temperature indicates that material motion has occurred during this event and is associated with a reduction in convective instability. We again analyze this event in terms of turbulent transport and determine the eddy diffusion coefficient and energy dissipation rate associated with the turbulence following the method developed in section 2.3.2.

2.4.2. Estimate of turbulent diffusion coefficient and energy dissipation rate

We calculate the sodium mixing ratio averaged between 75.6 km and 76.6 km, and the scale height over the 74.6 km to 77.6 km range. The average sodium mixing ratio reaches a local maximum of 1.3 PPT at 01:00 LST that is larger than the local maximum value of 0.4 PPT at 04:00 LST (Figure 2.8). Thus we choose 01:00 LST as t_m. The scale height of sodium mixing ratio has typical value of 0.9 km before the spreading event begins (23:00 LST). The scale height has a value of 9.5 km at 01:00 LST. The sodium density profile and the sodium mixing ratio profile both show decreased vertical gradient and increased scale height at t_m (Figure 2. 9). The behavior of the sodium mixing ratio is consistent with our model of turbulent diffusion.

In Figure 2.10, we plot the temperature and potential temperature profiles measured at t_m. The MIL is clearly evident in the temperature profile. The MIL has an amplitude of 23.3 ± 7.3 K at an altitude of 74.6 km. The topside lapse rate of the MIL has a value of -9.0 ± 0.5 K and the width of the MIL is 5.3 km. A layer of nearly constant potential temperature coincides with the topside of the MIL. The value of the squared buoyancy frequency calculated from a 3 km range between 74.8 and 77.8 km is 3.3×10^{-6} s^{-2}. This indicates a layer of reduced stability (equation 2.17) and mixing that corresponds to the spreading in both the number density and mixing ratio profiles. To further analyze this layer, we plot the vertical gradient of the potential temperature in Figure 2.11. We plot three profiles that are processed in the same manner as described in section 2.3.2. We use the 1 km profile to determine that the layer is between 75.7 and 76.5 km, with a thickness, L, of 0.8 km. We calculate the chemical time constant from the disappearance of sodium mixing ratio between 01:00 LST and 04:00 LST as 67 minutes (Figure 2.8). We summarize the pertinent values derived from the temperature and sodium mixing ratio

measurements in Table 2.1. Using equations 2.15 and 2.16, we estimate an eddy diffusion coefficient of 1.1×10^3 m^2s^{-1} and an energy dissipation rate of 4.6 mW/kg (Table 2.2).
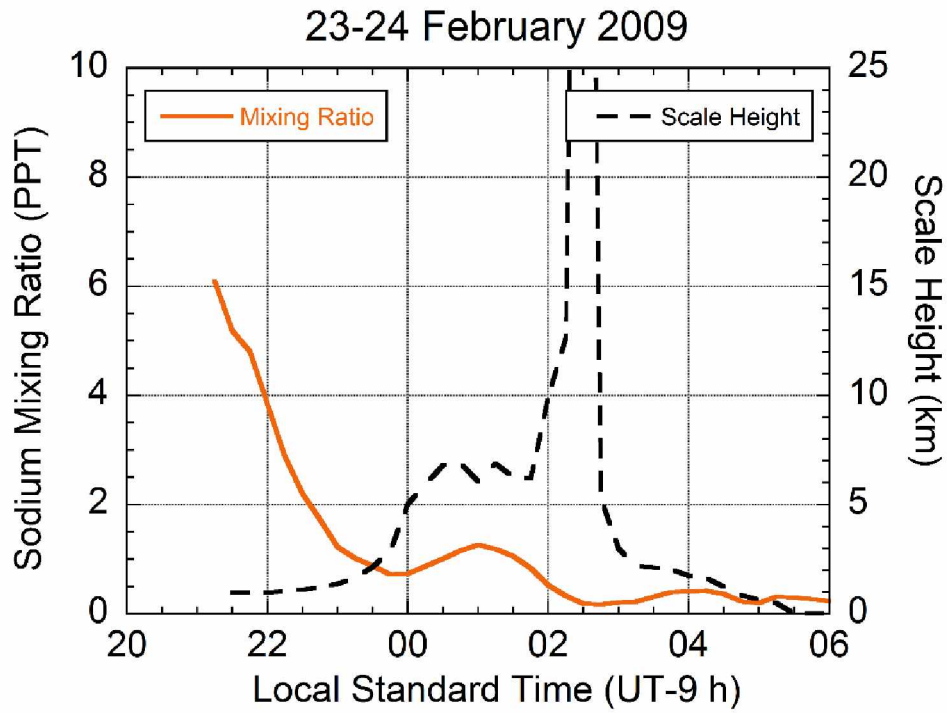
Figure 2.8. Average sodium mixing ratio measured by the RDTL and SRDL between 75.2 km and 76.2 km on the night of 23-24 February 2009.
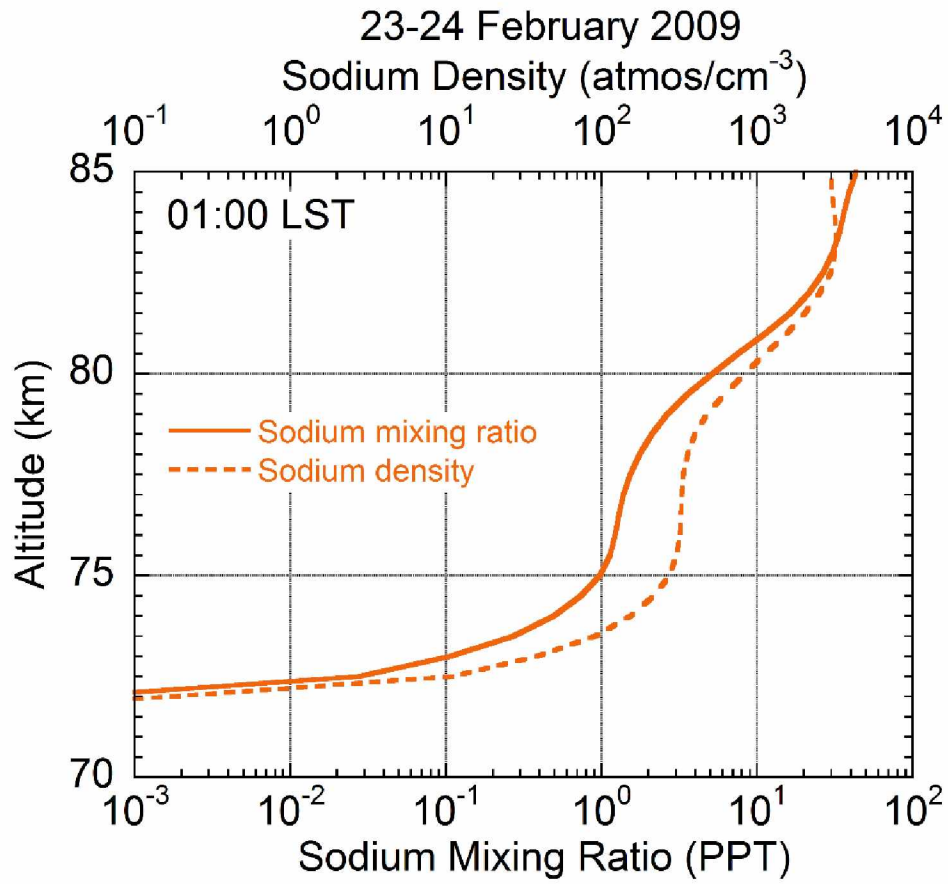
Figure 2.9. Profiles sodium mixing ratio (solid) and sodium density (dashed) measured by the RDTL and SRDL between 00:30 LST and 01:30 LST on the night of 23-24 February 2009.

Figure 2.10. Profiles of temperature (red) and potential temperature (blue) measured by the RDTL between 00:30 LST and 01:30 LST on the night of 23-24 February 2009.

Figure 2.11. Vertical gradient of potential temperature measured by the RDTL between 00:30 LST and 01:30 LST on the night of 23-24 February 2009. See text for details.

2.4.3. Gravity waves as source of turbulence

We now investigate GWs as sources of energy for the turbulence on the night of 23-24 February 2009. The relative density fluctuations over the 37.5 km - 52.5 km and 62.5 km -77.5 km altitude ranges show downward phase progressions typical of upward propagating gravity waves (Figure 2.12). In the lower range, we find a specific potential energy of 1.3 J/kg. In the upper range, we find a specific potential energy of 4.3 J/kg. The specific potential energy increased by a factor of 3.3, which corresponds to a scale height of 21 km. The scale height of the atmospheric density is 7 km indicating that the specific energy of freely propagating GWs would increase by a factor of 33. These GWs are losing energy as they propagate upward. We summarize the characteristics of the GW ensemble in Table 2.3 and derived parameters in Table 2.4. We estimate an energy dissipation rate of 3.6 mW/kg. This value is comparable to the value of 4.6 mW/kg that we estimated from the spreading event.

We find a 2.3-h monochromatic wave in the density profiles. We investigated this wave in two ranges, the stratosphere (37.5-52.5 km) and the mesosphere (62.5-77.5 km). This wave exhibits a downward phase progression consistent with a vertical wavelength of 8 km in the stratosphere (42-48 km) and 5 km in the mesosphere (66-77 km). The amplitude of the wave is 0.2% in the stratosphere and 1.5% in the mesosphere. The SNR of the wave is 0.3 in the stratosphere and 0.2 in the mesosphere. The specific potential energy of the wave is 0.4 J/kg in the stratosphere and 25.0 J/kg in the mesosphere. We also investigate this wave during the first half of the night until the spreading event (23:00 LST) in the mesosphere and find that the amplitude of the wave is 1.7%, and the SNR is 0.8 in the range of 63-71 km. The specific potential energy of the wave is 34.3 J/kg. The possible turbulence energy dissipation rate is estimated using the same method as

47

described in section 2.3.3. We estimate an energy dissipation rate of 45.8 mW/kg associated with this monochromatic wave. This is larger than the value of 4.6 mW/kg that we estimated from the diffusion of sodium in section 2.4.2.
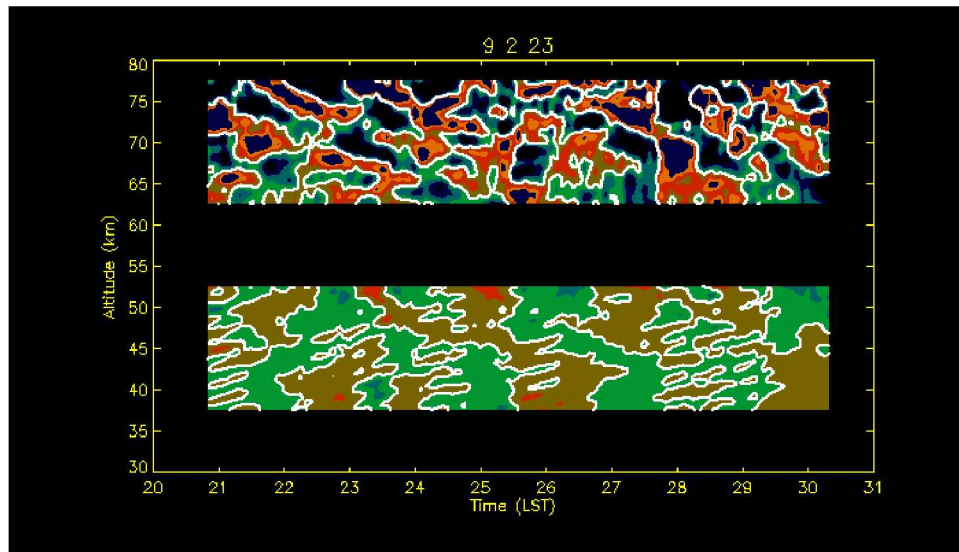
Figure 2.12. Gravity waves as seen in the Rayleigh lidar density perturbations on the night of 23-24 February 2009. The perturbations are derived from 30 minutes data. See text for details.

2.5. Case study on 25-26 January 2015

2.5.1. Evolution of temperature and sodium

On the night of 25-26 January 2015, a MIL forms at 22:45 LST at 84.0 km and ascends to 85.0 km at 00:15 LST (Figure 2.13, top panel). The MIL reaches its maximum amplitude of 13.4 ± 9.3 K at an altitude of 85.0 km at 24:15 LST. At this time the topside lapse rate of the MIL is -14.1 ± 0.4 K and the width of the MIL is 1.9 km. Over the observation the amplitude of the MIL is between 8.1 K and 13.4 K with an average value of 10.6 K. The peak altitude of the MIL varies between 84.0 km and 85.0 km with an average value of 84.4 km. The width of the MIL varies between 0.9 and 2.0 km with an average value of 1.4 km. The topside gradient of the MIL varies between -14.1 K/km and -10.4 K/km with an average value of -12.1 K/km. In comparison the stratopause remains relatively constant with a temperature that varies between 237.4 K and 238.8 K, with an average value of 238.2 K, and an altitude between 45.5 and 45.8 km, with an average value of 45.7 km.

The sodium layer has an average peak altitude of 88.6 km that varies between 84.3 km and 92.7 km (Figure 2.13, middle panel). The average peak sodium number density is 2.2×10^3 atom/cm^{-3} and varies between 8.5×10^2 atom/cm^{-3} and 3.5×10^3 atom/cm^{-3}. The sodium layer has a scale height of 6.4 km on the topside and a scale height of 5.5 km on the bottomside that is reflected in the narrower spacing of the sodium density contours on the bottomside. Wave activity is evident with overturning in the sodium density (~ 85 km at 00:00 LST) that is consistent with the passage of large amplitude and or/breaking gravity waves as well. We highlight the overturning of the sodium density contours in the central region of the sodium layer from 12:00 LST to 01:00

LST. The height of the overturning coincides with the height of the MIL (85 km) and the time of the overturning coincides with the time when MIL has the largest amplitude.

This event is observed between 22:00 LST and 01:00 LST and over ~83-88 km. The event is characterized by vertical spreading in both the sodium mixing ratio and potential temperature as well (Figure 2.13, bottom panel). The distance between the two mixing ratio contours, 1.0×10^{-11} and 2.0×10^{-11}, shows the same behavior, having a mean value of 2.9 km before 22:00 LST, and then increasing to a maximum of 7.3 km at 23:45 LST, before returning to 3.0 km. The spreading is clearly seen in the distance between the 560 K and 600 K potential temperature contours. The distance between the contours increases from a mean value of 2.3 km before 22:00 LST to a maximum of 6.6 km at 23:45 LST. Once again, the fact that the spreading appears consistently in both the sodium mixing ratio and the potential temperature indicates that material motion has occurred during this event and is associated with a reduction in convective instability. We will analyze this event in terms of turbulent transport and determine the eddy diffusion coefficient and energy dissipation rate associated with the turbulence using the method developed in section 2.3.2.
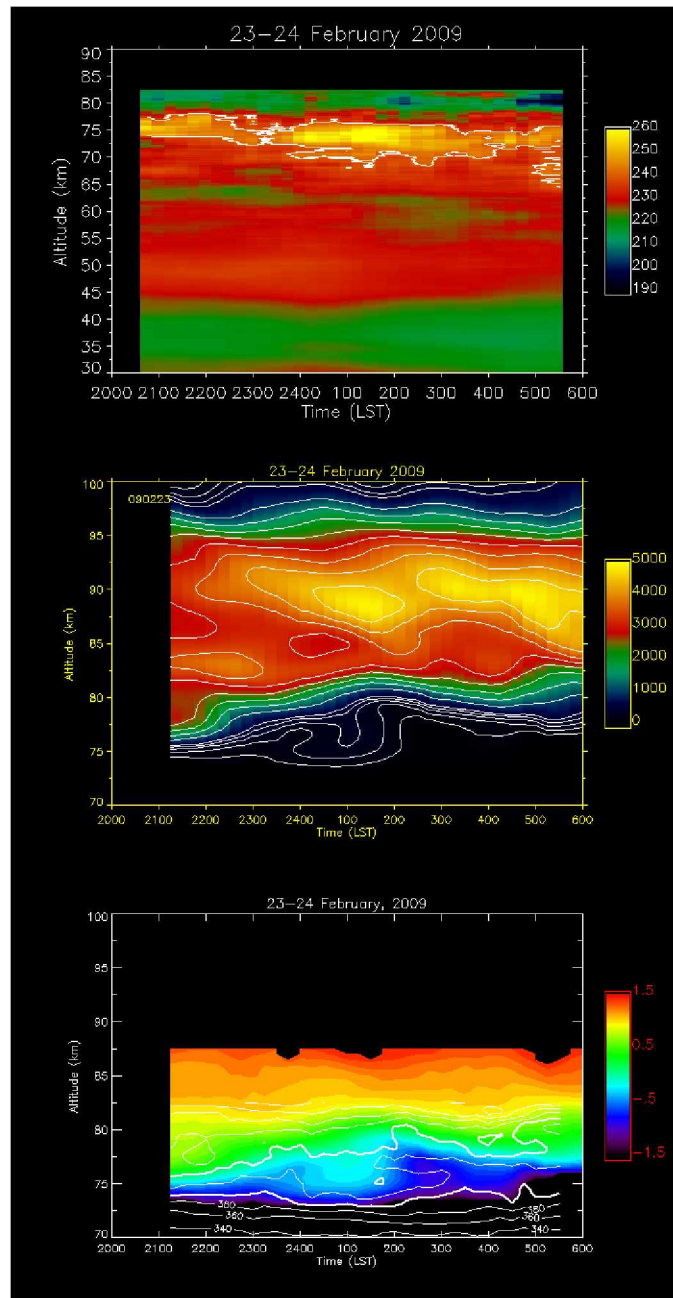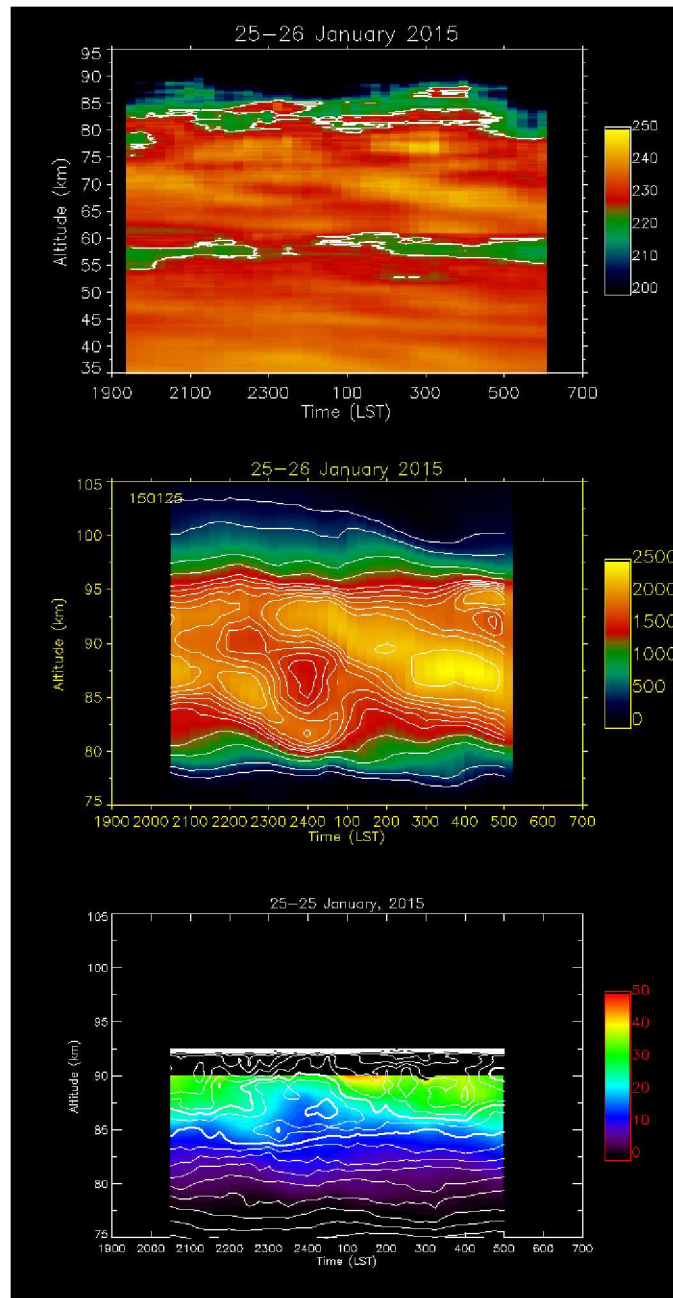
Figure 2.13. Temperature (top), sodium density (middle), potential temperature (bottom, contour) and sodium mixing ratio measured by the RDTL and SRDL on the night of 25-26 January 2015. See text for details.

2.5.2. Estimate of turbulent diffusion and energy dissipation rate

We calculate the average sodium mixing ratio between 84.4 km and 87.4 km, and the scale height of the mixing ratio over the 85.4 km to 86.4 km altitude range. The average sodium mixing ratio reaches a local minimum of 14.7 PPT at 00:00 LST that is considerably smaller than the local minimum value of 19.1 PPT at 22:15 LST (Figure 2.14). Thus we choose 00:00 LST as t_m. The scale height of the sodium mixing ratio has typical value of 4.0 km before the spreading event begins (23:00 LST) and reaches a local maximum of 21.8 km at 23:45 LST (Figure 2.14). The scale height has a value of 14.5 km at 00:00 LST. The sodium density profile and the sodium mixing ratio profile both show the decreased vertical gradient and increased scale height at t_m (Figure 2.15). The behavior of the sodium mixing ratio is consistent with our model of turbulent diffusion.

In Figure 2.16, we plot the temperature and potential temperature profiles and the sodium number density and mixing ratio measured by the resonance lidar at t_m. The MIL is clearly evident in the temperature profile. The MIL has an amplitude of 11.1±9.3 K at an altitude of 85.0 km. The topside lapse rate of the MIL has a value of -11.8±0.4 K and the width of the MIL is 1.9 km. Meanwhile, a layer of nearly constant potential temperature coincides with the topside of the MIL. The value of the squared buoyancy frequency calculated from a 3km range between 85.4 and 88.4 km is 2.8×10^{-6} s^{-2}. This indicates a layer of reduced stability (equation 2.17). The sodium layer also shows diffusion and overturning in both the number density and mixing ratio profiles. To further analyze this layer, we plot the vertical gradient of the potential temperature in Figure 2.17. We plot three profiles that are processed in the same manner as described in section 2.3.2. We use the 1 km- profile (red) to determine that the layer is between 85.1 and 86.6 km,

52

with a thickness, L, of 1.5 km. We calculate the chemical time constant from the disappearance

of sodium mixing ratio between 01:00 LST and 04:00 LST (Figure 2.14) as 130 minutes. We

summarize the pertinent values derived from the temperature and sodium mixing ratio

measurements in Table 2.1. Using equations 2.15 and 2.16, we estimate an eddy diffusion

coefficient of 2.8×10^3 m^2s^{-1} and energy dissipation rate of 9.7 mW/kg (Table 2.2).
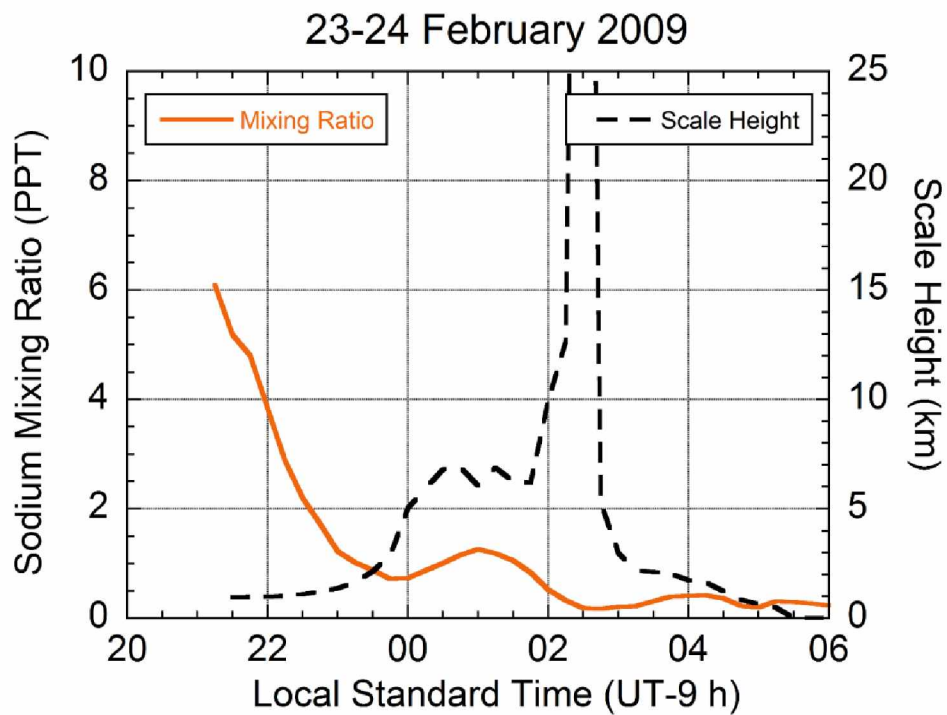
Figure 2.14. Average sodium mixing ratio measured by the RDTL and SRDL between 85.4 km
and 86.4 km on the night of 25-26 January 2015.
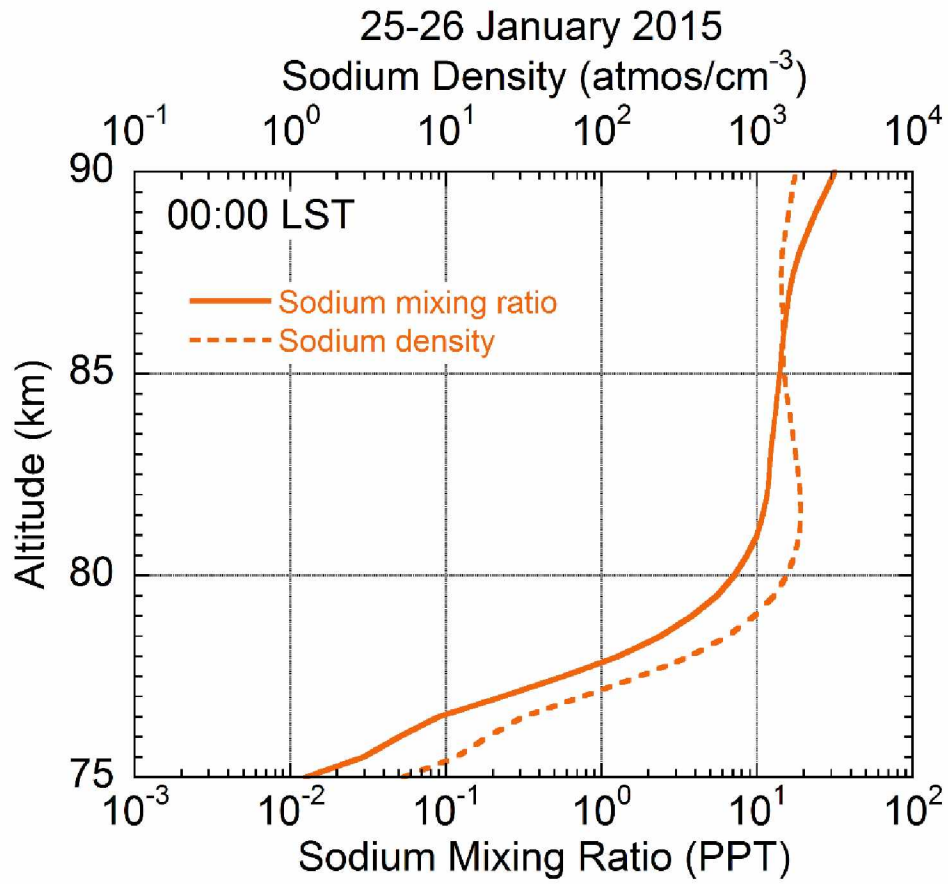
Figure 2.15. Profiles of sodium mixing ratio (solid) and sodium density (dashed) measured by the RDTL and SRDL between 23:30 LST and 00:30 LST on the night of 25-26 January 2015.
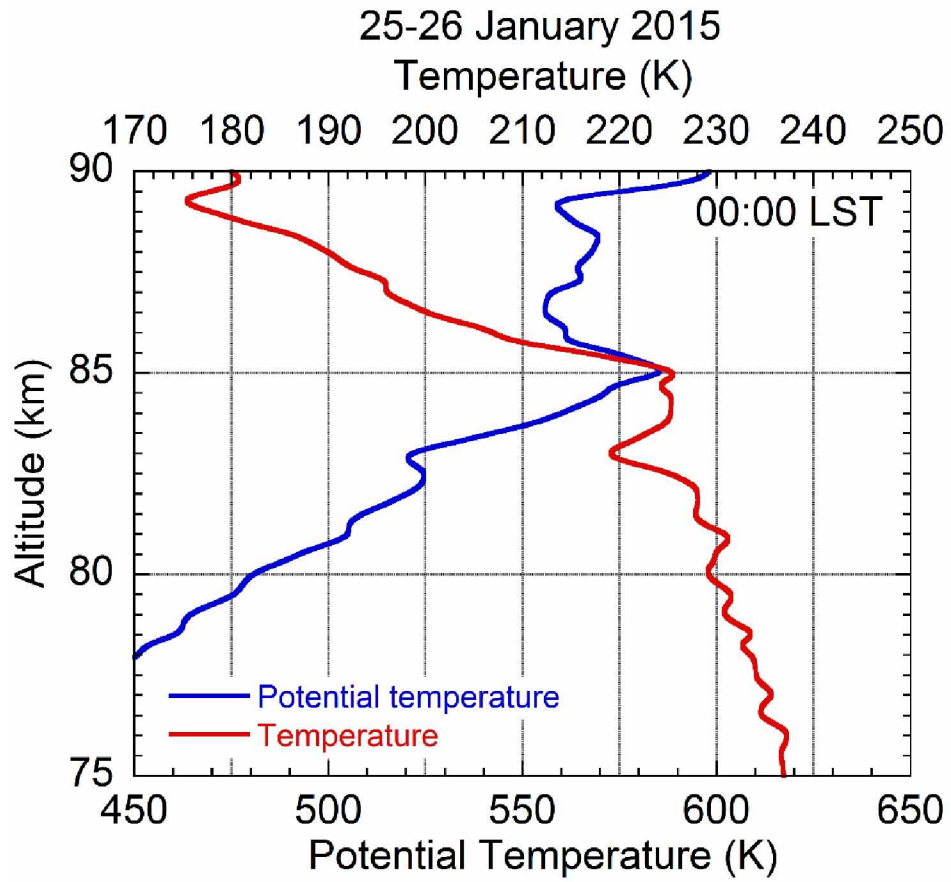
Figure 2.16. Profiles of temperature (red) and potential temperature (blue) measured by the RDTL between 23:30 LST and 00:30 LST on the night of 25-26 January 2015.
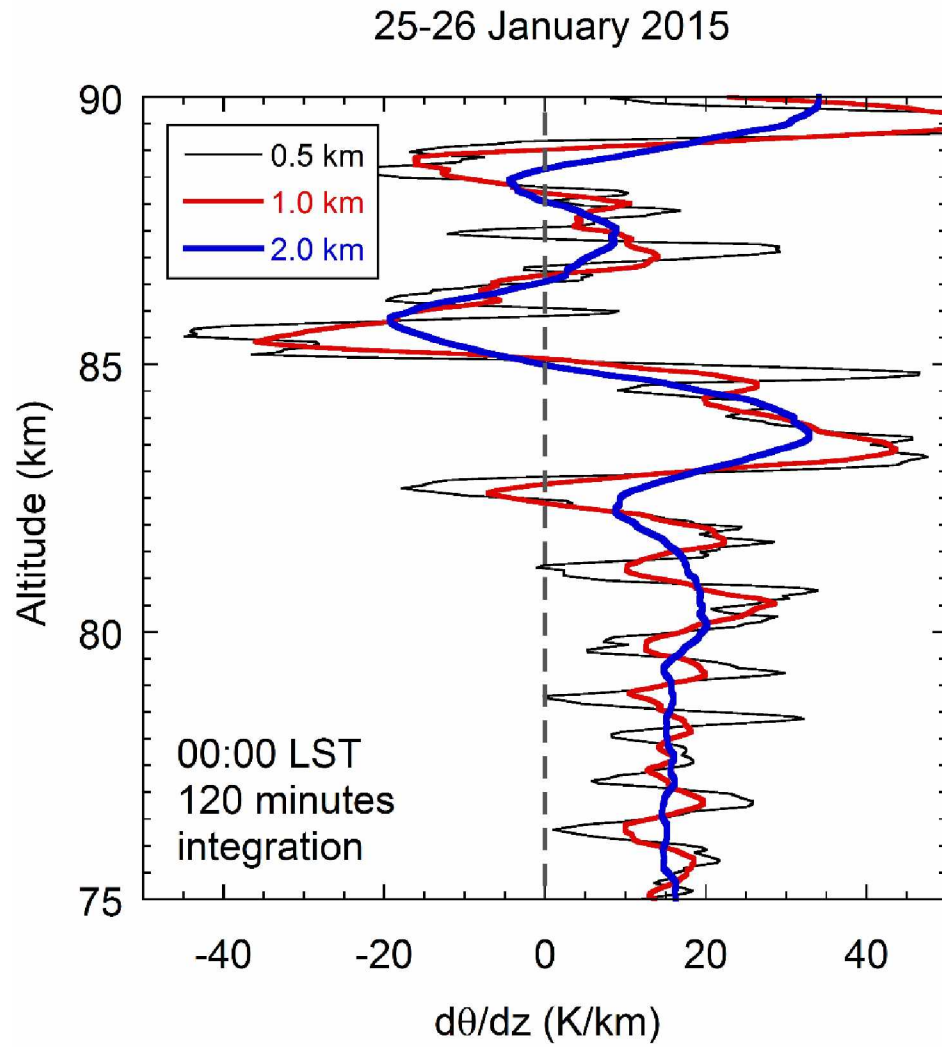
Figure 2.17. Vertical gradient of potential temperature measured by the RDTL between 23:30 LST and 00:30 LST on the night of 25-25 January 2015. See text for details.

2.5.3. Gravity waves as source of turbulence

We now consider the gravity waves as sources energy for turbulence on the night of 25-25 January 2015. The relative density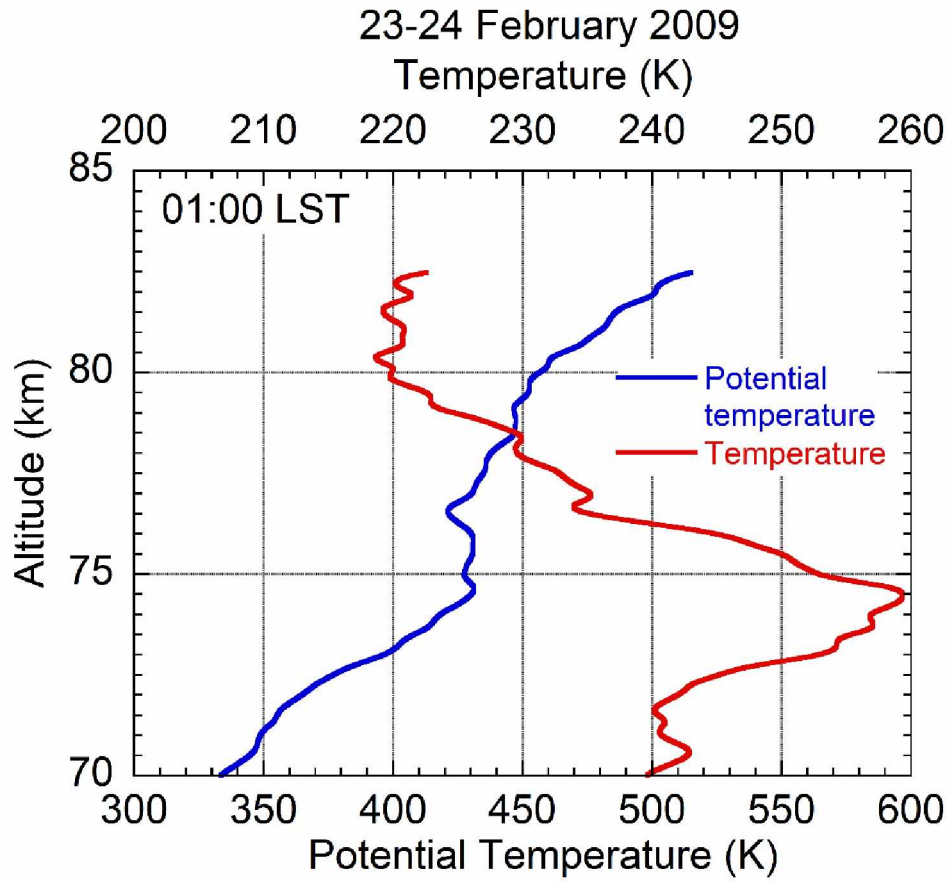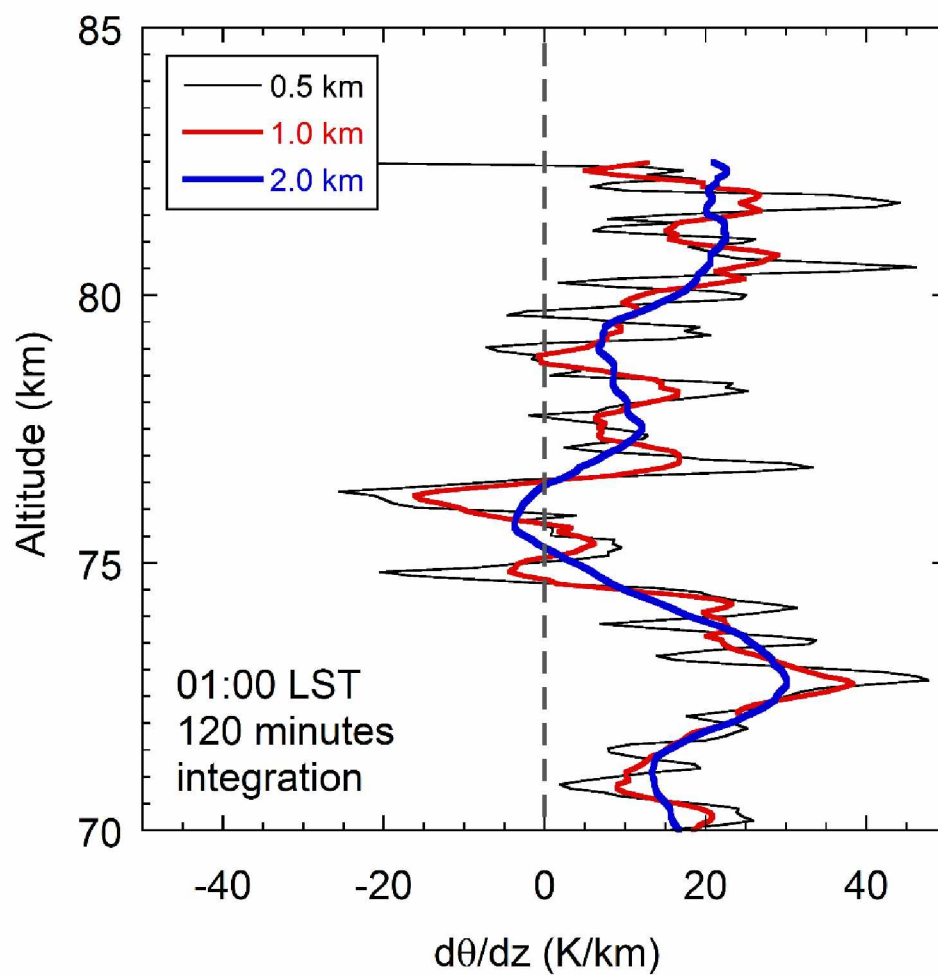 fluctuations over the 37.5 km - 52.5 km and 62.5 km -77.5 km altitude ranges show downward phase progressions typical of upward propagating gravity waves (Figure 2.18). In the lower range, we find a specific potential energy of 1.7 J/kg. In the upper range, we find a specific potential energy 6.4 J/kg. The specific potential energy increased by a factor of 3.8, which corresponds to a scale height of 19 km. The scale height of the atmospheric density is 7 km indicating that the specific energy of freely propagating GWs would increase by a factor of 33. These GWs are losing energy as they propagate upward. We summarize the characteristics of the GW ensemble in Table 2.3 and derived parameters in Table 2.4. We estimate an energy dissipation rate of 23.7 mW/kg. This value is larger than the value of 9.7 mW/kg that we estimated from the spreading event.

We find a 2.5-h monochromatic in the density profiles. We investigated this wave in two ranges, the stratosphere (37.5-52.5 km) and the mesosphere (62.5-77.5 km). This wave exhibits a downward phase progression consistent with a vertical wavelength of 11 km in the stratosphere (44-50 km). The wave is not evident in the mesosphere when investigating the whole observation period (SNR<0.1). The amplitude of the wave is 0.2% and SNR is 0.3 in the stratosphere. The specific potential energy of the wave is 0.4 J/kg in the stratosphere. We also investigate this wave during the first half of the night (before 24:00 LST) in the mesosphere and find that the amplitude of the wave is 1.0%, and the SNR is 0.5 in the range of 65-77 km. The specific potential energy of the wave is 1.1 J/kg. The possible turbulence energy dissipation rate is estimated using the same method as described in section 2.3.3. We estimated an energy

dissipation rate of 0.86 mW/kg associated with this monochromatic wave. This is considerably

lower than the value of 9.7 mW that we estimated from the diffusion of sodium in section 2.5.2.
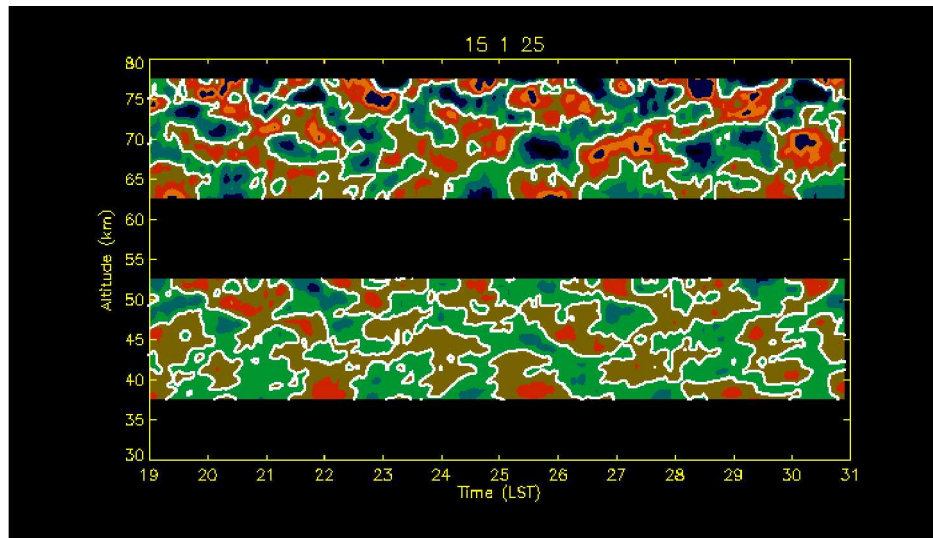
Figure 2.18. Gravity waves as seen in the Rayleigh lidar density perturbations on the night of 25-26 January 2015. The perturbations are derived from 30 minutes data. See text for details.

2.6. Discussion and conclusions

We have estimated values of turbulent eddy diffusion coefficients, K, and energy dissipation rates, ε, associated with instabilities from the diffusion of sodium from three case studies. The values of K are 4.1×10^2 m^2/s, 1.1×10^3 m^2/s, and 2.8×10^3 m^2/s and the corresponding values of ε are 21 mW/kg, 5 mW/kg and 10 mW/kg respectively. Previous studies report values of K in the range of 1-100 m^2/s and ε in the range of 1-1000 m^2/s (e.g., Gardner, 2018; Swenson et al., 2018; Triplett et al., 2018). Our values of K are larger than typically reported while the values of ε are more typical. It is worth noting that all of the measurements in this study are associated with unstable layers where the value of the buoyancy frequency is very small and thus, following equation 2.17, for a given value of the turbulent energy dissipation rate, ε, the values of K will be very large. Rocket-borne ionization gauge measures detected turbulent fluctuations in the 70-88 km altitude region on the night of January 25-26, 2015 as part of MTeX (Triplett et al., 2018). The value of ε that we have derived from these lidar measurements of 11.5 mW/kg is in good agreement with the values reported by the MTeX ionization gauge measurements of 6-30 mW/kg.

However, there are two immediate sources of uncertainty in our analysis of turbulence from sodium diffusion. The first source of uncertainty arises from the thickness of the turbulent layer, L. In the analysis, L is assumed to be the thickness of the convectively unstable layer ($\frac{d\theta}{dz} < 0$), and the values are in the range of 1-2 km. However, the actual thickness of the turbulence layer can be much smaller than these values. The ionization gauge measurements show that even though multiple turbulent layers can exist in an altitude range of a few kilometers, the thickness of a single layer is in the order of a few hundred meters, while the thinnest layer has thickness of

59

50 m. Meanwhile, the measured outer scales of turbulence vary from 129 m to 360 m in the altitude range of 70 to 88 km (e.g., Triplett et al., 2018). Hence our estimate of L may be a factor of 5-20 larger than the actual thickness of the turbulent layers. Thus we may overestimate of K and ε by the same factor. The second source of uncertainty arises from the estimate of the chemical time constant. Our estimates of chemical time constant are consistent with the chemistry of the sodium layer where sodium has a longer lifetime in the center of the layer than at the edge. The values are consistent with those obtained in simulations (Xu & Smith, 2003, 2005). It is assumed that the observed loss time of sodium mixing ratio represents the chemical time constant. This is only absolutely correct if the atmosphere is at rest. The measured loss time and the true chemical time constant may be significantly different due to advection. For a layer with horizontal scale length, L_h, and a vertical scale height, H_v, in the presence of winds with horizontal velocity V_h, and vertical velocity V_v, the observed loss time, τ_{obs}, is related to the true loss time, τ, by

$$\frac{1}{\tau_{obs}} = \frac{1}{\tau} \pm \frac{1}{\tau_h} \pm \frac{1}{\tau_v} \qquad (21)$$

where $\tau_h = L_h/V_h$ and $\tau_v = H_v/V_v$ are the horizontal and vertical advection timescales, respectively. Using typical values for the horizontal and vertical scales and advection velocities we expect that the time constants could vary by a factor of 3 (Collins et al., 2011).

The major source of uncertainty in our analysis of energy available from GWs is the intrinsic frequency of the wave (see Appendix A). As we established in Appendix A, we assumed zero background wind in the analysis. The assumption induces a typical uncertainty of factor of two in the estimate of the intrinsic frequency. Even though this uncertainty does no induce

uncertainty in the estimate of the wave energy (equation A29), it does induce an uncertainty of the same factor in the estimate of the vertical group velocity (equations A31 and A32), which in turn induces an uncertainty of the same factor in the estimate of the GW energy dissipation rate. Thus an uncertainty of a factor of two exist in our estimate of the GW energy dissipation rate.

This study has been based on case studies where MILs, measured by RDTL, were found at altitudes overlapping the mesospheric sodium layer, measured by a SRDL. In this study we have extended the scope of previous studies by developing retrievals of potential temperature and sodium mixing ratio from the RDTL and SRDL measurements. The study is limited by the Rayleigh lidar signal in the first two case studies associated with the 2009 Turbopause measurements when the RDTL included smaller telescope than that during the MTeX investigation. The study is also limited by the lack of wind measurements at the sodium layer altitudes. New Rayleigh lidar measurements based on the larger telescope and coordinated with a new sodium resonance wind temperature lidar at PFRR will support more complete studies.

This page intentionally left blank

Chapter 3. Sodium resonance wind-temperature lidar

3.1. Introduction

Resonance lidar systems have proven a particularly valuable tool for studies of wave activity in the upper mesosphere and lower thermosphere or mesopause region (~80-110 km). The dynamical processes of gravity-wave instability, overturning, breaking and nonlinear behavior have an important impact on the circulation and mixing in the mesosphere (see collections edited by Johnson and Killeen (1995); and Siskind et al. (2000) and reviews by Fritts and Alexander (2003); and Hecht (2004)). Much effort has focused on developing instruments that can make accurate and precise high-resolution wind and temperature measurements of these dynamical events.

Resonance lidar systems have proven a particularly valuable tool for studies of wave activity in the upper mesosphere and lower thermosphere (~80-110 km). Using resonance scattering from the mesospheric metal layers (i.e., calcium, iron, lithium, potassium, sodium), basic metal density systems have routinely yielded density profiles of the mesospheric metal layers since the 1960s (Bowman et al., 1969). Temperature measurements derived from spectroscopic probing of the hyperfine structure were demonstrated in the late 1970s (Gibson et al., 1979) and further developed in the 1980s (Fricke & von Zahn, 1985). Current sodium resonance wind-temperature lidars (SRWTL), employing Doppler-free spectroscopic techniques, have been operated since the 1990s (Bills et al., 1991b; She et al., 1990; She & Yu, 1994; She et al., 1992) and been progressively refined to provide routine high-resolution measurements of sodium density, temperature, and wind (e.g., Li et al., 2012; Liu et al., 2004; She et al., 2004; Yuan et al., 2014). The development of magneto-optic filters has also supported SRWTL measurements of

temperature and wind in daytime (Chen et al., 1996; Yuan et al., 2008). Temperature systems based on resonance scattering from the potassium and iron layers have also been developed that yield measurements of temperature as well as metal densities (Gardner et al., 2001; von Zahn & Höffner, 1996). Comprehensive reviews of resonance lidars in general and SRWTLs in particular have been presented by Chu and Papen (2005) and Krueger et al. (2015) respectively. A collection of milestone papers on the development of resonance fluorescence lidar has been presented by Grant et al. (1997).

In this chapter we present a new SRWTL that was installed at the Lidar Research Laboratory at Poker Flat Research Range (LRL-PFRR) in fall 2017. This SRWTL, the PFRR SRWTL, has the same architecture as current systems and incorporates a state-of-the-art tunable diode laser master oscillator. In section 3.2 we review the theory of SRWTL. In section 3.3 we describe the SRWTL at LRL-PFRR. In section 3.4 we analyze the measurement performance of the SRWTL. In section 3.5 we summarize the performance of the lidar system and identify areas for further system development and improvement.

3.2. Theory of sodium wind-temperature measurement

3.2.1. Spectroscopy of sodium atoms

The spectroscopy of the sodium atoms, a light alkali metal, is very well understood. The energy levels of the ground state and the first excited state of sodium atoms can be described by three models, with progressively more quantum mechanical processes included (Figure 3.1). In the first model, or basic model, the sodium atom is a two-state system with only one transition from the 3S to the 3P states. We plot the transitions with the transition line strength (not bracketed)

and the Einstein A coefficient (bracketed) in the unit of the first model. In the second model, or intermediate or fine model, the spin-orbit coupling effect is included. The spin-orbit coupling splits the excited state into two states, $^3P_{1/2}$ and $^3P_{3/2}$, while the ground state remains as a single state, $^3S_{1/2}$. The splitting in the energy levels of the excited state lead to two different transitions, namely, the D_1 and D_2 line at 589.6 nm and 589.16 nm. In the third model, or final or hyperfine model, the nuclear spin and associated hyperfine interaction are included. The excited states, $^3P_{1/2}$ and $^3P_{3/2}$, split into two and four hyperfine levels respectively, while the ground state, $^2S_{1/2}$, splits into two hyperfine levels (F= 1, 2). In this model, the D_2 line includes two groups of line, i.e., D_{2a} and D_{2b}, corresponding to the two hyperfine energy levels of the ground state. The D_{2a} line is composed of the three lines that have the $^2S_{1/2}$ (F=2) level as their ground state. The D_{2b} line is composed of the three lines that have the $^2S_{1/2}$ (F=1) level as their ground state. The center frequencies of the three D_{2a} hyperfine lines differ by less than 51 MHz and the center frequencies of the three D_{2b} hyperfine lines differ by less than 94 MHz (Chu & Papen, 2005).
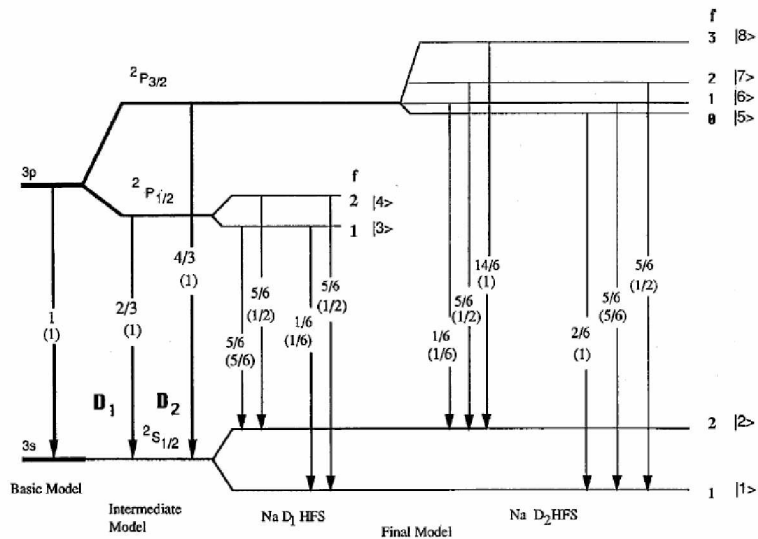
Figure 3.1. Energy levels diagram of atomic sodium adapted from She and Yu (1995).

This hyperfine structure allows sodium atoms to absorb or emit photons at different wavelengths. Each of these hyperfine lines is broadened by two different mechanisms, natural broadening and Doppler broadening. The natural linewidth broadening is due to the finite lifetime of the excited state. The natural broadening results in a Lorentzian line shape and has a Full Width Half Maximum (FWHM) value of about 10 MHz. Under thermodynamic equilibrium, the velocity distribution of sodium atoms (or any atoms or molecules) obeys the Maxwell-Boltzmann distribution. This velocity distribution causes Doppler shifting of the frequencies and results in broadening of the lines. At 200 K, the Doppler broadening FWHM linewidth is about 1 GHz, which is far greater than both the differences in the hyperfine frequencies and the width of the natural broadening. The absorption spectrum shows the fine structure of the sodium spectrum, where the hyperfine structure is blurred, and the D_{2a} and D_{2b} spectral lines overlap (Figure 3.2).

66

Doppler broadening is sensitive to the temperature since the RMS width of the Doppler-broadened line increases as the Maxwell velocities increase. Thus by measuring the width of the Doppler broadened linewidth, we can retrieve the temperature of the sodium atoms. Since the sodium atoms are in thermal equilibrium with their environment, the temperature of the sodium atoms is the temperature of the ambient atmosphere. In addition to the random thermal motion, the sodium atoms also move with the bulk motion of the atmosphere. Thus the D_{2a} and D_{2b} spectral lines are shifted in frequency by the background wind. By measuring this shift, we can derive the wind from the spectrum of D2 line of sodium atoms.
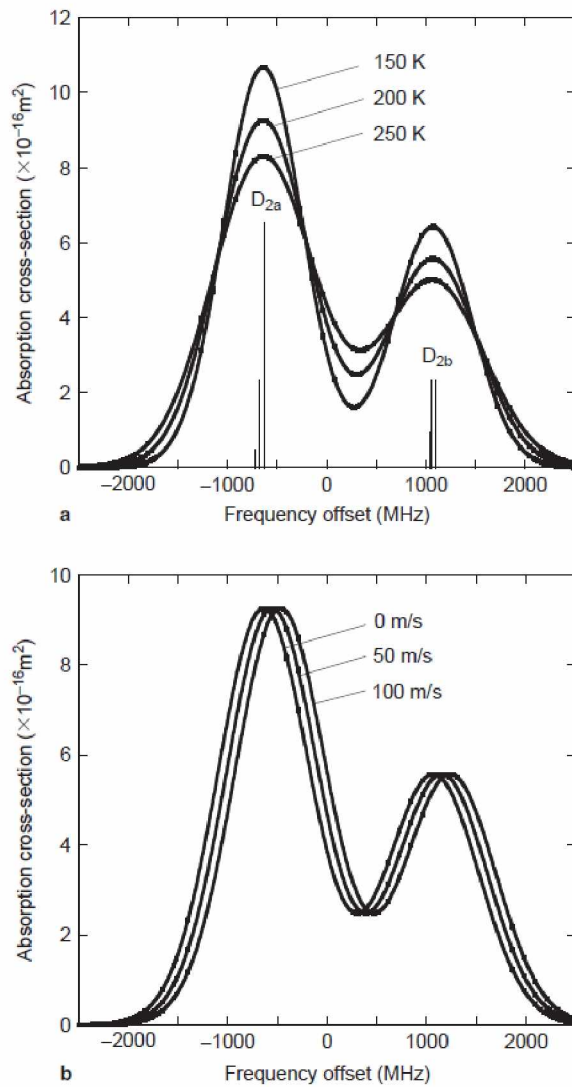
Figure 3.2. Sodium absorption cross section as a function of frequency at: (a) three temperatures and; (b) three radial velocities from Chu and Papen (2005).

3.2.2. The lidar equation

The scattered signal received by a lidar system arises from the absorption and scattering of the laser beam by the atoms and molecules in the atmosphere. For a sodium resonance lidar, the signal results from the resonance fluorescence of photons by the sodium atoms in the mesospheric sodium layer. Consider a lidar that transmits pulses of light at frequency v_L, with an average power of P_L, and has a receiving telescope of area A. For a SRWTL, the frequency of the laser is close to the D_{2a} line of the sodium atom. The number of photons returned from the resonance fluorescence by sodium atoms in a range bin of depth Δz at a distance z to the lidar may be expressed by the resonance lidar equation,

$$N_s(v,z) = \left(\frac{P_L(v_L)\Delta t}{hv_L}\right) * \left[\sigma_{eff}(v_L)n_{na}(z)\Delta z\right] * \left(\frac{A}{4\pi z^2}\right) * \left[\eta(v)T_a^2(v_L,z)E^2(v_L,z)G(z)\right] + N_B\Delta t, \quad (3.1)$$

where $N_s(v,z)$ is the number of photons detected in a range bin of depth Δz (z-Δz/2 and z+Δz/2) at frequency v, Δt (= 2 × Δz/c, where c is the speed of light) is the corresponding duration of the depth Δz, h is Plank's constant, $T_a(v_L,z)$ is the one-way transmittance of the atmosphere for light at frequency v_L from the transmitter to the range z, $\sigma_{eff}(v_L)$ is the effective scattering cross-section of sodium atoms at the lidar frequency v_L, $n_{na}(z)$ is the number density of sodium atoms at altitude z, $\eta(v_L)$ is the optical efficiency of the system at frequency, v_L, $E(v_L,z)$ is the extinction of light from the ground to range z, G(z) is the overlap geometrical factor describing the overlap of the transmitter and receiver at range z, and N_B is photon counts in the range bin per unit time due to background skylight and detector dark counts.

The effective cross-section is defined as the averaged photon number scattered by an atom to the total incident photon number per unit area (Chu & Papen, 2005). It is determined by the convolution of the absorption cross-section σ_{abs} and the laser spectral lineshape g_L,

$$\sigma_{eff}(v_L, v_0) = \int_{-\infty}^{+\infty} \sigma_{abs}(v, v_0) g_L(v, v_L) dv. \tag{3.2}$$

The Doppler broadened absorption cross-section for each transition line is expressed as

$$\sigma_{abs}(v, v_0) = \sigma_0 \exp(-\frac{(v-v_0)^2}{2\sigma_D^2}), \tag{3.3}$$

where v_0 is the frequency of each transition line σ_D $(= , v_0\sqrt{\frac{k_B T}{Mc^2}}$ where k_B is the Boltzmann constant, T is the temperature, M is the mass of the atom) is the rms linewidth of Doppler broadening, σ_0 is the peak absorption cross-section at resonance.

The laser lineshape is approximated by a Gaussian function with a rms width σ_L. Thus the effective cross-section for a resonance line can be expressed as

$$\sigma_{eff}(v_L, v_0) = \frac{\sigma_D \sigma_0}{\sqrt{\sigma_L^2 + \sigma_D^2}} \exp(-\frac{(v_0 - v_L)^2}{2(\sigma_L^2 + \sigma_D^2)}). \tag{3.4}$$

Given that there are six lines in the D_{2a} transition, and that the line of sight wind speed is v_R, the total effective cross-section is expressed as

$$\sigma_{eff}(v_L) = \sum_{n=1}^{6} w_i \frac{\sigma_D \sigma_{0i}}{\sqrt{\sigma_L^2 + \sigma_{Di}^2}} \exp(-\frac{[v_{0i} - v_L(1 - \frac{v_R}{c})]^2}{2(\sigma_L^2 + \sigma_{Di}^2)}), \tag{3.5}$$

where w_i is the weighing factor of the i_{th} line.

The number of photons returned from the Rayleigh scattering by air molecules in a range bin of thickness at a distance z_R to the lidar may be expressed by the Rayleigh lidar equation,

$$N_R(v, z_R) = \left(\frac{P_L(v_L)\Delta t}{hv_L}\right) * [\sigma_R(\pi, v_L)n_R(z_R)\Delta z] * \left(\frac{A}{z_R^2}\right) * [\eta(v)T_a^2(v_L, z_R)G(z_R)] + N_B\Delta t, \quad (3.6)$$

where σ_R is the Rayleigh backscatter cross-section, and n_R is the number density of the atmosphere. The product of the backscatter cross-section and atmosphere number density (also known as the volume backscatter coefficient) can be calculated from the temperature and pressure of the atmosphere as

$$\sigma_R(\pi, v_L)n_R(z) = 2.938 \times 10^{-32}\left(\frac{P(z)}{T(z)}\right)\frac{1}{\lambda^{4.0117}}, \quad (3.7)$$

where λ is the wavelength of the laser (Chu & Papen, 2005). From equations 3.1 and 3.6, we relate the effective cross-section of sodium to the detected resonance lidar signal and the Rayleigh signal through

$$\sigma_{eff}(v, z) = \frac{C(z)}{E^2(v,z)}\frac{N_s(v,z)-N_B}{N_R(v,z_R)-N_B}, \quad (3.8)$$

where

$$C(z) = \frac{\sigma_R(\pi,v_L)n_R(z_R)}{n_{na}(z)}\frac{4\pi z^2}{z_R^2}, \quad (3.9)$$

and we have chosen the Rayleigh altitude to be sufficiently high in the atmosphere (i.e., $z_R > 30$ km) so that there is no change in atmospheric transmission between the Rayleigh altitude and the sodium layer (i.e., $T_a(v_L, z_R) = T_a(v_L, z)$), and the transmitter and receiver are aligned so that the

receiver captures all the signal from the Rayleigh altitude and the sodium altitude (i.e., $G(z_R) =$ $G(z) = 1$).

From equations 3.5 and 3.8, it is clear that we can obtain the line shape of the total effective cross-section of sodium atoms at different altitude through measuring the resonance lidar signal and Rayleigh lidar signal at different frequencies, and thus measure the wind and temperature of the sodium layer. In practice, this is achieved through measuring the resonance fluorescence signal at three frequencies, v_a, $v_+ = v_a + \Delta v$, and $v_- = v_a - \Delta v$, where v_a is the frequency of the D$_{2a}$ line, and Δv is the frequency shift of 630 MHz. The value of Δv is chosen to yield the highest sensitivity of the measurements to wind variations. This technique is known as the three-frequency ratio technique, which was first proposed by Bills and coworkers (Bills et al., 1991a; Bills et al., 1991b) and She and coworkers (She & Yu, 1994; She et al., 1992). The temperature is derived from the ratio

$$R_T(z) = \frac{N_{norm}(v_+,z)+N_{norm}(v_-,z)}{N_{norm}(v_a,z)} \cong \frac{\sigma_{eff}(v_+,z)+\sigma_{eff}(v_-,z)}{2*\sigma_{eff}(v_a,z)}, \tag{3.10}$$

where

$$N_{norm}(v,z) = \frac{N_S(v,z)-N_B}{(N_R(v,z_R)-N_B)E^2(v,z)}. \tag{3.11}$$

The wind is derived from the ratio

$$R_W(z) = \frac{N_{norm}(v_+,z)-N_{norm}(v_-,z)}{N_{norm}(v_a,z)} \cong \frac{\sigma_{eff}(v_+,z)-\sigma_{eff}(v_-,z)}{\sigma_{eff}(v_a,z)}. \tag{3.12}$$

It is obvious from equations 3.5, 3.11 and 3.12 that for a SRWTL system to work, the frequency and lineshape of the laser pulses must be repeatable and well-known and the linewidth of the

laser pulse must be sufficiently narrow to resolve the Doppler broadened sodium D_{2a} fluorescence spectrum. In the next section, we will discuss the architecture of such a lidar system in detail. The temperature and winds are then determined from the temperature and wind ratios by a look-up table (e.g., Su et al., 2008).

3.3. Sodium wind temperature lidar system

As we discussed in section 3.1, the ability to produce repeatable narrow-band laser pulses with accurate frequency and well known lineshape is critical to the success of a sodium wind temperature system. To fulfill these requirements, the SRWTL transmitter is designed with four main components or subsystems. The first component is a master oscillator that produces continuous wave (CW) beam with narrow linewidth (less than 10 kHz). The second component is a frequency control system that monitors and locks the frequency. The third component is a frequency shifter that shifts the frequency of the CW laser beam on a pulse-to-pulse basis. The fourth component is a pulsed amplifier that coverts the CW beam to high power pulsed beam. We plot a schematic of the SRWTL as it was initially deployed at LRL-PFRR in Figure 3.3. The SRWTL at LRL-PFRR is an upgraded version of a preexisting SRWTL. The master oscillator of the SRWTL was acquired as a complete upgrade, while the frequency control and pulsed dye amplifier subsystems were part of an existing SRWTL that was relocated to PFRR. The SRWTL was configured with two transmitted beams, one in the vertical, and one that is 20° off-vertical to the north.
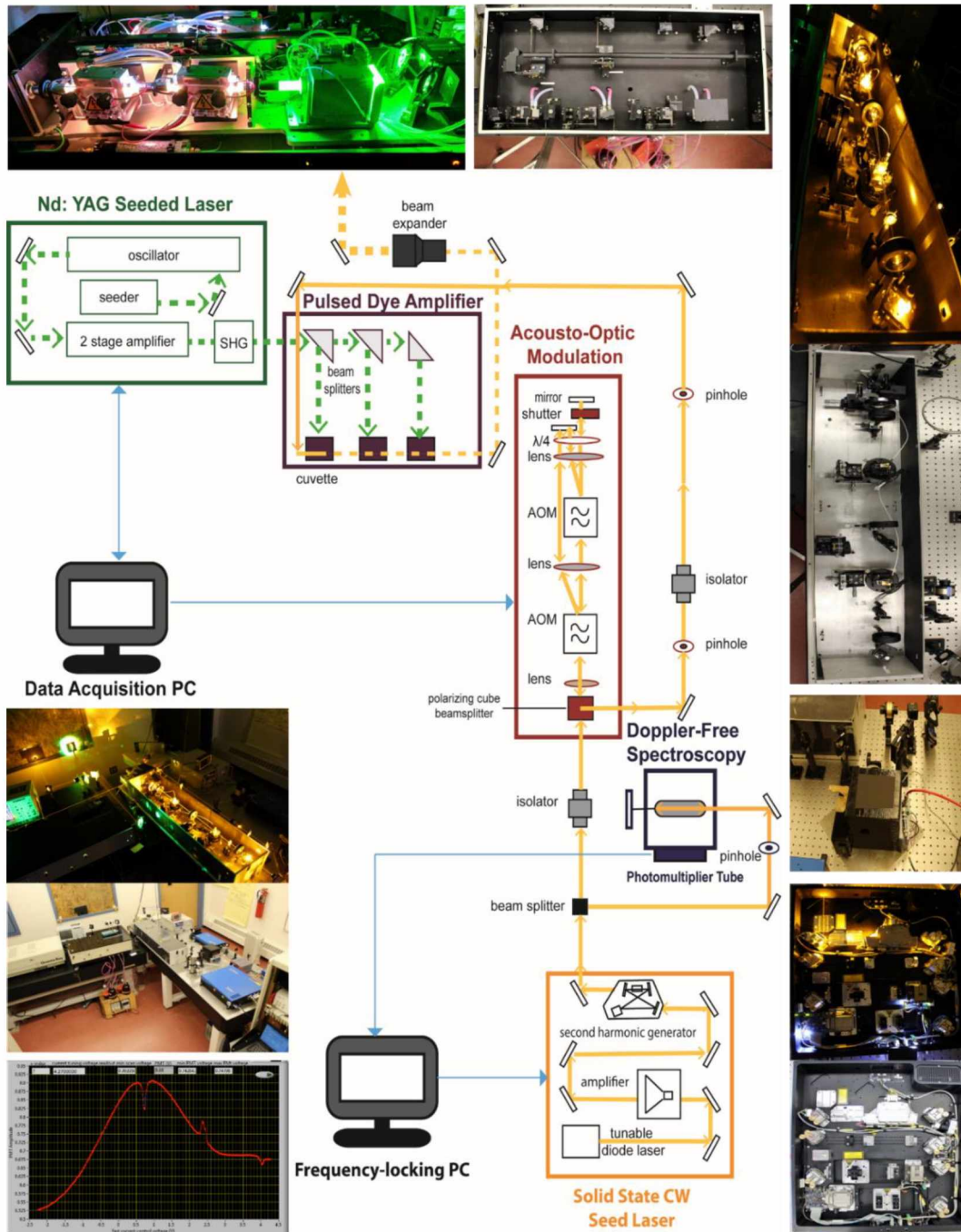
Figure 3.3. A sketch of the SRWTL system along with pictures of key components (Alspach et al., 2018).

3.3.1. The master oscillator

In the original SRWTL in the 1990s, the master oscillator was a CW frequency-stabilized single-mode ring dye laser (Bills et al., 1991a; Bills et al., 1991b; She et al., 1990; She & Yu, 1994; She et al., 1992). The ring dye laser produced a CW beam with average power of 500-600 mW and linewidth of 500 kHz. The frequency of the ring dye laser could be tuned over a range of more than 30 GHz (White, 1999). The main disadvantage of the ring dye laser was that its frequency was very sensitive to both mechanical vibrations and changes in temperature. Thus it required a very stable and well-controlled environment, which made it challenging to deploy in the field or on mobile platforms (e.g., airplane). It required operators with significant experience to maintain the laser at the desired frequency over the duration of an observing period. To overcome these challenges, researchers at Colorado State University developed a solid-state oscillator using a Sum Frequency Generator (SFG) that mixes radiation of Nd:YAG lasers at 1319 nm and at 1064 nm in a lithium niobite resonator to generate a CW beam at 589 nm (Vance, 2004; Vance et al., 1998). The laser was capable of generating more than 400 mW of CW single frequency 589 nm radiation of linewidth 10 kHz (Vance, 2004). Compared to the ring dye laser, the SFG was easier to operate and was capable of continuous operation without the need to periodicaly change the dye. The frequency stability of the SFG also exceeded that of the ring dye laser (Vance, 2004). However, despite this success the SFG approach was limited by the ability to acquire high quality lithium niobite crystals with durable optical coatings. Only one prototype SFG laser was constructed and incorporated into an operating SRWTL, the Weber lidar (She et al., 2002). However, more general advances in semiconductor amplifier and frequency-doubling technology expanded the operating range of tunable lasers based on external cavity diode laser to more than 1000 mW at yellow and orange wavelengths (Heine, 2013). These developments were spurred

by the need for precise and stable CW lasers in astronomical guide stars, laser cooling and trapping, Bose-Einstein condensation etc. and resulted in the commercial development of such laser systems (e.g., TA-SHG Pro, Toptica Photonics AG). The TA-SHG Pro laser system comprises a tunable diode laser, a high-power semiconductor amplifier, and an integrated frequency doubling stage, or second harmonic generator (SHG). The tunable diode laser has an external cavity configuration where the wavelength is tuned by a piezoelectric that modifies the cavity length. The SHG stage is a folded ring cavity in bow-tie configuration that results in highly efficient generation of light at 589 nm. This class of CW lasers can generate light from 330 nm to 780 nm with individual lasers tunable over several nm. The laser generates single frequency radiation with a bandwidth of less than 200 kHz and power of up to 1.2 W. The system includes a DLC pro controller that provides stability, ease of use, thermal and acoustic ruggedness, and stable operation. These lasers are currently being incorporated in SRWTLs around the world as researchers phase out the use of ring-dye laser systems. The laser was incorporated into the SRWTL at PFRR as the master oscillator in November 2017.

3.3.2. The frequency control components

3.3.2.1. Doppler-free spectroscopy

Two conter-propagating beams of large enough intensity (typically ~ 0.4 mW/mm^2) in a sodium vapor cell will give rise to a fluorescence spectrum that has three features that are narrower than the Doppler width of the spectrum. These features, called Doppler-free features, appear as two dips in the emission light at ν_a and ν_b and a peak at crossover frequency ν_c. (Figure 3.4). These features can be explained by a simple three state system. Assume that the ground state of sodium has two separate levels, 'a' and 'b', and the excited state 'e'. The atoms can be excited from 'a'

and 'b' to 'e' through absorbing photons with frequency ν_a and ν_b respectively. If the incident beam has frequency ν, then the incident light from the left can only interact with atoms of speed ν_R such that the Doppler-shifted frequency matches ν_a or ν_b, while the incident light from the right can only interact with atoms of speed $-\nu_R$. Thus, if the frequency of the incident light does not match ν_a or ν_b, the incident light from the left and the right interact with different atoms, and the laser induced fluorescence scatter is twice of what it was with one beam. However, if ν matches ν_a or ν_b, the incident light from the left and right both interact with the same atoms that have zero speed relative to the beam. If the beam has enough intensity, there is a saturation effect that dramatically reduce the population of atoms at ground state, thus induce a dip (called the Lamp dip) exactly at ν_a or ν_b. At the crossover frequency ν_c, an atom that in the ground state 'a' has the right speed to interact to with the incident light from the right and will be excited to the state 'e'. Then it can either decay to state 'a' and be available to interact with the same incident light, or decay to state 'b' and be available to interact with the incident light from the left. Thus there is a larger population of atoms that are available for fluorescence interactions and an enhancement peak occurs. The central frequencies of these dips and peak are independent of the temperature, and thus can serve as the absolute frequency reference for the wind and temperature measurements. Thus the frequency of the CW laser can be locked precisely to one of the three frequencies, ν_a, ν_b or ν_c. These absolute frequency references are the key to the success of SRWTLs.

The spectroscopic control system is set up as follows. A small portion of the light from the master oscillator is split and directed into a sodium vapor cell. A mirror is placed at the other end of the cell and retroreflects the beam through the same path. The temperature of the cell is

stabilized at 80°C to provide sufficient number of sodium atoms as a vapor in the cell. A photomultiplier tube (PMT) is placed against the side of the cell to measure the signal emitted by the sodium atoms. An example of the resultant Doppler-free saturation absorption spectrum is shown in Figure 3.4. The plot shows the signal received by the signal when the frequency of the CW laser is tuned by a piezo. This spectrum is termed an absorption spectrum as it arises due to the manner in which the counter rotating beams are absorbed by the sodium vapor. However, the spectrum represents the signal detected from the light that is re-emitted from the sodium atoms. This signal is used to lock the frequency at the D_{2a} peak by dithering the frequency of the laser around $\nu_a \pm 1.6$ MHz every 1 s. The frequency is dithered by applying a small voltage offset (3 mV) to the CW laser piezo.
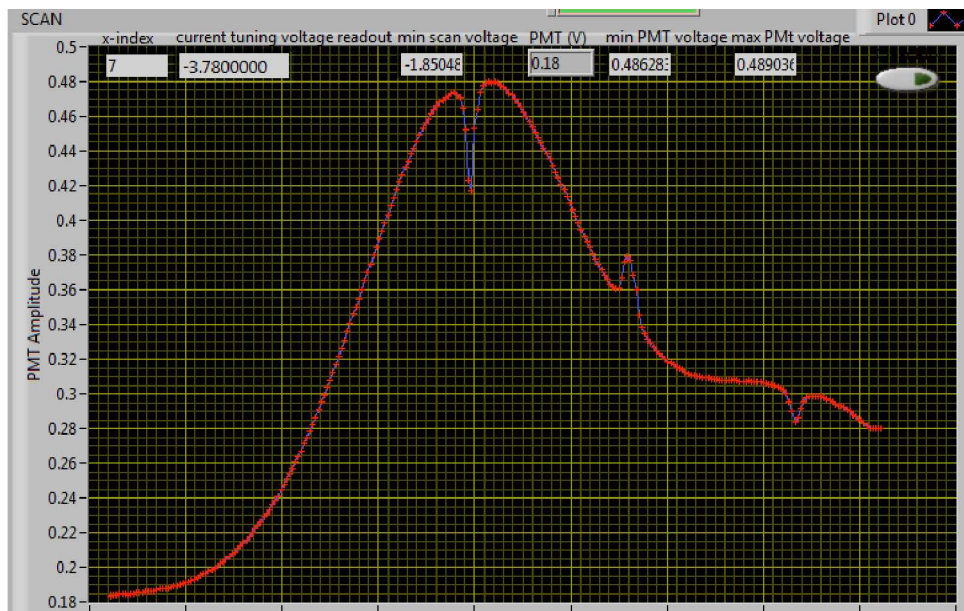
Figure 3.4. Doppler-free saturation-absorption spectrum measured from a sodium cell in the SRWTL system. The temperature of the cell is set at 353 K (80°C). The plot shows the signal received by the PMT plot against the offset applied to the piezo voltage (-4V to +4V). The piezo tunes the frequency of the CW laser. See text for details.

3.3.2.2. The frequency shifter

Once the CW seeding laser is locked to the center of the D_{2a} transition, we have an absolute frequency reference. The output of the CW laser is then directed into the frequency shifter to generate the two shifted frequencies required for wind and temperature measurements. The frequency shifter is a dual acousto-optic modulator (AOM) unit that shifts the CW seed beam through unshifted (0 MHz), upshifted (+630 MHz) and downshifted (-630 MHz) frequencies. The system is a composed of two acoustic-optic (AO) crystals and a series of lenses, waveplates and mirrors. The optics select desired frequencies and block undesired frequencies at each shift. These optics also ensure the output beam of different frequencies follow the same path the maintain their alignment into the PDA.

An acoustic-optic crystal is a piece of transparent material chosen with a small transducer on one side. The most important property of the crystal is that the refractive index changes with compression or expansion. A sinusoidal voltage drives the transducer, which applies a strain to the crystal and changes the refractive index of the crystal. This creates a travelling acoustic wave front across the crystal. As a laser beam travels through these wave front, Bragg scattering effect occurs. This yields an angular dependent outgoing beam that has a maximum intensity at a certain angle θ, where $\sin\theta = \lambda/2\Lambda$, λ is the laser wavelength, an Λ is the wavelength of the acoustic wave. The laser beam also experiences a frequency shift as it travels through the travelling refractive index due to the Doppler shift of the outgoing light by the acoustic wave. As a result, the outgoing Bragg scattered light is an angular dependent beam that has a maximum at Bragg angle θ with a frequency that is upshifted or downshifted by exactly the frequency of the sinusoidal voltage. The sign of the frequency shift is determined by the sign of θ. Thus for a laser

beam incident at the Bragg angle, θ, upon an AO crystal with an acoustic wave applied, two principal beams exit the crystal. One is the unshifted beam following the direction of the incident beam with the same frequency. The other is an off-axis frequency-shifted beam that is spatially separated from the incident beam by 2θ, with a frequency shifted by the frequency of the acoustic wave.

In the AOM unit, two acoustic crystals are placed in the beam path. The crystals shift the frequency of the laser beam by +315 MHz or -315 MHz, depending on the direction of the acoustic wave relative to the laser beam. The frequency shifted beam is then retroreflected and shifted again as it passes through the crystal a second time. This yields a beam that shifted by +630 MHz or -630 MHz, while maintaining its path. The redirection of the beam to its original path requires careful alignment such that the active region of the crystal is placed at the focal point of the lens such that the all three beams coming from the crystal can be retroflected to the same point. Furthermore, it is necessary that the beam is well collimated to yield good efficiency with the crystal. Theoretically, the efficiency of the shifted frequency to the input light is ~ 80% for a single pass, and ~64% for the double pass. The actual efficiency of the whole frequency shifter subsystem is often lower due to misalignment, optical loss at surfaces, and aging of the AO crystals.

Thus a sequence of unshifted, upshifted, and downshifted beams is output by the AOM unit. A optical shutter is placed in front of the mirror. When the shutter is closed, the unshifted beam is blocked. During observations, synchronized signals from the data acquisition system determines which crystal, if either, receives a sinusoidal driving voltage. When both crystals are 'off', and the shutter is open, the input light is passes through the crystals without experiencing a Bragg

scattering effect, and the unshifted beam is output. When only one the crystals is 'on', and the shutter is closed, the input light is passes through the crystals while experiencing a Bragg scattering effect, and the corresponding upshifted or downshifted beam is output.

3.3.3. The pulsed dye amplifier

The CW beam generated by the frequency shifter unit is then amplified and pulsed by a Pulsed Dye Amplifier (PDA) (PDA-1, Spectra Physics). The PDA is a three-stage amplifier. The first two stages are transversely pumped dye cells, while the last stage is a longitudinally pumped dye cell. The PDA is pumped by a frequency-doubled Nd:YAG laser at 532 nm. Under ideal conditions, the PDA output pulsed beam has a Fourier-transform-limited Gaussian lineshape with a narrow linewidth (~100 MHz) centered at the frequency of the CW seed beam. However, the lineshape of the actual output pulses are both broadened and shifted by processes inherent in the dye amplification process.

The PDA output is broadened by two processes. The first process that broadens the PDA output is amplified spontaneous emission (ASE). The ASE is produced by the spontaneous emission when the dye is excited by the pump beam. The lineshape of the ASE is very broad (~5 nm). If the ASE is amplified by the following stages, the effect is to add a broad component to the output line shape. Fortunately, ASE can be reduced to a few percent (<10%) of the total output power with careful optical alignment that eliminates reflections along the beam path. Meanwhile, due to the broad line width, the sodium atoms barely scatter the ASE, and the narrowband (1 nm) filter in the receiver eliminates most of the scattered signal. If the PDA is well aligned the effect of ASE is negligible. Thus at the beginning of each observation period, the operator aligns the PDA to maximize the output power of the PDA beam while maintaining the ASE at low power.

The second process that broadens the PDA output is the spectral quality of the Nd:YAG pump laser pulses. The pump Nd:YAG laser is an injection-seeded single-mode laser (Quanta Ray Pro, Spectra Physics). If the pump beam maintains a single mode beam the output pulsed beam from the PDA has a linewidth of ~100 MHz. However, if the Nd:YAG laser has a multi-mode beam the output pulsed beam from the PDA will have a much broader linewidth (~1 GHz). This broadening arrises from mode beating in the Nd:YAG laser that is preserved in the dye amplification process. Furthermore, the effect will yield significant pulse-to-pulse variations in the output pulsed beam from the PDA. The mode structure of the Nd:YAG pump laser can be monitored by recording the shape of the Nd:YAG laser pulses with a high-speed photodiode. When the laser is well-seeded and has a single mode, the laser pulse profile in time is regular and smooth (Figure 3.5, top panel). When the laser is unseeded and has a multiple modes, the laser pulse profile in time is irregular and ragged (Figure 3.5, bottom panel). The Nd:YAG laser will generate multiple-modes if it is not thermally stable. There is a transition period after the laser is started where the laser is not thermally stable and the laser generates multi-modes. Once the laser has stabilized the operator monitors the Nd:YAG laser for single-mode operation.

The amplification process can also generate a frequency shift between the input CW seed beam and the output pulsed beam. This effect is caused by nonlinearities in the amplification process. These nonlinearities are attributed to inhomogeneous heating of the dye solvent, the intensity dependence of the refractive index, and the time dependence of the dye amplification. This shift causes a smaller error in the temperature measurement (~0.2 K) than in the line-of-sight wind (5-15 m/s). This effect can be corrected operationally by examining the vertical wind measurements. The correction assumes that the vertical wind is zero when averaged over the height of the sodium layer for periods of 1 hour or longer, and a non-zero average represents the

bias in this line-of-sight wind due to the frequency shift effect. The off-vertical beams include a component of the horizontal wind which has a non-zero average due to the non-zero mean horizontal winds. This operational correction can only be made if the SRWTL includes a vertical beam. The bias in the vertical wind is subtracted from the line-of-sight wind measurements and then the horizontal winds are calculated. Another operational method to correct the laser and vertical wind bias from the horizontal wind is to average coplanar beams (e.g., east-west beams, north-south beams). A spectroscopic correction is based on monitoring the spectra of the PDA output beam on a pulse-by-pulse basis. The variations in frequency can be estimated using the absorption of the pulsed beam in an absorbing cell. The frequency of the ratio of an attenuated beam after it passes through the absorption iodine cell to an unattenuated beam is a measure of the frequency of the beam, where the ratio and frequency shift can be calibrated by the CW seed laser beam (Yuan et al., 2009). We are currently using the operational correction for the frequency shift. In the future, an iodine vapor cell will be incorporated into the system to provide a spectroscopic correction for the frequency shift.
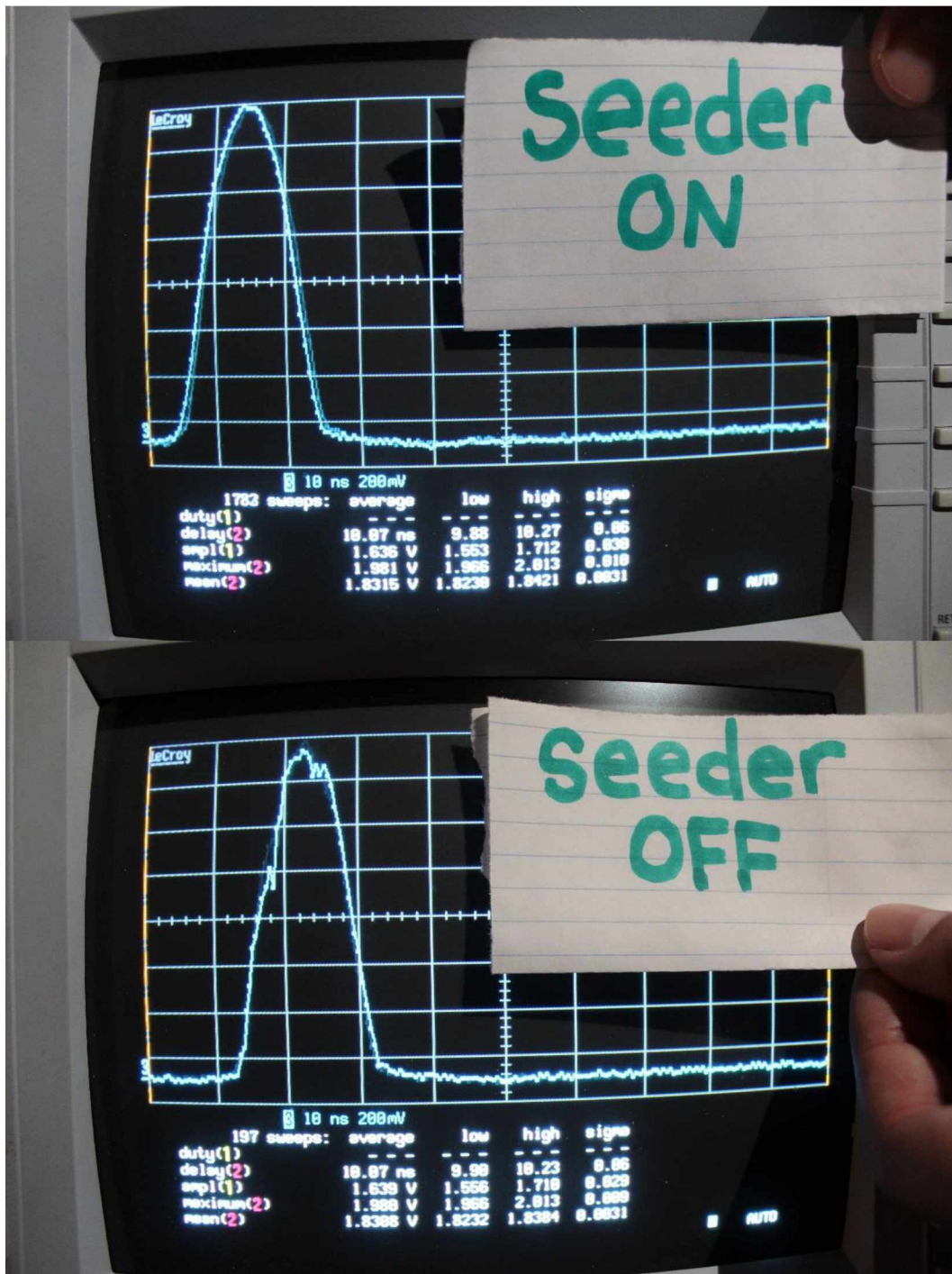
Figure 3.5. Monitoring of the temporal behavior of the Nd:YAG laser output with the seed laser on and off.

3.4. The PFRR SRWTL

A schematic of the SRWTL at LRL-PFRR, or PFRR SRWTL, is shown in Figure 3.3. The seed laser (TA-SHG, Toptica Photonics AG) outputs a CW monochromatic beam with power of 500 mW. A 92/8 beam-splitter is used to direct a small part (30 mW) of this beam through a neutral density (ND) filter into the sodium cell to obtain Doppler-free spectroscopy. Feedback from the cell is used to lock the seed laser frequency at the D_{2a} peak. The remainder of the seed laser beam is sent through the frequency shifter, which can shift the seed laser frequency up by 630 MHz, down by 630 MHz or leave it unshifted. During the Lidar Studies of Coupling in the Arctic Atmosphere and Geospace (LCAGe-1) campaign in fall 2018, the two AOM crystals were synchronized to shift the SRWTL frequency among the three frequencies every 60 laser pulses. The laser beam out of the frequency shifter has a power of ~200 mW and ~100 mW for the unshifted and shifted frequencies respectively due to losses in the AOM crystals. This beam was then used to seed the PDA. The PDA is pumped by a Nd-YAG laser running at 30 Hz with an average power of 13.5 W. The emitted PDA pulses have a full-width-half-maximum (FWHM) linewidth of 100 MHz. The power output of the PDA is typically 900 mW at the unshifted frequency, and 700 mW for the two shifted frequencies.

The SRWTL is a two-channel lidar system that makes simultaneous measurements in two directions. The PDA output beam is expanded to a 20 mm beam and then split into two beams by a 50/50 beam splitter. The two beams are pointed to two directions, one in the vertical and one 20° off-vertical towards north, by two motor-controlled steering mirrors. Two telescopes are pointed to the same two directions to receive the return signal. The vertical telescope is a 24-inch (62 cm) Newtonian telescope where a plane secondary mirror directs the light onto a fiber. The

20° off-vertical telescope is a 36-inch reflector mirror that focusses the light directly on a fiber. The steering mirrors align the transmitted beam to the receiver telescopes by maximizing the received signal from the sodium layer. The telescopes are fiber-coupled to an optical chopper that runs at 300 Hz and synchronizes the firing of the Nd:YAG laser and receiver electronics to block larger near-field signals and avoid overloading the detectors. The signal is detected by a Hamamatsu PMT that operates in photon counting mode and recorded by a high-speed multi-channel scaler unit. The scaler unit forms the raw lidar signal profile by co-adding the signals from 60 laser pulses. The raw data profiles are then stored on the data acquisition personal computer (PC). The raw lidar signal from each frequency are recorded at a range resolution of 30 m every 2 s before shifting to the next frequency. A sequence of three frequencies takes about 8 s to acquire and record before the next sequence begins. The ratio technique can then be applied to the recorded lidar signal profiles to retrieve the wind and temperature over the height of the sodium layer.

We compare the operating characteristics of the PFRR SRWTL and seven other previous and currently operating SRWTLs. The previous systems include the original system developed at Colorado State University (CSU) (Acott, 2009; She et al., 1992; White, 1999), the system developed at the University of Illinois at Urbana-Champaign (UIUC) (Bills et al, 1991 a&b), the Weber system deployed at the Arctic Light Detection and Ranging Observatory for Middle Atmosphere Research (ALOMAR) at Andoya (She et al., 2002; Vance, 2004; Vance et al., 1998). The original CSU lidar was upgraded from a 20 pps system to a 50 pps system (CSU1 and CSU2). The current systems are the Utah State University (USU) system, the Andes Lidar Observatory (ALO) system, the University of Science and Technology of China (USTC) system and our system (PFRR). The USU system incorporates elements of the original CSU system,

which was relocated from CSU to USU in 2010. The system was upgraded with a high-power

tunable diode laser (TA-SHG Pro, Toptica Photonics AG) as the master oscillator in 2017. The

ALO system incorporates the UIUC system, which was relocated to ALO from UIUC in 2009.

The system was upgraded in 2014 with the same Toptica high-power tunable diode laser as the

master oscillator. The USTC system was developed in 2011 and employs a ring dye laser as a

master oscillator (Li et al., 2012). The PFRR system incorporates the Weber sodium lidar, which

was relocated to LRL-PFRR in 2017. The system was upgraded in 2017 with the same a Toptica

high-power tunable diode laser. We present the characteristics of these seven SWRTLs in Table

3.1 where the systems are listed in chronological order of their development.

Table 3.1: Parameters of several SRWTL transmitters

	CW laser	Pulsed Pump Laser			Pulsed Dye Amplifier		Transmitter
	Type	Power (mW)	Repetition Rate (pps)	Energy (mJ)	Input Power (mW)	Pulse Energy (mJ)	Power (mW)
CSU1 [a, b]	Ring Dye	500	20	300	100	30	600
CSU2 [a, b]	Ring Dye	500	50	300	110	22	1100
UIUC [c]	Ring Dye	550	30	300	375	45	1350
Weber [d, e]	SFG	400[d]	50	400	100	22	1100
ALO [f]	TA-SHG	500[f]	50	320	220	30	1500
USU [g]	TA-SHG	1000[g]	50	300	300	30	1500
USTC [h]	Ring Dye	1300[h]	30	566	350	43	1290
PFRR	TA-SHG	500	30	450	210	30	900

a: She et al., 1992; b: Acott, 2009; c: Chu and Papen, 2005; d: She et al., 2002; e: Vance, 2004;
f: Liu, 2019, personal communication; g: Yuan, 2019, personal communication; h: Li et al.,
2012

The PFRR SWRTL combines a 500 mW CW seed beam at 589 nm and a pulsed Nd:YAG laser

with 450 mJ pulses at 532 nm operating at 30 pps to yield a transmitter with an average output

power of 900 mW. The seven other SRWTLS have CW seed beams with powers between 400

and 1000 mW, are pumped by Nd:YAG lasers with pulse energies between 300 and 566 mJ, and have output powers between 600 mW and 1500 mW. We consider the performance of the transmitter in terms of three efficiencies. The first is the efficiency of the frequency shifter and is defined as the ratio of the CW power into the PDA to the power of the CW laser. The second is the PDA pump efficiency and is defined as the ratio of the pump Nd:YAG energy into the PDA and the output pulse energy of the PDA. The third is the PDA seed efficiency and is defined as the ratio of the seed power into the PDA and the output pulse energy of the PDA. For the PFRR system we have a frequency shifting efficiency of 42%, a PDA pump efficiency of 7%, and a PDA seed efficiency of 14%. We plot the transmitted power and efficiencies of all eight systems in Figure 3.5. We see that the PFRR system has a relatively high frequency shifting efficiency, a typical PDA seed efficiency, and a relatively low PDA pump efficiency. Clearly the area of greatest potential improvement in the PFRR SWRTL transmitter is in the Nd:YAG pumping of the PDA. We are currently investigating the coupling, alignment and optics of the PDA to improve the pump efficiency.
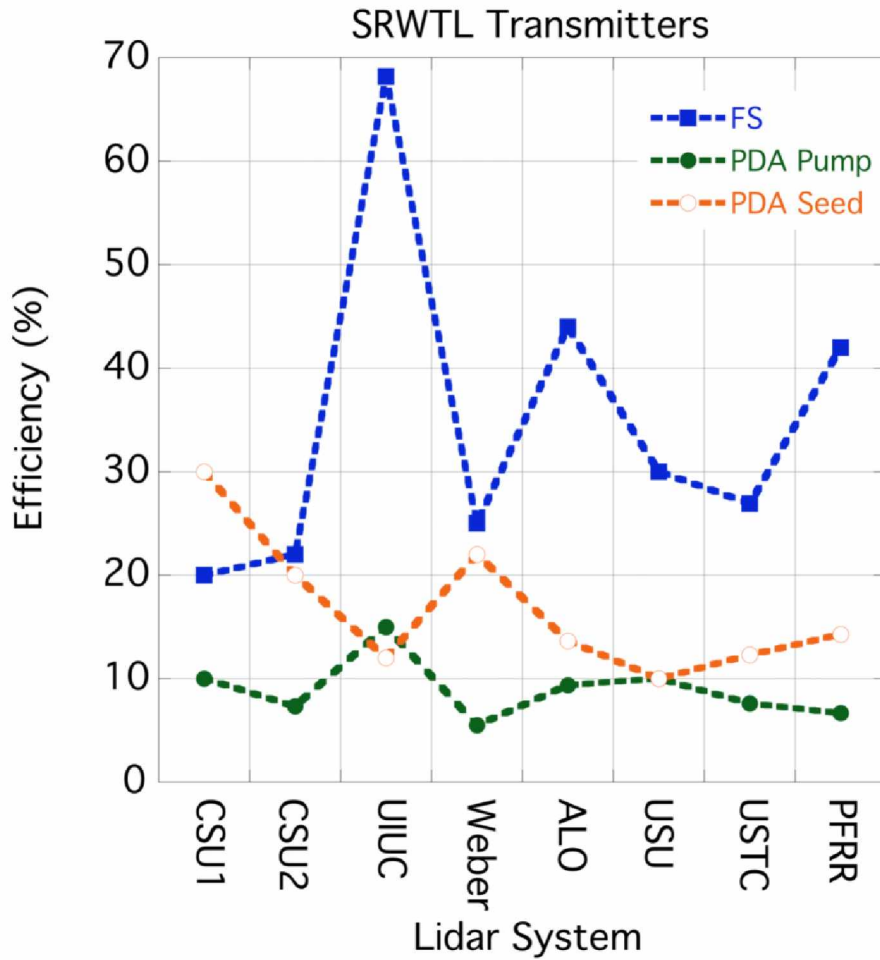
Figure 3.6. Efficiency of the PFRR-SRWTL compare with other SRWTL systems. Blue: the efficiency of the frequency shifter (FS); Green: Puping efficiency of the PDA; Orange: Seeding efficiency of the PDA. See text for details.

3.5. Analysis of PFRR SRWTL performance

We now determine the performance of the SRWTL by reviewing data from the LCAGe-1 campaign that we conducted from 29 September 2018 to 2 October 2018 (271 to day 275 UT). We analyze the performance of the system in terms of the uncertainties in the sodium density, temperature and wind measurements due to the statistics of the photon counting process, which is the dominant source of statistical uncertainty in the lidar signals. The lidar signals are detected by the PMTs, and the statistics of the signal obeys a Poisson distribution (Engstrom, 1980). Thus the variance of the signal equals the mean value of the signal (Papoulis & Pillai, 2002). Given the definition of R_T and R_W in equations 3.10 and 3.12, we use a propagation of error technique to quantify the uncertainties of R_T and R_W as

$$\Delta R_T = R_T \sqrt{(\frac{\Delta N_a}{N_a})^2 + (\frac{\Delta N_{sum}}{N_{sum}})^2} \qquad (3.13)$$

$$\Delta R_W = R_W \sqrt{(\frac{\Delta N_a}{N_a})^2 + (\frac{\Delta N_{diff}}{N_{diff}})^2} \qquad (3.14)$$

where N_a is the lidar signal (total signal minus background) when the laser is tuned to the D_{2a} line, N_{sum} is the sum of the upshifted and downshifted signals, and N_{diff} is the difference in the upshifted and downshifted signals. To determine these uncertainties, we first smooth the data in both time and altitude (5 minutes and 1 km) and use this smoothed data as the expected signal. The uncertainty in the signal is then taken as the square root of the expected total signal. We estimate the background signal by calculating the average lidar signal in the range of 150-225 km, where we assume that there is no backscatter signal from the atmosphere. We then subtract this background from the total signal and obtain the lidar backscatter signal. We calculate the

Rayleigh backscatter signal by averaging the backscatter signal profile over the range of 25 km to 35 km. We use this averaged Rayleigh signal to normalize the sodium backscatter signal, and then determine the ratios, R_T and R_W. By averaging the Rayleigh signal over a much larger range (10 km) than the sodium signal (1 km) we reduce the relative uncertainty in the Rayleigh signal and thus uncertainty in the estimate of the temperature and wind ratios are dominated by the uncertainties in the resonance signals. We thus use equations 3.13 and 3.14 to characterize the uncertainties in these ratios.

During the LCAG-1 campaign we obtained both nighttime and daytime measurements of the sodium layer in both daytime and nighttime (Figure 3.7). We identify representative signal profiles from the nighttime and daytime measurement to demonstrate the performance of the system on 1-2 October 2018 (day 275 UT). These two profiles were chosen as they had the largest backscattered signal measured in the range of 70 km to 120 km, which we will refer to as the sodium signal hereafter.

For the nighttime measurements, we found that the layer sodium signal is the highest at 20:12:27 on 1 October 2018 (05:12:27 on day 275 UT). At the peak of the sodium layer, 91 km overhead, the sodium density, temperature and wind are 4170 cm^{-3}, 204.2 K and 0.6 m/s respectively. The resonance backscatter signal in the vertical channel at the D$_{2a}$, upshifted, and downshifted frequencies are 14.0, 4.4 and 4.0 counts respectively. The corresponding Rayleigh backscatter signals are, 5.9, 4.1 and 4.3 counts, respectively. The background signals are 0.036, 0.033 and 0.033 counts. The relative uncertainty in R_T and R_W are 1 % and 16 %. The absolute uncertainties in temperature and wind are 2 K and 0.1 m/s respectively. At the peak of the sodium layer 20° to the north, the sodium density, temperature and wind are 4045 cm^{-3}, 201.3 K

and -3.0 m/s respectively, The resonance backscatter signal in the off-vertical channel at the three frequencies at 91 km are 18.0, 5.3 and 5.8 counts, the Rayleigh backscatter signals are, 7.9, 5.6 and 5.9 counts, and the background signals are 0.019, 0.019, and 0.019 counts respectively. The relative uncertainties in R_T and R_W are 1 % and 15 %. The absolute uncertainties in temperature and wind are 2 K and 7 m/s respectively.
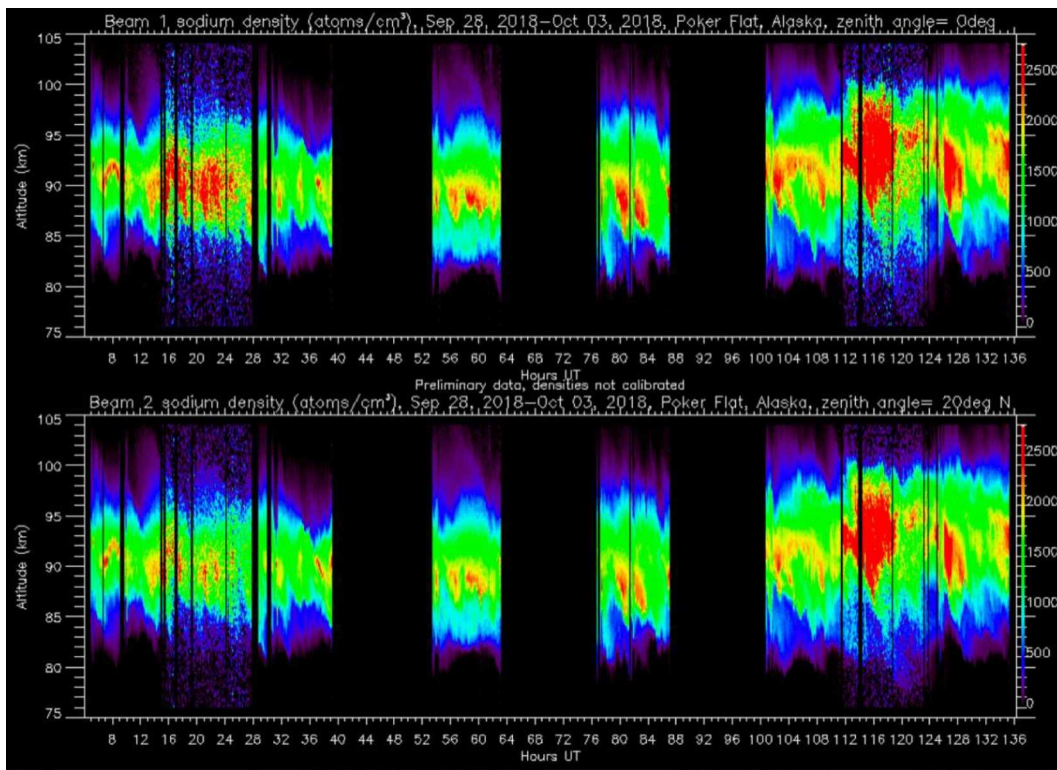
Figure 3.7. First order sodium number density measured by the SRWTL during a campaign in the Fall of 2018.

For the daytime measurements, we found that the total sodium signal is the highest at 08:21:17 on 2 October 2018 (17:21:17 on day 275 UT). At the peak of the sodium layer, 93 km overhead, the sodium density, temperature and wind are 5460 cm^{-3}, 166.6 K and 5.7 m/s respectively. The backscatter signal detected by the vertical beam in the D$_{2a}$, upshifted, and downshifted frequencies are 1.9, 0.4 and 0.5 counts respectively. The Rayleigh backscatter signal are, 0.55, 0.55 and 0.34 counts respectively. The background signals are 3.6, 3.7 and 3.7 counts respectively. The relative uncertainty in R_T and R_W are 9 % and 59%. The uncertainties in the temperature and wind are 15 K and 3 m/s respectively. In the 20° north beam, At the peak of the sodium layer, 93 km overhead, the sodium density, temperature and wind are 5430 cm^{-3}, 167.9 K and 20.0 m/s respectively. The backscatter signal detected at the three frequencies at 92 km are 2.8, 0.50 and 0.77 counts, the Rayleigh backscatter signal are 0.92, 0.75 and 0.50 counts, and the background signals are 3.0, 3.0 and 3.0 counts respectively. The relative uncertainty in R_T and R_W and the temperatures and winds are 6 % and 23 %. The uncertainties in the temperature and wind are 10 K and 4 m/s respectively. The increase in the uncertainties in the daytime measurements are due to the decrease in signal due the insertion loss of the magnetro-optic optical filter (~1/7) in the receiver and the increase in the background skylight (~160).

We compare the nighttime lidar signals from the PFRR SRWTL with nighttime signals from the USTC SRWTL (Li et al., 2012). The comparison is conducted in terms of both the resonance and Rayleigh signal where we normalize the signals to allow for the transmitter power and receiver aperture. The PFRR lidar has a power of 875 mW, split 50-50 between two beams pointing at the vertical and 20° off-vertical to the north. The two-channel receiver has one telescope pointing vertical of diameter 0.61 m and another telescope pointing 20° off-vertical to the north of diameter 0.91 m. The power aperture product of the two channels is 0.128 and 0.288 W-m^2

94

respectively. The USTC lidar has a power of 1300 mW, split 40-60 between two beams pointing to the east and north respectively. The two-channel receiver has two telescopes, both of diameter 0.76 m, with one pointing 30° off-vertical to the east and one pointing 30° off-vertical to the north. The power aperture product of the two channels are 0.236 and 0.354 W-m^2 respectively. In Figure 3.8 we plot the raw lidar signal measured by the PFRR SRWTL system at 20:12:27 LST on October 1, 2018 (05:12:27 02 October 2018 UT). These profiles represent lidar signal acquired over 2 s (60 laser pulses) at each frequency at 30 m range resolution. In Figure 3.9 we show the raw lidar photon count signal measured by the USTC SRWTL at 01:30 LST on 23 November 23, 2017 (17:30:13 22 November 2017 UT). These profiles represent lidar signal acquired over 40 s (1200 laser pulses) for each frequency at 150 m range resolution.
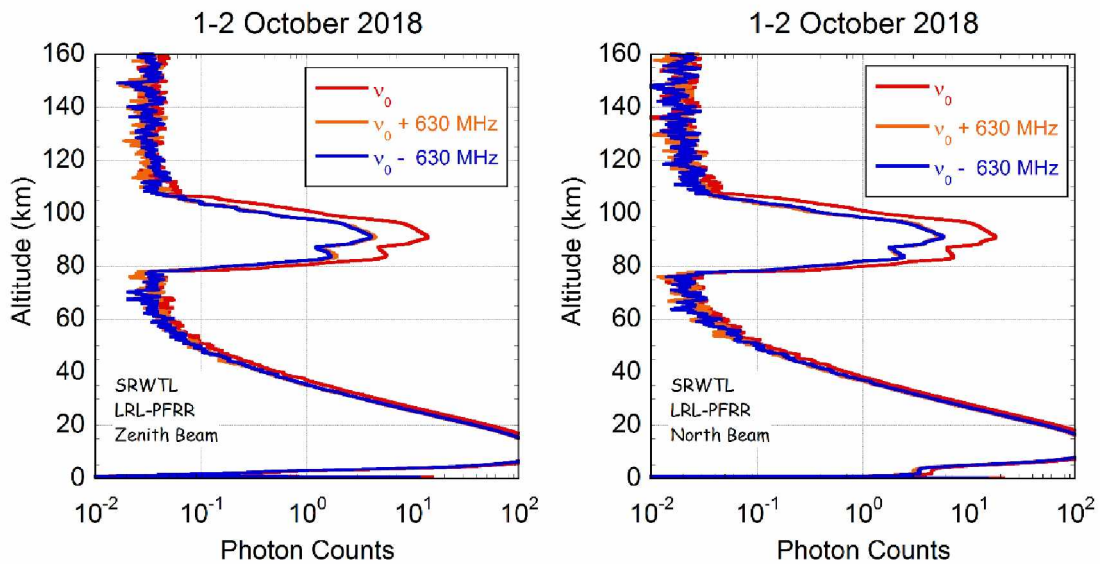
Figure 3.8. Nighttime raw photon profiles at three frequencies obtained on 01-02 October 2018 LST by the SRWTL for zenith (a) and north (b) channels. The red, orange and blue curves denote the signals at frequencies of D2a peak, +630 MHz, and -630 MHz.
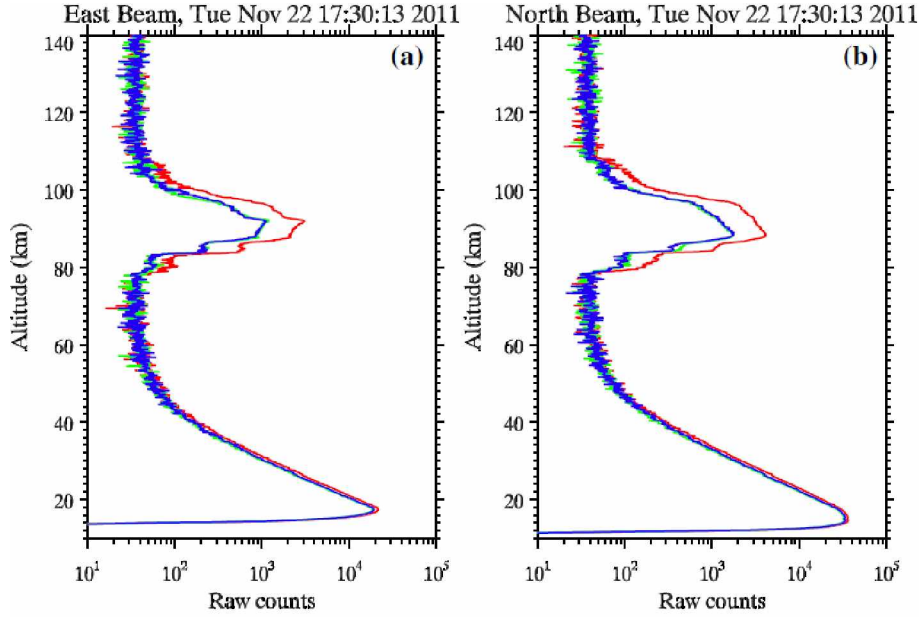
Figure 3.9. Nighttime raw photon profiles at three frequencies obtained on 23 November 2011 local time by the USTC sodium wind temperature lidar for east (a) and north (b) channels. The red, blue and green curves denote the signals at frequencies of D2a peak, +630 MHz, and -630 MHz.

To compare the lidar signals we must compensate the signals for the differences in the pointing angle, the range resolution, the temporal resolution or number of laser pulses, and power-aperture product. The range, r, and altitude, z, are related as

$$r = {}^{z}\!/\!_{\cos(\alpha)} \qquad (3.15)$$

where α is the angle off-vertical. The equivalent vertical signal, N_{ev}, at a given altitude, z, and resolution, Δz, can be determined from the off-vertical signal, N, as follows,

$$N_{ev} = N \times \frac{r^2}{z^2} \times \frac{\Delta z}{\Delta r} \qquad (3.16)$$

where r is the range of the measurement and Δr is the range resolution of the measurement. We first calculate the lidar signals normalized by the number of laser pulses at ranges corresponding to an altitude of 40 km (N_R) and at the peak of the sodium layer (N_S) (Table 3.2). At PFRR the sodium layer peak was detected at 91 km in both beams while at USTC the peak was detected at 92 km in the east beam and 88 km in the north beam. The peak density of the sodium layer was similar at both sites (3000-4000 cm^{-3}). We then convert these to equivalent signals at an altitude of 40 km (N_{Rev}) and 90 km (N_{Sev}) with a vertical resolution of 1 km (Table 3.2). We then normalize these signals by the power-aperture product, Q_R and Q_S, to compare the relative efficiency of the lidar system channels.

Table 3.2: PFRR and USTC SRWTL lidar signals and characteristics

	PA (W-m^2)	N_R	N_S	N_{Rev}	N_{Sev}	Q_R	Q_S
PFRR SRWTL							
Vertical	0.128	9.3×10^{-3}	2.3×10^{-1}	0.31	7.6	2.4	59
North	0.287	1.2×10^{-2}	3.0×10^{-1}	0.45	9.8	1.6	34
USTC SRWTL							
East	0.236	1.0×10^{-1}	2.5×10^{0}	0.89	16	3.8	68
North	0.354	1.9×10^{-1}	3.1×10^{0}	1.7	22	4.8	62

Examining these relative efficiencies for the PFRR SRWTL we see that the vertical channel is significantly more efficient than the north channel. The north channel is 60-70% as efficient as the vertical channel. Examining these relative efficiencies for the USTC SRWTL we see that the east channel is 80-100% as efficient as the north channel. There is an inconsistency when we compare the efficiency of the two channels based on the sodium resonance signal and Rayleigh signal. Based on the sodium resonance signal, the north channel is 91% as efficient as the east channel. However, based on the Rayleigh signal, the east channel is 80% as efficient as the north

channel. We do not expect the sodium density or air density to have large enough variation to cause this difference and do not have an immediate explanation for this. When we compare the PFRR and USTC system, we find that the PFRR vertical channel is 60-90% as efficient as the USTC system and the north channel is 40-50% as efficient as the USTC system. Again there is an inconsistency when comparing the efficiency of the two channels based on the sodium resonance signal and Rayleigh signal. Based on the sodium resonance signal, the north channel is 60% as efficient as the east channel. However, based on the Rayleigh signal, the east channel is 70% as efficient as the north channel. The vertical channel of the PFRR lidar is operating reasonably relative to the USTC system and the lower efficiency may be attributed to differences in the age of the detectors where the USTC system has newer PMTs than the PFRR system.

The lower efficiency of the PFRR north channel relative to the vertical channel may be attributed to the alignment of the receiver optics. Since the beam divergence is more than 0.5 mrad, and the focal length of the north channel telescope is long (3 m), the focused signal at the focal plane of the telescope completely fills the fiber (1.5 mm). Thus the north channel is very sensitive to the position of the fiber across the optical axis of the telescope. Alignment of the fiber along the optical axis of the telescope may be necessary as well.

3.6. Summary and conclusion

A sodium resonance wind-temperature lidar system has been deployed at LRL-PFRR. This lidar is capable of measuring sodium density, wind and temperature at the sodium layer altitude range (70-120 km). The transmitter of the system has been aligned and optimized to a typical level compare to other similar systems in the community. However, more effort needs to be devoted to the alignment of the PDA in terms of the pumping efficiency to obtain more output power

(~20%). The receiver of the vertical channel is mostly optimized, while the north channel

appears to require some adjustment to improve the received signal (50%).

This page intentionally left blank

Chapter 4. Study of gravity wave breaking by Rayleigh lidar and Sodium Resonance Wind-Temperature Lidar

4.1. Introduction

In this chapter we explore waves, instability and turbulence as we did earlier in Chapter 2. The resonance lidar is the Poker Flat Research Range (PFRR) sodium resonance wind-temperature lidar (SRWTL) that we described in Chapter 3. The PFRR-SRWTL provides simultaneous measurements of the temperature (T) and meridional wind (V). The Rayleigh lidar is based on the Rayleigh Density Temperature Lidar (RDTL) as used in the Mesosphere Lower Thermosphere Turbulence Experiment (MTeX) with a modified receiver. The PFRR SRWTL allows us to extend the Chapter 2 study in several distinct ways. First, the wind measurements provide one more independent characterization of the waves and allows us to have a more complete understanding to the wave dynamics. Second, the temperature measurements allow us to better characterize the convective instabilities. Third the resonance lidar provides an initial temperature for the temperature for the RDTL retrieval.

We present three case studies from two nights of observations at PFRR, Chatanika, Alaska (65°N, 147°W). The two nights are 8-9 October 2018, and 18-19 October 2018. We analyze the wave activity and turbulence in the mesosphere-lower-thermosphere (MLT) region based on RDTL measurements of temperature and density and SRWTL measurements of sodium density, temperature and meridional wind. We use the temperature measurements to determine the potential temperature and combine the density and sodium measurements to determine the sodium mixing ratio. This combination of measurements provides simultaneous characterization of the atmospheric waves, stability and material transport. These three cases provide a range of

activity with stronger instability present on 18-19 October 2019 than on 8-9 October 2018. On both 18-19 and 8-9 October, consistent spreading and overturning are observed in the sodium mixing ratio and potential temperature. We apply the methods developed in Chapter 2 to characterize instability, wave activity and turbulence. We estimate the energy available from the monochromatic waves to generate turbulence. We estimate the turbulence from the vertical transport of sodium mixing ratio.

4.2. Experiment and methods

4.2.1. The sodium resonance wind-temperature lidar

The raw resolution of the SRWTL measurements was eight seconds and 30 m. We then integrate the signal over five minute intervals and spatially smooth the data over 500 m (1 km) to reduce the statistical uncertainty and determine the temperature and wind following the methods described in Chapter 3. The retrieval yields temperature and wind profiles with a resolution of five minutes and 30 m which are used to characterize the waves. We integrate the temperature data over 2 h intervals at 15 minutes steps to provide the initial temperature for the RDTL temperature profiles. We then integrate the temperature and sodium density data over 1 h intervals at 15 minutes steps to calculate the sodium mixing ratio. The potential temperature profiles are calculated from the temperature profiles by integration upward from 83 km as we did in section 2.3.3.

4.2.2. The Rayleigh lidar

The configuration of the RDTL system was similar to that used during the MTeX investigation. The transmitter was exactly the same Nd:YAG pulsed laser (Powerlite 8020, Continuum) as

described in Chapter 2. The output power of the laser was ~8 W. The receiver was based on the same 1.06 m Cassegrain telescope as described in Chapter 2. However, during MTeX the first channel of the receiver was used to collect resonance lidar signals, while the second and third channel were used to collect Rayleigh lidar signals. In this study all three receiver channels were used to collect Rayleigh lidar signals. The first channel is a low-altitude channel that receives ~20% of the total Rayleigh lidar signal. The second and third channel are high altitude channels that each receives 40% of the total Rayleigh lidar signal. The signals from all three channels are combined to yield a profile of the density and temperature from 40 km up to 90 km. The signal from the low altitude channel alone contributes to the density and temperature over the lower altitudes (~ 40-60 km), while the combined signal from all three channels contributes to the density and temperature over the higher altitudes (~60-90 km). The transition altitude (~60 km) is determined based on the continuity in the Rayleigh density profiles (Triplett, 2016). The total Rayleigh lidar signal levels were over a factor of two larger than during MTeX. This increase in signal reflects the increase in the transmission of the atmosphere due to a combination of clearer skies during these observations and the fact that there are fewer ice crystals in the air in October than in January.

The raw resolution of the RDTL measurements was 50 s and 48 m. As described in section 2.2.1, we then integrate the Rayleigh lidar data in time and smooth it in altitude to reduce the statistical uncertainty in the density and temperature measurements. We use the temperature measured by the SRWTL to provide the initial temperature and calculate temperature profiles over 2 h intervals at 15 minute and use these profiles to characterize the temperature structure the stratosphere and mesosphere and calculate potential temperature profiles. The potential temperature profiles are calculated from the temperature profiles by integration upward from 62

103

km as we did in section 2.3.3. We calculate density profiles over 1 h intervals at 15 minutes steps and normalize these to radiosonde measurements of the density over the 30-32 km altitude range. The radiosonde measurements are made at the Fairbanks International Airport about 50 km from PFRR. We then combine the normalized density profiles with sodium density profiles to calculate the sodium mixing ratio in the MLT.

4.2.3. Characterization of monochromatic gravity waves

We characterize the monochromatic gravity waves from the SRWTL data by applying the observed frequency, observed vertical wavelength, and temperature fluctuations to the gravity wave polarization and dispersion relations (Appendix A). Having characterized the gravity waves we use the meridional wind perturbation to determine whether the wave is propagating primarily zonally or meridionally. We characterize the monochromatic gravity waves from the RDTL data using the observed frequency, observed vertical wavelength, and relative density fluctuations.

4.3. Turbulence estimates from the vertical transport

4.3.1. Case 1: Strong instability

The first case was observed on the night of 18-19 October 2018. We plot the temperature profile averaged over the whole observation period derived from the SRWTL (80-105 km) and RDTL (40-85 km) measurements. The temperature profiles measured by the two lidars are consistent in the overlapping region of 80-90 km to within ± 3 K (Figure 4.1). The temperature profile has a stratopause at 53.0 km with a temperature of 265.0 K and a mesopause at 98.7 km with a temperature of 180.5 K. The stratopause altitude is typical of that reported in multi-year

104

Rayleigh lidar measurements at Chatanika and the temperature is about 10 K higher (Thurairajah et al., 2010b). The mesopause altitude and temperature are typical of those reported in satellite studies (Xu et al., 2007). False color plots of the sodium density (top), temperature (middle), and meridional wind (bottom) on this night are shown in Figure 4.2. The sodium density and temperature are measured by the vertical channel of the SRWTL, while the meridional wind is derived from the combination of both channels of the SRWTL. The sodium layer has an average peak altitude of 89.7 km that varies between 84.84 km and 92.6 km (Figure 4.2, top panel). The average peak sodium density is 4.5×10^3 atom/cm^{-3} and varies between 3.7×10^3 atom/cm^{-3} and 6.1×10^3 atom/cm^{-3}. The sodium layer has a scale height of 6.1 km on the topside and a scale height of 4.1 km on the bottomside that is reflected in the narrower spacing of the sodium density contours on the bottomside. Wave structures of different time and vertical scales are clearly visible in the sodium density, temperature (Figure 4.2, middle panel) and meridional wind (Figure 4.2, bottom panel) where there are downward phase progressions consistent with upward propagating waves. There is an overturning signature in the sodium density plot around 20:35 LST and 87 km (Figure 4.2, top panel). Meanwhile, there are strong negative gradient (~ -13K/km) in the temperature (Figure 4.2 middle panel) and strong shear (-40 m/s/km) in the meridional wind (Figure 4.2, bottom panel) which coincide with the overturning in the sodium. In the temperature measurements, the wave signature disappears around 20:35 LST and 90 km. The RDTL temperature measurements show that the stratopause is relatively undisturbed through the observations while the amplitude of the temperature fluctuations increases with altitude (Figure 4.3). Temperature fluctuations with downward phase progression are evident and become increasingly prominent with altitude.
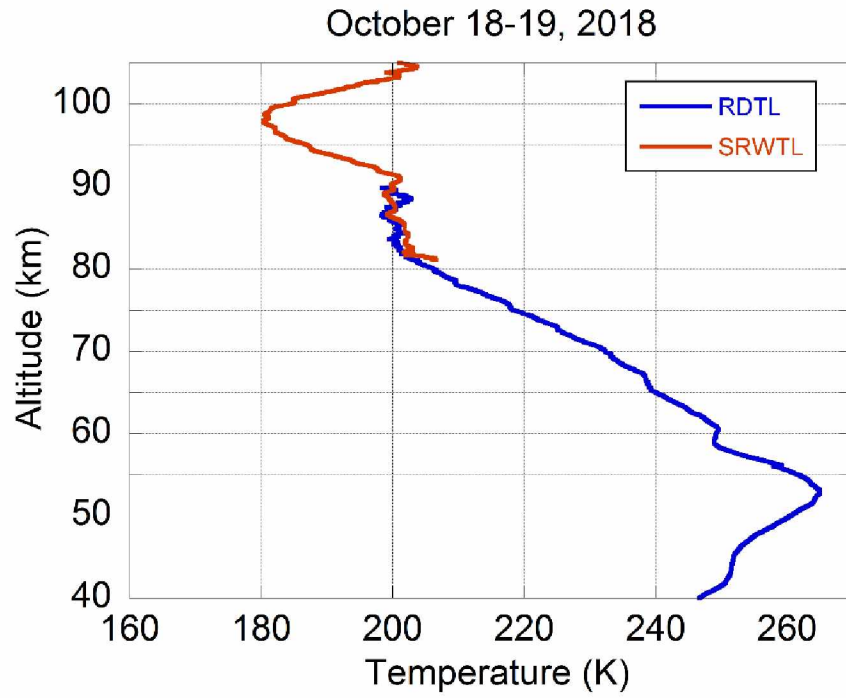
Figure 4.1. Total temperature profiles measured by the RDTL (blue) and SRWTL (red) on the night of 18-19 October 2018.
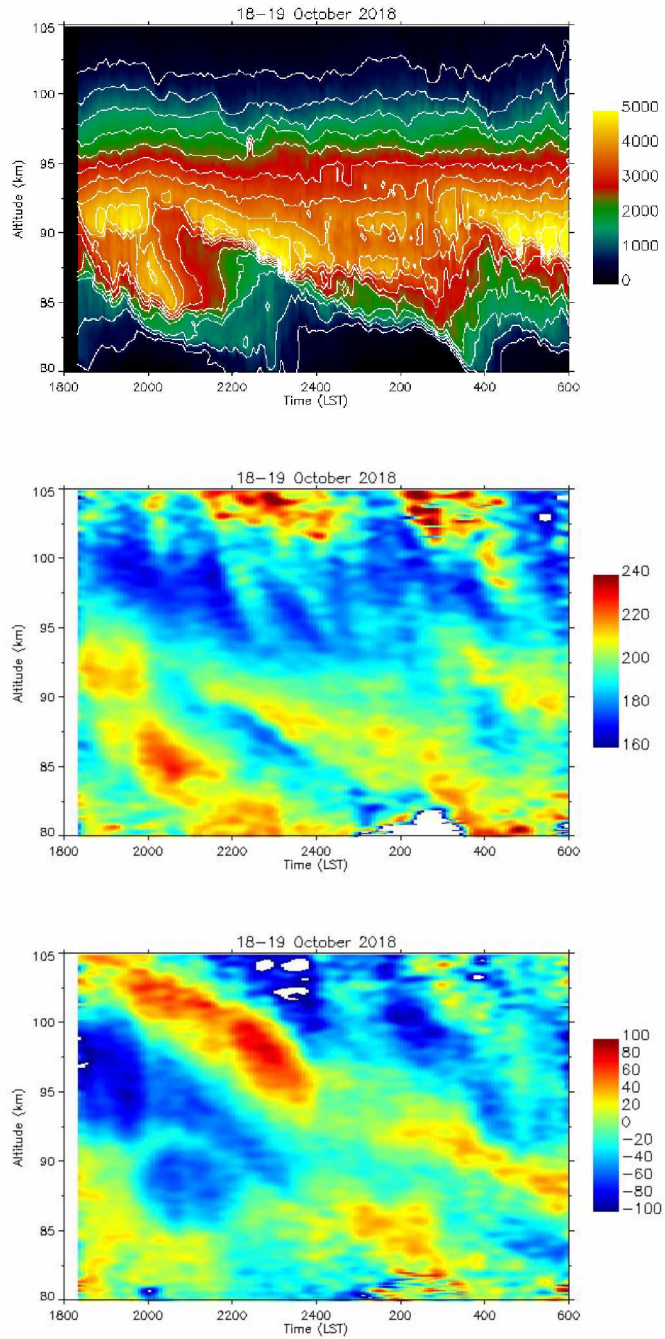
Figure 4.2. Sodium density (top), temperature (middle) and meridional wind (bottom) measured by the SRWTL on the night of 18-19 October 2018.
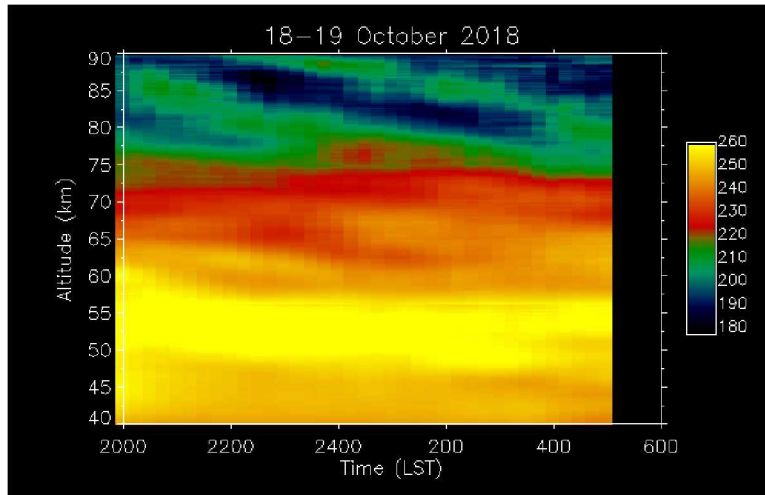
Figure 4.3. Temperature measured by the RDTL on the night of 18-19 October 2018.

The potential temperature derived from the SRWTL temperatures shows broadening and steepening of the potential temperature contours (Figure 4.4, top panel). The potential temperature contours are vertical at 20:15 LST near 87 km and indicate the presence of convective instability (Franke & Collins, 2003). The contours of potential temperature derived from the RDTL measurements show similar behavior with steepening at the same time and altitude (Figure 4.4, bottom panel). The sodium mixing ratio plotted in false color follows the potential temperature and shows broadening and steepening that confirms behavior of the potential temperatures at 20:15 LST and 87 km (Figure 4.4, bottom panel). The fact that the potential temperature derived from the SRWTL temperature measurements and RDTL measurements show consistent instability structure validates the RDTL measurements and confirms that the spreading and instability structure we observed in chapter 2 are valid.

We analyze this case in terms of turbulent transport and estimate the eddy diffusion coefficient and energy dissipation rate from the spreading of sodium mixing ratio using the method we

developed in section 2.3.2. We calculate the sodium mixing ratio averaged between 87.1 km and 88.1 km, and the scale height of the mixing ratio over the 86.1 km to 89.1 km range. The average sodium mixing ratio reaches a local maximum of 33.7 PPT at 20:15 LST, which we choose as t_m (Figure 4.5, solid, yellow). The scale height of sodium mixing ratio has typical value of 3 km before the spreading event begins (19:30 LST), and then increases significantly to 10.6 km at 20:15 LST and reaches a local maximum of 20.5 km at 20:45 LST (Figure 4.5, dashed, black). The sodium density profile and the sodium mixing ratio profile both show decreased vertical gradient and increased scale height at t_m (Figure 4.6). The behavior of the sodium mixing ratio is consistent with our model of turbulent diffusion as discussed in section 2.3.2. We calculate the chemical time constant from the decrease in the sodium mixing ratio between 20:15 LST and 22:45 LST (Figure 4.5). We tabulate the measured characteristics of the diffusion event in Table 4.1.
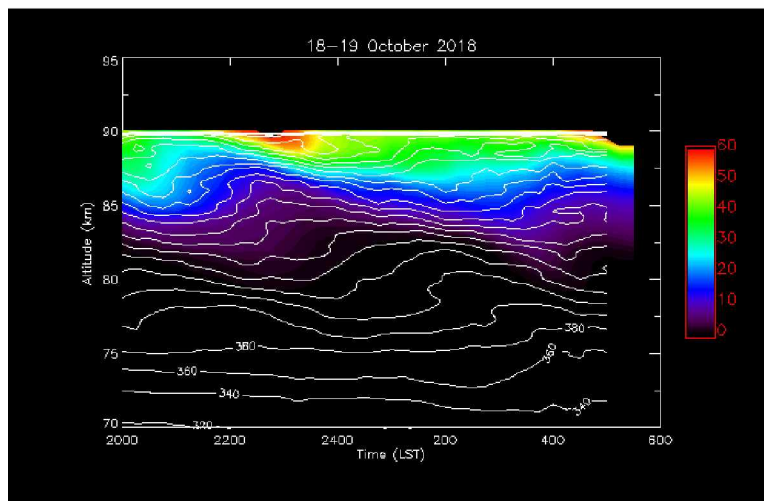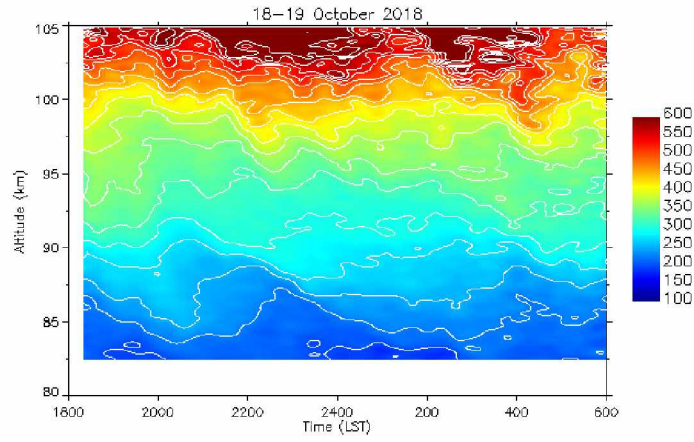
Figure 4.4. Potential temperature derived from SRWTL temperature measurements (top), sodium mixing ratio (bottom, false color) and potential temperature derived from RDTL temperature measurements (bottom, contours) on the night of 18-19 October 2018.
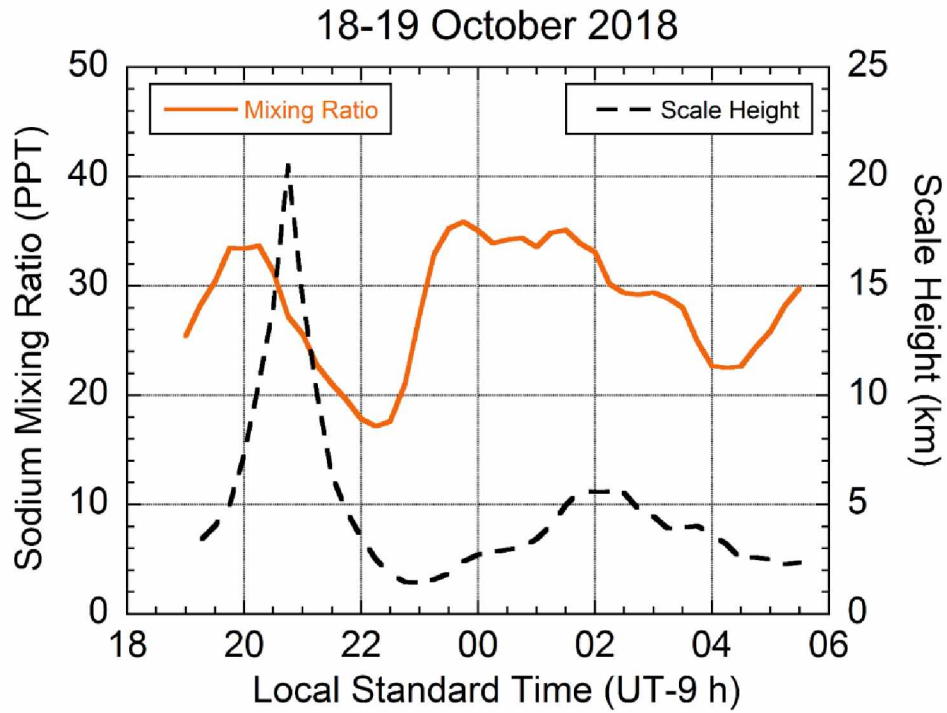
Figure 4.5. Average sodium mixing ratio measured by the RDTL and SRWTL between 87.1 km and 88.1 km (solid, yellow) and the scale height of sodium mixing ratio between 86.1 km and 89.1 km (dashed, black) on the night of 18-19 October 2018.

Table 4.1: Measured characteristics of the diffusion events			
Date	Time	Altitude	Value
18-19 Oct 2018			
Scale height of sodium mixing ratio, H_f	20:15	85.8-88.8 km	9.2 km
Sodium chemical time constant, τ	20:15-22:45	86.8-87.8 km	109 min
Lapse rate, γ	20:15	85.8-88.8 km	-7.3 K/km
Layer thickness, L	20:15		
5 min, 2 km		87.2-88.0 km	0.8 km
15 min, 1 km		87.3-88.1 km	0.8 km
30 min, 0.5 km		87.4-88.0 km	0.6 km
30 min, 1.0 km		87.4-88.0 km	0.6 km
60 min, 0.5 km		87.4-87.7 km	0.3 km
08-09 Oct 2009			
Scale height of sodium mixing ratio, H_f	23:00	86.6-89.6 km	4.3 km
Sodium chemical time constant, τ	23:00-01:30	87.6-88.6 km	81 min
Lapse rate, γ	23:00	86.6-89.6 km	-5.0 K/km
Layer thickness, L	23:00		
5 min, 2 km		87.2-87.9 km	0.7 km
15 min, 1 km		87.3-88.1 km	0.8 km
60 min, 0.5 km		87.9-88.2 km	0.3 km

The higher resolution and accuracy of the SRWTL temperature measurements allow us to better characterize the layer of instability. The temperature and potential temperature profiles show the presence of a temperature inversion with a negative topside temperature layer corresponding to a region of reduced potential temperature gradient (Figure 4.7). The MIL is clearly evident in the temperature profile about 87 km at t_m. The value of the squared buoyancy frequency calculated over the 3 km range between 86.1 km and 89.1 km is 1.0×10^{-5} s^{-2}. This indicates a layer of reduced stability (equation 2.17) and mixing that corresponds to the spreading in in both the number density and mixing ratio profiles (Figure 4.6).We investigate the instability by estimate the vertical gradient of the potential temperature over different temporal and spatial scales. We average the temperature profiles over different time resolutions (5 minute, 15 minute, 30 minute, 60 minute) before calculating the potential temperature profiles. We then calculate the gradients

112

by linear fit to the potential temperature profiles over different altitude intervals (0.5 km, 1.0 km, 2.0 km). We first note that the instability around 87 km becomes more pronounced as the temporal interval decreases and is most evident in the 5 minute profile. We find that the 2.0 km profiles have very similar structures at different time resolutions. The 1.0 km and 0.5 km profiles fluctuate around the 2.0 km and indicate multiple instable layers. A consistent instable layer is found near 86 km at different altitude and time resolutions. We summarize the pertinent parameters of the instable layers derived from these profiles in Table 4.1. We find that the depth of the layer varies by a factor of 3 (0.27 km to 0.81 km). We determine to use the depth derived from the 5 minutes, 2 km intervals (0.78 km) to estimate the strength of turbulence. Using equations 2.15 and 2.16, we estimate an eddy diffusion coefficient of 1.4×10^3 $m^2 s^{-1}$ and an energy dissipation rate of 16.7 mW/kg (Table 4.2).

Figure 4.6. Profiles of sodium mixing ratio (solid) and sodium density (dashed) measured by the RDTL and SRWTL between 19:45 LST and 20:45 LST on the night of 18-19 October 2018.

Figure 4.7. Profiles of temperature (red) and potential temperature (blue) measured by the SRWTL between 20:12:30 LST and 20:17:30 LST on the night of 18-19 October 2018.

Figure 4.8. Vertical gradient of potential temperature measured by the SRWTL on the night of 18-19 October 2018.

Table 4.2: Derived parameters from the diffusion events			
Date	Time	Altitude	Value
18-19 Oct 2018			
Buoyancy frequency squared, N^2	20:15	86.1-89.1 km	1.0×10^{-5} s^{-2}
Buoyancy period, T_B	20:15	86.1-89.1 km	33 min
Eddy diffusion coefficient, K	20:15	87.2-88.0 km	1.4×10^3 m^{2}s^{-1}
Energy dissipation rate, ε	20:15	87.2-88.0 km	16.7 mW/kg
08-09 Oct 2018			
Buoyancy frequency squared, N^2	23:00	86.0-89.0 km	3.4×10^{-4} s^{-2}
Buoyancy period, T_B	23:00	86.0-89.0 km	18 min
Eddy diffusion coefficient, K	23:00	87.2-87.9 km	2.6×10^2 m^{2}s^{-1}
Energy dissipation rate, ε	23:00	87.2-87.9 km	10.9 mW/kg

4.3.2. Case 2: Weak instability

The second case was observed on the night of 8-9 October 2018. The temperature profiles measured by the two lidars are consistent in the overlapping region of 80-90 km to within ±5 K. The temperature profile has a stratopause at 47.5 km with a temperature of 255.9 K and a mesopause at 100.0 km with a temperature of 177.0 K (Figure 4.9). False color plots of the sodium density (top), temperature (middle), and meridional wind (bottom) on this night are shown in Figure 4.10. The sodium layer has an average peak altitude of 90.7 km that varies between 88.7 km and 95.8 km (Figure 4.10, top panel). The average peak sodium number density is 3.6×10^3 atom/cm^{-3} and varies between 2.0×10^3 atom/cm^{-3} and 5.6×10^3 atom/cm^{-3}. The sodium layer has a scale height of 4.0 km on the topside and a scale height of 4.0 km on the bottomside. The shape of the sodium layer is not typical for this night. Wave structures of different time and vertical scales are clearly visible in the sodium density, temperature and meridional wind, where there are downward phase progressions consistent with upward propagating waves. There is overturning in the sodium density around 00:20 LST and 87 km. Meanwhile, there is a strong negative temperature gradient (~ -14 K/km) and a strong wind shear (12 m/s/km) which coincide with the overturning. In the temperature measurements, the wave signature disappears around 24:20 LST and 92 km. In Figure 4.11, we show the temperature measured by RDTL between 40 and 90 km varying with time. Consistent wave structures with downward phase progression are visible in the RDTL temperature measurements (Figure 4.11) and SRWTL temperature measurements (Figure 4.10, middle). The RDTL temperature measurements show that the stratopause is relatively undisturbed through the observations while

118

the amplitude of the temperature fluctuations increases with altitude (Figure 4.11). Fluctuations with downward phase progression are evident and become increasingly prominent with altitude.
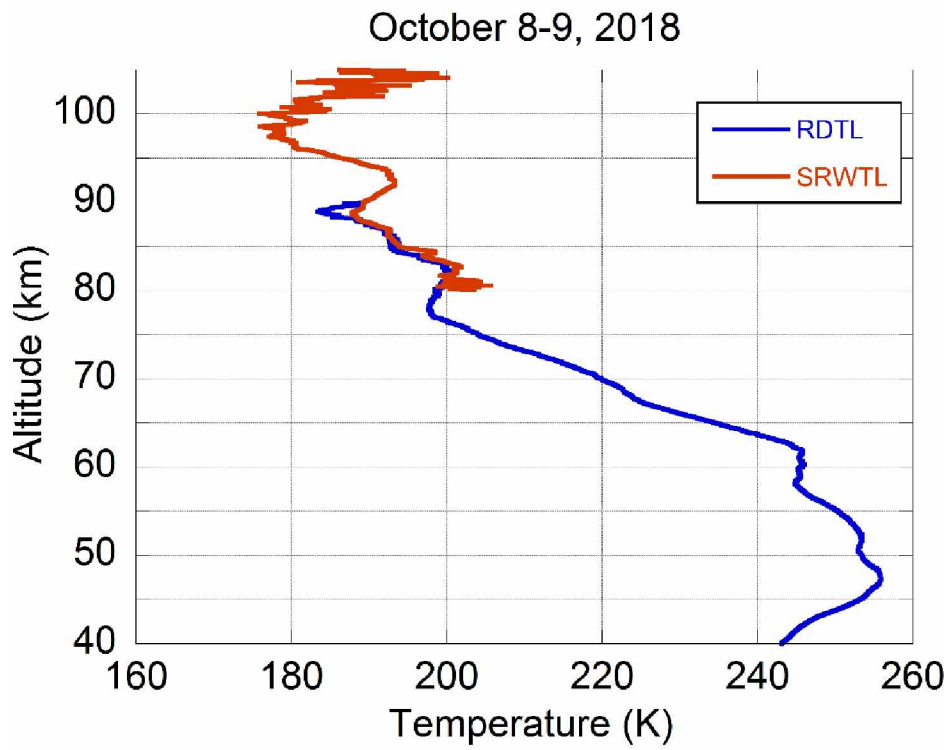
Figure 4.9. Total temperature profiles measured by the RDTL (blue) and SRWTL (red) on the night of 08-09 October 2018.
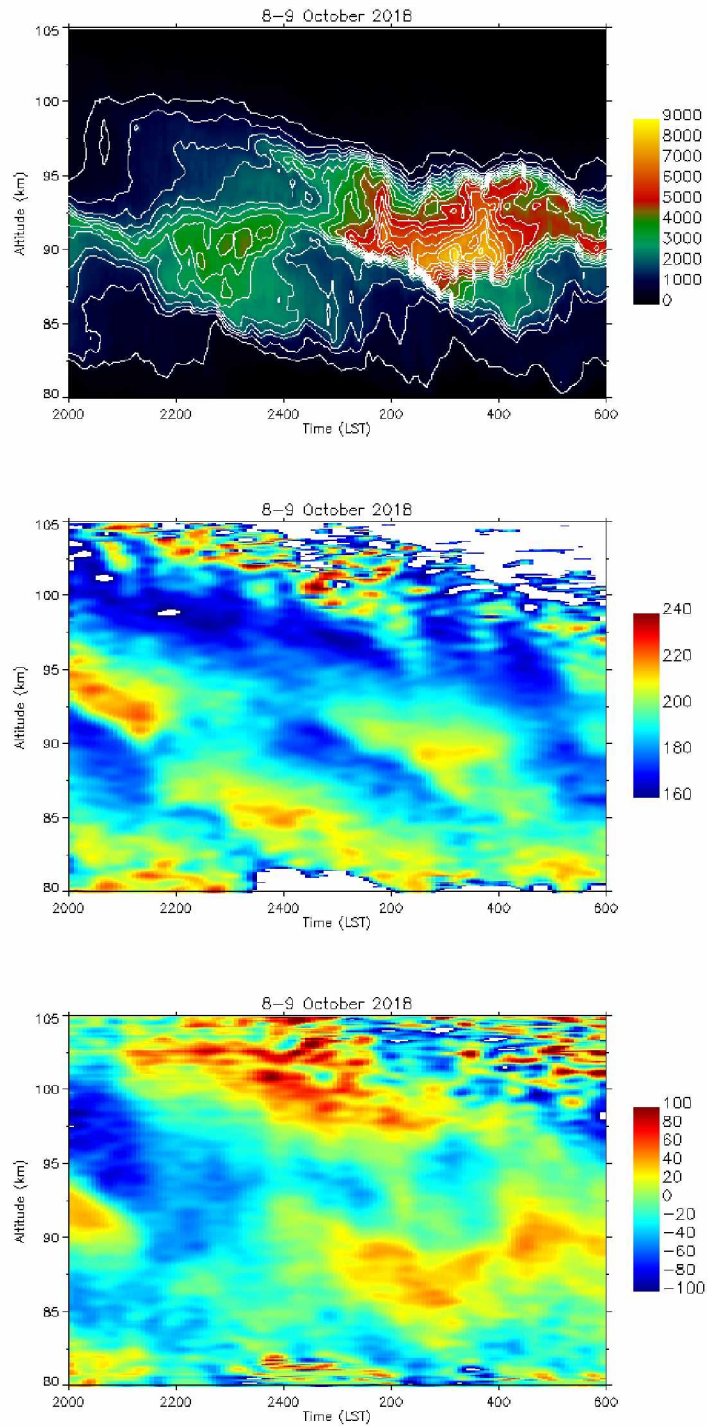
Figure 4.10. Sodium density (top), temperature (middle) and meridional wind (bottom) measured by the SRWTL on the night of 08-09 October 2018.
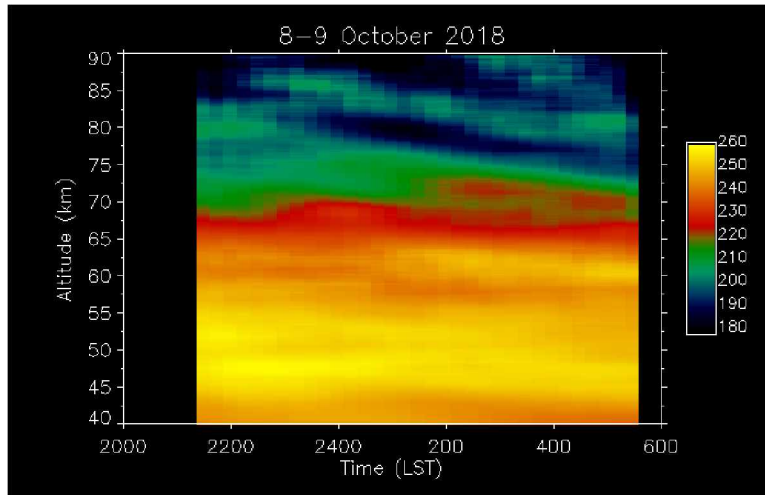
Figure 4.11. Temperature measured by the RDTL on the night of 08-09 October 2018.

The potential temperature derived from the SRWTL temperatures shows broadening and steepening of the potential temperature contours (Figure 4.12, top panel). The potential temperature contours are vertical at 23:00 LST near 87 km again indicating the presence of convective instability. The contours of potential temperature derived from the RDTL measurements show similar behavior with steepening at the same time and altitude (Figure 4.12, bottom panel). The sodium mixing ratio plotted in false color shows bands that follow the potential temperature and shows broadening of and steepening that confirms behavior in the potential temperatures at 23:00 LST and 87 km (Figure 4.12, bottom panel).

We calculate the sodium mixing ratio averaged between 87.0 km and 88.0 km, and the scale height of the mixing ratio over the 86.0 km to 89.0 km range (Figure 4.13). The average sodium mixing ratio reaches a local maximum of 53.3 PPT at 23:00 LST, which we choose as t_m. The scale height of sodium mixing ratio has typical value of 2 km before the spreading event begins (21:30 LST), and then increases significantly to 4.3 km at 23:00 LST and reaches a local

121

maximum of 16.9 km at 00:30 LST. The sodium density profile and the sodium mixing ratio profile both show decreased vertical gradient and increased scale height at t_m (Figure 4.14). The behavior of the sodium mixing ratio is consistent with our model of turbulent diffusion as discussed in section 2.3.2. We calculate the chemical time constant from the decrease in the sodium mixing ratio between 23:00 LST and 25:30 LST (Figure 4.13). We tabulate the measured characteristics of the diffusion event in Table 4.1.
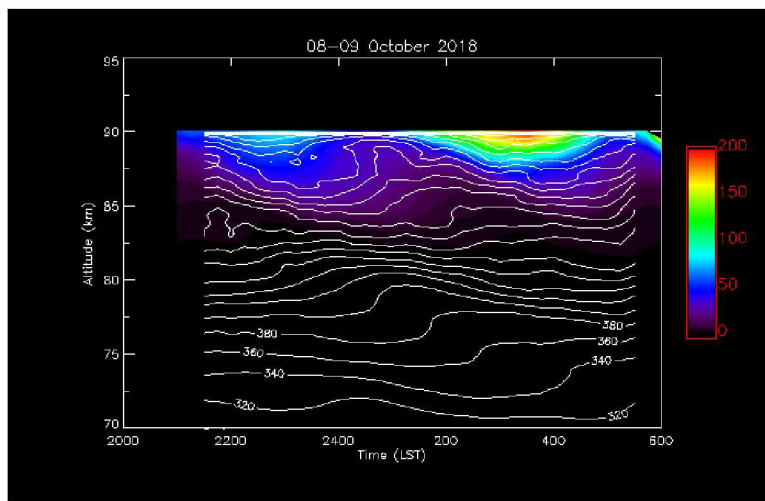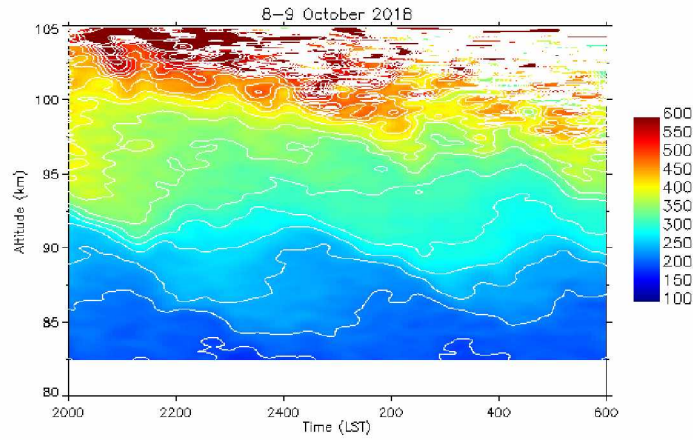
Figure 4.12. Potential temperature derived from SRWTL temperature measurements (top), sodium mixing ratio (bottom, false color) and potential temperature derived from RDTL temperature measurements (bottom, contours) on the night of 08-09 October 2018.
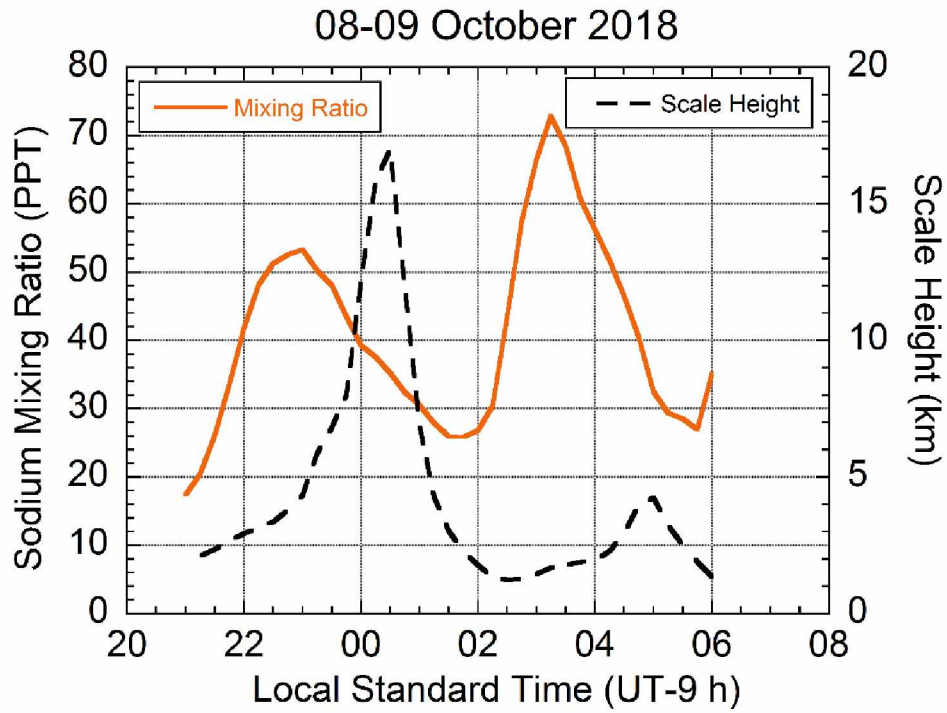
Figure 4.13. Average sodium mixing ratio measured by the RDTL and SRWTL between 87.0 km and 88.0 km (solid, yellow) and the scale height of sodium mixing ratio between 86.0 and 89.0 km (dashed, black) on the night of 08-09 October 2018.
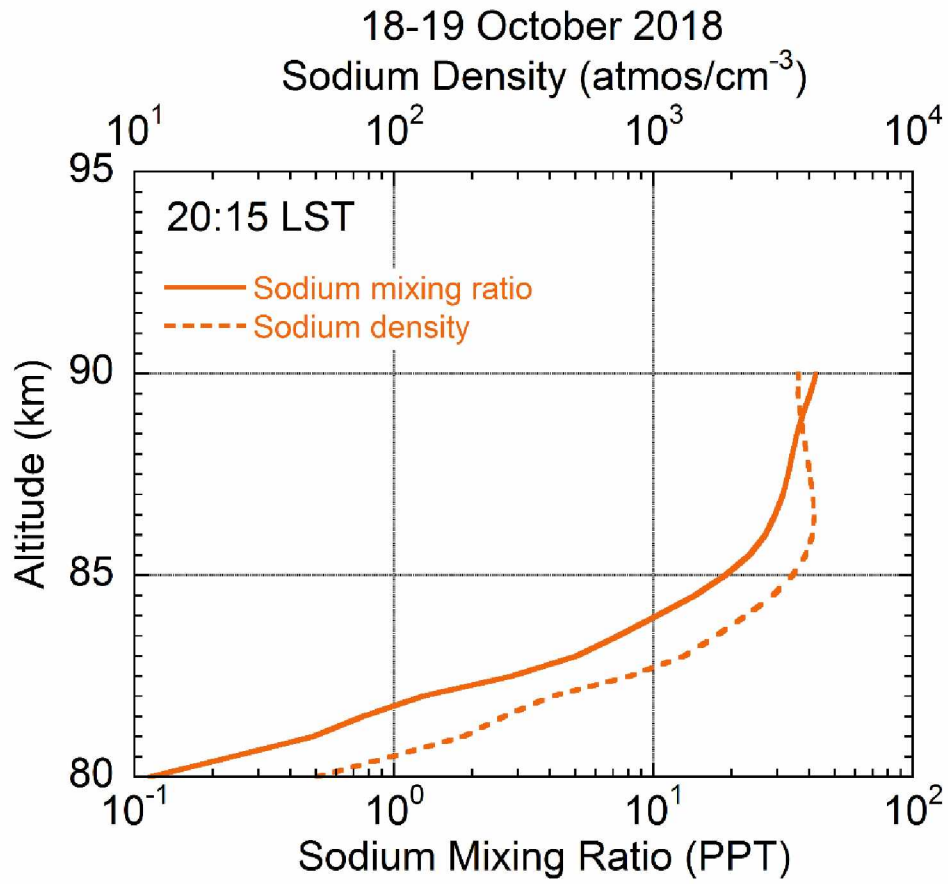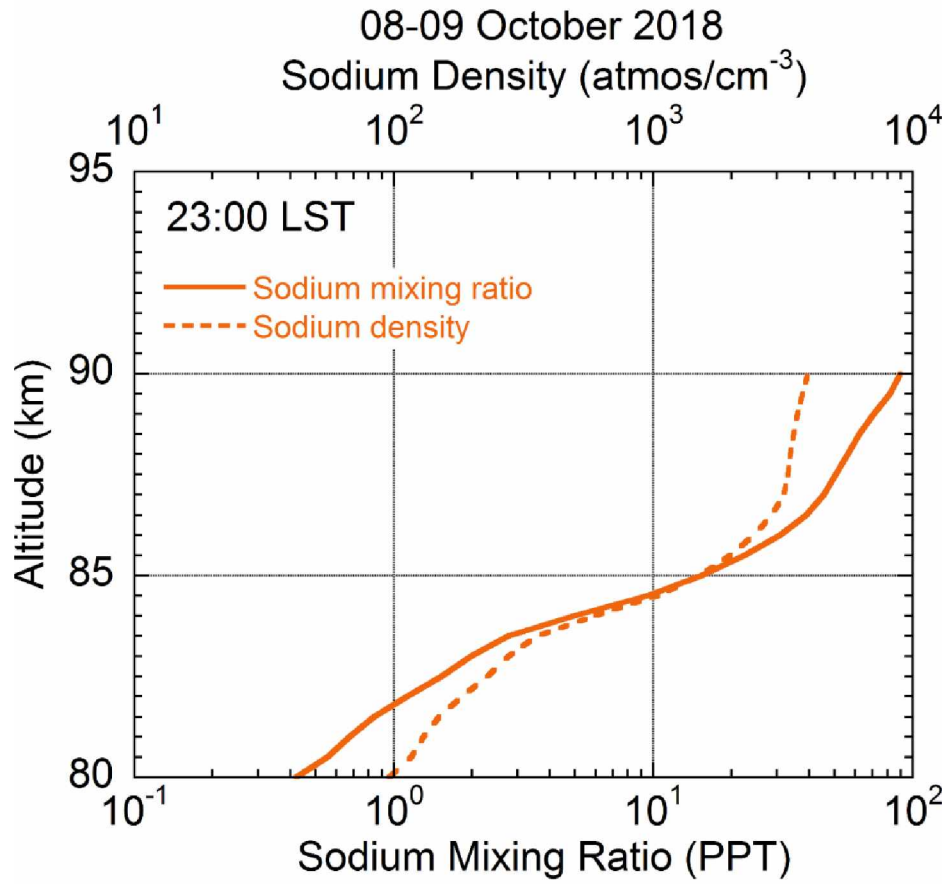
Figure 4.14. Profiles of sodium mixing ratio (solid) and sodium density (dashed) measured by the RDTL and SRWTL between 22:30 LST and 23:30 LST on the night of 08-09 October 2018.

The temperature and potential temperature profiles show the presence of a temperature inversion with a negative topside temperature layer corresponding to a region of reduced potential temperature gradient (Figure 4.15). The MIL is clearly evident in the temperature profile about 87 km at t_m. The value of the squared buoyancy frequency calculated over the 3 km range between 86.0 km and 89.0 km is 3.4×10^{-5} s^{-2}. This indicates a layer of reduced stability (equation 2.17) and mixing that corresponds to the spreading in in both the number density and mixing ratio profiles (Figure 4.14). The vertical gradients of the potential temperature are shown in Figure 4.16. Again, we see that the unstable regions become more pronounced as the length of the temporal integral decreases. Similar to section 4.3.1, we found different instable layers at different altitude and time resolutions. We summarize the pertinent parameters of the instable layers derived from different profiles in Table 4.1. We find that the depth of the layer varies by a factor of 2.3 (0.33 km to 0.75 km). As in the first case, we use the depth derived from the 5 minutes, 2 km intervals (0.66 km) to estimate the strength of turbulence. Using equations 2.15 and 2.16, we estimate an eddy diffusion coefficient of 2.6×10^2 m^{2}s^{-1} and an energy dissipation rate of 10.9 mW/kg (Table 4.2).
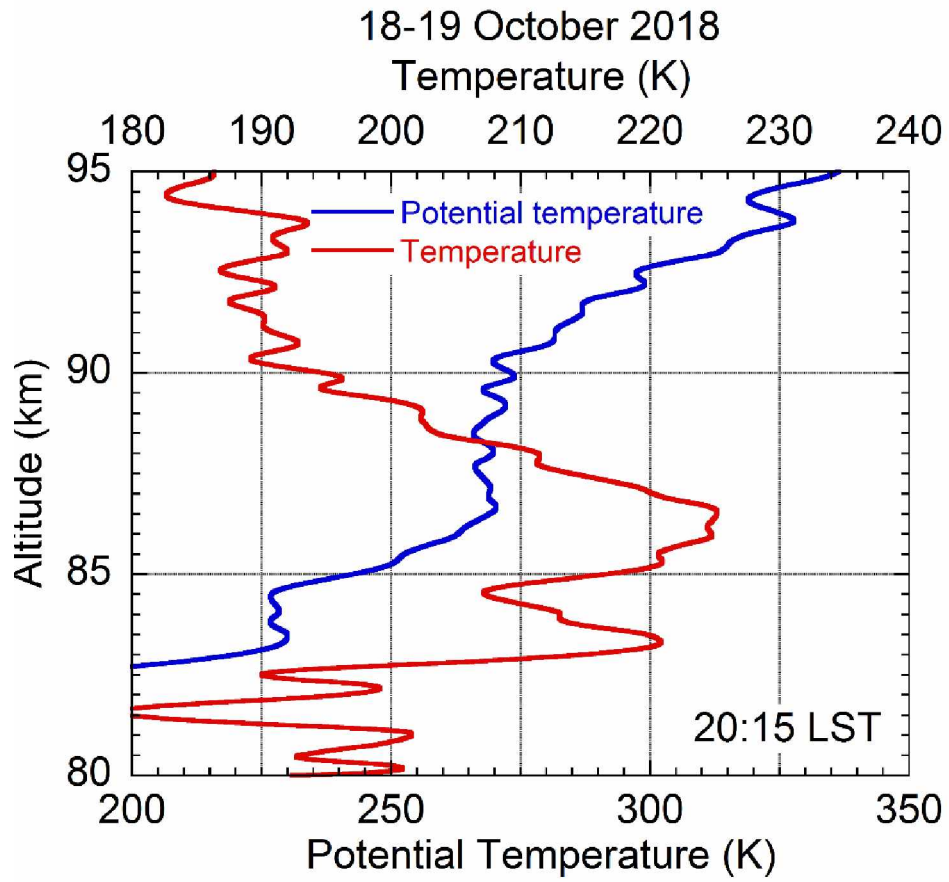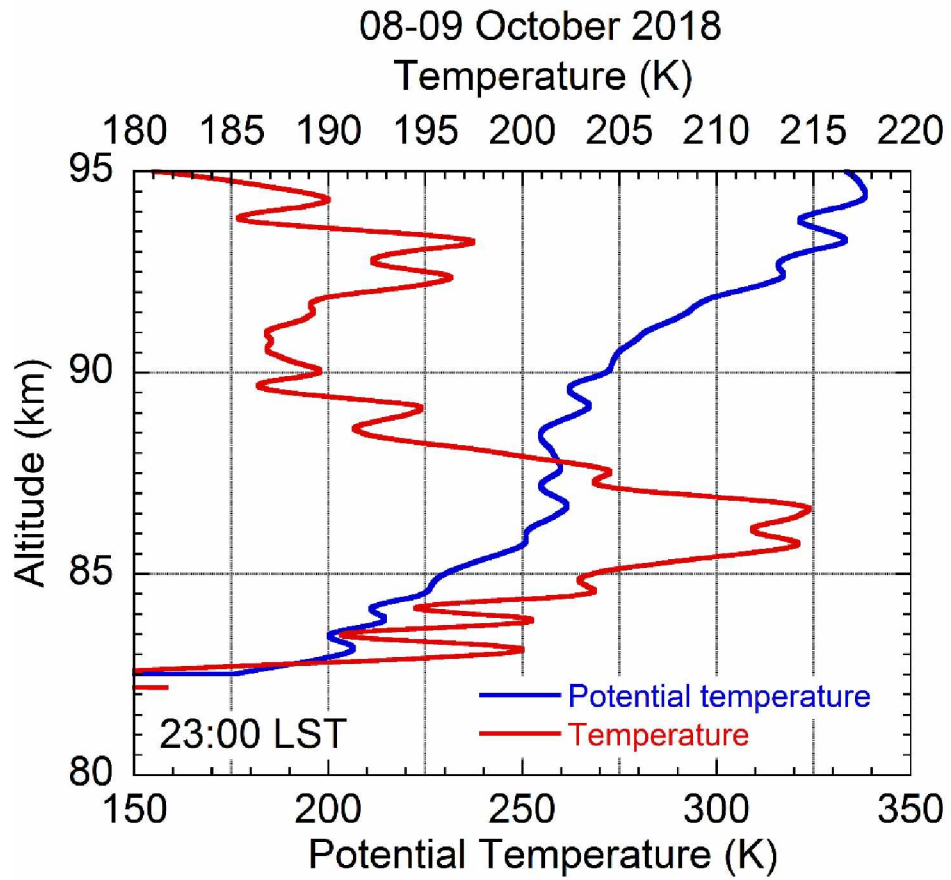
Figure 4.15. Profiles of temperature (red) and potential temperature (blue) measured by the SRWTL between 22:57:30 LST and 23:02:30 LST on the night of 08-09 October 2018.
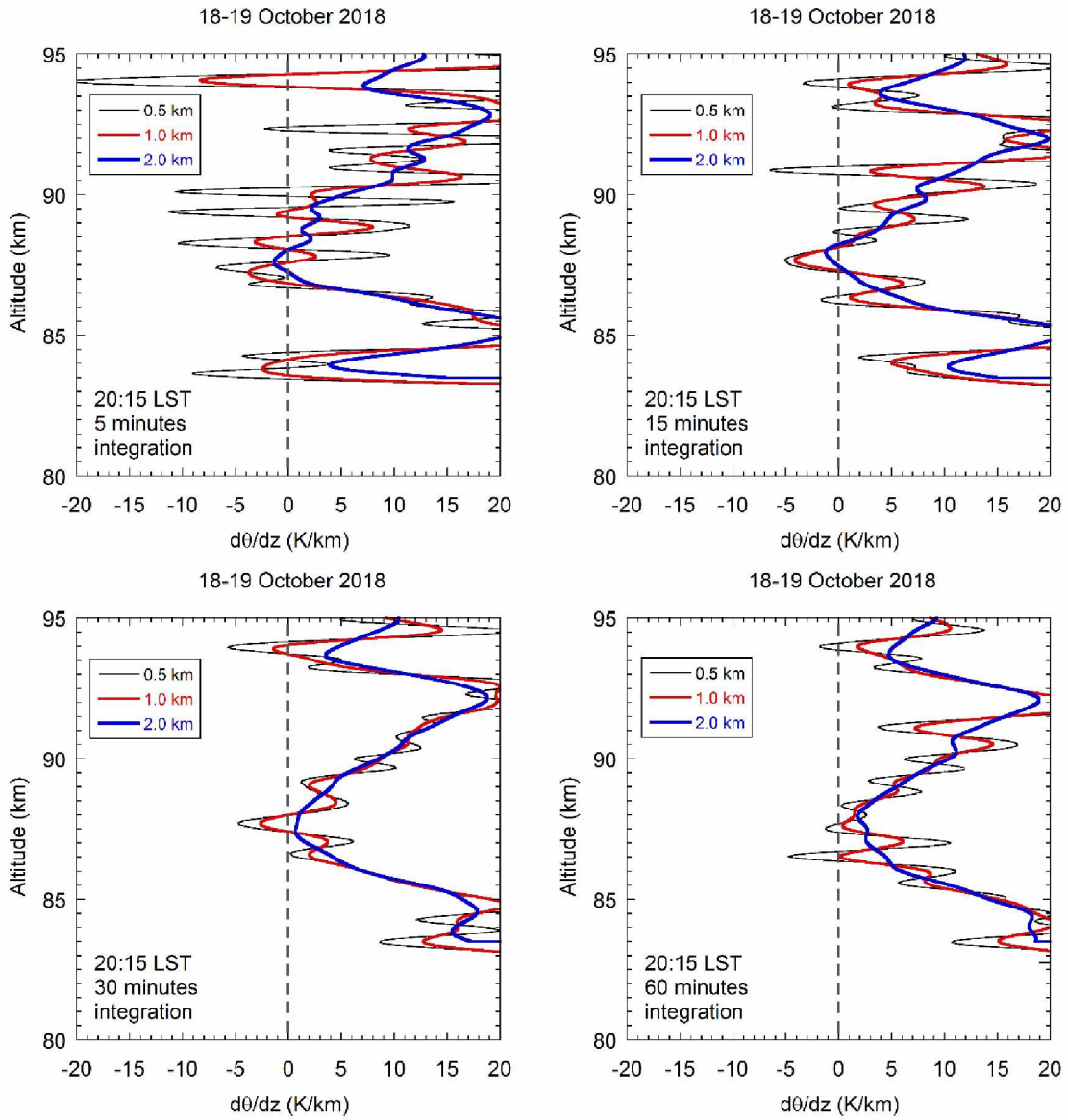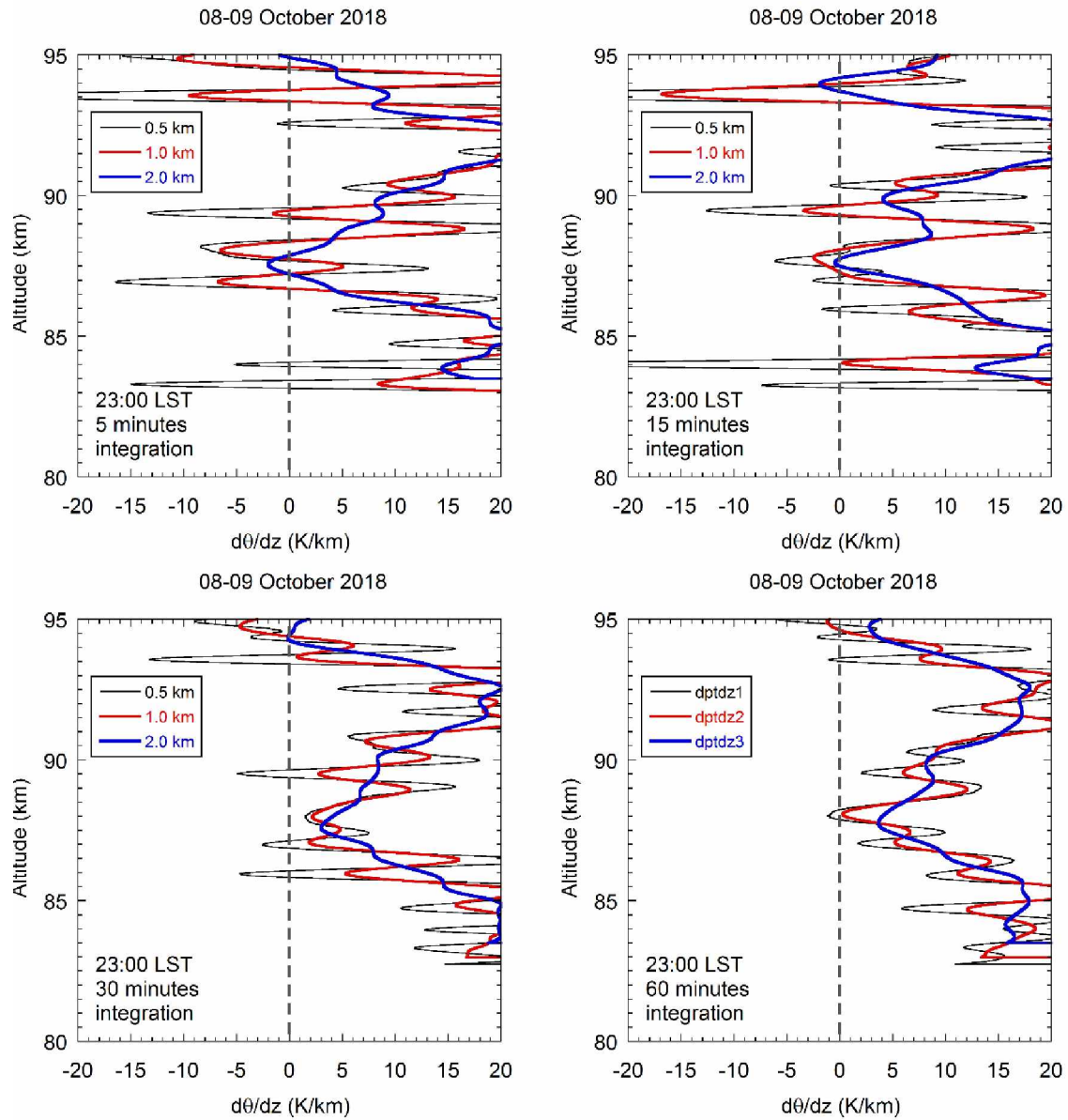
Figure 4.16. Vertical gradient of potential temperature measured by the SRWTL on the night of 08-09 October 2018. See text for details.

4.3.3. Discussion and summary

By examining the parameters related to the spreading events in Table 4.1, again, we find that these estimates of chemical time constant are consistent with the behavior of the sodium layer. These values, which are obtained near the center of the sodium layers, are significantly (a factor of 2-3) larger than those obtained near the bottom edge of the layers (see Chapter 2), which reflects the larger lifetime of sodium in the center of the layer. The chemical time constant are 1.6 h and 3.0 h, which are consistent with the values calculated by Xu and Smith (2003, 2005). This behavior is also consistent with the chemistry of the sodium layer.

We find that, as mentioned in Chapter 2, uncertainties exist in estimates of the depth of the layers, L, and the chemical time constant, τ. Using data with different altitude and temporal resolution, the values of L vary be a factor of 2-3. Wind measurements by the SRWTL show that the averaged value of vertical wind over the period of the event (1h) over the sodium layer (80-95 km) is less than 1 m/s. This is consistent with the analysis of Collins et. al. (2011). Following their analysis, we determine that an uncertainty of a factor of 2-3 exists in the estimate of τ. The values of the eddy diffusion coefficient, K, are higher than typical values, while the values of the energy dissipation rate, ε, are in reasonable agreement with typical values.

4.4. Gravity waves as sources of turbulence

Following our approach in Chapter 2, we estimate the energy available from the GWs as source of turbulence generation. We investigate both monochromatic GWs and ensemble of GWs. Since monochromatic GWs are clearly observed to break in these two cases, we investigate the monochromatic GWs in detail, and discuss the ensemble of GWs briefly.

4.4.1. Case 1: Stronger GWs

The relative temperature and density fluctuations show clear maxima and minima with downward phase progressions consistent with upwardly propagating waves (Figure 4.17). The temperature fluctuations in the MLT range from + 25 K to -25 K (Figure 4.17, top panel) and the density fluctuations in the upper stratosphere, mesosphere and MLT grow with altitude and reach amplitudes of ± 6% (Figure 4.17, bottom panel). As expected, the temperature and density fluctuations appear out of phase with warm (cold) phase of the fluctuations associated with the less (more) dense phase of the fluctuations. The frequency spectra of the relative sodium density and temperature fluctuations shows the presence of a 5.6 h harmonic between 80 km and 90 km in both spectra (Figure 4.18). This 5.6 h harmonic disappears around 90 km indicating that this wave dissipated around this altitude.

Figure 4.17. Temperature fluctuations derived from SRWTL measurements (top) and relative density fluctuations derived from RDTL measurements (bottom) on the night of 18-19 October 2018.
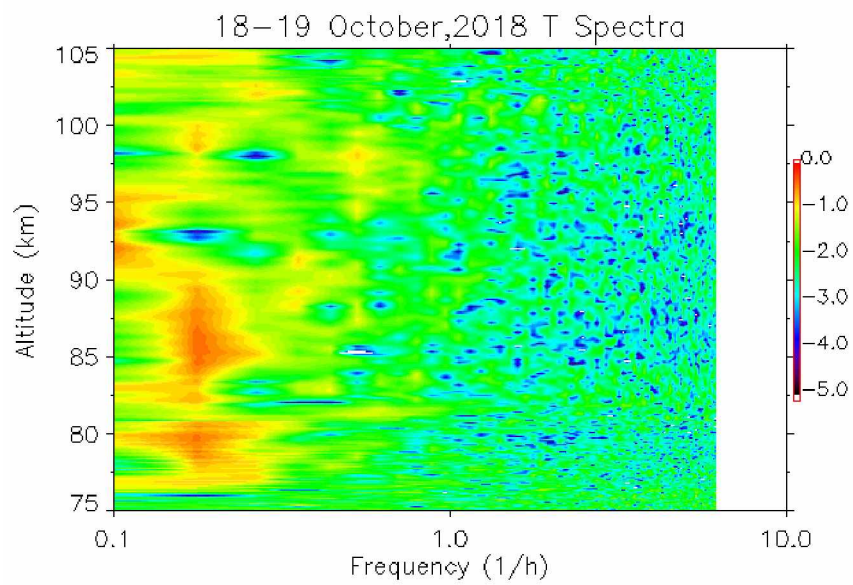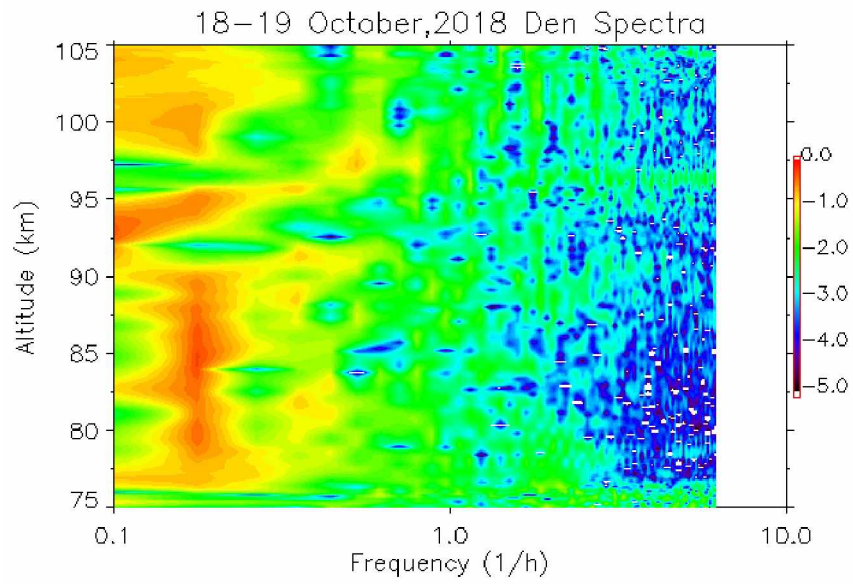
Figure 4.18. Frequency spectrum of sodium density and temperature fluctuations at different altitude measured by the SRWTL on the night of 18-19 October 2018.The color is on log scale.

The characteristics of this wave are determined by fitting a 5.6 h harmonic to the perturbations. We fit the 5.6 h wave to the temperature and meridional wind perturbations and determine how the amplitude and phase of the wave vary with altitude (Figure 4.19). The amplitude of the wave grows exponentially with altitude in the upper mesosphere, maximizes at 80-85 km, and then decreases with altitude. The vertical wavelength of the wave is derived from the vertical phase progression (section 2.3.3). In the altitude range of 58 km to 72 km, the temperature measurements (RDTL) show that the wave has a vertical wavelength of 8 km. The vertical wavelength increases to over 10 km (11.5 km, RDTL temperature, 10.4 km SRWTL temperature, 14.4 km SRWTL meridional wind) in the range of 80 km to 90 km. We summarize the observed characteristics of the wave in Table 4.3. The observed period and vertical wavelength indicate that this wave is an inertia gravity wave. We determine the characteristics of the wave using the gravity wave polarization and dispersion relationships based on the SRWTL temperature measurements, which are the highest quality of the three measurements (Table 4.4). The horizontal wind amplitude of 32.6 m/s compares with the measured meridional wind amplitude of 19.2 m/s and suggests a zonal wind amplitude of 26.3 m/s. The gravity wave characteristics indicate that this wave is approaching linear instability as the ratio of the horizontal wind amplitude and the horizontal phase velocity (32.6 m/s) is over 80% of the horizontal phase velocity (39.5 m/s). Thus we conclude that a 5.6 h gravity wave propagates from the stratosphere up to the mesosphere and dissipates near 90 km.
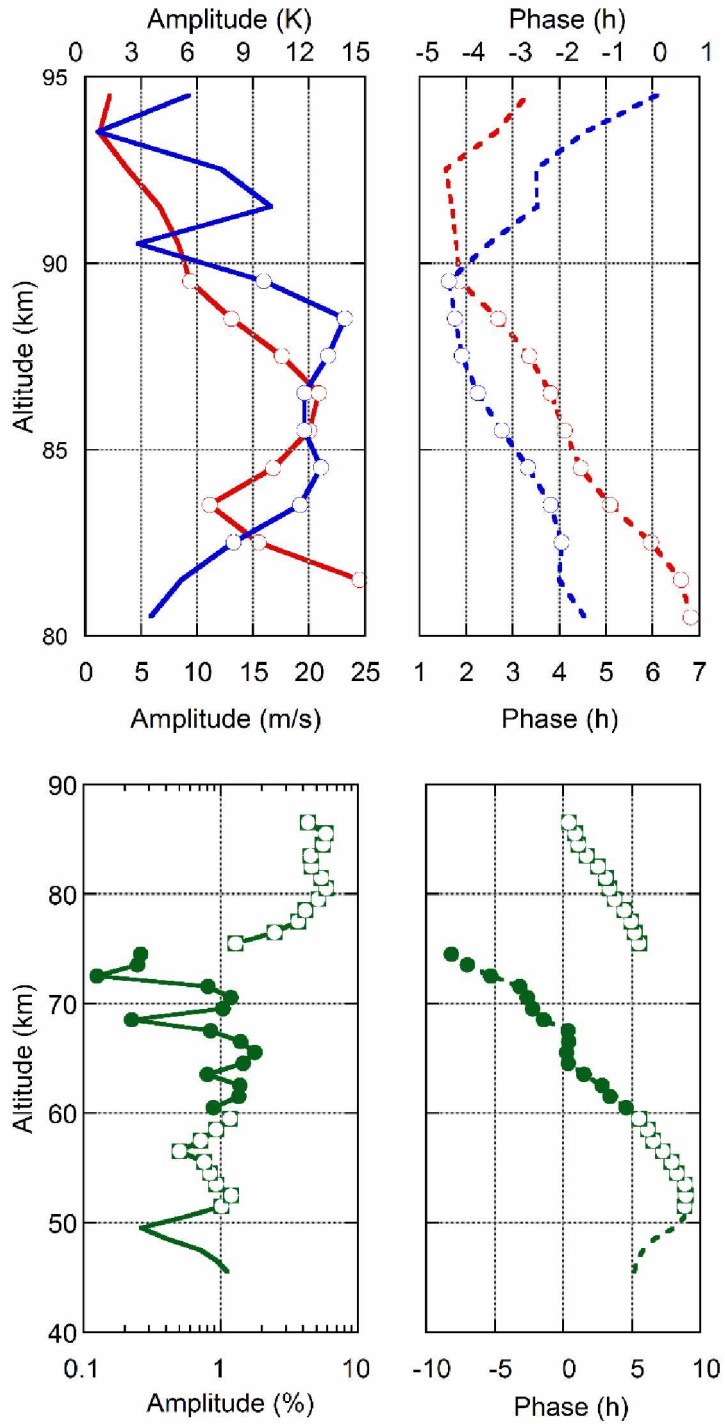
Figure 4.19. The amplitude and phase of a 5.6 h harmonic fits to SRWTL temperature measurements (top, red), wind measurements (top, blue) and RDTL temperature measurements (bottom) on the night of 18-19 October 2018.

We now investigate the possible energy from the monochromatic wave for turbulence generation. Similar to section 2.3.3, we estimate the possible turbulent energy dissipation rate by assuming the specific potential energy of the wave is dissipated over the thickness of the layer, L, at the speed of the vertical group velocity of the wave. Using the gravity wave parameters (Table 4.3) and the thickness of the layer (Table 4.1), we estimate that the possible turbulent energy dissipation rate associated with this wave breaking and spreading event is 149.7 mW/kg. This value is larger than the value of 16.7 mW/kg that we have estimated from the diffusion of sodium.

We also investigate the possible energy from the ensemble of GWs for turbulence generation. We investigate the relative density fluctuations over the 37.5-52.5 km and 60.0-75.0 km altitude ranges. In the lower range, we find a specific potential energy of 2.1 J/kg. In the upper range, we find a specific potential energy 11.3 J/kg. The specific potential energy increased by a factor of 5.4 over the 22.5 km range, which corresponds to a scale height of 13 km. The scale height of the atmospheric density is 7 km indicating that the specific energy of freely propagating GWs would increase by a factor of 24.8. These GWs are losing energy as they propagate upward. We summarize the characteristics of the GW ensemble in Table 4.5 and derived parameters in Table 4.6. We estimate an energy dissipation rate of 107.9 mW/kg. This value is larger than the value of 16.9 mW/kg that we estimated from the diffusion of sodium.

Table 4.3: Measured characteristics of monochromatic GWs

	Altitude	Period	λ_z	amplitude
18-19 Oct 2018				
RDTL	57.5-72.5 km	5.6 h	8.0 km	1.0 %
	72.5-87.5 km	5.6 h	11.6 km	4.2 %
SRWTL T	80.5-89.5 km	5.6 h	10.4 km	12.2 K
SRWTL V	82.5-89.5 km	5.6 h	14.4 km	19.2 m/s
08-09 Oct 2018				
RDTL	57.5-72.5 km	4.6 h	10.6 km	1.2 %
	72.5-87.5 km	4.6 h	7.8 km	2.5 %
SRWTL T	80.5-94.5 km	4.6 h	11.5 km	10.7 K
SRWTL V	82.5-89.5 km	4.6 h	10.9 km	12.8 m/s
02-03 Oct 2018				
RDTL	57.5-72.5 km	9.1 h	16.2 km	2.0 %
	72.5-87.5 km	9.1 h	15.8 km	2.6 %
SRWTL T	80.5-94.5 km	9.1 h	17.6 km	11.1 K
SRWTL V	82.5-89.5 km	9.1 h	20.0 km	46.7 m/s

Table 4.4: Derived characteristics of monochromatic GWs

Intrinsic period (h)	λ_H (km)	c_{gH} (m/s)	c_{gz} (m/s)	PE (J/kg)	ε (mW/kg)
18-19 Oct 2018					
4.1-10.0	635-2323	30.2-43.9	0.13-0.69	154	17.7-55.7
08-09 Oct 2018					
8.2-10.8	1159-2082	17.9-24.3	0.064-0.16	57	7.3-10.8
02-03 Oct 2018					
12.7	10186	68.3	0.024	68	NAN

Table 4.5: Ensemble gravity-wave activity measured by Rayleigh Lidar

18-19 Oct 2018

Altitude Range	37.5-52.5 km	62.5-77.5 km
RMS relative density	0.60%	0.99%
RMS vertical displacement	141 m	310 m
Specific potential energy	4.1 J/kg	14.7 J/kg

08-09 Oct 2018

Altitude Range	37.5-52.5 km	62.5-77.5 km
RMS relative density	0.29%	0.98%
RMS vertical displacement	68 m	331 m
Specific potential energy	0.97 J/kg	15.6 J/kg

02-03 Oct 2018

Altitude Range	37.5-52.5 km	62.5-77.5 km
RMS relative density	0.23%	0.91%
RMS vertical displacement	55 m	260
Specific potential energy	0.62 J/kg	11.4 J/kg

Table 4.6: Parameters used to estimate turbulent energy dissipation rate from gravity-wave activities.

	H_{air} (km)	H_{diss} (km)	c_{gz} (m/s)	L_d (km)	t_d (hr)	ε_{GW} (mW/kg)
18-19 Oct 2018						
	7	19.6	0.74	0.8	0.29	105.6
08-09 Oct 2018						
	7	9.1	0.74	0.7	0.25	70.5
02-03 Oct 2018						
	7	8.6	0.74	-	-	-

4.4.2. Case 2: Weaker gravity waves

The relative temperature and density fluctuations show clear maxima and minima with downward phase progressions consistent with upwardly propagating waves (Figure 4.20). The temperature fluctuations in the MLT range from + 25 K to -25 K (Figure 4.20, top panel) and the density fluctuations in the upper stratosphere, mesosphere and MLT grow with altitude and reach amplitudes of ± 6% (Figure 4.20, bottom panel). Once again, the temperature and density fluctuations appear out of phase with warm (cold) phase of the fluctuations associated with the less (more) dense phase of the fluctuations. The frequency spectra of the relative sodium density and temperature fluctuations shows the presence of a 4.6 h harmonic between 84 km and 92 km in both spectra (Figure 4.21). In both spectra, a 4.6 h harmonic exists between 84 km and 92 km. This 4.6 h harmonic disappears around 92 km indicating that this wave dissipated around this altitude.
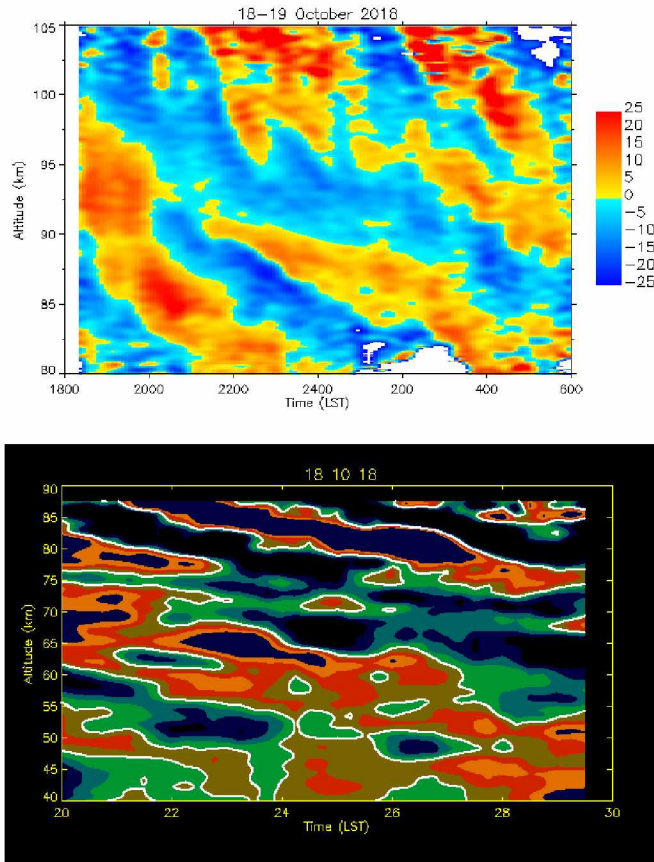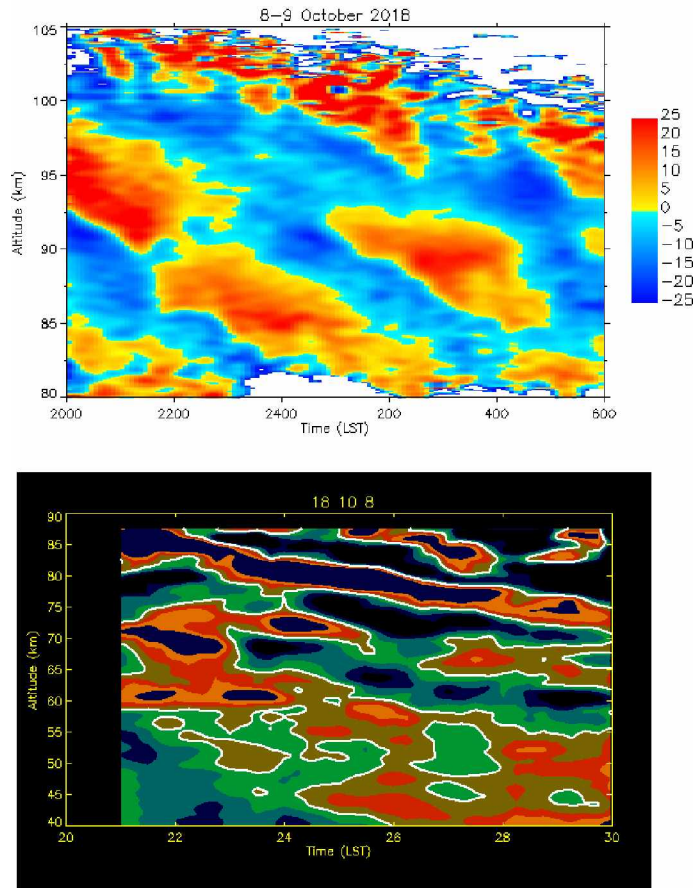
Figure 4.20. Temperature fluctuations derived from SRWTL measurements (top) and relative density fluctuations derived from RDTL measurements (bottom) on the night of 08-09 October 2018.
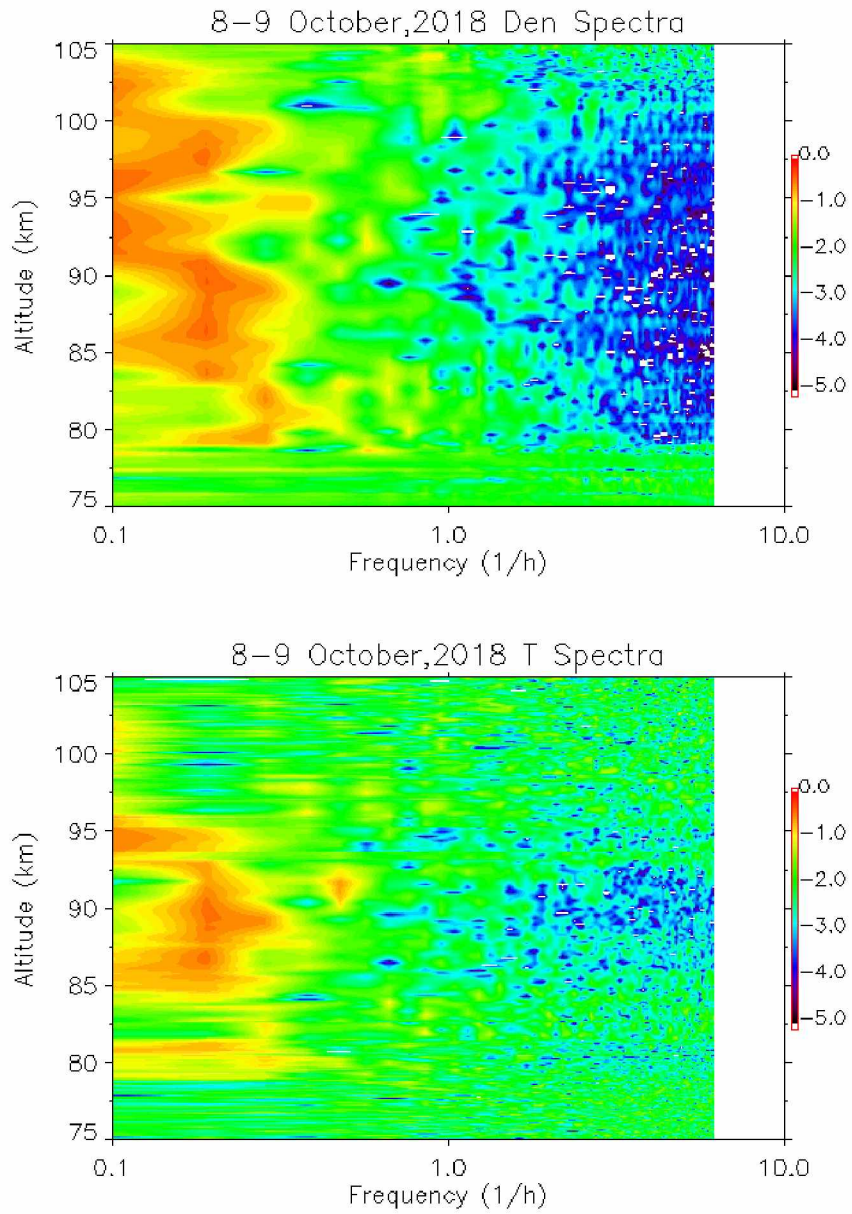
Figure 4.21. Frequency spectrum of sodium density (top panel) and temperature (bottom panel) at different altitude measured by SRWTL on the night of 08-09 October 2018.
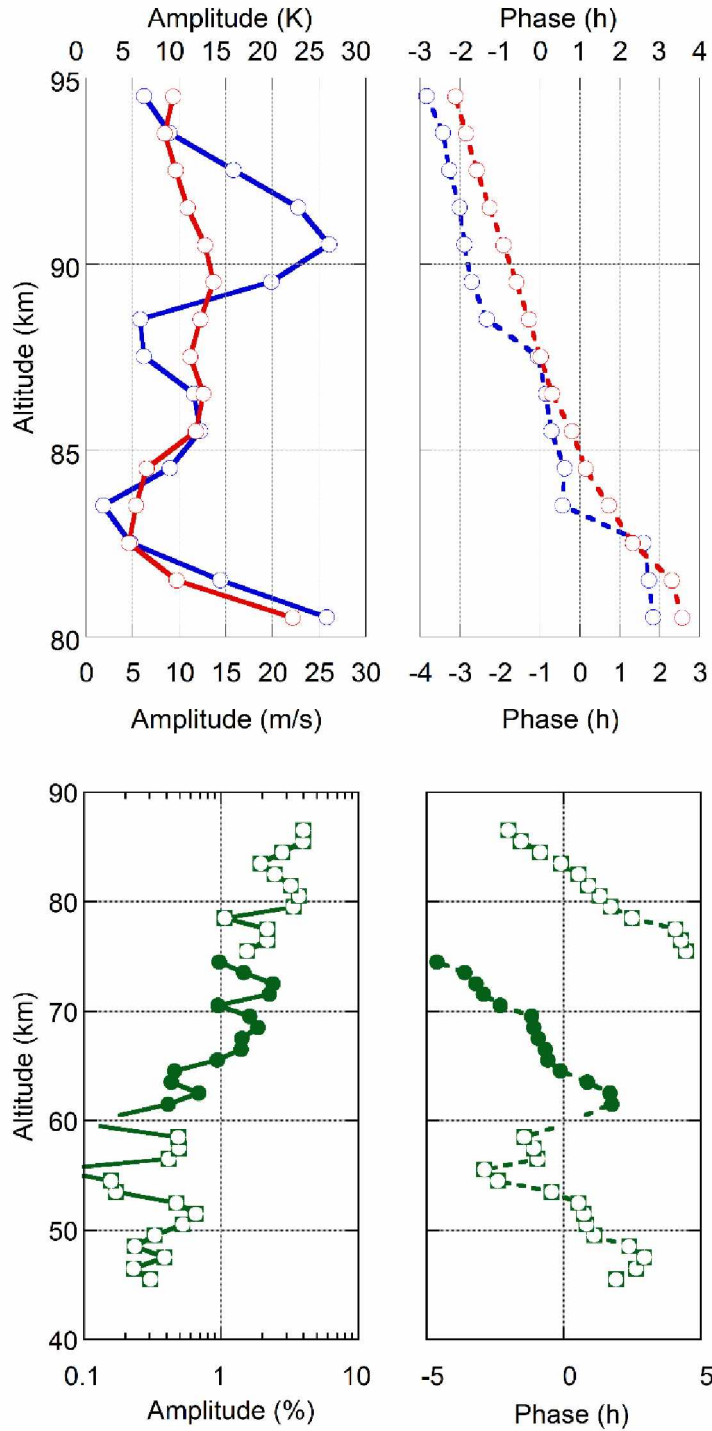
Figure 4.22. The amplitude and phase of a 4.6 h harmonic fits to the SRWTL temperature measurements (top, red), wind measurements (top, blue) and RDTL temperature measurements (bottom) on the night of 08-09 October 2018.

The characteristics of this wave are determined by fitting a 4.6 h harmonic to the temperature perturbations. We fit the 4.6 h wave to the temperature and meridional wind and determine how the amplitude and phase of the wave vary with altitude (Figure 4.22). The amplitude of the wave grows exponentially with altitude in the upper mesosphere, reaches a maximum near 80 km, decreases and then increases again near 90 km. The vertical wavelength of the wave is derived from the vertical phase progression. In the altitude range of 58 km to 72 km, the temperature measurements (RDTL) show that the wave has a vertical wavelength of 10.6 km. The vertical wavelength increases to about 10 km (7.8 km, RDTL temperature, 11.5 km SRWTL temperature, 10.9 km SRWTL meridional wind) in the range of 80 km to 90 km. We summarize the observed characteristics of the wave in Table 4.3. The observed period and vertical wavelength indicate that this wave is an inertia gravity wave. We determine the characteristics of the wave using the gravity wave polarization and dispersion relationships based on the SRWTL temperature measurements. (Table 4.4). The horizontal wind amplitude of 27.5 m/s compares with the measured meridional wind amplitude of 12.8 m/s and suggests a zonal wind amplitude of 24.3 m/s. The ratio of the horizontal wind amplitude and the horizontal phase velocity (27.5 m/s) is over 50% of the horizontal phase velocity (42.9 m/s) for this wave. We conclude that a 4.6 h gravity wave propagates from the stratosphere up to the mesosphere and it is more stable than the wave observed on 18-19 October, and contributes to a weaker instability in the MLT.

We now investigate the possible energy from the monochromatic wave for turbulence generation. Again, following our approach in section 2.3.3, we estimate the possible turbulent energy dissipation rate by assuming the specific potential energy of the wave is dissipated over the thickness of the layer, L, at the speed of the vertical group velocity of the wave. Using the gravity wave parameters (Table 4.4) and the thickness of the layer (Table 4.1), we estimate that

142

the possible turbulent energy dissipation rate associated with this wave breaking and spreading event is 89.1 mW/kg. This value is in reasonable agreement with the value of 10.9 mW/kg that we estimated from the diffusion of sodium.

We also investigate the possible energy from the ensemble of GWs for turbulence generation. Similar to Chapter 2, we investigate the relative density fluctuations over the 37.5-52.5 km and 60.0-75.0 km altitude ranges. In the lower range, we find a specific potential energy of 0.5 J/kg. In the upper range, we find a specific potential energy 10.4 J/kg. The specific potential energy increased by a factor of 20.8 over the 22.5 km range, which corresponds to a scale height of 7.4 km. The scale height of the atmospheric density is 7 km indicating that the specific energy of freely propagating GWs would increase by a factor of 24.8. These GWs are losing energy as they propagate upward. The GWs are much less dissipated compare to the case on 18-19 October 2018. This is consistent with the more stable environment on this night. We summarize the characteristics of the GW ensemble in Table 4.5 and derived parameters in Table 4.6. We estimate an energy dissipation rate of 22.5 mW/kg. This value is larger than the value of 10.9 mW/kg that we estimated from the diffusion of sodium.

4.5. Discussion and conclusion

In this Chapter we have presented two sets of simultaneous SRWTL an RDTL observations to investigate waves, instabilities, and turbulence. In the two cases, instability and spreading are consistently observed in the sodium mixing ratio and in the potential temperature measured by both the SRWTL and RDTL. We found that on each night a GW is observed to propagate from the stratosphere to the mesosphere. GWs are observed to dissipate in the region of the instability and spreading. We have investigated turbulent transport associated with the instability. We find

that the gravity waves can support energy dissipation rates of 61.4 mW/kg and 265.2 mW/kg. As we analyzed in Chapter 2, due to the assumption of zero background wind, the same uncertainty of factor of two exist in the estimate of the GW energy dissipation rate. These values of energy dissipation are typical in the MLT but higher than those that have been reported in mid-winter during periods of reduced GW activity. From our diffusion analysis based we estimate turbulent eddy diffusion coefficients, K, of 2.7×10^3 m^2/s and 4.0×10^2 m^2/s, and energy dissipation rates, ε, of 325.5 mW/kg and 108.1 mW/kg associated with the instabilities.

We found a correlation between the characteristics of the breaking monochromatic GW and the reduction of convective stability. The amplitudes of the breaking GW are 12.2 K and 10.7 K for the cases observed on 18-19 October 2018 and 08-09 October 2018. The ratios of the horizontal wind amplitude and the horizontal phase velocity are 80% and 50% for these two cases respectively, which indicates that the wave on the night of 18-19 October 2018 is closer to linear instability then that on the night of 08-09 October 2018. The propagation of the ensemble of GWs also indicate that the waves on the first night are more dissipated. The values of the squared buoyancy frequency, N^2, in the region of wave breaking are 1.0×10^{-5} s^{-2} and 3.4×10^{-5} s^{-2} respectively, which indicates that the environment is more convectively stable on the night 18-19 October 2018 than on the night of 18-19 October 2018.

Chapter 5. On the detection and characterization of turbulence in the mesosphere by incoherent scatter radar

5.1. Introduction

Turbulence plays an important role in structure, energetics, dynamics and coupling in the mesosphere-lower-thermosphere (MLT) as it does throughout the atmosphere. In the MLT turbulence is generated by local wave-driven instabilities (Fritts & Alexander, 2003; Fritts et al., 2018a; Fritts et al., 2018b; Fritts et al., 2017; Hines & Reddy, 1967; Lindzen, 1981; Sutherland, 2010). Observational and modeling studies have shown that turbulent heating in the MLT is on average as strong as radiative and chemical heating (Becker, 2012; Guo et al., 2017; Lübken, 1997). Turbulence also couples the MLT both upward to the upper thermosphere and F-region and downward to the mesosphere and stratosphere. Turbulence in the MLT influences the thermospheric composition and density through mixing and transport of chemical species (e.g., O, CO_2) (Garcia et al., 2014; Qian et al., 2009; Wu et al., 2017). Turbulence in the MLT influences stratospheric composition through downward transport of nitrogen oxides (NOx) (Meraner & Schmidt, 2016; Randall et al., 2006; Smith et al., 2011). A major challenge in measuring and characterizing mesosphere turbulence is that the measured turbulent parameters vary significantly with the meteorological conditions and measurement techniques. This is illustrated in studies where rocket-borne ionization gauges have been used to measure turbulent fluctuations at high-resolution (~ 1m) and attributed order-of-magnitude variations in turbulent dissipation rates to variations in wave activity and stability (Collins et al., 2011; Lehmacher et al., 2006; Lehmacher & Lübken, 1995; Lehmacher et al., 2011; Lübken, 1997; Osman et al., 2016; Szewczyk et al., 2013; Triplett et al., 2018).

Unlike rocket-borne instruments, radars have the potential to make measurements of turbulence on an ongoing basis and provide measurements under a wide variety of meteorological conditions. Mesosphere-Stratosphere-Troposphere (MST) radars were originally developed to make measurements of the structure and dynamics of the atmosphere from the lower troposphere (~ 1km) to the lower thermosphere (~100 km). While these radars have yielded measurements of turbulence in the troposphere, stratosphere, and mesosphere, most studies have focused on clear-air turbulence in the troposphere (See review by Hocking et al., 2016). MST radars have been used to make measurements of turbulence in the mesosphere since the 1970s (Hocking, 1985, 1996; Rastogi & Bowhill, 1976; Woodman & Guillen, 1974) and are still used for that purpose (Selvaraj et al., 2016). The method is based on the fact that the random motion due to turbulence broadens the power spectrum of the returned radar echoes, where the increase in the width of the power spectrum is proportional to the mean-square velocity of the turbulent fluctuations.

Like MST radars, Incoherent Scatter Radars (ISR) also exhibit spectral broadening due to turbulence and have been used to measure turbulence in the MLT (Nicolls et al., 2010). The ISR spectrum is broadened and the shape of the spectrum is systematically changed by the turbulence. In the mesosphere (or D-region), where collision rates are high, scattering yields a narrow Lorentzian line shape, termed the ion-line, superimposed on a broad electron line (Bhattacharyya, 1992; Dougherty & Farley, 1963; Kudeki & Milla, 2011). Turbulent eddies within the beam volume Doppler shift the Lorentzian line for each scatterer and yield an ISR spectrum that has Voigt function line shape, similar to the broadening of a natural line in optics by the thermal motion or absorbers or emitters (e.g. Demtröder, 1981; Verdeyen, 1981). Measurements from the Poker Flat ISR (PFISR) have been analyzed with a Voigt function and

yielded estimates of turbulent velocity variances and hence turbulent dissipation rates (Nicolls et al., 2010). The ISR spectral model has been extended to include the effects of charged ice particles that yields an additional narrower line that is superimposed on the ion-line (Cho et al., 1998). This extension has been further developed to infer the size of meteoric smoke particles (MSPs) from PFISR measurements (Fentzke et al., 2012). Thus, in the presence of charged MSPs the ISR spectrum can be modeled as the superposition of two Lorentzian lines and in the presence of MSPs and turbulence the ISR spectrum as the superposition of two Voigt functions.

In this study we investigate PFISR-based turbulence measurements. We develop a hypothesis test to distinguish between the presence and absence of turbulence using the quality of the spectral fit to Voigt- or Lorentzian-based spectral line shapes. We then use a Monte Carlo approach to determine the uncertainties in the fit and the significance of the turbulence identification. We compare the retrieval of turbulent parameters from the statistically significant retrievals with all possible retrievals. We present our methods using two data sets of vertical beam measurements on 22-23 May 2017 and on 23 April 2008. The measurements of 23 April 2008 have been previously analyzed for waves and turbulence (Nicolls et al., 2010). We discuss the technique in terms of measurements with more powerful ISR, for example the European Incoherent Scatter Scientific Association (EISCAT) 3D radar (McCrea et al., 2015).

5.2. The Poker Flat Incoherent Scatter Radar

PFISR is an Advanced Modular Incoherent Scatter Radar (AMISR) class radar system (Heinselman & Nicolls, 2008; Nicolls et al., 2007). The AMISR class radars are composed of phased arrays of dipole antennas and are capable of pulse-to-pulse steering. PFISR is composed of 4096 dipole antennas arranged and constructed in 128 panels of 32 antennas each. The radar

operates at 450 MHz with a wavelength of 0.67 m and a beam width of approximately 1°. The total power of the radar is ~2 MW. This radar wavelength is much greater than the Debye length (< 0.07 m) of the D-region plasma. Thus the resulting lineshape for ISR scatter from non-turbulent plasma is Lorentzian (Kudeki & Milla, 2011). For the observations presented in this study the radar operated in a D-region mode, where the radar transmitted a 280 μs, 28-baud binary-phase coded pulse with 10 μs bauds sampled at 5 μs. This yielded measurements at 750 m range resolution. Pulses were transmitted every 3 ms with 128 pulses transmitted in a given direction and the pulse-to-pulse autocorrelation function was estimated. Thus the spectrum of the autocorrelation function is acquired over 384 ms. The spectral resolution of the spectrum was 1.3 Hz extending ± 167 Hz corresponding to a radial velocity range of ± 57 m/s and resolution of 0.43 m/s. The combination of the narrow-beam width and high range resolution reduce beam- and shear-broadening effects to less than 0.75 m/s or 2.25 Hz (Nicolls et al., 2010).

We consider two sets of PFISR observations. On 22-23 May 2017 the radar operated with one vertical beam from 03:06 until 05:36 UT. Forty-nine successive pulse spectra were acquired from the vertical beam every 18.8 s and averaged. We average 32 of these average spectra to yield a single spectrum representing 1568 pulse spectra over 602 s. We then fit spectral models to these 602 s spectra. On 23 April 2008 the radar operated with seven beams and so the vertical beam measurements recurred every 2.7 s. Seven successive pulse spectra were acquired from the vertical beam every 18.8 s and averaged. We again average 32 of these average spectra to yield a spectrum representing 224 pulse spectra over 602 s and fit spectral models to these spectra.

5.3. The Incoherent Scatter Radar Spectrum

5.3.1. Spectral Models

In the mesosphere the ISR spectrum, in the absence of turbulence and charged particles (e.g., meteoric smoke or ice particles), is given by the superposition of two components, a broad low-amplitude electron-line and a narrow high-amplitude ion-line. The electron-line arises from (free) electrons moving with the thermal motion of electrons (Gordon, 1958). The ion-line arises from scattering from (bound) electrons moving with the thermal motions of the ions (Bowles, 1958). The narrow ion-line is superimposed on the broader electron line which can be treated as a constant spectral background relative to the ion-line (Hagen & Behnke, 1976). The ion-line has a Lorentzian line shape and is given by

$$S_L(\omega; \omega_0, \gamma) = \frac{\gamma}{\pi[(\omega-\omega_0)^2+\gamma^2]}, \tag{5.1}$$

where ω is the frequency, ω_0 is the Doppler shift frequency due to the mean wind, and γ is the half-width-half-maximum (HWHM) of the line. The Lorentzian HWHM, γ, is given by

$$S_L(\omega; \omega_0, \gamma) = \frac{\gamma}{\pi[(\omega-\omega_0)^2+\gamma^2]}, \tag{5.1}$$

where ω is the frequency, ω_0 is the Doppler shift frequency due to the mean wind, and γ is the half-width-half-maximum (HWHM) of the line. The Lorentzian HWHM, γ, is given by

149

$$\gamma = \frac{8\pi^2 kT_i}{\lambda^2 m_i \nu_{in}}, \tag{5.2}$$

where k is Boltzmann's constant, T_i is the ion temperature, λ is the radar wavelength, m_i is the ion mass, and ν_{in} is the ion-neutral collision frequency. In the D-region the ion temperature, T_i, is equal to the neutral temperature, T. The measurements of the Lorentzian width is used to determine the temperature (e.g., Nicolls et al., 2010). In the presence of turbulence, the scatters move with the turbulent motion with a Maxwell-Boltzmann velocity distribution function. Thus the ion-line spectrum is represented by the convolution of the Lorentzian line with a Gaussian line and has a Voigt line shape given by

$$S_V(\omega; \omega_0, \gamma, \sigma) = \int_{-\infty}^{\infty} S_L(\omega - \omega'; \omega_0, \gamma) f_v(\omega'; \sigma) \, d\omega', \tag{5.3}$$

where f_v is the velocity distribution function given by

$$f_v(\omega; \sigma) = \frac{1}{\sigma\sqrt{2\pi}} \exp\left(-\frac{\omega^2}{2\sigma^2}\right), \tag{5.4}$$

and σ is the root-mean-square (RMS) width due to the Doppler shifting by turbulent velocity. The ISR spectrum includes an additional component in the presence of charged MSPs. These charged particles behave like massive ions and so the spectrum includes an even narrower MSP-line superimposed on the original ion-line. The Lorentzian HWHM, γ, is now given by

$$\gamma = \frac{8\pi^2 kT}{\lambda^2 m_p \nu_{pn}}, \tag{5.5}$$

where T is the neutral temperature, λ is the radar wavelength, m_p is the particle mass, and ν_{pn} is the particle-neutral collision frequency. Thus in the absence of turbulence the spectrum becomes

150

the superposition of two Lorentzian lines, while in the presence of turbulence the spectrum becomes the sum of two Voigt lines.

Thus, the ISR spectrum associated with scattering from the D-region can have one of four line shapes associated with four distinct scenarios. The first scenario is incoherent scatter, in the absence of turbulence and MSPs, where the ISR spectrum is a single Lorentzian line,

$$S_0(\omega) = A_0 S_L(\omega; \omega_0, \gamma_0), \tag{5.6}$$

where A_0 is the amplitude of the ion-line and γ_0 is the HWHM of the ion-line. The second scenario is incoherent scatter with turbulence and no MSPs, where the spectrum is a single Voigt line,

$$S_T(\omega) = A_T S_V(\omega; \omega_0, \gamma_T, \sigma_T), \tag{5.7}$$

where A_T is the amplitude of the turbulence-broadened Voigt ion-line, γ_T is the HWHM of the Lorentzian component, and σ_T is the RMS width of the turbulent Gaussian component of the line. The Gaussian RMS width, σ_T, is given in terms of the RMS turbulent velocity, u_{rms}, as

$$\sigma_T = \frac{2}{\lambda} \times u_{rms}, \tag{5.8}$$

where λ is the radar wavelength. The strength of the turbulence is given by the turbulent dissipation rate, ε, as

$$\varepsilon = \frac{1}{2} u_{rms}^2 \times N, \tag{5.9}$$

where, N is the buoyancy (or Brunt-Väisälä) frequency (Hocking, 1985; Weinstock, 1981). In the absence of direct measurements of the buoyancy frequency, a representative value of the buoyancy period of 320 s yields the nominal estimate of ε,

$$\varepsilon = 9.8 \times u_{rms}^2 \text{ mW/kg} \tag{5.10}$$

(Nicolls et al., 2010).

The third scenario is incoherent scatter, in the absence of turbulence and presence of MSPs, where the ISR spectrum is the superposition of two Lorentzian lines (or a double-Lorentzian line) with distinct HWHM,

$$S_{0M}(\omega) = A_{0M1}S_L(\omega; \omega_0, \gamma_{0M1}) + A_{0M2}S_L(\omega; \omega_0, \gamma_{0M2}), \tag{5.11}$$

where A_{0M1} is the amplitude of ion-line, γ_{0M1} is the HWHM of the ion-line, A_{0M2} is the amplitude of the meteoric smoke line, and γ_{0M1} is the HWHM of the meteoric smoke-line. The fourth scenario is incoherent scatter, in the presence of both turbulence and MSPs, where the ISR spectrum is the superposition of two Voigt lines (or a double-Voigt line) with distinct HWHM and common RMS width of the turbulent velocity distribution,

$$S_{TM}(\omega) = A_{TM1}S_V(\omega; \omega_0, \gamma_{TM1}, \sigma_{TM}) + A_{TM2}S_V(\omega; \omega_0, \gamma_{TM2}, \sigma_{TM}), \tag{5.12}$$

where A_{TM1} is the amplitude of the turbulence-broadened ion-line, γ_{0M1} is the HWHM of the Lorentzian component of the Voigt ion-line, σ_{TM} is the RMS width of the turbulent Gaussian component, A_{TM2} is the amplitude of the turbulence broadened meteoric smoke line, and γ_{TM2} is the HWHM of the meteoric smoke line. The ion temperature, meteoric smoke particle radius and the turbulent dissipation rate can then be determined from the ion-line Lorentzian HWHM

(γ_0, γ_T, γ_{0M1}, γ_{TM1}) the meteoric smoke line Lorentzian HWHM (γ_{0M2}, γ_{TM2}) and the Gaussian RMS width (σ_T, σ_{TM}) (e.g., Fentzke et al., 2012; Nicolls et al., 2010).

5.3.2. Fitting Algorithm

Our fitting algorithm is based on the NS2SOL adaptive nonlinear least square fitting (Dennis et al., 1981; Dennis & Schnabel, 1996). NS2SOL uses a trust-region approach with a locally constrained optimal (or "hook") step. This method is more reliable than the Levenberg-Marquardt method (Press et al., 1992). The fitting algorithm incorporates one other feature in addition to the NS2SOL algorithm, a scaling of the model so that the algorithm finds fit parameters of similar magnitude that are then rescaled to yield the best fit (Madsen et al., 2004). In the single-Lorentzian (or Lorentzian) fit, we use the HWHM of the observed spectrum as the initial estimate of γ_0. In the double-Lorentzian fit, we use the γ_0 from the Lorentzian fit and $\gamma_0/10$ as an initial estimate of γ_{0M1}, and γ_{0M2}. In the single-Voigt (or Voigt) fit, we use a nominal value of 1 Hz (corresponding to 0.33 m/s) as an initial estimate of σ_T and γ_0 from the Lorentzian fit as an initial estimate of γ_T. In the double-Voigt fit, we use the γ_T from the Voigt fit and $\gamma_T/10$ as an initial estimate of γ_{TM1}, and γ_{TM2}, and σ_T as an initial estimate of σ_{TM}. We fit to the natural logarithm of the Lorentzian and Gaussian width (i.e., γ_0, γ_T, γ_{TM1}, γ_{TM2}, σ_T and σ_{TM}) to avoid converging on negative values. The fitting algorithm estimates all the of the parameters of the model spectra and allows us to avoid the use of a climatological-based estimate of γ_{0M1} that has been used in determining γ_{0M2} in previous ISR-based studies of MSPs (Strelnikova et al., 2007). The fitting algorithm also compensates for the fact that a triangle window is applied to the radar data before the spectrum is calculated (e.g., Harris, 1978). The triangle window reduces the effects of aliasing in the radar measurement. We include the effects of the triangle window in

the spectral fitting so that we are actually fitting to modified (single- and double-) Lorentztian- and Voigt-lines.

5.3.3. Measured Spectra and Spectral Fitting

In Figure 5.1 we plot four examples of PFISR spectra measured on the 22-23 May 2017. The ion-line is offset from zero as it is superimposed on the broad electron-line that appears as a constant offset over the spectral band of the measurement. The measured spectrum appears as the sum of a smooth spectral line and additive white noise. In each spectrum we plot the best fit to each of the four model spectra (i.e., single-Lorentzian, single-Voigt, double-Lorentzian, and double-Voigt). These four spectra have been chosen to show that the PFISR measurements yield spectra consistent with all four scenarios (i.e., absence of turbulence and MSPs (Figure 5.1a), presence of turbulence and absence of MSPs (Figure 5.1b), absence of turbulence and presence of MSPs (Figure 5.1c), and presence of both turbulence and MSPs (Figure 5.1d)). Each fit represents the best fit to the spectral line and the constant offset over the bandwidth of the spectrum due to the electron line (Strelnikova et al., 2007). We characterize the quality of the spectral fitting terms of a Spectral Quality Factor (SQF). The quality of the fitting is based on the magnitude of the residual to the fit. The SQF is defined as the ratio of the power in the model fit to the power in the RMS residual over the bandwidth where the amplitude of the spectral line fit is greater than the RMS residual.

154
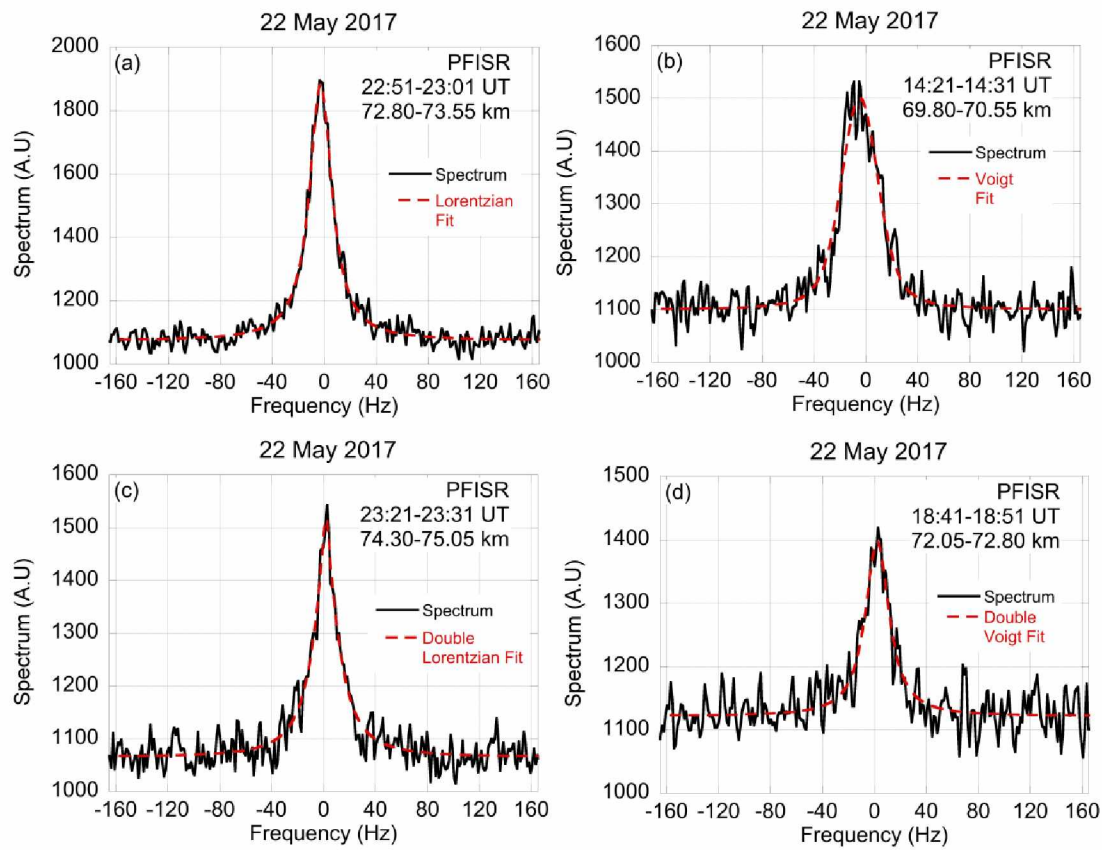
Figure 5.1. Sample spectra measured by PFISR (black) and the corresponding fits with four different models (a) single-Lorentzian, (b) single-Voigt, (c) double-Lorentzian, and (d) double-Voigt. The spectra are plotted in arbitrary units of power.

Table 5.1: PFISR Example Spectra on 22-23 May 2017				
Time (UT)	22:51-23:01	14:21-14:31	23:21–23:31	18:41-18:51
Altitude (km)	72.80-73.55	69.80-70.55	74.30-75.05	72.05-72.80
Spectral Fit				
Spectral Fit Model	Lorentzian	Voigt	Double Lorentzian	Double Voigt
Background (A.U.)	1,070	1,097	1,063	1,120
f_0 (Hz)	-2.9	-4.8	1.8	2.1
$A_{0, T, 0M1, TM1}$ (A.U.)	20,331	13,245	10,275	7,092
$\gamma_{0, T, 0M1, TM1}$ (Hz)	10.0	6.82	12.6	10.0
$\sigma_{T, TM}$ (Hz)	-	10.8	-	2.6
$A_{0M2, TM2}$ (A.U.)	-	-	1036.4	84.2
$\gamma_{0M2, TM2}$ (Hz)	-	-	2.89	2.22
e_{rms} (A.U.)	26.5	31.0	26.9	29.2
SQF	7.5	6.0	5.1	4.1
Derived Properties				
T_{ion} (K)	193	202	204	218
w (m/s)	-0.97	-1.6	0.60	0.69
r_p (nm)	-	-	0.95	0.95
u_{rms} (m/s)	-	3.6	-	0.86
ε (mW/kg)		128		7.3

The measured characteristics of the four model fits are listed in Table 5.1. The ion temperatures are between 190 K and 220 K and MSP radii of approximately 1 nm. The vertical winds are between 1.6 m/s downward and 0.6 m/s upward. The RMS turbulent velocities are between 0.9 and 4 m/s yielding turbulent dissipation rates between 7 mW/kg and 130 mW/kg. The parameters retrieved from these spectra yield reasonable estimates of the ion temperature (T_{ion}) and MSP radius (r_p) (Fentzke et al., 2012; Nicolls et al., 2010). The turbulent RMS velocity (u_{rms}) and energy dissipation rate are similar to those measured by other instruments and techniques (e.g., Lehmacher et al., 2006; Lehmacher & Lübken, 1995; Lübken et al., 2007; Szewczyk et al., 2013; Triplett et al., 2018).

Given that all four scenarios appear in the ISR measurements, we can now use the fitting of the four spectral models to test the hypothesis "is the observed spectrum broadened by turbulence" and thus determine the significance of the turbulence measurement. In order to demonstrate the method, we consider the presence of turbulence in both the presence and absence of MSPs separately. In the absence of MSPs, we distinguish between the Lorentzian and Voigt line shapes, while in the presence of meteoric smoke we distinguish between the double-Lorentzian and double-Voigt line shapes.

We conduct several screening tests before we accept the fitting results for a given spectrum. The width of the spectral line must be greater than the resolution of the spectrum and less than the one-half the bandwidth of the spectrum. The spectral fit yields lines that are too narrow when the measured spectrum is too noisy, and the spectral fit is biased by the background level when the spectrum is too broad.

5.3.4. Uncertainty and Significance of Fit

A given spectral model provides the best fit to a given spectrum if the RMS residual of that fit is significantly less than the RMS residual of the alternative model spectral fit. The RMS residual to a model i, e_{RMSi}, is significantly less than RMS residual to a model j, e_{RMSj}, when it is less by a margin of the uncertainty in the residuals, Δe_{RMS},

$$e_{RMSi} < e_{RMSj} - \Delta e_{RMS}. \qquad (5.13)$$

This comparison of the residual in non-turbulent (Lorentzian or double-Lorentzian) and turbulent (Voigt or double-Voigt) model spectra fit is the basis of our hypothesis test. We conclude that a spectrum provides a significant measurement of turbulence if the residual associated with a fit to a turbulent spectral model is significantly less than that associated with a non-turbulent spectral model. Thus we consider the retrievals in three levels of increasing significance; all turbulent fits, weakly significant turbulent fits where the turbulent fit has a smaller residual than the non-turbulent fit ($e_{RMSi} < e_{RMSj}$), and significant turbulent fits where the turbulent fit has a significantly smaller residual than the non-turbulent satisfying Equation 5.13.

Having established the best fit to the measured spectrum, we now use a Monte Carlo technique to determine the uncertainty in the fit, determine the significance of the fit, and the likelihood of the detecting turbulence in the atmosphere. We generate synthetic spectra as the sum of a deterministic line shape, background, and an additive white noise. We model the white noise as a zero-mean Normal random variable with standard deviation equal to the RMS residual of the measured spectrum. We conduct repeated fits to these synthetic spectra to determine both the uncertainty in the fit and the significance of the fit. The uncertainty is taken as the sample

158

standard deviation in the estimated turbulent parameters. The significance of a given spectrum is determined by fitting the synthetic spectrum to two competing models and determining the probability that the spectrum is best fit by either one of the two models. We can then determine the confidence in the turbulent detection given by the probability that turbulence is present when a turbulent spectrum (Voigt or double-Voigt) is detected, P(T/V) (Puga et al., 2015). From Bayes theorem, P(T/V) is given by,

$$P(T/V) = P(V/T)\frac{P(T)}{P(V)}, \tag{5.14}$$

where, P(V/T) is the probability of a best fit by a Voigt (or double-Voigt) line shape given a turbulent spectrum, P(T) is the probability that turbulence is present, and P(V) is the probability that any spectrum is best fit by a Voigt (or double-Voigt) line shape. P(V) is given by,

$$P(V) = P(V/T)P(T) + P(V/\overline{T})P(\overline{T}), \tag{5.15}$$

where, $P(V/\overline{T})$ is the probability that a non-turbulent spectrum (Lorentzian or double-Lorentzian) is best fit by a Voigt (or double Voigt) line shape, and $P(\overline{T})$ is the probability that turbulence is not present. $P(\overline{T})$ is given by,

$$P(\overline{T}) = 1 - P(T). \tag{5.16}$$

P(V/T) is the probability of a true positive and $P(V/\overline{T})$ is the probability of a false positive detection by the radar. We determine P(V/T) and $P(V/\overline{T})$ from our Monte Carlo simulation as the fraction of trials where a turbulent spectrum or non-turbulent spectrum with noise is best fit by a Voigt (or double-Voigt) line shape respectively. We illustrate the method based on the spectrum shown in Figure 5.1b. The spectrum is best fit by a Voigt spectrum and the fit is

significantly better than the Lorentzian fit. We generate a synthetic turbulent spectrum using the Voigt fit to the spectrum and a synthetic non-turbulent spectrum using the Lorentzian fit to the spectrum. We then conduct 16,384 trials where we fit Voigt and Lorentzian spectra to the synthetic spectra with additive white noise and determine how often the spectrum is best fit by the different spectral models. We plot the results in Figure 5.2. We find that the Voigt fit to the turbulent spectrum is significantly better (i.e., the residuals to the Lorentzian fit and to the Voigt fit differ by more than the uncertainty in the residuals) in 5,875 of the trials, while the Lorentzian fit is never significantly better than the Voigt fit, and the results are ambiguous (i.e., the residuals to the Lorentzian fit and to the Voigt fit differ by less than the uncertainty in the residuals) in 10,509 trials. $P(L/T)$ represents the probability of a false negative. We determine $P(V/T)$ as 5,875/16,384 or 36% and $P(L/T)$, by rounding up from 0 to 1 trial in 16,384 trials as 0.01%. In the fitting to a non-turbulent spectrum in 16,384 trials we find that neither the Voigt or Lorentzian fits are better and the results are ambiguous. $P(L/\overline{T})$ represents the probability of a true negative. We determine both $P(V/\overline{T})$, and $P(L/\overline{T})$ by rounding up from 0 to 1 trial in 16,384 trials as 0.01%. For these values of $P(V/T)$ and $P(V/\overline{T})$, we find that the confidence in the detection, $P(T/V)$, is greater than 99% when $P(T)$ is 3% or more, and greater than 99.9% when $P(T)$ is 22% or more. The high values of $P(T/V)$ reflect the very low values of $P(V/\overline{T})$. This Bayesian analysis shows that for the PFISR spectrum shown in Figure 5.1b the statistically significant detection of turbulence is physically significant.
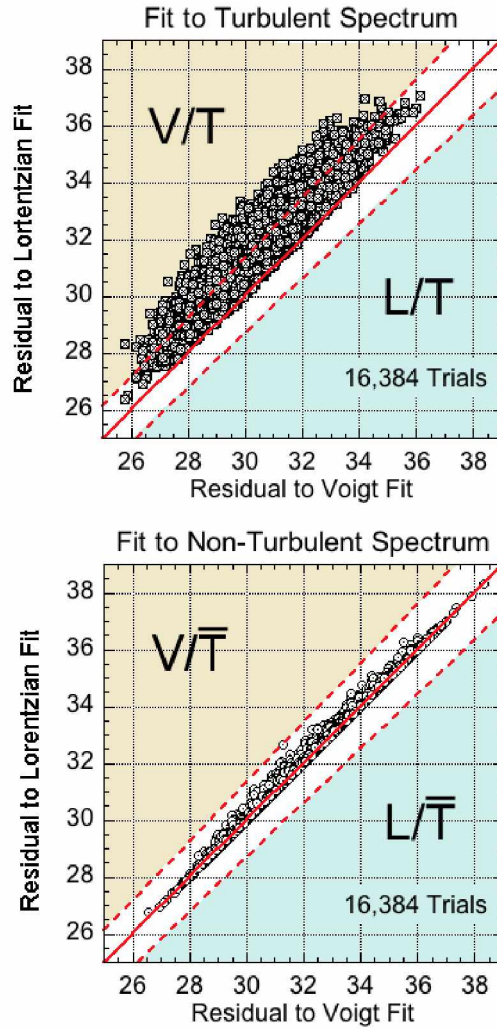
Figure 5.2. Plot of Lorentzian fitting residual against Voigt fitting residual to 16,384 synthesised Voigt spectra (top) and Lorentzian spectra (bottom). The synthesised spectra are constructed based spectrum measured by PFISR between 14:21-14:31 UT and 69.80-70.55 km.

5.4. PFISR Turbulence Measurements

5.4.1. Turbulence measurements on 22-23 May 2017

On 22-23 May 2017, PFISR operated with a single vertical beam. We average the individual ISR spectra over 10 minutes to yield 4,320 spectra between 70 km and 90 km. In the analysis without MSPs we distinguish between Lorentzian and Voigt spectra. We find 3,295 spectra that yield Voigt fits, 1,780 yield a lower RMS residual in the Voigt fits than the Lorentzian fits. These spectra have SQF values between 1.0 and 22.0 with an average value of 3.2. We find five spectra near 71 km that yield significant detection of turbulence with ion temperatures between 120 K and 320 K. These spectra have SQF values between 6.0 and 7.4 with an average value of 6.6. In the analysis with MSPs we distinguish between double-Lorentz and double-Voigt spectra. We find 1867 spectra that yield double-Voigt fits, 797 yield a lower RMS residual in the double-Voigt fits than the double-Lorentzian fits. These spectra have SQF values between 1.1 and 20.4 with an average value of 4.0. We find four spectra near 71 km that yield significant detection of turbulence with ion temperatures between 120 K and 320 K. These spectra have SQF values between 6.0 and 7.7 with an average value of 6.9. We plot all the PFISR estimates of the Gaussian width and RMS turbulent velocity with altitude in Figure 5.3. We tabulate the significant turbulent estimates in Table 5.2. In Figure 5.3 we identify the retrievals by their level of significance and plot the individual retrievals with altitude as well as the profile of the RMS mean. We consider the retrievals from all spectra (grey circles and dashed black line), the retrievals that are weakly significant (blue circles and dashed blue line), and the significant retrievals (red square).

Figure 5.3. The Gaussian width and RMS turbulent velocity measured by PFISR on 22-23 May 2017 UT. The plot shows the retrievals from all spectra (grey circles) and the RMS profile (dashed black line), the weakly significant retrievals (blue circles) and the RMS profile (dashed blue line), and the significant retrievals (red squares).

Table 5.2: Turbulence measured by PFISR					
Time(UT)	Altitude (km)	σ_T (Hz)	u_{rms} (m/s)	ε (mW/kg)	SQF
22-23 May 2017 Voigt					
12:11-12:21	71.30-72.05	11.0±1.2	3.7±0.4	131±29	7.0
12:11-12:21	72.05-72.80	11.1±1.6	3.7±0.6	135±39	6.1
14:21-14:31	69.80-70.55	10.8±1.6	3.6±0.5	128±36	6.0
22:51-23:01	70.55-71.30	11.9±1.4	4.0±0.5	155±36	6.6
22:51-23:01	71.30-72.05	9.7±1.0	3.2±0.4	102±22	7.4
Average	71.4	10.9	3.6	130	6.6
22-23 May 2017 Double-Voigt					
14:21-14:31	69.80-70.55	10.8±1.6	3.6±0.5	128±40	6.0
22:51-23:01	70.55-71.30	11.9±1.4	4.0±0.5	155±37	6.6
22:51-23:01	71.30-72.05	9.7±1.3	3.2±0.4	103±29	7.4
23:11-23:21	71.30-72.05	10.3±1.0	3.4±0.3	115±22	7.7
Average	71.1	10.7	3.6	125	6.9
Voigt 23 April 2008					
22:13-23:23	73.55-74.30	9.5±1.4	3.2±0.5	99±29	6.1

For the significant estimates with no MSPs, the RMS turbulent velocities are between 3.2 and 4.0 m/s with an RMS value of 3.6 m/s. The uncertainty in the estimates of the RMS turbulent velocities are between 11 and 15%. The corresponding turbulent dissipation rates are between 103 and 155 mW/kg with an average value of 130 mW/kg. We calculate the RMS values of the turbulent profiles over the same altitudes as the significant retrievals. The significant turbulent estimates are larger than the RMS of all estimates (2.1 m/s, 45 mW/kg) and those estimates where the turbulent fit is better (2.8 m/s, 66 mW/kg). For the estimates with MSPs, the RMS turbulent velocities are also between 3.2 and 4.0 m/s with an RMS value of 3.6 m/s. The uncertainties in the estimates of the RMS turbulent velocities are between 10 and 15%. The corresponding turbulent dissipation rates are between 103 and 155 mW/kg with an average value of 125 mW/kg. The significant turbulent estimates are larger than the RMS of all estimates (2.2 m/s, 46 mW/kg), and those estimates where the turbulent fit is better (2.6 m/s, 67 mW/kg). For retrievals in both the absence and presence of MSPs, where the turbulent fit is better than the non-turbulent fit, the RMS turbulent velocities increase with altitude with scale height of 12 km – 18 km.

5.4.2. Turbulence measurements on 23 April 2008

On 23 April 2008, PFISR operated sequentially with seven beams. We average the individual ISR spectra from the vertical beam over 10 minutes to yield 1809 spectra between 70 km and 90 km. These measurements are associated with high electron densities that yielded large amplitudes in the ion-lines of the spectra (Nicolls et al., 2010). The amplitudes of the ion-lines in the spectra are on average a factor of 8 larger than on May 2017. The RMS residuals are on average $\sqrt{7}$ times larger than the residuals in May 2017 consistent with the fact that these

spectra include seven times fewer pulse spectra. The SQF values are on average about 20% larger than the values on May 2017.

In the analysis without MSPs we distinguish between Lorentz and Voigt spectra. We find 1,180 spectra that yield Voigt fits, 497 yield a lower RMS residual in the fit to a turbulent spectrum than a non-turbulent spectrum. These spectra have SQF values between 1.0 and 11.5 with an average value of 4.0. We find one spectrum at 73.9 km that yields a significant detection of turbulence with ion temperatures between 120 K and 320 K. This spectrum has an SQF of 6.1. In the analysis with MSPs we distinguish between double-Lorentz and double-Voigt spectra. We find 735 spectra that yield double-Voigt fits, 357 yield a lower RMS residual in the fit to a turbulent spectrum than a non-turbulent spectrum. These spectra have SQF values between 1.2 and 10.4 with an average value of 4.0. We find no spectra that yield significant detection of turbulence with ion temperatures between 120 K and 320 K. We plot the PFISR estimates of the Gaussian width and RMS turbulent velocity with altitude in Figure 5.4. We present this significant estimate in Table 5.2.
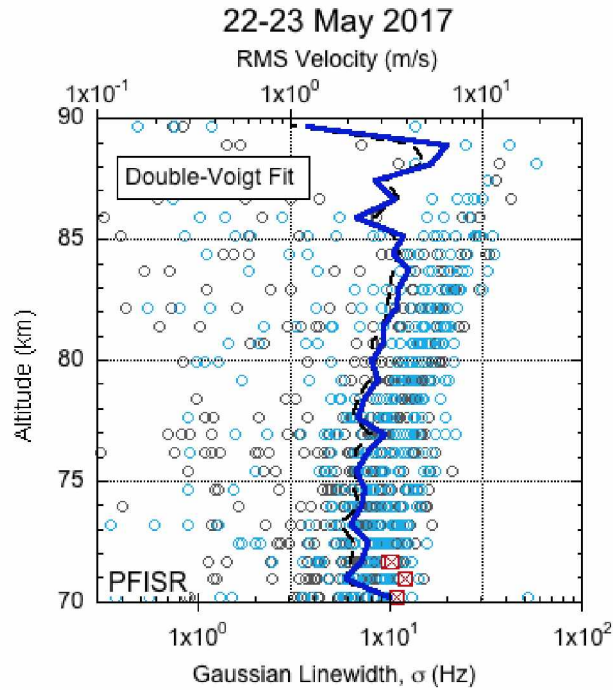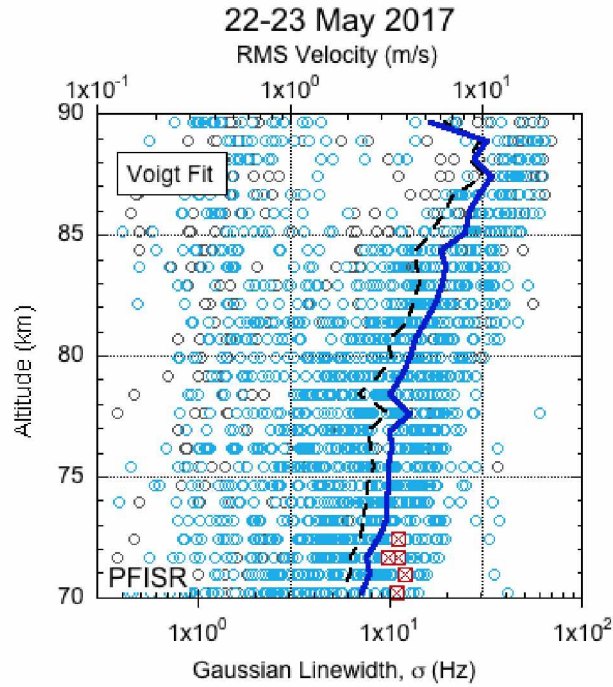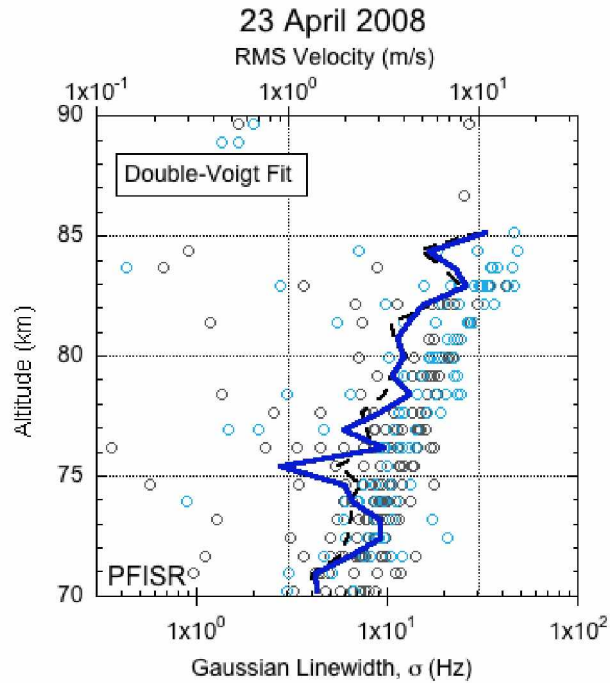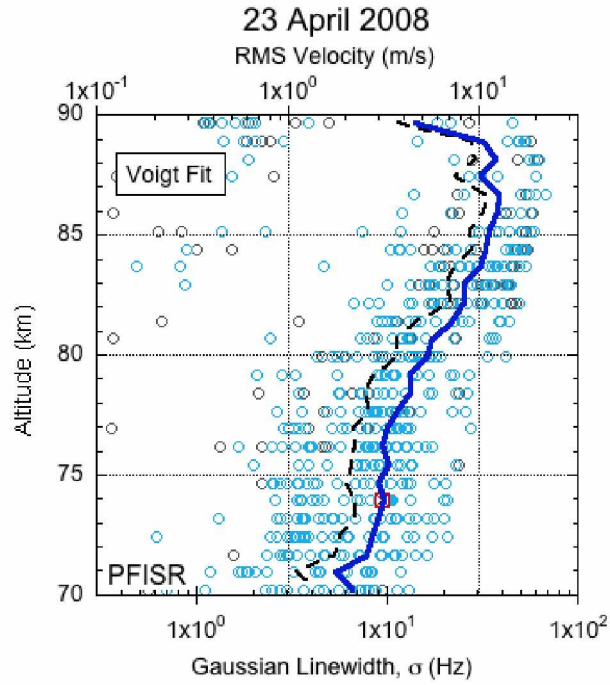
Figure 5.4. The Gaussian width and RMS turbulent velocity measured by PFISR on 23 April 2008 UT. The plot shows the retrievals from all spectra (grey circles) and the RMS profile (dashed black line), the weakly significant retrievals (blue circles) and the RMS profile (dashed blue line), and the significant retrievals (red squares).

For the significant estimate with no MSPs, the RMS turbulent velocity is 3.2 m/s. The uncertainty in the estimates of the RMS turbulent velocity is 15%. The corresponding turbulent dissipation rate is 99 mW/kg. Again we find that the estimates of the turbulent strength increases as we increase the significance of the estimates. The significant turbulent estimates are larger than the RMS of all estimates (2.2 m/s, 49 mW/kg), and similar to those estimates where the turbulent fit is better (3.2 m/s, 99 mW/kg). For retrievals in both the absence and presence of MSPs, where the turbulent fit is better than the non-turbulent fit, the RMS turbulent velocities increase with altitude with scale height of 6 km – 8 km. Our estimates compares with the median estimate of 40 mW/kg at 74 km based on single-Voigt fits to all retrievals that also increase with altitude (Nicolls et al., 2010).

5.4.3. Significance of turbulence detection

We determine the uncertainty and significance of the turbulence measurements using the Monte Carlo-based approach. We report the uncertainties as the sample standard deviation in the simulations in section 3.2 and Table 5.2. We determine $P(V/T)$ and $P(V/\overline{T})$ for each measurement and tabulate them in Table 5.3. We find that values of $P(V/T)$ vary between 31% and 84% for the Voigt fits and between 39% and 96% for the double-Voigt fits. For $P(V/\overline{T})$ we report a value of 0.01% as we find no trials that yield a Voigt (or double-Voigt) best fit to a Lorentzian (or double-Lorentzian) spectrum. For both Voigt and double-Voigt fits the value of $P(V/T)$ increases with the quality of the spectrum. We plot the values of $P(V/T)$ with Spectral Quality Factor (SQF) in Figure 5.5. The values are correlated with values of the Pearson correlation coefficient of greater than 90% showing that as the quality of the measurements improves the probability of detecting turbulence increases.

Time(UT)	Altitude (km)	P(V/T) (%)	P(V/$\bar{\text{T}}$) (%)
22-23 May 2017			
Voigt			
12:11-12:21	71.30-72.05	79	0.01
12:11-12:21	72.05-72.80	31	0.01
14:21-14:31	69.80-70.55	36	0.01
22:51-23:01	70.55-71.30	74	0.01
22:51-23:01	71.30-72.05	84	0.01
Average	71.4	61	0.01
Double-Voigt			
14:21-14:31	69.80-70.55	39	0.01
22:51-23:01	70.55-71.30	75	0.01
22:51-23:01	71.30-72.05	83	0.01
23:11-23:21	71.30-72.05	96	0.01
Average	71.1	73	0.01
23 April 2008			
Voigt			
22:13-23:23	73.55-74.30	31	0.01

Table 5.3: Probability of turbulent detection by PFISR

We use the Bayesian approach to estimate the physical significance of the retrievals. We determine the probability of a true detection that turbulence is present given the detection of a Voigt or double-Voigt spectrum, P(T/V), or the minimum value of a true positive, P(V/T), of 31%. We find that when P(T) is greater than 4%, P(T/V) is greater than 99%, and when P(T) is greater than 25%, P(T/V) is greater than 99.9%. This high level of confidence in the turbulent detections is due to the very low values of the probability of a false negative, $P(\overline{V/T})$.
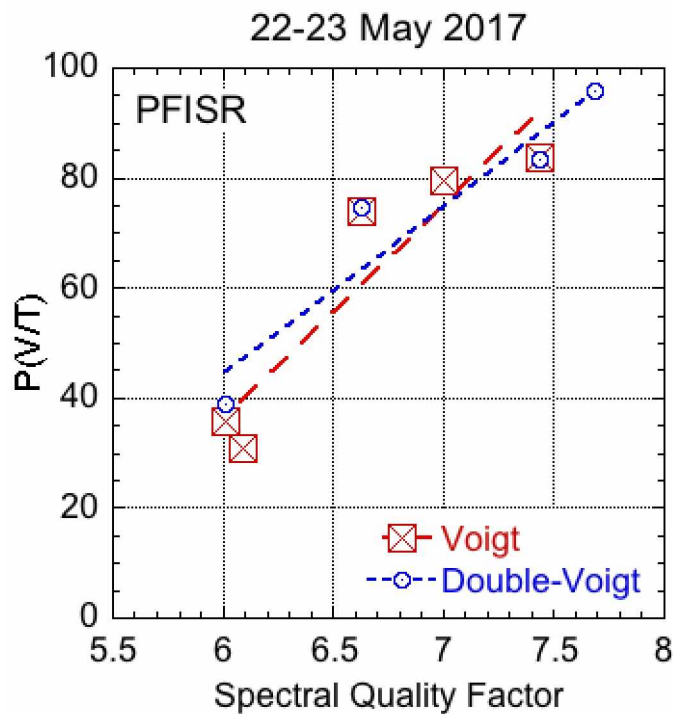
Figure 5.5. The values of P(V/T) plotted against the Spectral Quality Factor (SQF) for the significant turbulent spectra measured on 22-23 May 2017. The results for the Voigt fits are plotted in red (squares with crosses) and the double-Voigt fits are plotted in blue (circles with dots). The dashed lines are fits to the data with Pearson correlation coefficients of greater than 90%.

5.5. Summary and Conclusions

We have conducted a retrieval of turbulent parameters in the mesosphere (70-90 km) from PFISR based on a hypothesis test. The investigation highlights the challenge in determining estimates of turbulence in the physically diverse ionospheric environment. We distinguish between the presence and absence of turbulence based on fitting Voigt-based and Lorentzian-based line shapes to the radar spectra. We also allow for the presence and absence of MSPs in the retrievals. We analyzed data from two observation periods in April 2008 and May 2017. We find examples of PFISR spectra showing both the presence and absence of turbulence and the presence and absence of MSPs in the upper mesosphere.

Based on the analysis of these two observation periods we find that relatively few of the radar measurements yield significant measurements of turbulence. The significant estimates of turbulence have a strength that is over a factor of two larger than the average of the estimates from all of the radar measurements. The probability of true positives increases with the quality factor of the spectrum. The method yields significant measurements of turbulence with probabilities of true positives of greater than 30% and false positives less than 0.01%. The negligible probability of false positives yields high confidence in the significant detections.

There are more significant detections in the measurements in May 2017 observations than in April 2008 suggesting that the instrumental noise is more important than the signal amplitude in determining the ability of the radar to discriminate between turbulent and non-turbulent echoes. The new ISR EISCAT 3D with peak power ~10 MW and low noise is currently being constructed in Scandinavia (McCrea et al., 2015). The combination of this hypothesis-testing

retrieval method and the measurement capabilities of EISCAT 3D will facilitate more comprehensive measurements of turbulence in the upper mesosphere and lower thermosphere.

Chapter 6. Summary and conclusions

In this study we have extended the scope of previous studies of waves and turbulence in the Arctic middle atmosphere at Poker Flat Research Range (PFRR), Chatanika, Alaska in several ways. We have developed and deployed a new sodium resonance wind-temperature lidar (SRWTL) at the Lidar Research Laboratory (LRL) at PFRR and conducted an initial series of observations. We have developed a consistent analysis of resonance and Rayleigh lidar data to conduct studies of turbulent transport in the presence of instabilities in the middle atmosphere. We have developed a hypothesis-based analysis of radar measurements of turbulence in the measurements. This series of studies has investigated wave-turbulence interactions as well as assess the ability of current lidar and radar systems to detect and characterize waves and turbulence.

We deployed a SRWTL system at LRL-PFRR as a two-beam system, making measurements in the vertical and 20° off-vertical to the north. We have conducted a series of observations measuring sodium density, temperature, vertical wind, and meridional wind in both daytime and nighttime. We have analyzed the quality of the lidar measurements and found that at a resolution of five minutes and one km resolution, the relative error of the temperature and wind measurements are 1% and 15%, respectively at night and 10% and 60%, respectively in daytime. We have compared the performance of the PFRR-SRWTL system with other SRWTL systems. We found that the transmitter of the system is operating at an efficiency comparable to other SRWTLs in terms of the CW seeding of the pulse dye amplifier but appears to be operating at an efficiency lower than other SRWTLs in terms of the pumping of the pulse dye amplifier. We found that vertical channel is operating at an efficiency close to other SRWTLs. However, the

173

north channel is operating at a lower efficiency, about 60% of the efficiency of the vertical channel and other SRWTLs. Based on these analyses we will focus on improving the pump efficiency of the pulse dye amplifier by upgrading the optics in the pulse dye amplifier and improving the efficiency of the north beam receiver through optimizing the placement of the optical fiber in the telescope.

We have investigated instabilities and turbulence, identifying a series of test cases where convective instabilities are found in the presence of with near-adiabatic and super-adiabatic lapse rates and signatures of overturning in the sodium layer. We have identified the instabilities based on the temperature, potential temperature, and mixing ratio. We find that the instabilities are consistently detected in the potential temperatures derived from both the SRWTL and the RDTL. We have developed a turbulent transport model based on material continuity of the sodium mixing ratio that yields more accurate estimates of the transport than a previous model. Based on this model we have estimated values of the turbulent eddy diffusion coefficients, K, and energy dissipation rates, ε. We compare our estimates with other rocket borne measurements in the Arctic in Figure 6.1. We find that our values of K (~ 1000 m^2/s) are larger than typically reported while the values of ε ($\sim$10-100 mW/kg) are similar and are in good agreement with the values reported by ionization gauge measurements at PFRR. The combination of reasonable values of typical values of ε and large values of K reflects the fact that the measurements are made in regions of convective instability where turbulence with relatively small amounts of energy can achieve a large amount of mixing.
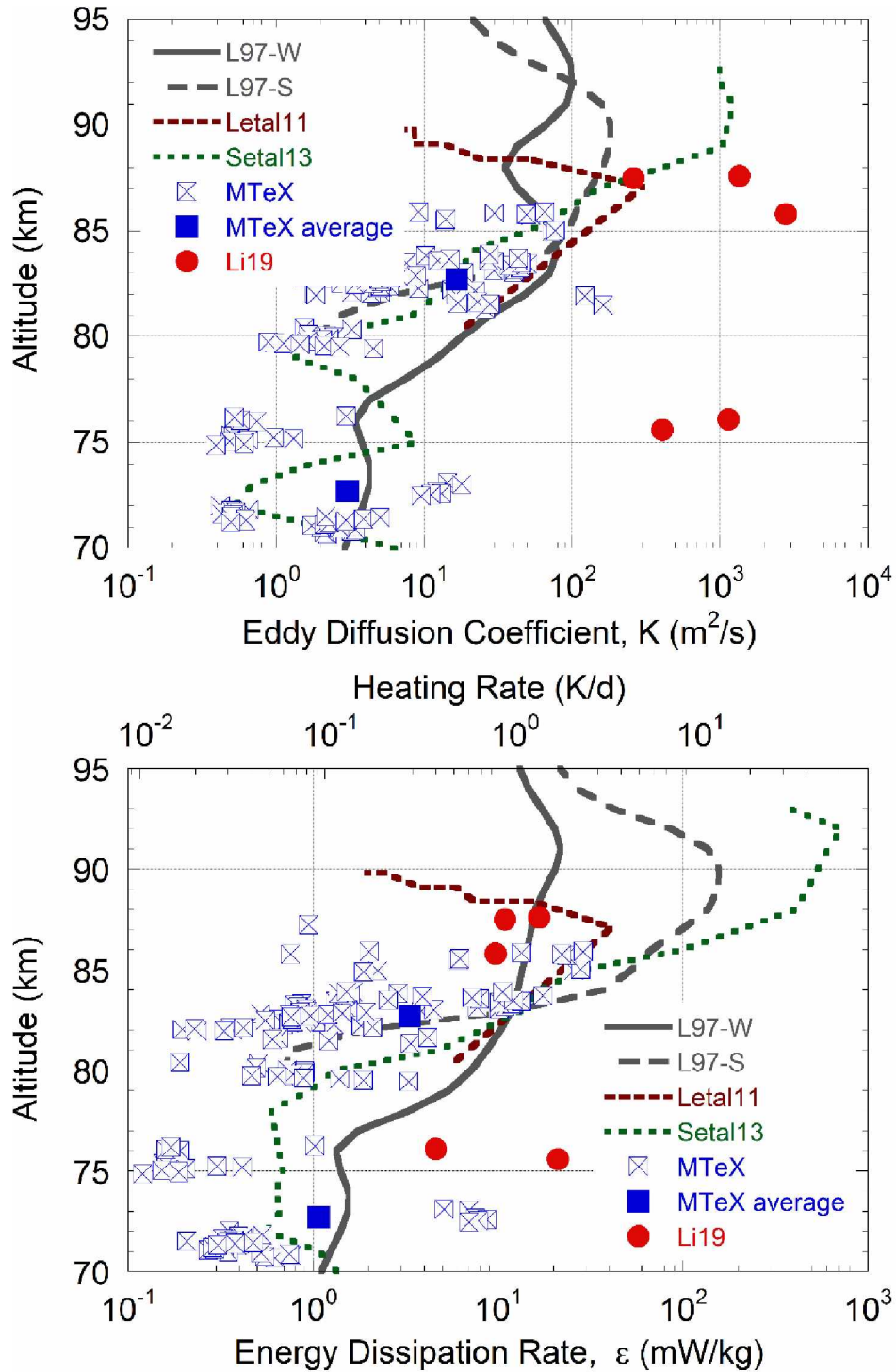
Figure 6.1. Summary of turbulent eddy diffusion coefficients (top panel) and energy dissipation rate (bottom panel) measured in the Arctic MLT region (see Chapter 1 for details). Values presented in this study are marked by red circles.

We have also investigated the role of gravity waves in generating turbulence. We find that upwardly propagating gravity waves accompany the instabilities. In the presence of instabilities, we find that the gravity waves are dissipating as they propagate upward, and when the environment is less stable, the GWs are more dissipated. We estimate the wave energy dissipation rate available to drive turbulence. We find that the wave energy dissipation rate available can be lower or larger than the turbulent energy dissipation rate. However, the estimates of the energy dissipation rates are very sensitive to the estimates of the depth of the instabilities. We find depths from the lidar measurements on the order of kilometers. If these depths were sub-kilometer, as suggested by high-resolution turbulence measurements, then our estimates of the wave energy dissipation rates would increase while our estimates of the turbulent energy dissipation rates would decrease.

The SRTL is scheduled for a series of upgrades. Based on our performance analysis, the transmitter and receiver will be optimized to provide higher signal measurements. Furthermore, a third channel will be incorporated in the system to provide measurements of the zonal wind. This will allow us to investigate wind-driven instabilities as well as provide a complete characterization of gravity waves.

In the study of turbulence with the Poker Flat Incoherent Scatter Radar (PFISR), we conducted a retrieval of turbulent parameters in the mesosphere based on a hypothesis test approach. Our hypothesis test uses the shape of the frequency spectra of the radar signal to distinguish between both the presence and absence of turbulence and the presence and absence of meteoric smoke particles. This avoids the reliance on visual inspection that has characterized earlier studies. We find that our method is robust to false negatives, and we identify statistically significant

estimates of turbulence. We find that the estimates of turbulent activity are higher by a factor of two when only the significant estimates are considered than when all estimates are considered. However, based on the analysis, we find that relatively few of the PFISR measurements yield significant measurements of turbulence. Our analyses show that the sensitivity of the radar to measure turbulence is a function of the quality of the measured spectrum and not just related to the strength of the radar signal. The new ISR EISCAT 3D with high peak power and low noise is under construction. The combination of this hypothesis-testing retrieval method and the measurement capabilities of EISCAT 3D will facilitate more comprehensive measurements of turbulence in the upper mesosphere and lower thermosphere.

This page intentionally left blank

Appendix A. Gravity wave theory

A1. Linear theory of gravity wave

The linear inviscid theory of GWs describes them as small perturbations from stably stratified background atmosphere that is only varying in the vertical. In this section, we will first solve the linearized forms of the fundamental equations that follow from the conservation of momentum, mass, and energy (e.g, Holton & Hakim, 2013):

$$\frac{du}{dt} - fv + \frac{1}{\rho}\frac{\partial p}{\partial x} = X, \tag{A1}$$

$$\frac{dv}{dt} + fu + \frac{1}{\rho}\frac{\partial p}{\partial y} = Y, \tag{A2}$$

$$\frac{dw}{dt} + \frac{1}{\rho}\frac{\partial p}{\partial z} + g = 0, \tag{A3}$$

$$\frac{1}{\rho}\frac{d\rho}{dt} + \frac{\partial u}{\partial x} + \frac{\partial v}{\partial y} + \frac{\partial w}{\partial z} = 0, \tag{A4}$$

$$\frac{d\theta}{dt} = Q, \tag{A5}$$

$$\theta = \frac{p}{\rho R}\left(\frac{p_0}{p}\right)^{\kappa}, \tag{A6}$$

where d/dt represents a total derivative; (u, v, w) is the velocity vector of the atmosphere; $f = 2\Omega sin\phi$ is the Coriolis parameter, where Ω is the rotation rate of the earth, and ϕ is the latitude; p is the pressure; θ is the potential temperature; $X, Y \ and \ Q$ represent unspecified forces and heating sources; R is the ideal gas constant, and $\kappa = c_p/c_v$ is the ratio of specific heats at constant pressure and volume. Equations A1-A6 can be linearized by assuming that the total fields are superposition of a mean steady state flow and a perturbation ($q = \bar{q} + q'$), q is any

flow variable, $\bar{q}$ is the mean state, and q' is the perturbation, and the pressure and density perturbations are much smaller than the mean state. It is also assumed that all the high order perturbation terms can be ignored and that there are now external force or heating. The background state is a horizontally uniform hydrostatic flow with background wind ($\bar{u}, \bar{v}, 0$), $\bar{\rho} = \rho_0 \, exp(-(z - z_0) \, / \, H)$, where H is the scale height, and ρ_0 is the density at a reference height z_0. The linearized equations can be written as

$$\frac{Du'}{Dt} + w'\frac{\partial \bar{u}}{\partial z} - fv' + \frac{\partial}{\partial x}\left(\frac{p'}{\bar{\rho}}\right) = 0, \tag{A7}$$

$$\frac{Dv'}{Dt} + w'\frac{\partial \bar{v}}{\partial z} + fu' + \frac{\partial}{\partial y}\left(\frac{p'}{\bar{\rho}}\right) = 0, \tag{A8}$$

$$\frac{Dw'}{Dt} + \frac{\partial}{\partial y}\left(\frac{p'}{\bar{\rho}}\right) - \frac{1}{H}\left(\frac{p'}{\bar{\rho}}\right) + g\frac{p'}{\bar{\rho}} = 0, \tag{A9}$$

$$\frac{D}{Dt}\left(\frac{\theta'}{\bar{\theta}}\right) + w'\frac{N^2}{g} = 0, \tag{A10}$$

$$\frac{\rho'}{\bar{\rho}} + \frac{\partial u'}{\partial x} + \frac{\partial v'}{\partial y} + \frac{\partial w'}{\partial z} - \frac{w'}{H} = 0, \tag{A11}$$

$$\frac{\theta'}{\bar{\theta}} = \frac{1}{c_s^2}\left(\frac{p'}{\bar{\rho}}\right) - \frac{\rho'}{\bar{\rho}}, \tag{A12}$$

where D/Dt is the linearized form of material derivative

$$\frac{D}{Dt} = \frac{\partial}{\partial t} + \bar{u}\frac{\partial}{\partial x} + \bar{v}\frac{\partial}{\partial y}, \tag{A13}$$

and $N = \sqrt{g\partial \, ln \, \theta \, / \, \partial z}$ is the buoyancy frequency. Assume that the background winds and N only vary slowly in the vertical over a wave cycle, and the solutions take the form of monochromatic waves

180

$$\left(u', v', w', \frac{\theta'}{\bar{\theta}}, \frac{p'}{\bar{p}}, \frac{\rho'}{\bar{\rho}}\right) = (\tilde{u}, \tilde{v}, \tilde{w}, \tilde{\theta}, \tilde{p}, \tilde{\rho}) \cdot exp[i(kx + ly + mz) - \omega t + \frac{z}{2H}], \text{(A14)}$$

where (k, l, m) are the wave number components, and ω is the ground-relative frequency. Substitution into equations A7-A12 yields

$$-i\hat{\omega}\tilde{u} - f\tilde{v} + ik\tilde{p} = 0, \tag{A15}$$

$$-i\hat{\omega}\tilde{v} + f\tilde{u} + ik\tilde{p} = 0, \tag{A16}$$

$$-i\hat{\omega}\tilde{w} + (im - \frac{1}{2H})\tilde{p} = -g\tilde{\rho}, \tag{A17}$$

$$-i\hat{\omega}\tilde{\theta} + (N^2/g)\tilde{w} = -g\tilde{\rho}, \tag{A18}$$

$$-i\hat{\omega}\tilde{\rho} + ik\tilde{u} + il\tilde{v} + (im - \frac{1}{2H})\tilde{w} = 0, \tag{A19}$$

$$\tilde{\theta} = \tilde{p}/c_s^2 - \tilde{\rho}, \tag{A20}$$

where $\hat{\omega} = \omega - k\bar{u} - l\bar{v}$ is known as the intrinsic frequency, which is the frequency that would be observed in a frame of reference moving with the background wind. These equations can be combined to form a single equation. Demanding the imaginary coefficients of this equation to be zero, and assuming $c_s \to \infty$, we can yield the GW dispersion relation

$$\hat{\omega}^2 = \frac{N^2(k^2 + l^2) + f^2\left(m^2 + \frac{1}{4H^2}\right)}{k^2 + l^2 + m^2 + \frac{1}{4H^2}}, \tag{A21}$$

or for the vertical wavenumber as

$$m^2 = \frac{(k^2 + l^2)(N^2 - \hat{\omega}^2)}{(\hat{\omega}^2 - f^2)} - \frac{1}{4H^2}. \tag{A22}$$

The dispersion relation relates the intrinsic frequency $\hat{\omega}$ and the wavenumbers and reveals important properties of GWs. For the GWs to propagate, the wave numbers must be real, thus the intrinsic frequency is limited in the range $f < \hat{\omega} < N$. Given the vertical wavenumber, m, we can derive the horizonal wavenumber, h, from equation A22 as

$$h = \sqrt{k^2 + l^2} = \frac{\left(m^2 + \frac{1}{4H^2}\right)(\hat{\omega}^2 - f^2)}{(N^2 - \hat{\omega}^2)}.$$

(A23)

From equations A15-A20, we can also derive the relations between amplitudes of the different variables (known as the polarization relations). The following polarization relations are particularly useful in this study:

$$\tilde{p} = \frac{g\left(\frac{\hat{\omega}^2}{N^2} - 1\right)}{\left(\frac{\hat{\omega}^2}{N^2}\frac{g}{c_s^2} + im - \frac{1}{2H}\right)} \cdot \tilde{\rho},$$

(A24)

$$\tilde{T} = \frac{1}{R\bar{T}}\tilde{p} - \tilde{\rho},$$

(A25)

$$\tilde{v} = \frac{\hat{\omega}l - ikf}{\hat{\omega}^2 - f^2}\tilde{p},$$

(A26)

$$\tilde{u} = \frac{\hat{\omega}k + ilf}{\hat{\omega}^2 - f^2}\tilde{p},$$

(A27)

where $\tilde{T} = T'/\bar{T}$ is the relative temperature perturbation. In this study, the frequency relative to the ground (ω), the vertical wavenumber (m), the amplitude of the temperature perturbation ($\tilde{T}$), density perturbation ($\tilde{\rho}$) and meridional wind ($\tilde{v}$) of the GWs are directly derived from the lidar measurements. However, due to the lack of zonal measurements ($\tilde{u}$), the propagation direction of the waves can not be determined without any assumptions. In this study, we assume that the background wind is zero, namely the intrinsic frequency $\hat{\omega} = \omega$.

From equations A26 and A27, we can derive the amplitude of horizontal wind velocity, $\tilde{u}_H$, as

$$\tilde{u}_H = \sqrt{\tilde{u}^2 + \tilde{v}^2} = \frac{\sqrt{(\hat{\omega}^2 + f^2)h^2}}{\hat{\omega}^2 - f^2}\,\tilde{p}. \tag{A28}$$

We then use the measured value of $\tilde{v}$ to solve for $\tilde{u}$, k and l.

The specific potential energy of the wave can be derived from the amplitude of temperature as

$$PE = \frac{1}{2}\frac{g^2}{N^2}\tilde{T}^2. \tag{A29}$$

The vertical group velocity of the wave can be expressed as

$$c_{gz} = -\frac{m(\hat{\omega}^2 - f^2)}{\hat{\omega}(k^2 + l^2 + m^2 + \frac{1}{4H^2})}. \tag{A30}$$

From equations A23 and A30, we can derive

$$c_{gz} = -\frac{m(\hat{\omega}^2 - f^2)(N^2 - \hat{\omega}^2)}{\hat{\omega}(m^2 + \frac{1}{4H^2})(N^2 - f^2)}. \tag{A31}$$

Under the assumption that $f^2 \ll \hat{\omega}^2 \ll N^2$, which is valid for medium frequency waves with period in the range of ~1h to 7 h, equation A31 can be written as

$$c_{gz} = -\frac{m\hat{\omega}}{(m^2 + \frac{1}{4H^2})}, \tag{A32}$$

The assumption of zero background wind is not a strong assumption and induces significant uncertainties in the characteristics of the waves. For instance, for a wave with period of 5 hours, assuming typical values of background wind, 50 m/s, and horizonal wavelength of 1000 km, the possible range of intrinsic period is 2.6 h to 13.2 h. Notice that the wave is still a inertial period wave and this uncertainty in intrinsic frequency do not affect our estimate of the specific

183

potential of the wave (equation A29). However, this introduces an uncertainty in the vertical group velocity (equations A31 and A32).

Appendix B. Steerable Rayleigh lidar system to support rocket investigation

B1. The Super Soaker investigation

The Transport, Chemistry, and Energetics of Water in the Mesosphere and Lower Thermosphere and Implications for Polar Mesospheric Cloud Occurrence (or Super Soaker) experiment was a rocket investigation to study a controlled water release in the MLT region, and its influence to the formation and occurrences of Polar Mesospheric Clouds (PMCs, also known as Noctilucent Clouds, or NLCs). PMCs are thin water-ice clouds that form due to naturally occurring water vapor and extremely cold temperature in the polar mesopause region in the summer (see review by Thomas (1991)). These clouds form in thin layers at the edge of space near 83 km, over 50 km above polar stratospheric clouds. The occurrence rate of PMCs is considered an indicator of trends in temperature and water in the middle atmosphere and has drawn great interests (e.g., Beig et al., 2003; Danilov, 2012; Hervig et al., 2016; Russell et al., 2014; Siskind et al., 2013; Thomas & Olivero, 2001). Several investigations have shown the occurrence of PMCs has increased based on both visual observations (Gadsden, 1997; Klostermeyer, 2002) and satellite observations (DeLand & Thomas, 2015; Hervig & Stevens, 2014; Russell et al., 2014; Shettle et al., 2009; Shettle et al., 2002).

Investigations have shown that exhaust from rockets and the space shuttle lead to the formation of PMCs (Dalin et al., 2013; Kelley et al., 2010; Stevens et al., 2012). A single launch of the space shuttle can contribute 20% to the PMC ice mass for a summer cloud season (Stevens et al., 2005). This contribution is significant compared to the long-term increase in PMCs of 1%/decade (e.g., DeLand & Thomas, 2015; Hervig & Stevens, 2014). While the total contribution of space traffic to the PMC record is not quantified, an increase in space traffic

between 2007 and 2012 has been considered the reason for the observed increase of PMCs (Siskind et al., 2013). However, to date, no study has ever directly explored the transport, chemistry and energetics of the water from space traffic in the mesosphere-lower-thermosphere (MLT) region and the influences to PMC occurrences.

During the Super Soaker experiment, 220 kg of water was released into the mesopause region (~80 km) at Poker Flat Research Range (PFRR, 65°N, 147°W) on the night of 25-26 January 2018. The water release was conducted as one of three rockets that were launched. Two Trimethyl aluminum (TMA) trials are released by rockets 30 minutes and 90 s before the water release to measure the neutral winds (Larsen et al., 2003; Lehmacher et al., 2011). The rocket launches were supported by a suite of ground-based instruments. At the Lidar Research Lab (LRL), a new steerable Rayleigh lidar and the SRWTL (described in Chapter 3) were operated before, during, and after the launches to measure the temperature and winds as well as to observe the cloud directly. At the Davis Science Operations Center an Advanced Mesospheric Temperature Mapper was operated to measure temperatures (Pautet et al., 2014). The Poker Flat Incoherent Scatter Radar (PFISR) was operated to measure the plasma environment (Varney et al., 2011).

Rayleigh lidar is an established robust technique for measuring the temperature and density profile of the atmosphere in the stratosphere and mesosphere region (30-100 km) (Collins et al., 2011; Hauchecorne & Chanin, 1980; Irving et al., 2014). Rayleigh lidars are also used to study PMCs and their environment (e.g., density, temperature, wave activity) as the lidars can characterize the parameters (e.g., height, thickness) of these optically thin clouds (e.g., Collins et al., 2009; Fiedler et al., 2011; Gerding et al., 2007; Kaifler et al., 2011; Stebel et al., 2000;

Thayer et al., 1995; Thomas, 1991). In this Appendix we describe the new steerable Rayleigh lidar that was developed specifically to support the Super Soaker investigation.

B2. The steerable Rayleigh lidar

We developed the steerable Rayleigh lidar based on the existing RDTL and designed a monostatic coaxial steerable Rayleigh lidar system. This system is capable of steering in both the elevation and azimuth direction. During the night of campaign, we pointed the lidar to the predicted location of the water release before, during and after the release, and characterized both the middle atmosphere temperatures and the cloud that formed after the water release.

B2.1. System description

Two major features had to be implemented to the Rayleigh lidar system to meet the needs of the Super Soaker investigation. First we had to configure a fixed Newtonian telescope with a transmit-receive steerable mirror (TRSM). The Newtonian telescope is fixed and sits horizontally under an astronomical dome. The TRSM is a flat mirror that can move in azimuth and elevation. A cartoon figure of the system if shown in Figure B1. Second we had to implement a mechanical chopper system to prevent distortion of the lidar signal due to strong signals from close to the ground. This steerable Rayleigh lidar system is a coaxial lidar system. In a coaxial lidar system, the axis of the transmitted laser beam coincides with the optical axis of the receiver. Thus the lidar beam enters the field-of-view (FOV) of the receiver immediately and the near-field backscatter signal is so strong that it overloads the detector and results in distortion of the entire lidar signal profile. In contrast the RDTL is a bistatic lidar system where the lidar beam is transmitted vertically about 6 m away from the vertical-pointing telescope. Thus in the

187

RDTL the lidar beam enters the FOV at an altitude of 6 km to 12 km and an electronic switching system is used to prevent overloading of the detector and distortion of the lidar signal profile. The electronic system is not sufficient to prevent distortion of the lidar signal by the stronger near-field signal close to the ground (< 6 km) and we use a mechanical chopper system to block the near-field signal.
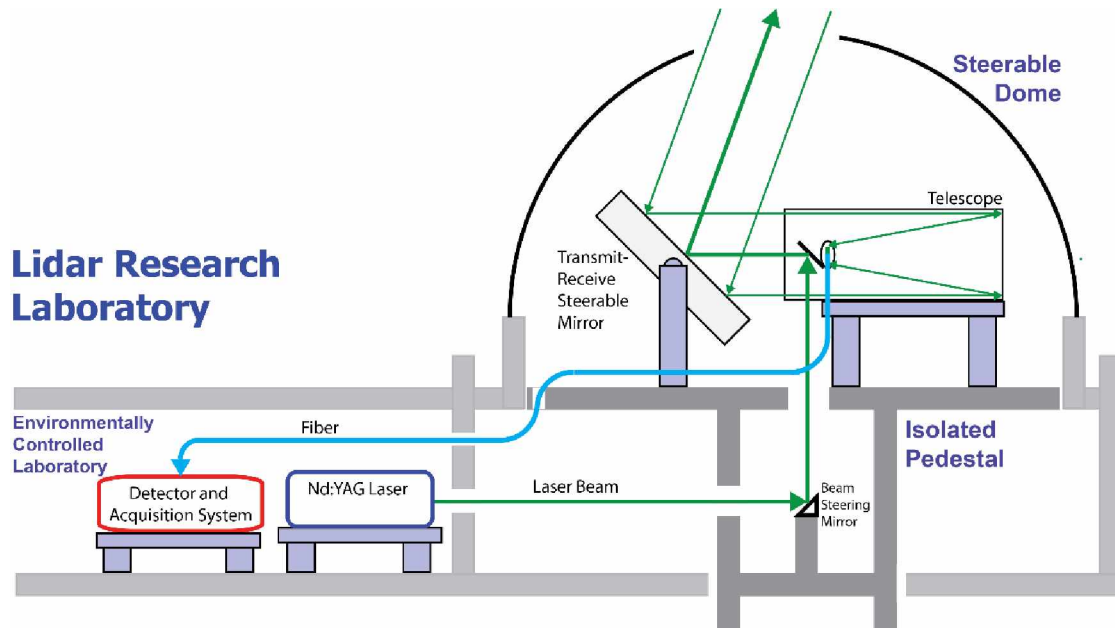
Figure B1. A cartoon figure of the steerable Rayleigh lidar system.

We show a diagram of the steerable Rayleigh lidar system in Figure B2. We use the same transmitter laser (Powerlite 8020, Continuum) of the RDTL as the transmitter of the steerable Rayleigh lidar. The details of the of this laser can be found in Chapter 2. The laser beam passes through a beam expander (BE) to reduce it's divergence. The laser sits in a ground floor laboratory while the telecope and TRSM sit on the second floor under a steerable dome. Two beam reflecting mirrors (BRMs) and a beam steering mirror (BSM) then direct the transmitted

beam through the Lidar Research Laboratory onto the TSRM. The laser beam travels about 10 m from the laser to the TSRM. The first BRM is a fixed mirror that turns the laser beam 90° horizontally, while the BSM steers the beam vertically from the first to the second floor. The BSM is a steerable mirror that is manually adjusted with micrometers and is used to align the transmitted beam with the receiver. The second BRM sits inside the telescope on the backside of the secondary mirror and reflects the vertically pointing beam horizontally along the optical axis of the telescope onto the TRSM. The backscattered signal is reflected by the TSRM along the optical axis of the telescope to the primary mirror (PM). The TRSM is a circular mirror of diameter of 1035 mm that sits inside a circular mirror holder of diameter 1173 mm. The telescope includes a primary mirror (PM) and a secondary mirror (SM) that sit inside an aluminum frame. The frame is 900 mm high, 900 mm wide, and 2915 mm long. The PM has a diameter of 782 mm, a focal length of 2895 mm, and a f-number of 3.7. The PM reflects the light onto the secondary mirror (SM). The SM is a square flat mirror with width of 248 mm. The SM then reflects the light onto the fiber coupler (FC). The FC is a lens that focuses the light onto the optical fiber (OF). The FC is an aspheric lens mounted in a SMA connector, with a numerical aperture (NA) of 0.55, effective focal length of 4.5 mm, and a clear aperture of 4.95 mm. The OF (FT1500UMT, Thorlabs) has a length of 12 m, a NA of 0.39 and a diameter of 1.5 mm. The OF transmits the light to the optical chopper (OC). The wheel of the OC (New Focus 3501, Newport) has a diameter of 110 mm with two slots in a bow-tie shape (Figure B3). The chopper rotates at 100 cycles per second and blocks and unblocks lidar signal, thus the effectively opening and closing the receiver detector. With two slots in the chopper wheel the OC produces a 200 Hz signal in Transistor-transistor logic (TTL) that is the fundamental synchronization signal of the lidar system. The chopper wheel 'chops' a 1.5 mm beam centered at 54 mm from the center of

the wheel in 44 μs, where it takes 44 μs (equivalent to 6.6 km in altitude) for the OF to become unblocked and fully blocked again. It then stays open for 2456 μs (368 km), and then starts to close again. In reality, the beam size at the chopper is larger than 1.5 mm, and the receiver channel opens in ~11 km. The light that passes through the chopper wheel then passes through an aspheric collimating lens (CL), an interference filter (IF), and a focusing lens (FL). The CL (ACL5040U-A) has a focal length of 40 mm and a clear aperture of 45 mm. The IF has a central wavelength of 532 nm and a full width half maximum (FWHM) of 0.3 nm. The FL (LA1401-A, Thorlabs) has a focal length of 60 mm and a clear aperture of 45 mm. The FL focusses the light on the detector of a photomultiplier tube (PMT). The PMT (R3234-01, Hamamatsu) has a square effective area of 100 mm^2 and a pulse with of less than 5 ns. The PMT converts the light into an electronic signal that is amplified by a preamplifier (PA), and recorded by a multi-channel scaler (MCS). The PA (SR445A, Stanford Research Systems) is a 300 MHz preamplifier. The MCS (SR430, Stanford Research Systems) can count signal pulses up to 100 MHz. Once recorded by the MCS, the signal is stored on a desktop personal computer (PC). The MCS communicates with the PC using a GPIB interface. The high-voltage power supply (HVPS) provides a negative supply voltage (-2000 V) for the PMT. In Figure B2 the optical signals, controlling signals, data stream, and power supplies are illustrated by green, blue, red, and black lines respectively.

The 200 Hz signal from the OC serves as the master clock of the entire lidar system, as both the transmitter and receiver must be synchronized to this signal. Two 20-Hz signals are derived from the master clock to trigger the Nd:YAG laser using two delay generators (DG535, Stanford Research). The first delay generator (DG#1) is triggered by every tenth input TTL pulse, yielding an output signal of 20 Hz. The output of the first DG (DG#1) is used to trigger the second DG (DG#2). DG#2 outputs two 20 Hz TTL signals, one of which is used to fire the

190

Nd:YAG laser flashlamps and one of which is used to fire the Nd:YAG laser Q-switch. The delay between the two DG#2 outputs is selected to maximize the output power of the laser. A laser pulse detector (LPD) detects the out pulse of the laser and triggers the MCS to begin acquiring the signal from PMT pulses. The delay time between the input and output of DG#2 can be adjusted to control the timing between when the laser fires and when the receiver is open and thus choose the altitude range over which the lidar signal is detected. We set the delay between the chopper signal and laser firing such that the receiver stays closed until ~14 km and becomes fully open around 25 km. This configuration avoids saturating the receiver and guarantees valid measurement of the atmosphere from 30 km and above.
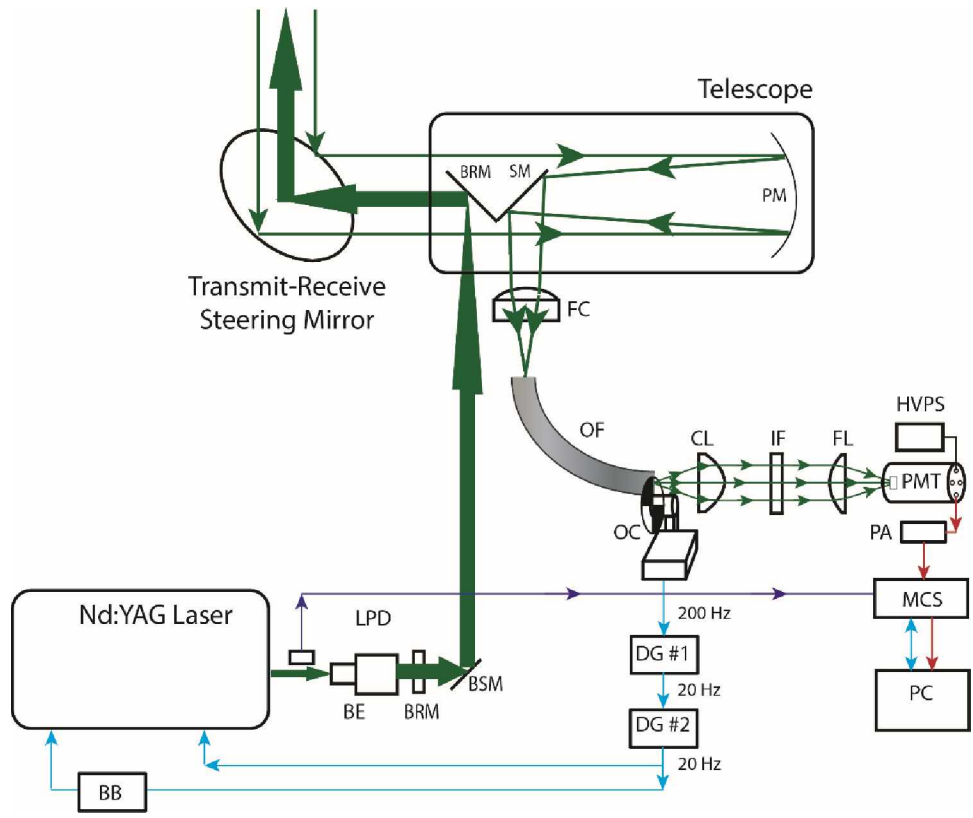
Figure B2. Schematic diagram of the steerable Rayleigh lidar system. See text for details.
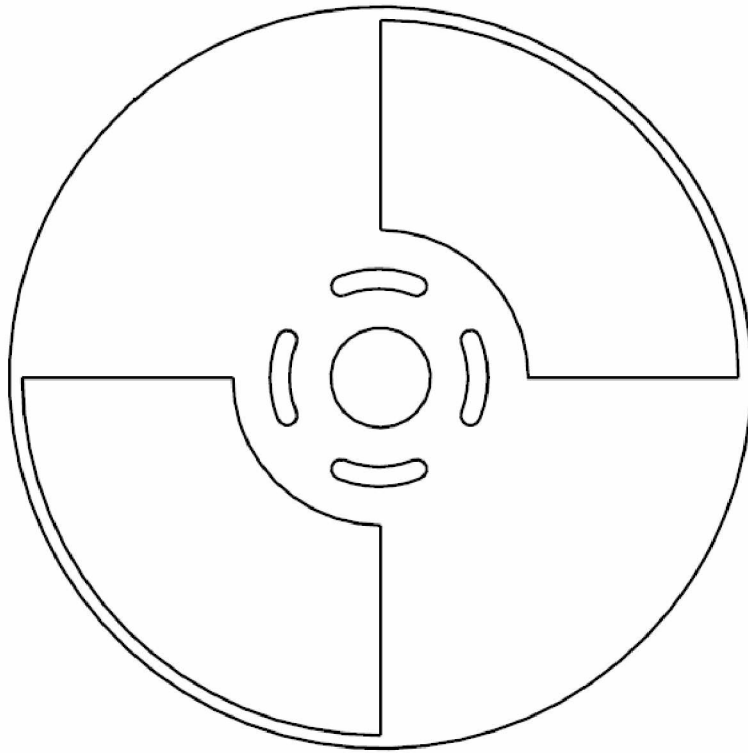
Figure B3. The bow-tie chopper wheel used in the steerable Rayleigh lidar. The chopper wheel

has a diameter of 110 mm.

B2.2. Examination and alignment

B2.2.1. The steerable mirror and the telescope

The receiver required careful alignment to achieve optimized optical efficiency. We surveyed the dome room and established a true north-south axis with a line on the floor. We leveled the TRSM and the telescope and positioned the telescope axis along the south-north axis and positioned the TRSM to the telescope and the north-south axis. It is essential to ensure that the TRSM and the PM of the telescope are co-centered. However, the rotation axis of the TRSM mirror is 130 mm behind the mirror surface. This causes the center of the mirror surface to change in height as the mirror rotates in elevation. We aligned the system so that TRSM and the PM were co-centered when the mirror was at an elevation angle (EL) of 45° off-vertical and an azimuth angle (AZ) of 180° and the lidar makes measurements in the vertical. We used string to measure the distance between the four corner points on the front of telescope frame and four cardinal points on the mirror case when the mirror is turned 45° off-vertical. We used these measured distances to determine the relative positions of the mirror and the telescope. We found that relative to the frame of the telescope, the TRSM was 3.5 mm to the west, 94 mm too low, and 1745 mm to the south. We lowered the telescope by 94 mm and moved the mirror 3.5 mm to the east.

We then built a software model to simulate the 3-D rotation and displacement of the mirror surface. This model simulated the projection of the TRSM onto the primary mirror of the telescope to calculate the overlap ratio of at different angles. With an EL of 45° and an AZ of 180° (mirror facing north, laser beam vertical), the overlap ratio was 78%. With an EL of 35.3°

and an AZ of 185.1° (beam pointing 20° off-vertical to the north, 10° to the east corresponding to the Super Soaker water release) the overlap ratio was 70%.

B2.2.2. The telescope

We confirmed the geometry of the telescope itself. We first examined the relative position between the PM and SM. Following the same approach in section B2.2.1, we used the distances between identified points on the PM and SM to calculate the relative position of the two mirrors. We found that the angle of the SM relative to the PM is 45°, which is exactly as required for the system. We found the distance between the center of the SM and the outer edge of the PM was 2229 mm. The PM center of curvature is 13 mm below the outer edge of the PM. We used a modern optical design software package (OpticStudio, Zemax) to simulate the telescope and found that the SM was too close to the PM by 51 mm, and the SM could not completely intercept all the light reflected by the PM. We moved the SM and increased the distance between the SM and the PM by 101 mm to 2330 mm to ensure that the SM intercepts all the light from the PM.

We then confirmed the location of the telescope focus and the position of the FC and OF. We used laser beams to examine the optical integrity of the telescope. We first aligned a helium-neon (He-Ne) laser beam along the axis of the telescope towards the TRSM. We then adjusted the TRSM in azimuth and elevation such that the He-Ne beam was retroflected back to the telescope. This established that the mirror was vertical and facing north along the axis of the telescope. We then steered the steerable mirror 90° in elevation such that the mirror is horizontal. We then set a He-Ne laser above the steerable mirror and used beam splitters to divide the beam into three beams directed downwards. We put jars with olive oil below each beam and used the liquid surface as retroflector. We adjusted the three beams such that each beam was retroreflected back

to their beamsplitters. This procedure guaranteed that the three beams were parallel and vertical. We then steered the steerable mirror to 45° in elevation and directed the beams into the telescope horizontally. We set up a retroreflector perpendicular to the optical axis of the telescope to confirm that the beams are parallel to the optical axis. In Figure B4, we show the distribution of the three beams at a plane before the focal plane as well as the focal plane. We found that the beams were well focused at the focal plane and validated the optical integrity of the telescope. We found that the focal point was 89 mm from the outer surface of the telescope frame. Given the width of the telescope frame of 900 mm and the distance between the PM and SM of 2343 mm (= 2330 mm + 13 mm), this indicates a focal length of 2869 mm. This is 13 mm less than the specified focal length or a relative difference of less than 0.5%.
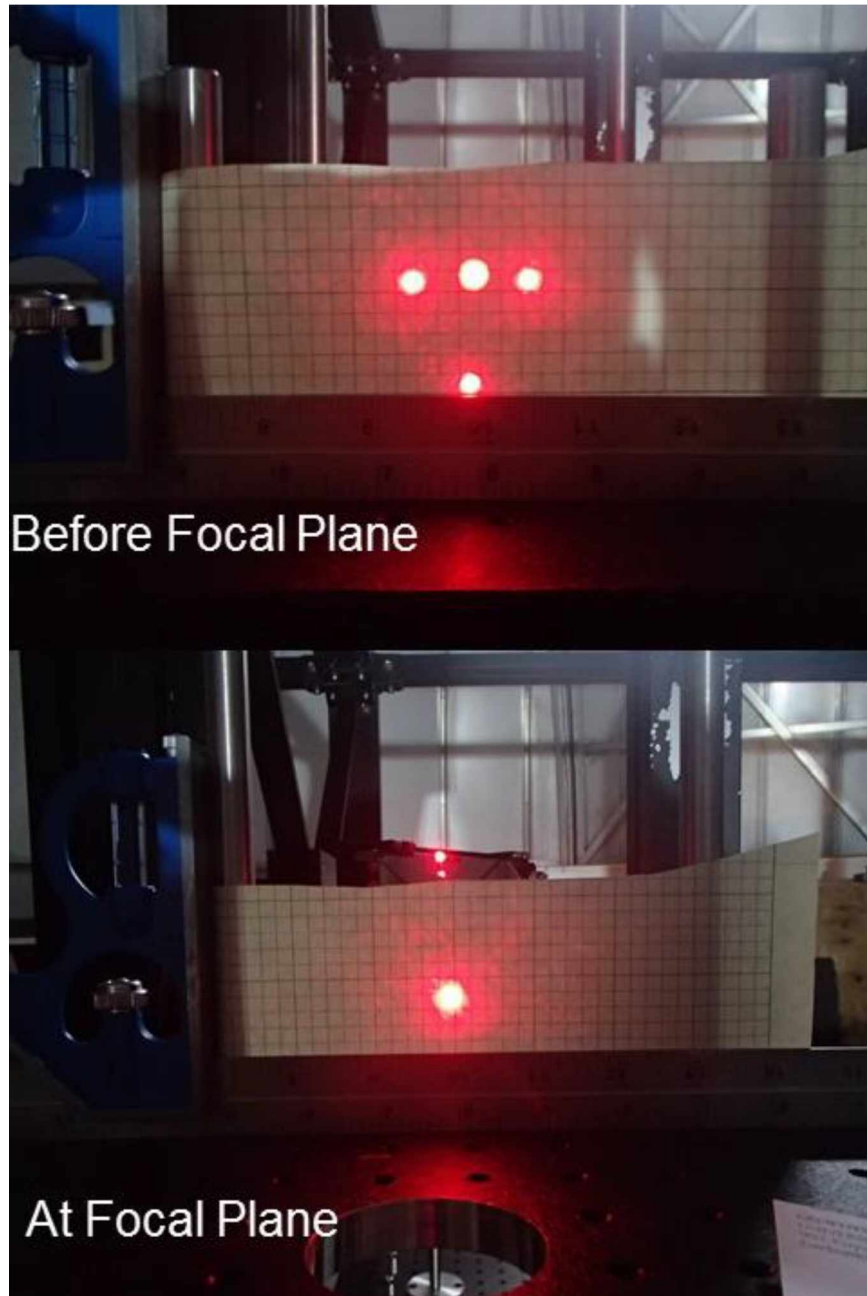
Figure B4. Focusing of paralleled He-Ne laser beams before and at the focal plane of the telescope of the steerable liar system.

B2.2.3 The telescope and fiber

We then simulated the coupling between the telescope and the fiber using the OpticStudio software. In the simulation, we required a FOV of the telescope of 1.0 mrad. The simulation confirmed that the NA of the telescope was 0.14 and indicated that at the focus of the telescope the lidar signal beam would have a diameter of 3 mm, consistent with the geometrical optics. However, the largest fiber available has a core diameter of 1.5 mm and a NA of 0.39. Thus a coupling lens between the telescope and the fiber is necessary to avoid any signal loss. After simulating lenses with various shapes, effective focal lengths and clear apertures, we determined that a FC that incorporates an aspheric lens with EFL of 4.5 mm, NA of 0.55 and clear aperture of 4.95 mm, as described in section B2.1, would couple the signal into the fiber completely and adequately fulfills our requirements. Given that the NA of the FC is greater than the NA of the telescope, the effective FOV of the receiver is defined by the clear aperture of the FC and the focal length of the telescope, and has a value of 1.7 mrad.

B2.2.4. The post fiber optics

We also simulated the post-fiber optics. We simulated the three principal components, the collimating lens (CL), the interference filter (IF) and the focusing lens (FL). We chose the specific CL and FL as described in section B2.1 such that the signal from the OF is collimated at the IF surface and focused at the PMT (Figure B5, left). The distances between the optical components were determined by the simulation. We customized an adjustable and detachable optical tube (ThorLabs) to house these post fiber optics. We then placed the FC and OF at the designated focal point of the telescope (section B2.2.2) and sent a He-Ne beam through the receiver to validate the design. We confirmed that the diameter of the beam is 33 mm between

the collimating lenses, which was consistent with our design (Figure B5, upper right). This verified that the signal was well-collimated and the efficiency of the IF will be maximized. We also confirmed that the diameter of the beam at the PMT detector plane was 2.5 mm (Figure B5, lower right). This is much smaller than the effective area of the PMT (10 mm x 10 mm) and confirms there will be no loss of signal at the PMT.
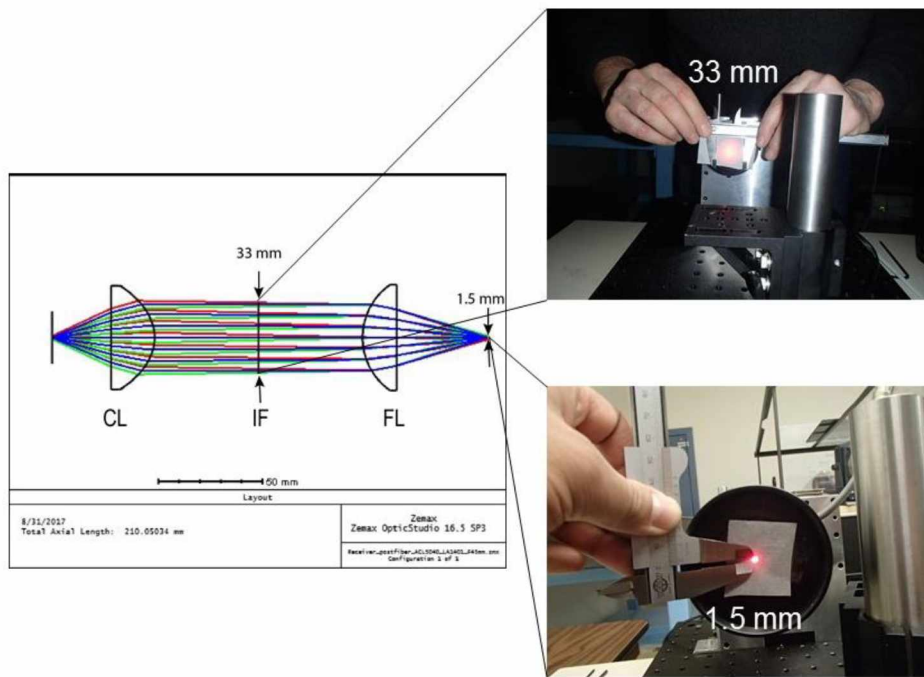
Figure B5. Design and pictures of the He-Ne beam at different positions in the post fiber section of the receiver. Left: ray tracing using OpticStudio software package; Upper right: He-Ne beam after CL; Lower right: He-Ne beam after FL.

B2.3. Test of the steering ability

We obtained field measurements to verify the steering ability of the system on the night of 21-22 March 2018. We steered the lidar beam to three different directions: vertical (V), 20° off-vertical towards north (20° N), and 20° off vertical to the north and 10° to the east (20° NE). We obtained three sets of data at one direction before steering to the next direction in the order of V, N, NE. We repeated this sequence twice and then obtained one last set of data in the vertical direction to confirm the status of the system. Each set of data contains 16 raw lidar signal profiles, and each raw profile represents the signal integrated from 1000 laser pulses. In summary, we obtained nine sets of data in V (set 1, 2, 3, 10, 11, 12, 19, 20, 21), six sets of data in 20° N (set 4, 5, 6, 13, 14, 15) and six sets of data in 20° NE (set 7, 8, 9, 16, 17, 18). Due to the accuracy of the steering mount of the mirror, the elevation angle of the 20° NE data was 70.7° instead of 70°.

We use the signal to characterize the performance of the system at different beam directions. We first integrate the 16 raw photon profiles signal in each set and then calculate the background signal in the range of 150 km and 175 km. We subtract the background signal to yield the lidar backscatter signal, and then normalize these signals by the total number of laser pulses in each set (16,000). We find that the signal levels from the range of 60 km to 65 km are relatively constant in each direction over the observation period, and are reproducible as the beam direction changes (Figure B6, top). The average signals from this range over the whole observation period are 1.14, 2.03 and 2.04 counts/pulse for the V, 20° N, and 20° NE directions respectively. The signals from the 20° N direction and 20° NE directions are similar, and are both higher than

those from the V direction as they represent echoes from lower altitudes than the V signals. The V signal is centered at 62.5 km, the 20°N signal is centered at 58.7 km, and the 20°NE signal is centered at 59.0 km. Given a density scale height of 6 km, the off-vertical signals should be a factor of 1.8-1.9 greater than the vertical signal which is consistent with our measured values. This indicates that there is no significant loss of signal between the TRSM and the telescope as the TRSM is pointed in different directions within the range required for the Super Soaker investigation.

We then consider the signals from a common altitude of 60 km to 65 km. We find that the signals from the 20° NE direction are the higher than those from the 20° N, which are higher than those from the V direction (Figure B6, middle). The average signals in this altitude range over the whole observation period are 1.21, 1.24 and 1.29 counts/pulse for the V, 20° N, and 20° NE directions respectively. Due to the difference in the elevation angles, the signals in the same altitude range represent signals from different distances and distance intervals. The signals from the off-vertical directions arise from further distance and larger distance intervals than those from the vertical direction. We expect the off-vertical signals to be lower than the vertical signals by a factor of $\sin(\theta)$ where θ is the elevation angle. For an elevation angle of 70°, the value of off-vertical signals should be 94% the value of the vertical signal. The fact that the off-vertical signals are 3-7% larger than the vertical signal is unexpected. Finally, we compensate the signals for the differences in pointing angle and normalize the signals to the signal in the vertical direction (Figure B6, bottom). The average normalized signals over the whole observation period are 1.00, 1.09 and 1.13 for the V, 20° N, and 20° NE directions respectively. This unexpected increase of 9-13% represents the combination of the unexpected 3-7% increase and the 94%

angle correction. While we cannot explain the fact that the off-vertical signals are larger than the vertical signal, the field test confirmed that there is no significant loss of signal due to the steering and that the TRSM and telescope are sufficiently well-aligned.
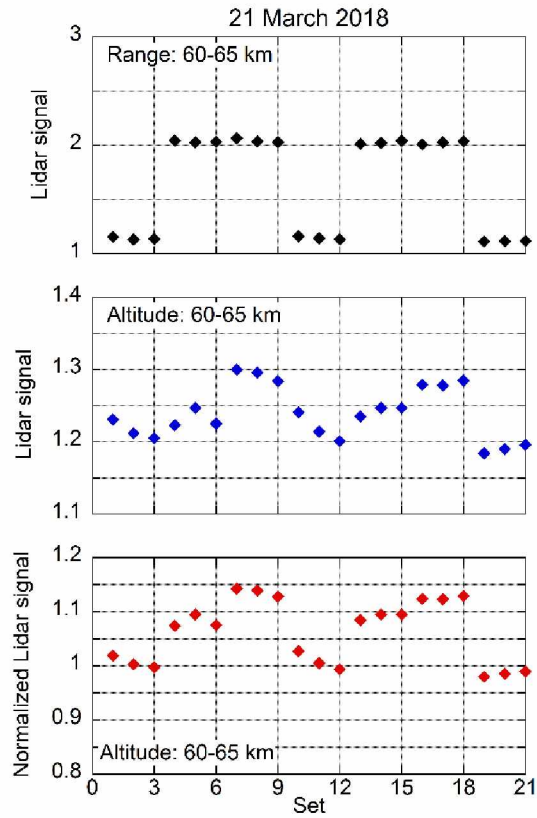
Figure B6. Lidar signals measured by the steerable Rayleigh lidar on the night 21 March 2018. See text for details.

B3. Super Soaker measurements

The "Super Soaker" rocket experiment was carried out on the night of 25-26 January 2018 local standard time (LST, universal time-9 h) at PFRR. The sequence of rocket launches is as follows: the first sounding rocket carrying a TMA canister was launched at 05:11:34 LST, the second rocket, also carrying a TMA canister, was launched at 05:48:19 LST, and the final rocket carrying 220 kg of water was launched 90 seconds later at 05:49:49 LST. The third rocket, upon reaching 85 km altitude 100.5 seconds after launch (at 05:51:29 LST), explosively released 220 kg of water. The steerable Rayleigh lidar was located at 65.12° N and 147.47° W and the water was released above 65.33° N and 147.34° W.

The Rayleigh lidar began observations at 18:37 LST and ended at 08:12 LST on 25-26 January 2018. The steerable telescope was pointed 18° off-vertical and 10° East-of-North to direct the laser beam toward the expected release point of the rocket. We show the raw lidar signal obtained around the time of water release as a function of time and altitude in Figure B7. The raw lidar data was acquired at 25 s resolution (500 laser pulses) at 48 m range resolution. Each profile is smothered with a running average over five range bins (240 m). The lidar detected a cloud in eight successive profiles between 05:51 LST and 05:55 LST. The vertical white line corresponds to the time when the water was released and the cloud appears about 25 s after the water was released. The rapid formation of a cloud after the release is unexpected and these measurements are undergoing further analysis using microphysical models of clouds.
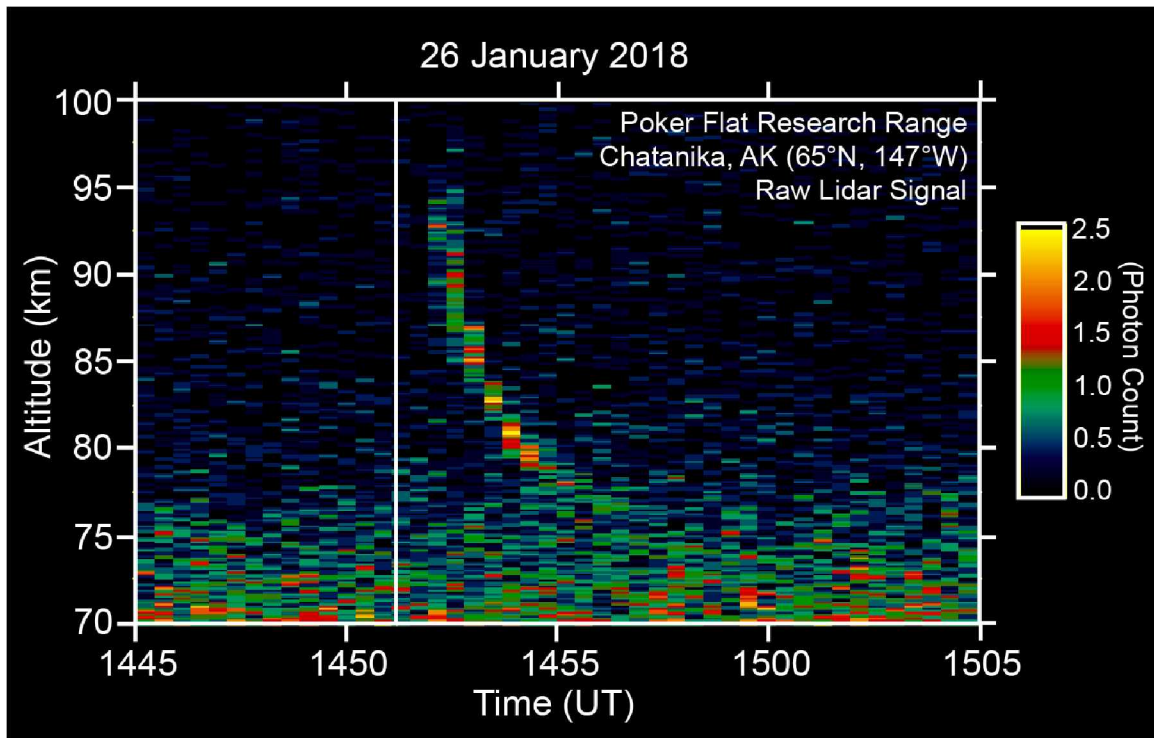
Figure B7. Raw Rayleigh lidar signal from artificial cloud released at PFRR on 26 January plotted as a function of time and altitude. The raw signal is acquired at an altitude resolution of 45.7 m and a temporal resolution of 25 s. The vertical profiles are smoothed with a 240 m running average. The cloud is clearly visible between 14:51 and 14:55 UT and 92 and 78 km. The vertical white line marks the time of the water release at 14:51 UT, 25 s before the first lidar profile with signal from the cloud. The signal below 77 km represents the Rayleigh scatter from the atmosphere which increases with decreasing altitude.

References

Acott, P. E. (2009). *Mesospheric momentum flux studies over Fort Collins CO (41N, 105W).* (Ph.D. dissertation), Colorado State University.

Alspach, J. H., B. P. Williams, J. Li, & R. L. Collins. (2018). *New Sodium Resonance Wind Temperature Lidarat Poker Flat Research Range: Initial Observations During SuperSoaker.* Paper presented at the Coupling, Energetics and Dynamics of Atmospheric Regions (CEDAR), Santa Fe, NM.

Andrews, D. G., J. R. Holton, & C. B. Leovy. (1987). *Middle Atmosphere Dynamics* (Vol. 40). Orlando, Florida 32887: Academic Press Inc.

Becker, E. (2004). Direct heating rates associated with gravity wave saturation. *Journal of Atmospheric and Solar-Terrestrial Physics, 66*(6), 683-696. doi:10.1016/j.jastp.2004.01.019

Becker, E. (2012). Dynamical Control of the Middle Atmosphere. *Space Science Reviews, 168*(1), 283-314. doi:10.1007/s11214-011-9841-5

Beig, G., P. Keckhut, R. P. Lowe, R. G. Roble, M. G. Mlynczak, J. Scheer, et al. (2003). Review of mesospheric temperature trends. *Reviews of Geophysics, 41*(4). doi:10.1029/2002rg000121

Bhattacharyya, S. (1992). *Incoherent scatter radar as a D region probe.* (Master's thesis), University of Alaska Fairbanks.

Bills, R. E., C. S. Gardner, & S. J. Franke. (1991a). Na Doppler/temperature lidar: Initial mesopause region observations and comparison with the Urbana medium frequency radar. *Journal of Geophysical Research: Atmospheres, 96*(D12), 22701-22707. doi:10.1029/91jd02206

Bills, R. E., C. S. Gardner, & C. Y. She. (1991b). *Narrowband lidar technique for sodium temperature and Doppler wind observations of the upper atmosphere* (Vol. 30): SPIE.

Bishop, R. L., M. F. Larsen, J. H. Hecht, A. Z. Liu, & C. S. Gardner. (2004). TOMEX: Mesospheric and lower thermospheric diffusivities and instability layers. *Journal of Geophysical Research: Atmospheres, 109*(D2). doi:10.1029/2002jd003079

Bowles, K. L. (1958). Observation of Vertical-Incidence Scatter from the Ionosphere at 41 Mc/sec. *Physical Review Letters, 1*(12), 454-455. doi:10.1103/PhysRevLett.1.454

Bowman, M. R., A. J. Gibson, & M. C. W. Sandford. (1969). Atmospheric Sodium measured by a Tuned Laser Radar. *Nature, 221*(5179), 456-457. doi:10.1038/221456a0

Chen, H., M. A. White, D. A. Krueger, & C. Y. She. (1996). Daytime mesopause temperature measurements with a sodium-vapor dispersive Faraday filter in a lidar receiver. *Optics Letters, 21*(15), 1093-1095. doi:10.1364/OL.21.001093

Cho, J. Y. N., M. P. Sulzer, & M. C. Kelley. (1998). Meteoric dust effects on D-region incoherent scatter radar spectra. *Journal of Atmospheric and Solar-Terrestrial Physics, 60*(3), 349-357.

Chu, X., & G. C. Papen. (2005). Resonance fluorescence lidar for measurements of the middle and upper atmosphere. In T. Fujii & T. Fukuchi (Eds.), *Laser remote sensing*. Boca Raton, FL: CRC Press.

Colegrove, F. D., W. B. Hanson, & F. S. Johnson. (1965). Eddy diffusion and oxygen transport in the lower thermosphere. *Journal of Geophysical Research (1896-1977), 70*(19), 4931-4941. doi:10.1029/JZ070i019p04931

Colegrove, F. D., F. S. Johnson, & W. B. Hanson. (1966). Atmospheric composition in the lower thermosphere. *Journal of Geophysical Research (1896-1977), 71*(9), 2227-2236. doi:10.1029/JZ071i009p02227

Collins, R. L., T. J. Hallinan, R. W. Smith, & G. Hernandez. (1996). Lidar observations of a large high-altitude sporadic Na layer during active aurora. *Geophysical Research Letters, 23*(24), 3655-3658. doi:10.1029/96GL03337

Collins, R. L., G. A. Lehmacher, M. F. Larsen, & K. Mizutani. (2011). Estimates of vertical eddy diffusivity in the upper mesosphere in the presence of a mesospheric inversion layer. *Annales Geophysicae, 29*(11), 2019-2029. doi:10.5194/angeo-29-2019-2011

Collins, R. L., & R. W. Smith. (2004). Evidence of damping and overturning of gravity waves in the Arctic mesosphere: Na lidar and OH temperature observations. *Journal of Atmospheric and Solar-Terrestrial Physics, 66*(10), 867-879. doi:10.1016/j.jastp.2004.01.038

Collins, R. L., M. J. Taylor, K. Nielsen, K. Mizutani, Y. Murayama, K. Sakanoi, & M. T. DeLand. (2009). Noctilucent cloud in the western Arctic in 2005: Simultaneous lidar and camera observations and analysis. *Journal of Atmospheric and Solar-Terrestrial Physics, 71*(3), 446-452. doi:10.1016/j.jastp.2008.09.044

Cutler, L. J., R. L. Collins, K. Mizutani, & T. Itabe. (2001). Rayleigh lidar observations of mesospheric inversion layers at Poker Flat, Alaska (65 °N, 147°W). *Geophysical Research Letters, 28*(8), 1467-1470. doi:10.1029/2000gl012535

Dalin, P., V. Perminov, N. Pertsev, A. Dubietis, A. Zadorozhny, A. Smirnov, et al. (2013). Optical studies of rocket exhaust trails and artificial noctilucent clouds produced by Soyuz rocket launches. *Journal of Geophysical Research: Atmospheres, 118*(14), 7850-7863. doi:10.1002/jgrd.50549

Danilov, A. D. (2012). Long-term trends in the upper atmosphere and ionosphere (a review). *Geomagnetism and Aeronomy, 52*(3), 271-291. doi:10.1134/s0016793212030036

DeLand, M. T., & G. E. Thomas. (2015). Updated PMC trends derived from SBUV data. *Journal of Geophysical Research: Atmospheres, 120*(5), 2140-2166. doi:10.1002/2014jd022253

Demtröder, W. (1981). *Laser Spectroscopy-Basic Concepts and Instrumentation* (1st ed.): Springer-Verlag Berlin Heidelberg.

Dennis, J. E., D. M. Gay, & R. E. Welsch. (1981). NL2SOL-An adaptive nonlinear least-squares algorithm. *ACM Trans. Math. Softw., 7*(3), 369-383.

Dennis, J. E., & R. B. Schnabel. (1996). *Numerical methods for unconstrained optimization and nonlinear equations-Society for Industrial and Applied Mathematics.* Philadelphia, PA: Society for Industrial and Applied Mathematics.

Dougherty, J. P., & D. T. Farley. (1963). A theory of incoherent scattering of radio waves by a plasma: 3. Scattering in a partly ionized gas. *Journal of Geophysical Research, 68*(19), 5473-5486. doi:10.1029/JZ068i019p05473

Dutton, J. A. (1986). *The Ceaseless Wind : An Introduction to the Theory of Atmospheric Motion* (1st ed.). New York, USA: Dover Publications Inc.

Engstrom, R. W. (1980). *Photomultiplier handbook*. USA: Burle Industries Inc.

Fentzke, J. T., V. Hsu, C. G. M. Brum, I. Strelnikova, M. Rapp, & M. Nicolls. (2012). D region meteoric smoke and neutral temperature retrieval using the poker flat incoherent scatter radar. *Geophysical Research Letters, 39*(21), 6. doi:10.1029/2012gl053841

Fiedler, J., G. Baumgarten, U. Berger, P. Hoffmann, N. Kaifler, & F. J. Lübken. (2011). NLC and the background atmosphere above ALOMAR. *Atmos. Chem. Phys., 11*(12), 5701-5717. doi:10.5194/acp-11-5701-2011

Franke, P. M., & R. L. Collins. (2003). Evidence of gravity wave breaking in lidar data from the mesopause region. *Geophysical Research Letters, 30*(4). doi:10.1029/2001gl014477

Fricke, K. H., & U. von Zahn. (1985). Mesopause temperatures derived from probing the hyperfine structure of the D2 resonance line of sodium by lidar. *Journal of Atmospheric and Terrestrial Physics, 47*(5), 499-512. doi:10.1016/0021-9169(85)90116-3

Fritts, D. C., & M. J. Alexander. (2003). Gravity wave dynamics and effects in the middle atmosphere. *Reviews of Geophysics, 41*(1). doi:10.1029/2001rg000106

Fritts, D. C., B. Laughman, L. Wang, T. S. Lund, & R. L. Collins. (2018a). Gravity Wave Dynamics in a Mesospheric Inversion Layer: 1. Reflection, Trapping, and Instability Dynamics. *Journal of Geophysical Research, 123*(2), 626-648. doi:10.1002/2017JD027440

Fritts, D. C., S. B. Vosper, B. P. Williams, K. Bossert, J. M. C. Plane, M. J. Taylor, et al. (2018b). Large‐Amplitude Mountain Waves in the Mesosphere Accompanying Weak Cross‐Mountain Flow During DEEPWAVE Research Flight RF22. *Journal of Geophysical Research, 123*(18). doi:10.1029/2017JD028250

Fritts, D. C., L. Wang, G. Baumgarten, A. D. Miller, M. A. Geller, G. Jones, et al. (2017). High-resolution observations and modeling of turbulence sources, structures, and intensities in the upper mesosphere. *Journal of Atmospheric and Solar-Terrestrial Physics, 162*, 57-78. doi:10.1016/j.jastp.2016.11.006

Gadsden, M. (1997). The secular changes in noctilucent cloud occurrence: Study of a 31-year sequence to clarify the causes. *Advances in Space Research, 20*(11), 2097-2100. doi:10.1016/S0273-1177(97)00601-7

Gan, Q., S. D. Zhang, & F. Yi. (2012). TIMED/SABER observations of lower mesospheric inversion layers at low and middle latitudes. *Journal of Geophysical Research: Atmospheres, 117*(D7). doi:10.1029/2012jd017455

Garcia, R. R., M. López-Puertas, B. Funke, D. R. Marsh, D. E. Kinnison, A. K. Smith, & F. González-Galindo. (2014). On the distribution of CO_2 and CO in the mesosphere and lower thermosphere. *Journal of Geophysical Research, 119*(9), 5700-5718. doi:10.1002/2013jd021208

Garcia, R. R., & S. Solomon. (1985). The effect of breaking gravity waves on the dynamics and chemical composition of the mesosphere and lower thermosphere. *Journal of Geophysical Research: Atmospheres, 90*(D2), 3850-3868. doi:10.1029/JD090iD02p03850

Gardner, C. S. (2018). Role of Wave-Induced Diffusion and Energy Flux in the Vertical Transport of Atmospheric Constituents in the Mesopause Region. *Journal of Geophysical Research: Atmospheres, 123*(12), 6581-6604. doi:10.1029/2018jd028359

Gardner, C. S., G. C. Papen, X. Chu, & W. Pan. (2001). First lidar observations of middle atmosphere temperatures, Fe densities, and polar mesospheric clouds over the north and south poles. *Geophysical Research Letters, 28*(7), 1199-1202. doi:10.1029/2000gl012622

Gerding, M., J. Höffner, M. Rauthe, W. Singer, M. Zecha, & F.-J. Lübken. (2007). Simultaneous observation of noctilucent clouds, mesospheric summer echoes, and temperature at a midlatitude station (54°N). *Journal of Geophysical Research: Atmospheres, 112*(D12). doi:10.1029/2006jd008135

Gibson, A. J., L. Thomas, & S. K. Bhattachacharyya. (1979). Laser observations of the ground-state hyperfine structure of sodium and of temperatures in the upper atmosphere. *Nature, 281*(5727), 131-132. doi:10.1038/281131a0

Gordon, W. E. (1958). Incoherent Scattering of Radio Waves by Free Electrons with Applications to Space Exploration by Radar. *Proceedings of the IRE, 46*(11), 1824-1829. doi:10.1109/JRPROC.1958.286852

Grant, W. B., E. Browell, R. T. Menzies, K. Sassen, & C. Y. She. (1997). *Selected papers on laser applications in remote sensing.*

Guo, Y., A. Z. Liu, & C. S. Gardner. (2017). First Na lidar measurements of turbulence heat flux, thermal diffusivity, and energy dissipation rate in the mesopause region. *Geophysical Research Letters, 44*(11), 5782-5790. doi:10.1002/2017gl073807

Hagen, J. B., & R. A. Behnke. (1976). Detection of the electron component of the spectrum in incoherent scatter of radio waves by the ionosphere. *Journal of Geophysical Research, 81*(19), 3441-3443. doi:10.1029/JA081i019p03441

Harris, F. J. (1978). On the use of windows for harmonic analysis with the discrete Fourier transform. *Proceedings of the IEEE, 66*(1), 51-83. doi:10.1109/PROC.1978.10837

Hauchecorne, A., & M.-L. Chanin. (1980). Density and temperature profiles obtained by lidar between 35 and 70 km. *Geophysical Research Letters, 7*(8), 565-568. doi:10.1029/GL007i008p00565

Hauchecorne, A., M. L. Chanin, & R. Wilson. (1987). Mesospheric temperature inversion and gravity wave breaking. *Geophysical Research Letters, 14*(9), 933-936. doi:10.1029/GL014i009p00933

Hecht, J. H. (2004). Instability layers and airglow imaging. *Reviews of Geophysics, 42*(1). doi:10.1029/2003rg000131

Hecht, J. H., C. Fricke-Begemann, R. L. Walterscheid, & J. Höffner. (2000). Observations of the breakdown of an atmospheric gravity wave near the cold summer mesopause at 54N. *Geophysical Research Letters, 27*(6), 879-882. doi:10.1029/1999gl010792

Heine, T. (2013). More colors! Diode laser reach yellow and orange. *Physics' Best,* 21-23.

Heinselman, C. J., & M. J. Nicolls. (2008). A Bayesian approach to electric field and E-region neutral wind estimation with the Poker Flat Advanced Modular Incoherent Scatter Radar. *Radio Science, 43*(5). doi:10.1029/2007RS003805

Hervig, M. E., M. Gerding, M. H. Stevens, R. Stockwell, S. M. Bailey, J. M. Russell, & G. Stober. (2016). Mid-latitude mesospheric clouds and their environment from SOFIE

observations. *Journal of Atmospheric and Solar-Terrestrial Physics*, *149*, 1-14. doi:10.1016/j.jastp.2016.09.004

Hervig, M. E., & M. H. Stevens. (2014). Interpreting the 35 year SBUV PMC record with SOFIE observations. *Journal of Geophysical Research: Atmospheres*, *119*(22), 12,689-612,705. doi:10.1002/2014jd021923

Hines, C. O. (1960). Internal Atmospheric Gravity Waves at Ionospheric Heights. In C. O. Hines (Ed.), *The Upper Atmosphere in Motion* (Vol. 18, pp. 248-328).

Hines, C. O. (1988). Generation of Turbulence by Atmospheric Gravity Waves. *Journal of the Atmospheric Sciences*, *45*(7), 1269-1278. doi:10.1175/1520-0469(1988)045<1269:Gotbag>2.0.Co;2

Hines, C. O., & C. A. Reddy. (1967). On the propagation of atmospheric gravity waves through regions of wind shear. *Journal of Geophysical Research*, *72*(3), 1015-1034. doi:doi:10.1029/JZ072i003p01015

Hocking, W. K. (1985). Measurement of turbulent energy dissipation rates in the middle atmosphere by radar techniques: A review. *Radio Science*, *20*(6), 1403-1422. doi:10.1029/RS020i006p01403

Hocking, W. K. (1996). An assessment of the capabilities and limitations of radars in measurements of upper atmosphere turbulence. *Advances in Space Research*, *17*(11), 37-47. doi:10.1016/0273-1177(95)00728-W

Hocking, W. K., J. Röttger, R. D. Palmer, T. Sato, & P. B. Chilson. (2016). *Atmospheric Radar: Application and Science of MST Radars in the Earth's Mesosphere, Stratosphere, Troposphere, and Weakly Ionized Regions*. Cambridge: Cambridge University Press.

Hodges, R. R. (1969). Eddy diffusion coefficients due to instabilities in internal gravity waves. *Journal of Geophysical Research*, *74*(16), 4087-4090. doi:10.1029/JA074i016p04087

Holton, J. R. (1982). The Role of Gravity Wave Induced Drag and Diffusion in the Momentum Budget of the Mesosphere. *Journal of the Atmospheric Sciences*, *39*(4), 791-799. doi:10.1175/1520-0469(1982)039<0791:Trogwi>2.0.Co;2

Holton, J. R. (1983). The Influence of Gravity Wave Breaking on the General Circulation of the Middle Atmosphere. *Journal of the Atmospheric Sciences, 40*(10), 2497-2507. doi:10.1175/1520-0469(1983)040<2497:Tiogwb>2.0.Co;2

Holton, J. R., & M. J. Alexander. (2000). The Role of Waves in the Transport Circulation of the Middle Atmosphere. In D. E. Siskind, S. D. Eckermann, & M. E. Summers (Eds.), *Atmospheric Science Across the Stratopause* (Vol. 123). Washington, DC: American Geophysical Union.

Holton, J. R., & G. J. Hakim. (2013). *An introduction to dynamic meteorology* (5th ed.). Waltham, MA, USA: Academic Press.

Hou, T. (2002). *Development of high spectral resolution iron Boltamann lidar.* (Master's thesis), University of Alaska Fairbanks

Houghton, J. T. (1978). The stratosphere and mesosphere. *Quarterly Journal of the Royal Meteorological Society, 104*(439), 1-29. doi:10.1002/qj.49710443902

Irving, B. K., R. L. Collins, R. S. Lieberman, B. Thurairajah, & K. Mizutani. (2014). Mesospheric Inversion Layers at Chatanika, Alaska (65°N, 147°W): Rayleigh lidar observations and analysis. *Journal of Geophysical Research: Atmospheres, 119*(19), 11,235-211,249. doi:10.1002/2014jd021838

Jacob, D. J. (1999). *Introduction to atmospheric chemistry.* Princeton, New Jersey, USA: Princeton University Press.

Johnson, R. M., & T. L. Killeen (Eds.). (1995). *The upper mesosphere and lower thermosphere: a review of experiment and theory.* American Geophysical Union.

Kaifler, N., G. Baumgarten, J. Fiedler, R. Latteck, F. J. Lübken, & M. Rapp. (2011). Coincident measurements of PMSE and NLC above ALOMAR (69° N, 16° E) by radar and lidar from 1999–2008. *Atmos. Chem. Phys., 11*(4), 1355-1366. doi:10.5194/acp-11-1355-2011

Kelley, M. C., M. J. Nicolls, R. H. Varney, R. L. Collins, R. Doe, J. M. C. Plane, et al. (2010). Radar, lidar, and optical observations in the polar summer mesosphere shortly after a

space shuttle launch. *Journal of Geophysical Research: Space Physics, 115*(A5). doi:10.1029/2009ja014938

Klostermeyer, J. (2002). Noctilucent clouds getting brighter. *Journal of Geophysical Research: Atmospheres, 107*(D14), AAC 1-1-AAC 1-7. doi:10.1029/2001jd001345

Krueger, D. A., C.-Y. She, & T. Yuan. (2015). Retrieving mesopause temperature and line-of-sight wind from full-diurnal-cycle Na lidar observations. *Applied Optics, 54*(32), 9469-9489. doi:10.1364/AO.54.009469

Kudeki, E., & M. A. Milla. (2011). Incoherent Scatter Spectral Theories—Part I: A General Framework and Results for Small Magnetic Aspect Angles. *IEEE Transactions on Geoscience and Remote Sensing, 49*(1), 315-328. doi:10.1109/tgrs.2010.2057252

Larsen, M. F., A. Z. Liu, R. L. Bishop, & J. H. Hecht. (2003). TOMEX: A comparison of lidar and sounding rocket chemical tracer wind measurements. *Geophysical Research Letters, 30*(7). doi:10.1029/2002gl015678

Lehmacher, G. A., C. L. Croskey, J. D. Mitchell, M. Friedrich, F. J. Lübken, M. Rapp, et al. (2006). Intense turbulence observed above a mesospheric temperature inversion at equatorial latitude. *Geophysical Research Letters, 33*(8). doi:10.1029/2005gl024345

Lehmacher, G. A., & F. J. Lübken. (1995). Simultaneous observation of convective adjustment and turbulence generation in the mesosphere. *Geophysical Research Letters, 22*(18), 2477-2480. doi:10.1029/95GL02351

Lehmacher, G. A., T. D. Scott, M. F. Larsen, S. G. Bilén, C. L. Croskey, J. D. Mitchell, et al. (2011). The Turbopause experiment: atmospheric stability and turbulent structure spanning the turbopause altitude. *Annales Geophysicae, 29*(12), 2327-2339. doi:10.5194/angeo-29-2327-2011

Li, J., R. Varney, R. L. Collins, D. Thorsen, & D. E. Newman. (2018a). *PFISR detection of turbulence-A hypothesis test approach.* Paper presented at the Coupling, Energetics and Dynamics of Atmospheric Regions (CEDAR), Santa Fe, New Mexico.

Li, J., B. P. Williams, R. L. Collins, J. H. Alspach, & K. Bossert. (2018b). *Lidar studies of gravity wave breaking in Arctic mesosphere.* Paper presented at the AGU Fall Meeting, Washington D.C., Washington.

213

Li, T., X. Fang, W. Liu, S.-Y. Gu, & X. Dou. (2012). Narrowband sodium lidar for the measurements of mesopause region temperature and wind. *Applied Optics, 51*(22), 5401-5411. doi:10.1364/AO.51.005401

Lindzen, R. S. (1971). Tides and gravity waves in the upper atmosphere. In G. Fiocco (Ed.), *Mesospheric Models and Related Experiments: Proceedings of the Fourth Esrin-Eslab Symposium Held in Frascati, Italy, 6–10 July, 1970.* Dordrecht, Holland: Springer Netherlands.

Lindzen, R. S. (1981). Turbulence and stress owing to gravity wave and tidal breakdown. *Journal of Geophysical Research, 86*(C10), 9707-9714. doi:doi:10.1029/JC086iC10p09707

Liu, A. Z., R. G. Roble, J. H. Hecht, M. F. Larsen, & C. S. Gardner. (2004). Unstable layers in the mesopause region observed with Na lidar during the Turbulent Oxygen Mixing Experiment (TOMEX) campaign. *Journal of Geophysical Research: Atmospheres, 109*(D2). doi:10.1029/2002jd003056

López-Puertas, M., B. Funke, S. Gil-López, T. von Clarmann, G. P. Stiller, M. Höpfner, et al. (2005). Observation of NOx enhancement and ozone depletion in the Northern and Southern Hemispheres after the October–November 2003 solar proton events. *Journal of Geophysical Research: Space Physics, 110*(A9). doi:10.1029/2005ja011050

Lübken, F.-J. (1997). Seasonal variation of turbulent energy dissipation rates at high latitudes as determined by in situ measurements of neutral density fluctuations. *Journal of Geophysical Research, 102*(D12), 13441-13456. doi:10.1029/97jd00853

Lübken, F.-J., W. Singer, R. Latteck, & I. Strelnikova. (2007). Radar measurements of turbulence, electron densities, and absolute reflectivities during polar mesosphere winter echoes (PMWE). *Advances in Space Research, 40*(6), 758-764. doi:10.1016/j.asr.2007.01.015

Madsen, K., H. B. Heilsen, & O. Tingleff. (2004). *Method for non-linear least squares problems.* Kongens Lyngby: Informatics and Mathematical Modelling, Technical University of Denmark.

Martus, C. M. (2013). *Exploration of mesospheric metal layers from Chatanika, Alaska.* (M. S.), University of Alaska Fairbanks,

McCrea, I., A. Aikio, L. Alfonsi, E. Belova, S. Buchert, M. Clilverd, et al. (2015). The science case for the EISCAT_3D radar. *Progress in Earth and Planetary Science, 2*(1), 21. doi:10.1186/s40645-015-0051-8

Meraner, K., & H. Schmidt. (2016). Transport of nitrogen oxides through the winter mesopause in HAMMONIA. *Journal of Geophysical Research, 121*(6), 2556-2570. doi:10.1002/2015jd024136

Meraner, K., H. Schmidt, E. Manzini, B. Funke, & A. Gardini. (2016). Sensitivity of simulated mesospheric transport of nitrogen oxides to parameterized gravity waves. *Journal of Geophysical Research: Atmospheres, 121*(20), 12,045-012,061. doi:10.1002/2016JD025012

Meriwether, J. W., & A. J. Gerrard. (2004). Mesosphere inversion layers and stratosphere temperature enhancements. *Reviews of Geophysics, 42*(RG3003). doi:10.1029/2003RG000133

Mironova, I. A., K. L. Aplin, F. Arnold, G. A. Bazilevskaya, R. G. Harrison, A. A. Krivolutsky, et al. (2015). Energetic Particle Influence on the Earth's Atmosphere. *Space Science Reviews, 194*(1), 1-96. doi:10.1007/s11214-015-0185-4

Mlynczak, M. (2000). A Contemporary Assessment of the Mesospheric Energy Budget. In D. E. Siskind, E. S. D., & M. E. Summers (Eds.), *Mlynczak, M. G. (2013). A Contemporary Assessment of the Mesospheric Energy Budget.* Atmospheric Science Across the Stratopause: American Geophysical Union.

Montzka, S. A., G. S. Dutton, P. Yu, E. Ray, R. W. Portmann, J. S. Daniel, et al. (2018). An unexpected and persistent increase in global emissions of ozone-depleting CFC-11. *Nature, 557*(7705), 413-417. doi:10.1038/s41586-018-0106-2

Müllemann, A., M. Rapp, F.-J. Lübken, & P. Hoffmann. (2002). In situ measurements of mesospheric turbulence during spring transition of the Arctic mesosphere. *Geophysical Research Letters, 29*(10), 115-111-115-114. doi:10.1029/2002gl014841

National Research Council. (1994). *Solar influences on global change.* Washington D.C.: National Academy Press.

Newman, P. A., L. D. Oman, A. R. Douglass, E. L. Fleming, S. M. Frith, M. M. Hurwitz, et al. (2009). What would have happened to the ozone layer if chlorofluorocarbons (CFCs) had not been regulated? *Atmos. Chem. Phys., 9*(6), 2113-2128. doi:10.5194/acp-9-2113-2009

Nicolls, M. J., C. J. Heinselman, E. A. Hope, S. Ranjan, M. C. Kelley, & J. D. Kelly. (2007). Imaging of Polar Mesosphere Summer Echoes with the 450 MHz Poker Flat Advanced Modular Incoherent Scatter Radar. *Geophysical Research Letters, 34*(20). doi:10.1029/2007gl031476

Nicolls, M. J., R. H. Varney, S. L. Vadas, P. A. Stamus, C. J. Heinselman, R. B. Cosgrove, & M. C. Kelley. (2010). Influence of an inertia-gravity wave on mesospheric dynamics: A case study with the Poker Flat Incoherent Scatter Radar. *Journal of Geophysical Research, 115*. doi:10.1029/2010jd014042

Osman, M. K., W. K. Hocking, & D. W. Tarasick. (2016). Parameterization of large-scale turbulent diffusion in the presence of both well-mixed and weakly mixed patchy layers. *Journal of Atmospheric and Solar-Terrestrial Physics, 143-144*, 14-36. doi:10.1016/j.jastp.2016.02.025

Papoulis, A., & S. U. Pillai. (2002). *Probability, random variables and stochastic processes* (4th ed.). New York, NY, USA: The McGraw-Hill Companies.

Pautet, P. D., M. J. Taylor, W. R. Pendleton, Y. Zhao, T. Yuan, R. Esplin, & D. McLain. (2014). Advanced mesospheric temperature mapper for high-latitude airglow studies. *Applied Optics, 53*(26), 5934-5943. doi:10.1364/AO.53.005934

Press, W. H., S. A. Teukolsky, W. T. Vetterling, & B. P. Flannery. (1992). *Numerical recipes in Fortran: the art of scientific computing* (2nd ed.). New York, NY: the Press Syndicate of the University of Cambridge.

Puga, J. L., M. Krzywinski, & N. Altman. (2015). Bayes' theorem. *Nature Methods, 12*(4), 277-278. doi:10.1038/nmeth.3335

Qian, L., S. C. Solomon, & T. J. Kane. (2009). Seasonal variation of thermospheric density and composition. *Journal of Geophysical Research, 114*(A1). doi:10.1029/2008ja013643

Ramesh, K., & S. Sridharan. (2012). Large mesospheric inversion layer due to breaking of small-scale gravity waves: Evidence from Rayleigh lidar observations over Gadanki (13.5°N,

79.2°E). *Journal of Atmospheric and Solar-Terrestrial Physics, 89,* 90-97. doi:10.1016/j.jastp.2012.08.011

Ramesh, K., S. Sridharan, K. Raghunath, S. V. B. Rao, & Y. B. Kumar. (2013). Planetary wave‐gravity wave interactions during mesospheric inversion layer events. *Journal of Geophysical Research: Space Physics, 118*(7), 4503-4515. doi:10.1002/jgra.50379

Randall, C. E., V. L. Harvey, C. S. Singleton, P. F. Bernath, C. D. Boone, & J. U. Kozyra. (2006). Enhanced NOx in 2006 linked to strong upper stratospheric Arctic vortex. *Geophysical Research Letters, 33*(18). doi:10.1029/2006GL027160

Randall, C. E., V. L. Harvey, D. E. Siskind, J. France, P. F. Bernath, C. D. Boone, & K. A. Walker. (2009). NOx descent in the Arctic middle atmosphere in early 2009. *Geophysical Research Letters, 36*(18). doi:10.1029/2009gl039706

Rastogi, P. K., & S. A. Bowhill. (1976). Scattering of radio waves from the mesosphere—2. Evidence for intermittent mesospheric turbulence. *Journal of Atmospheric and Terrestrial Physics, 38*(5), 449-462.

Russell, J. M., P. Rong, M. E. Hervig, D. E. Siskind, M. H. Stevens, S. M. Bailey, & J. Gumbel. (2014). Analysis of northern midlatitude noctilucent cloud occurrences using satellite data and modeling. *Journal of Geophysical Research: Atmospheres, 119*(6), 3238-3250. doi:10.1002/2013jd021017

Schmidlin, F. J. (1976). Temperature inversions near 75 km. *Geophysical Research Letters, 3*(3), 173-176. doi:https://doi.org/10.1029/GL003i003p00173

Selvaraj, D., A. K. Patra, & D. Narayana Rao. (2016). On the seasonal variations of reflectivity and turbulence characteristics of low-latitude mesospheric echoes over Gadanki. *Journal of Geophysical Research, 121*(11), 6164-6177. doi:10.1002/2015jd024283

She, C. Y., H. Latifi, J. R. Yu, R. J. Alvarez II, R. E. Bills, & C. S. Gardner. (1990). Two-frequency Lidar technique for mesospheric Na temperature measurements. *Geophysical Research Letters, 17*(7), 929-932. doi:10.1029/GL017i007p00929

She, C. Y., T. Li, R. L. Collins, T. Yuan, B. P. Williams, T. D. Kawahara, et al. (2004). Tidal perturbations and variability in the mesopause region over Fort Collins, CO (41N, 105W): Continuous multi-day temperature and wind lidar observations. *Geophysical Research Letters, 31*(24). doi:10.1029/2004gl021165

217

She, C. Y., J. D. Vance, B. P. Williams, D. A. Krueger, H. Moosmüller, D. Gibson-Wilde, & D. Fritts. (2002). Lidar studies of atmospheric dynamics near polar mesopause. *Eos, Transactions American Geophysical Union, 83*(27). doi:10.1029/2002eo000206

She, C. Y., & J. R. Yu. (1994). Simultaneous three-frequency Na lidar measurements of radial wind and temperature in the mesopause region. *Geophysical Research Letters, 21*(17), 1771-1774. doi:10.1029/94gl01417

She, C. Y., J. R. Yu, H. Latifi, & R. E. Bills. (1992). High-spectral-resolution fluorescence light detection and ranging for mesospheric sodium temperature measurements. *Applied Optics, 31*(12), 2095-2106. doi:10.1364/AO.31.002095

Shettle, E. P., M. T. DeLand, G. E. Thomas, & J. J. Olivero. (2009). Long term variations in the frequency of polar mesospheric clouds in the Northern Hemisphere from SBUV. *Geophysical Research Letters, 36*(2). doi:10.1029/2008gl036048

Shettle, E. P., G. E. Thomas, J. J. Olivero, W. F. J. Evans, D. J. Debrestian, & L. Chardon. (2002). Three-satellite comparison of polar mesospheric clouds: Evidence for long-term change. *Journal of Geophysical Research: Atmospheres, 107*(D12). doi:10.1029/2001jd000668

Siskind, D. E., S. D. Eckermann, & M. E. Summers (Eds.). (2000). *Atmospheric science across the stratopause*. American Geophysical Union.

Siskind, D. E., M. H. Stevens, M. E. Hervig, & C. E. Randall. (2013). Recent observations of high mass density polar mesospheric clouds: A link to space traffic? *Geophysical Research Letters, 40*(11), 2813-2817. doi:10.1002/grl.50540

Smith, A. K., R. R. Garcia, D. R. Marsh, & J. H. Richter. (2011). WACCM simulations of the mean circulation and trace species transport in the winter mesosphere. *Journal of Geophysical Research, 116*(D20). doi:10.1029/2011jd016083

Solomon, S., D. J. Ivy, D. Kinnison, M. J. Mills, R. R. Neely, & A. Schmidt. (2016). Emergence of healing in the Antarctic ozone layer. *Science, 353*(6296), 269. doi:10.1126/science.aae0061

Stebel, K., V. Barabash, S. Kirkwood, J. Siebert, & K. H. Fricke. (2000). Polar mesosphere summer echoes and noctilucent clouds: Simultaneous and common-volume observations

by radar, lidar and CCD camera. *Geophysical Research Letters, 27*(5), 661-664. doi:10.1029/1999gl010844

Stevens, M. H., S. Lossow, J. Fiedler, G. Baumgarten, F.-J. Lübken, K. Hallgren, et al. (2012). Bright polar mesospheric clouds formed by main engine exhaust from the space shuttle's final launch. *Journal of Geophysical Research: Atmospheres, 117*(D19). doi:10.1029/2012jd017638

Stevens, M. H., R. R. Meier, X. Chu, M. T. DeLand, & J. M. C. Plane. (2005). Antarctic mesospheric clouds formed from space shuttle exhaust. *Geophysical Research Letters, 32*(13). doi:10.1029/2005gl023054

Strelnikov, B., A. Szewczyk, I. Strelnikova, R. Latteck, G. Baumgarten, F.-J. Lübken, et al. (2017). Spatial and temporal variability in MLT turbulence inferred from in situ and ground-based observations during the WADIS-1 sounding rocket campaign. *Annales Geophysicae, 35*(3), 547-565. doi:10.5194/angeo-35-547-2017

Strelnikova, I., M. Rapp, S. Raizada, & M. Sulzer. (2007). Meteor smoke particle properties derived from Arecibo incoherent scatter radar observations. *Geophysical Research Letters, 34*(15). doi:10.1029/2007gl030635

Su, L., R. L. Collins, D. A. Krueger, & C.-Y. She. (2008). Statistical Analysis of Sodium Doppler Wind–Temperature Lidar Measurements of Vertical Heat Flux. *Journal of Atmospheric and Oceanic Technology, 25*(3), 401-415. doi:10.1175/2007jtecha915.1

Sutherland, B. R. (2010). *Internal Gravity Waves.* Cambridge: Cambridge University Press.

Swenson, G., Y. Yee, F. Vargas, & A. Liu. (2018). Vertical diffusion transport of atomic oxygen in the mesopause region consistent with chemical losses and continuity: Global mean and inter-annual variability. *Journal of Atmospheric and Solar-Terrestrial Physics, 178*, 47-57. doi:10.1016/j.jastp.2018.05.014

Szewczyk, A. (2015). *Mesospheric turbulence: the role in the creation of mesospheric inversion layers and statistical results.* (Ph.D. Dissertation), Universit"at Rostock.

Szewczyk, A., B. Strelnikov, M. Rapp, I. Strelnikova, G. Baumgarten, N. Kaifler, et al. (2013). Simultaneous observations of a Mesospheric Inversion Layer and turbulence during the ECOMA-2010 rocket campaign. *Annales Geophysicae, 31*(5), 775-785. doi:10.5194/angeo-31-775-2013

Thayer, J. P., N. Nielsen, & J. Jacobsen. (1995). Noctilucent cloud observations over Greenland by a Rayleigh lidar. *Geophysical Research Letters, 22*(21), 2961-2964. doi:10.1029/95gl02126

Thomas, G. E. (1991). Mesospheric clouds and the physics of the mesopause region. *Reviews of Geophysics, 29*(4), 553-575. doi:10.1029/91rg01604

Thomas, G. E., & J. Olivero. (2001). Noctilucent clouds as possible indicators of global change in the mesosphere. *Advances in Space Research, 28*(7), 937-946.

Thomas, L., A. K. P. Marsh, D. P. Wareing, I. Astin, & H. Chandra. (1996). VHF echoes from the midlatitude mesosphere and the thermal structure observed by lidar. *Journal of Geophysical Research: Atmospheres, 101*(D8), 12867-12877. doi:10.1029/96jd00218

Thurairajah, B., R. L. Collins, V. L. Harvey, R. S. Lieberman, M. Gerding, K. Mizutani, & J. M. Livingston. (2010a). Gravity wave activity in the Arctic stratosphere and mesosphere during the 2007–2008 and 2008–2009 stratospheric sudden warming events. *Journal of Geophysical Research, 115*. doi:10.1029/2010jd014125

Thurairajah, B., R. L. Collins, V. L. Harvey, R. S. Lieberman, & K. Mizutani. (2010b). Rayleigh lidar observations of reduced gravity wave activity during the formation of an elevated stratopause in 2004 at Chatanika, Alaska (65°N, 147°W). *Journal of Geophysical Research: Atmospheres, 115*(D13). doi:10.1029/2009jd013036

Triplett, C. (2016). *Rocket and Lidar Studies of Waves and Turbulence in the Arctic Middle Atmosphere.* (Ph. D. dissertation), University of Alaska Fairbanks.

Triplett, C. C., J. Li, R. L. Collins, G. A. Lehmacher, A. Barjatya, D. C. Fritts, et al. (2018). Observations of Reduced Turbulence and Wave Activity in the Arctic Middle Atmosphere Following the January 2015 Sudden Stratospheric Warming. *Journal of Geophysical Research, 123*(23), 13,259-213,276. doi:10.1029/2018JD028788

Vance, J. D. (2004). *The sum frequency generator seeded, ALOMAR Weber sodium LIDAR and initial measurements of temperature and wind in the Norwegian Arctic mesopause region.* (Ph.D. dissertation), Colorado State University, Fort Collins, Colorado.

Vance, J. D., C.-Y. She, & H. Moosmüller. (1998). Continuous-wave, all-solid-state, single-frequency 400-mW source at 589 nm based on doubly resonant sum-frequency mixing in

a monolithic lithium niobate resonator. *Applied Optics, 37*(21), 4891-4896. doi:10.1364/AO.37.004891

Varney, R. H., M. C. Kelley, M. J. Nicolls, C. J. Heinselman, & R. L. Collins. (2011). The electron density dependence of polar mesospheric summer echoes. *Journal of Atmospheric and Solar-Terrestrial Physics, 73*(14-15), 2153-2165. doi:10.1016/j.jastp.2010.07.020

Verdeyen, J. T. (1981). *Laser electronics.* Englewood Cliffs, NJ: Prentice-Hall Inc.

von Zahn, U., & J. Höffner. (1996). Mesopause temperature profiling by potassium lidar. *Geophysical Research Letters, 23*(2), 141-144. doi:10.1029/95gl03688

Walterscheid, R. L. (2001). Gravity wave transports and their effects on the large-scale circulation of the upper mesosphere and lower thermosphere. *Advances in Space Research, 27*(10), 1713-1721. doi:10.1016/S0273-1177(01)00298-8

Wayne, R. P. (1991). *Chemistry of atmospheres: an introduction to the chemistry of the atmospheres of earth, the planets, and their satellites* (2nd Ed.). Walton Street, Oxford OX2 6DP: Oxford University Press Inc.

Weinstock, J. (1981). Energy Dissipation Rates of Turbulence in the Stable Free Atmosphere. *Journal of the Atmospheric Sciences, 38*(4), 880-883. doi:10.1175/1520-0469(1981)038<0880:EDROTI>2.0.CO;2

White, M. A. (1999). *A frequency-agile Na lidar for the measurement of temperature and velocity in the mesopause region.* (Ph.D. dissertation), Colorado State University.

Whiteway, J. A., A. I. Carswell, & W. E. Ward. (1995). Mesospheric temperature inversions with overlying nearly adiabatic lapse rate: An indication of a well-mixed turbulent layer. *Geophysical Research Letters, 22*(10), 1201-1294

Williams, B. P., M. A. White, D. A. Krueger, & C. Y. She. (2002). Observation of a large amplitude wave and inversion layer leading to convective instability in the mesopause region over Fort Collins, CO (41°N, 105°W). *Geophysical Research Letters, 29*(17), 31-31-31-34. doi:10.1029/2001gl014514

Woodman, R. F., & A. Guillen. (1974). Radar Observations of Winds and Turbulence in the Stratosphere and Mesosphere. *Journal of the Atmospheric Sciences, 31*(2), 493-505. doi:10.1175/1520-0469(1974)031<0493:Roowat>2.0.Co;2

Wu, Q., W. S. Schreiner, S. P. Ho, H. L. Liu, & L. Qian. (2017). Observations and Simulations of Eddy Diffusion and Tidal Effects on the Semiannual Oscillation in the Ionosphere. *Journal of Geophysical Research, 122*(10), 10,502-510,510. doi:10.1002/2017JA024341

Xu, J., & A. K. Smith. (2003). Perturbations of the sodium layer: controlled by chemistry or dynamics? *Geophysical Research Letters, 30*(20). doi:10.1029/2003gl018040

Xu, J., & A. K. Smith. (2005). Evaluation of processes that affect the photochemical timescale of the sodium layer. *Journal of Atmospheric and Solar-Terrestrial Physics, 67*(13), 1216-1225. doi:10.1016/j.jastp.2005.06.007

Xu, J., A. K. Smith, R. L. Collins, & C.-Y. She. (2006). Signature of an overturning gravity wave in the mesospheric sodium layer: Comparison of a nonlinear photochemical-dynamical model and lidar observations. *Journal of Geophysical Research, 111*(D17). doi:10.1029/2005jd006749

Xu, J., A. K. Smith, W. Yuan, H.-L. Liu, Q. Wu, M. G. Mlynczak, & J. M. Russell III. (2007). Global structure and long-term variations of zonal mean temperature observed by TIMED/SABER. *Journal of Geophysical Research: Atmospheres, 112*(D24). doi:10.1029/2007jd008546

Yuan, T., P. D. Pautet, Y. Zhao, X. Cai, N. R. Criddle, M. J. Taylor, & W. R. Pendleton. (2014). Coordinated investigation of midlatitude upper mesospheric temperature inversion layers and the associated gravity wave forcing by Na lidar and Advanced Mesospheric Temperature Mapper in Logan, Utah. *Journal of Geophysical Research: Atmospheres, 119*(7), 3756-3769. doi:10.1002/2013JD020586

Yuan, T., H. Schmidt, C. Y. She, D. A. Krueger, & S. Reising. (2008). Seasonal variations of semidiurnal tidal perturbations in mesopause region temperature and zonal and meridional winds above Fort Collins, Colorado (40.6°N, 105.1°W). *Journal of Geophysical Research: Atmospheres, 113*(D20). doi:10.1029/2007jd009687

Yuan, T., J. Yue, C.-Y. She, J. P. Sherman, M. A. White, S. D. Harrell, et al. (2009). Wind-bias correction method for narrowband sodium Doppler lidars using iodine absorption spectroscopy. *Applied Optics, 48*(20), 3988-3993. doi:10.1364/AO.48.003988

Yue, X., J. S. Friedman, Q. Zhou, X. Wu, & J. Lautenbach. (2019). Long-term lidar observations of the gravity wave activity near the mesopause at Arecibo. *Atmos. Chem. Phys.,* *19*(5), 3207-3221. doi:10.5194/acp-19-3207-2019